Development and Assessment of New Post-Processing Methodologies in 3D Contrast Enhanced MRI

David Brennan BSc, MSc

This thesis is submitted for the degree of PhD to

Glasgow University

Faculty of Medicine

March 2004

Acknowledgements

Out of all the pages in this PhD this was the hardest to write. My words will never do justice to the help and support I have received over the years. However, the risk of failure has never stopped me trying! I would like to thank all the following people that I have known and have helped me during this thesis.

Dr Jim Patterson and Prof Dave Wyper for their guidance and support and general cajoling. Anna, Miffy and Jen for putting up with my grumpiness and general despondency about everything 'PhD', and for reminding me every so often that I can do it. Everyone in clinical physics for making my work an enjoyable and fun place.

An extra big thanks go to Dr Barrie Condon for supervising me. Hopefully, I didn't stress you too much and I look forward to a pint (or three) at the end of this!

Prof Donald Hadley and Dr Joe Bhattacharya for their expert help in objectively assessing the venography data in chapter 2 (section 2.5.1.3) and thanks also to Donald for letting me print this thesis on his nice new printer! Also a big thank-you to everyone in Neuroradiology, especially the radiographers who were very accommodating, even when I barged in the way of their work! Thank you also to the radiographers for scanning the patients for this thesis (chapters 2, 3, 4, 5, 6 & 8).

For the supply of free software, Martin Connell (3dMRI and conv_analyze) and Prof J Hajnal and his group (MATCH).

I would also like to thank my many friends who have kept me sane during this marathon. Jerome and Lawrence (the Irish contingent), Chris Jarvis, Jens, Natalie and wee Marc (and the one that's on the way!), Rhona and Nick, Paul and Tanya, Big George and all at Glasgow University Judo Club. You all kept me laughing even when you injured me!!?!? Thanks also to Caroline and Ruth for keeping Philippa amused when I was working!

My mum and Jacqueline. Without your help, support and guidance I would never be anywhere near where I am today. Hopefully my dad would have been proud.

Also thanks to Bill for looking after my mum and being a good family friend.

And finally Philippa. Ever since you've known me you've had to deal with the baggage that a PhD brings with it. Your days as taxi driver are at an end (well almost!). You've always had faith in me and kept me smiling when I was feeling low. I'm looking forward to seeing you in the evening and at weekends (I hope you are too!). Thank-you!!!

Contents

List of Figures, Tables and Graphs

Figures

Graphs

Graphs

Tables

Publications and Presentations

Chapter 2

Brennan D, Condon B, Hadley D. The application of subvoxel coregistration in subtraction venography: a comparison with non-registered data. Proceedings of ISMRM (Philadelphia) 1999: 2177.

Chapter 3

Brennan D, Hadley D, Patterson J, Condon B. Comparison of MRI and SPECT volume measurement following minimally invasive surgery for a phase 1 trial of a genetically modified viral therapy. Proceedings of ISMRM 2001: 1397.

Brennan D, Hadley D, Patterson J, Condon B. Comparison of MRI and SPECT tumour volume measurement following minimally invasive surgery. 6th British ISMRM Meeting (Liverpool) 2000.

Chapter 4

Brennan D, Condon B, Hadley D. Determining the effects of segmentation accuracy on the registration of pre- and post-gadolinium MR images. Proceedings of the ISMRM (Glasgow) 2002: 2479.

Abbreviations

AVM	Arterio-Venous Malformation
BBB	Blood Brain Barrier
BOLD	Blood Oxygenation Level Dependant
CNR	Contrast to Noise Ratio
CSF	Cerbro Spinal Fluid
CT	Computed Tomography
CVT	Cerebral Venous Thrombosis
FLASH	Fast Low-Angle Shot
fMRI	Functional Magnetic Resonance Imaging
FOV	Field of View
GE	Gradient Echo
GRASS	Gradient Acquisition in Steady State
HSV	Herpes Simplex Virus
HUM	Homomorphic Unsharp Masking
IDL	Interactive Display Language
IR FSPGR	Inversion Recovery Fast Spoiled Gradient
MIP	Maximum Intensity Projection
MNI	Montreal Neurological Institute
MP RAGE	Magnetization Prepared Rapid Gradient Echo
MRA	Magnetic Resonance Angiography
MRI	Magnetic Resonance Imaging
MSV	MP RAGE Subtraction Venography
NMR	Nuclear Magnetic Resonance
PC	Phase Contrast
RF	Radio Frequency
ROI	Region of Interest
SNR	Signal to Noise Ratio
SPECT	Single Photon Emission Computed Tomography
SPGR	Spoiled Gradient
TE	Echo Time
TI	Inversion Time
TOF	Time of Flight
TR	Repetition Time
3D	Three Dimensional
2D	Two Dimensional

Summary

This thesis aims to investigate some of the methods currently used in contrast MR imaging. It specifically focuses on methods that require subtraction of non-contrast enhanced (pre) 3D imaging data sets from contrast-enhanced (post) data, collected within a single imaging session. Current methods assume that there is little or no intra-scan patient motion and thus do not attempt to correct for this. This thesis aims to determine if such motion does exist and if so what methods are best suited to correct it.

The thesis begins by describing some of the relevant MR physics and history of contrast enhancement in chapter 1, and expands on this in chapter 2 by focusing on angiographic, and contrast-enhanced techniques. Chapter 2 continues by investigating an MP RAGE subtraction technique for producing venograms, which requires pre and post-contrast data subtraction. Data is collected for 20 patients and the effects of motion correction on the resulting venograms are investigated. The use of a realignment algorithm, MATCH, is shown to improve venous visualisation demonstrating that intra-scan patient motion does indeed affect this type of study.

Chapter 3 investigates a different type of pre and post-contrast enhanced study where it is used for tumour volume measurement. Examining the effects on tumour volumes measured with and without the realignment correction provides quantitative evidence that realignment is a requirement in this and similar types of study.

It is a requirement of realignment algorithms in general that segmentation of brain parenchyma is provided to ensure that the realignment is as accurate as possible. It has previously been suggested that including structures in segmented data that change in signal or morphology between two data sets results in realignment

errors. However, accurate segmentation of the brain parenchyma requires either manual segmentation, which needs a skilled operator to achieve and is very time consuming, or a computer algorithm to do the segmentation automatically or semi-automatically. There is, however, no algorithm yet available that is designed to segment post-contrast data sets, therefore, it is important to determine the effects of segmentation accuracy on the accuracy of realignment of pre and post-contrast data set.

If segmentation is indeed required it is important to determine the effects that such inaccuracies in segmentation have on realignment. This knowledge would allow computational techniques to be developed. Therefore, to enable the significance of segmentation accuracy on realignment to be tested a phantom pre and post-contrast data set is developed in chapter 4.

Chapter 5 uses this data set to test the effects of differing segmentation accuracies, with respect to the accurately segmented phantom data, on realignment accuracy where the pre and post-contrast data differ by known rotations and translations. This provides information on the effects of contrast-enhancement on realignment accuracy, as well as providing information on the required brain segmentation accuracy required to accurately realign these data sets.

Chapter 6 expands on this work by testing segmentation accuracy effects on two real patient data sets. The first patient data set differs from the phantom data in terms of its noise characteristics and the second has a space occupying lesion similar to those regularly encountered in the clinical setting.

The results from chapters 5 and 6 suggest that all contrast-enhancement must be removed from post-contrast data to ensure that the resulting realignment is accurate. However, it is also found that the brain parenchyma can be over-segmented

by approximately 20% without seriously compromising realignment accuracy. This finding has important implications for the design of segmentation algorithms to be used with these data sets. Due to the varying nature of the contrast-enhancement from patient to patient, especially in the clinical setting, it is difficult to consistently segment post-contrast data sets to a high degree of accuracy. Therefore, knowing that significant over-segmentation is acceptable enables a simple yet robust method of segmentation to be developed.

Using the information from the previous chapters, chapter 7 aims to develop an automatic technique for segmenting, realigning and visualising venographic data using the venography technique described in chapter 2. It uses a histogram and morphological operations to ensure that all of the contrast-enhanced data is removed from the data, whilst attempting to segment the brain to an acceptable accuracy. Although this algorithm is specifically designed for venograms visualisation, it would require only a small amount of adjustment enabling it to be applied to the tumour volume measurement technique described in chapter 3.

Chapter 8 tests this algorithm using the data collected in chapter 2 and measures its performance in producing satisfactory brain segmentations, which is required for accurate realignment. This would also be required for accurate realignment in tumour volume measurement studies. Chapter 8 also measures the algorithms capabilities in correctly producing visualisation data sets for the purposes of venography.

The algorithm has limited success in both brain segmentation and venous visualisation, nevertheless this is encouraging as a first attempt as the algorithm is being applied to real patient data sets reflecting a range of pathological conditions and not only to selected normal data sets. Chapter 8 suggests some modifications that

could be applied to the algorithm that might improve its future success. This includes modifying it to become a semi-automated technique.

Chapter 1

Introduction

1.1 Historical Introduction

1.1.1 MRI

Magnetic resonance imaging, often referred to as MRI, has a history of development which began in 1936 when the Dutch physicist C.J. Gorter developed a technique for measuring the nuclear magnetic moment, although he was unsuccessful in detecting the effect. Rabi was finally successful in detecting the effect in 1938 (Rabi *et al* 1938). However, it was Bloch and Purcell who first demonstrated the NMR technique in 1946 with Bloch demonstrating NMR in water and Purcell demonstrating the technique in solid paraffin (Bloch *et al* 1946 and Purcell *et al* 1946). At the time these results were only of interest to those in the field of nuclear physics, however the technique was soon adopted in the field of chemistry with the development of NMR spectroscopy (Waugh 1993).

The first suggested use of magnetic resonance in the field of medicine was by Damadian in the early 1970's (Damadian 1971). He suggested that the technique of nuclear magnetic resonance could be used to differentiate tumour tissue from normal tissue using an NMR tissue parameter T1. His technique could however only be used in vitro and was not confirmed by other workers.

It was not until 1973, however, when Lauterbur first introduced the concept of using magnetic field gradients to encode position-dependant imaging information, that there was any suggestion of using the NMR technique for producing spatial NMR information (Lauterbur 1973). In this short paper Lauterbur described a technique using weak gradient fields in conjunction with a stronger main magnetic field that was able to spatially distinguish between two test tubes of water. This new technique, which Lauterbur described as zeugmatography later became known as Magnetic Resonance Imaging or MRI.

A few years passed before any major attempts were made to improve this technique. However in the late 1970's a number of groups began developing MRI systems including Nottingham (Mansfield & Maudsley 1977), Aberdeen (Mallard *et al* 1979) and EMI. During this time the imaging techniques were refined with the development of several new imaging techniques including the revolutionary development of spin warp imaging in 1980 (Edelstein *et al* 1980) following on from the two dimensional Fourier transform method developed by Kumar *et al* (Kumar *et al* 1975). The spin-warp technique proved to be the imaging technique utilised in most commercial MRI scanners to follow (Chen and Hoult 1989).

In the late 70's and early 80's a number of companies became involved in MRI scanner construction. These included eight companies who by 1983 had completed prototypes. These were: Bruker Instruments, Diagnostic Inc, FONAR, Philips Medical Systems, Picker International, Siemens Medical Systems, Technicare Corp, and Elscint Ltd (Stanford Research Institute (SRI) International web site, accessed August 2003). Other companies involved at this time were General Electric, M&D Technology, and Toshiba. With increased industrial input into scanner design and development and as a result of insurance companies beginning to provide remuneration for MRI scans in 1985, MRI scanners use began to grow and by 1988 approximately 1300 units had been sold worldwide.

Since then MRI has developed from its relatively modest roots into one of the most powerful diagnostic imaging aids of the 21st century, along with CT. According to Guerbet, who supply contrast agents for MRI, there are estimated to be approximately 13,000 MRI scanners currently worldwide (Guerbet website strategy document, March 2003) with many millions of examinations conducted each year.

The MRI hardware, along with the sequences and techniques used, has progressed at a great pace with a number of major advances taking place including: the introduction of gradient echo sequences (van der Meulen *et al* 1985) the introduction of contrast enhanced procedures (Carr *et al* 1984), development of echo planar imaging (EPI) (Mansfield and Morris 1982, Perkins and Wehrli 1986). Imaging gradients and main field strengths are also increasing especially in neurological imaging, with typical B_0 fields beginning to increase from a standard 1.5 Tesla field to 3 Tesla. These advances have led to new areas of research and new clinical techniques such as perfusion and diffusion imaging, fMRI and multi-voxel spectroscopy.

1.1.2 Contrast Imaging

Despite the improvements in image hardware and techniques, many of the sequences and principles have remained the same during the development and maturation of MRI.

For example Schering developed the first contrast agent in 1981 with a patent application for Gd-DTPA dimeglumine (Magnevist German Patent 1981). This was first used in human MRI in 1984 where the contrast agent was intravenously injected into 20 patients at a dose of 0.1 mmol/kg (Carr *et al* 1984). The injected contrast improved the delineation of cerebral and hepatic tumours, allowing tumour to be distinguished from peritumoural edema. The effect of this contrast agent on different sequences was theoretically assessed one year later (Gadian *et al* 1985). This method of using contrast enhancement can be described as static contrast enhanced MRI. Magnevist, as Scherings contrast agent later became known, soon became commercially available and to this day is still one of the contrast agents of choice,

especially in investigations of high-grade cerebral tumours where tumour progression is being assessed using the static contrast enhanced method.

Despite significant advances being made in the use of contrast agents with the development of new techniques such as timed contrast enhanced MRI and perfusion contrast enhanced MRI (Roberts *et al* 2000), in many MRI departments the vast majority of contrast use continues to be for static contrast enhanced MRI. The injection technique and dose have remained the same since the first set of investigations in 1984 (Carr *et al* 1984), although there are suggestions that the required dose is reduced at 3T. Figure 1.1 shows some typical slices from a contrast enhanced image set.

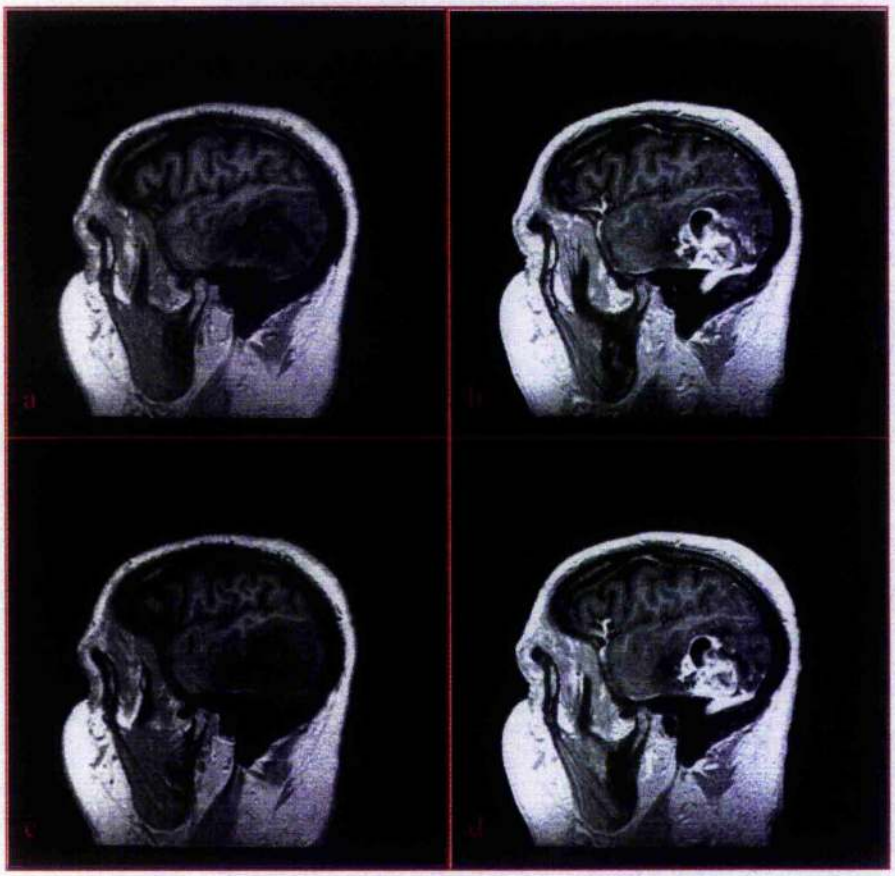

Figure 1.1: Two pre (a & c) and post (b & d) contrast enhanced sagittal slices from a 3D T1-weighted study: these slices show contrast enhancement of a high grade cerebral tumour (Glioblastoma)

1.2 Theory of Contrast Enhancement

1.2.1 Why do we need contrast agents?

Magnetic resonance imaging offers a variety of sensitivities to physiological parameters of tissue, allowing tissues and pathologies to be delineated on the basis of differences in the local physical and chemical microenvironment. By appropriate choice of pulse sequence parameters it is possible to produce imaging sequences with contrast dependant on one or more of a number of these physiological parameters.

For example sequences can be optimised to enhance the T_1 or T_2 characteristics or to display contrast weighted towards the proton density of the tissue, to enhance local blood or CSF flow, to determine the perfusion or diffusion of a tissue and so on. However, even with the large amount of physiological parameters available to measure in MRI there are still clinical situations and pathologies where the use of contrast increases the available information, such as in flow and perfusion studies (Merbach and Toth 2001). Therefore, as described in section 1.1.2, contrast media were introduced early in the development of MRI with the aim of enhancing the contrast between normal and diseased tissue, highlighting areas of blood brain barrier breakdown or to indicate organ function or blood flow.

However, to understand the theory behind using contrast agents in MRI we must first understand the basic principles underlying signal and contrast in MRI.

1.2.2 Signal in MRI – Macroscopic Magnetisation in a B_0 field

As has been described earlier MRI is fundamentally based on the principles of NMR, where NMR describes the interaction of spinning atomic nuclei and magnetic fields.

The spin of a nucleus is composed of the individual spins of the protons and neutrons contained within the nucleus. Nuclear spin (I) is a quantum mechanical quantity. It is represented by a vector which is orientated parallel to its axis of rotation, with a magnitude given by the following:

$$|\mathbf{I}| = \hbar\sqrt{I(I+1)} \tag{1.1}$$

and,

$$\hbar = h/2\pi \tag{1.2}$$

where $\hbar$ is the Planck constant and I is the spin quantum number. This overall spin depends on the number of unpaired protons and neutrons within the nuclear shells with each unpaired proton or neutron having a spin of either ½ or –½. Therefore different isotopes of the same element can have different nuclear spins. Nuclei with no overall spin cannot be investigated using NMR techniques, however, there are a significant number of nuclei with spin. Table 1 describes the spin state of some of the more important NMR nuclei.

Nuclei	Unpaired Protons	Unpaired Neutrons	Net Spin	γ (MHz/T)
^{1}H	1	0	½	42.58
^{2}H	1	1	1	6.53
^{31}P	1	0	½	17.25
^{23}Na	1	2	3/2	11.27
^{14}N	1	1	1	3.08
^{13}C	0	1	½	10.71
^{19}F	1	0	½	40.08

Table 1: Spin states in a selection of nuclei important to NMR

When a nucleus with a non zero spin is placed within an external magnetic field it acts in a similar fashion to a compass needle, i.e. it aligns itself with the main magnetic field. However, due to the rules of quantum mechanics, the nuclei can only align with the magnetic field in discrete directions which correspond to the energy levels of the nucleus. It can be shown that when a nucleus with a spin number I is placed within a magnetic field $\boldsymbol{B_0}$ that the magnetic quantum m_I number can take one of $2I+1$ values. So for example in a $\boldsymbol{B_0}$ field a ^{1}H nucleus can have one of two possible orientations with either $m_I = +½$ or $-½$ (see figure 1.2).

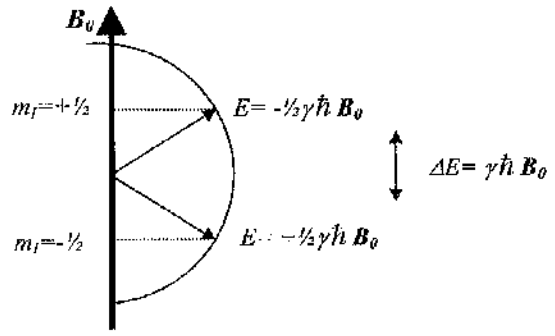

Figure 1.2: Orientation of the spin ½ nucleus (proton) in a $\boldsymbol{B_0}$ magnetic field along the z-direction

The nuclear spin angular magnetic moment, which can be assumed classically to represent a ring current with negligible dimension, results in a dipolar magnetic moment μ which is a vector quantity aligned parallel to nuclear spin $\boldsymbol{I}$. Its magnitude can be defined by the following relationship:

$$\mu = \gamma \mathbf{I} \tag{1.3}$$

where γ is the gyromagnetic ratio, which is specific for different nuclei and isotopes. Due to the relationship between the nuclear spin and the magnetic moment in the direction of the main field (the z direction by convention) μ_z is restricted to related values:

$$\mu_z = \gamma m_I \hbar \tag{1.4}$$

with

$$m_I = -I, -I+1, ..., I \tag{1.5}$$

When a magnetic moment is placed in a magnetic field $\boldsymbol{B_0}$ it represents a magnetic energy E such that:

$$E = -\mu \cdot \mathbf{B_0} \tag{1.6}$$

therefore, the energy states of the nucleus are given by the following equation:

$$E = -\gamma \hbar m_I B_0 \tag{1.7}$$

Figure 1.2 shows the resulting energy diagram for a hydrogen nucleus with $I = ½$.

Transitions between states can take place only if the quantum mechanical selection rule which states that m_I must change by ±1 is obeyed. Therefore, a change from one level to the next either requires energy input to go to a higher level, or requires emission of energy if it is to drop an energy level, equivalent to:

$$\Delta E = \gamma \hbar B_0 \tag{1.8}$$

The change in energy is supplied by, or emitted as, electromagnetic radiation where:

$$\Delta E = h\nu_0 \tag{1.9}$$

where ν_0 is the frequency of the electromagnetic radiation. Thus, with the angular frequency $\omega_0=2\pi\nu_0$ it is possible to relate this to the field:

$$\omega_0 = \gamma B_0 \tag{1.10}$$

As was described previously the magnetic moment and the nuclear spin are coupled together, therefore the magnetic moment will always be at an angle to the main magnetic field. Therefore, the nuclear spin will precess around the main $\boldsymbol{B_0}$ field with a frequency equivalent to the angular frequency of the magnetic moment:

$$\omega_L = \omega_0 \tag{1.11}$$

where ω_L is called the Larmor frequency.

Despite the large number of naturally occurring nuclei with appropriate spin values the vast majority of MRI techniques investigate the ^{1}H nucleus (i.e. a single proton). This is a result of the high natural abundance of this nuclei in the human body, which is made up of approximately 80% water and because of its favourable magnetic moment compared to other naturally occurring elements. The large number of nuclei allow for sufficient signal to be detected despite the small amount of signal per nucleus and the fact that only a small number of nuclei contribute to the final signal due to thermal motion effects.

In the steady state slightly more than half of the hydrogen nuclei are in the parallel low energy state, i.e. aligned with the field rather than against it. For example in a large population of hydrogen nuclei, which is common in a normal biological NMR sample ($\approx 10^{22}/cm^3$) with a spin quantum number of I and thus $2I+1$

energy states the distribution of the spins in each state is, in thermal equilibrium, governed by the Boltzmann law:

$$N_m = N_0 \frac{\exp(-E_m/(k_B T))}{\sum_{n=-I}^{n=I} \exp(-E_m/(k_B T))} \tag{1.12}$$

where N_m is the number of spins in the state m, N_0 is the total number of spins in the sample, E_m is the energy of the state m, T is the absolute temperature and k_B is the Boltzmann constant. Thus with increasing energy the number of spins in each energy state decreases with increasing energy (temperature).

In a large sample there will be a macroscopic magnetisation associated with the sum of all the individual microscopic magnetisations:

$$\mathbf{M} = \sum \mu \tag{1.13}$$

However, in an unexcited sample there will be no overall x or y component to the overall magnetisation due to the random phase distribution of the individual precessing magnetic moments.

Despite this incoherence in the x-y plane there will be coherence in the z direction due to the fact that there is a restricted number of discrete values for each individual magnetic moment. In ^{1}H there are only two possible states. Using Boltzmann's law it is possible to determine the relative concentration of these two energy states:

$$\frac{N\uparrow}{N\downarrow} = \exp(\gamma\hbar B_0/(k_B T)) \tag{1.14}$$

For example in a typical MRI magnetic field strength of 1.5T, at a room temperature of 295K the ratio of $\frac{N\uparrow}{N\downarrow}$ for a ^{1}H nucleus is 1.000010401. This represents a very small number of excess spins parallel to the $\boldsymbol{B_0}$ field, which results

in the macroscopic magnetisation M parallel to the applied field. Although in this situation M only has a z component M_z, it is useful to consider the magnetisation rotating in the x-y plane at the Larmor frequency ω_L. This becomes more apparent when the magnetisation is tipped into the x-y plane.

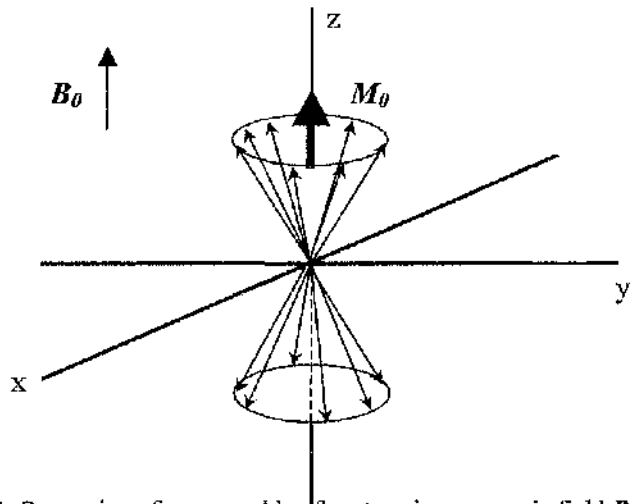

Figure 1.3: Precession of an ensemble of protons in a magnetic field B_0 producing a net magnetisation M_0 in the z-direction

1.2.3 Signal in MRI – Macroscopic Magnetisation in Presence of a B_1 field

In section 1.2.2 the sample was at equilibrium. It is therefore possible to describe the time variation of M using:

$$\frac{dM}{dt} = \gamma M \times B_0 \tag{1.15}$$

In this case all of the macroscopic magnetisation is in M_z. It is only possible to detect a time varying signal in the sample when a proportion of the magnetisation is in M_x or M_y. Therefore, before signal can be produced within the sample the magnetisation must be perturbed from its steady state. This is achieved by introducing a time varying B_1 magnetic field oscillating at radiofrequencies, referred to as the RF pulse.

The magnetic field vector of the RF pulse can be pictured as rotating in the xy plane perpendicular to $\boldsymbol{B_0}$. (See figure 1.4).

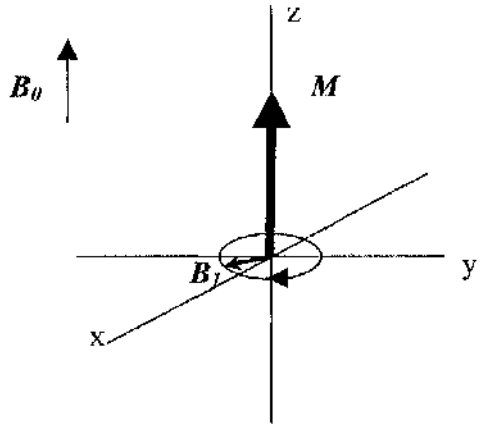

Figure 1.4: Rotation of the RF magnetic field ($\boldsymbol{B_1}$) just as the RF pulse is turned on (t=0)

Thus it is possible to determine the components of total field in the presence of the RF pulse with reference to the fixed laboratory frame of reference:

$$\boldsymbol{B}_x = \boldsymbol{B}_1 \cos \omega t, \qquad \boldsymbol{B}_y = -\boldsymbol{B}_1 \sin \omega t, \qquad \boldsymbol{B}_z = \boldsymbol{B}_0 \qquad (1.16)$$

Remembering equation (1.15) it is possible using matrix notation to determine the cross product of the magnetisation and field vectors:

$$\boldsymbol{M} \times \boldsymbol{B} = \begin{vmatrix} M_x & B_x & \mathbf{i} \\ M_y & B_y & \mathbf{j} \\ M_z & B_z & \mathbf{k} \end{vmatrix} = (M_y B_z - M_z B_y)\mathbf{i} + (M_z B_x - M_x B_z)\mathbf{j} + (M_x B_y - M_y B_x)\mathbf{k} \qquad (1.17)$$

It is therefore possible from the above three equations to determine the time dependence for the components of $\boldsymbol{M}$:

$$\frac{dM_x}{dt} = \gamma(M_y B_0 + M_z B_1 \sin \omega t),$$
$$\frac{dM_y}{dt} = \gamma(M_z B_1 \cos \omega t - M_x B_0), \qquad (1.18)$$
$$\frac{dM_z}{dt} = -\gamma(M_x B_1 \sin \omega t + M_y B_1 \cos \omega t)$$

We can now assume that we have a rotating frame of reference x' y' z', rotating at ω_0, to simplify the analysis. Therefore, if a $\boldsymbol{B_1}$ field is turned on during a time t_p, $\boldsymbol{M}$ will rotate an angle $\beta_1 = \omega_1 t_p$ from its original position down towards the x'y' plane. (see figure 1.5). The angle β_1 is usually called the flip angle of the pulse.

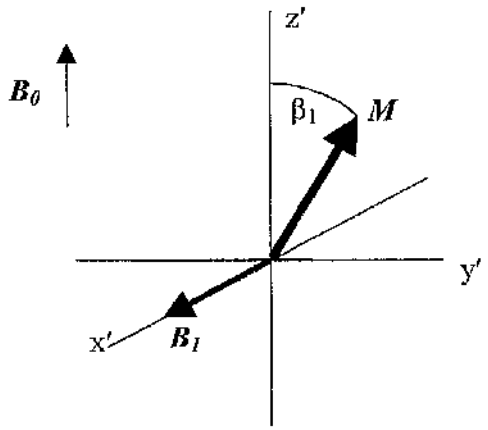

Figure 1.5: As a result of the $\boldsymbol{B_1}$ component of the RF pulse the magnetisation $\boldsymbol{M}$ is flipped towards the x'y' plane

1.2.4 Signal in MRI – Relaxation Processes

After the RF field is turned off, $\boldsymbol{M}$ will have a component in the x'y' plane. Viewed in the non-rotating laboratory frame this component will rotate around $\boldsymbol{B_0}$ at the Larmor frequency, inducing detectable current in any receiver coil within range of the signal.

However, the above equations are incomplete as they do not take into account the two relaxation processes present in these systems, namely T1 and T2. T1

relaxation is known as the spin lattice relaxation. This relaxation process involves the exchange of energy between the spin system (i.e. each individual proton in a large ensemble of similar protons) and the lattice in which they are embedded (i.e., the molecular framework). More precisely in quantum mechanical terms the majority of spins in the high energy state can only make the transition to the lower energy state by the process of stimulated emission. That is, to undergo a transition, the spin needs to be stimulated by a fluctuating magnetic field at the Larmor frequency. The random motion of the surrounding nuclei within the medium form these fluctuating magnetic fields. It is the rate of motion of the surrounding molecules that determines the time constant T1. T1 is often referred to as a longitudinal relaxation process.

T2 relaxation is known as spin-spin relaxation. In T2 relaxation no energy is transferred from the nuclei to the lattice, instead energy is redistributed between the spins. The simplest way to describe T2 relaxation is to introduce a 90^0 flip of the magnetisation $\boldsymbol{M}$ into the transverse (x'y'-plane). (See figure 1.6).

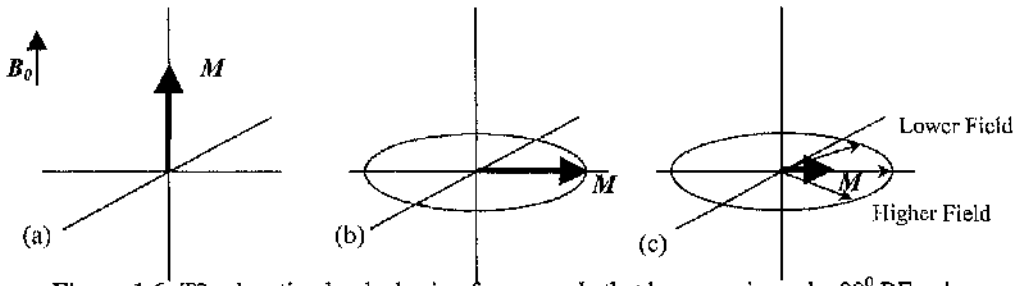

Figure 1.6: T2 relaxation by dephasing for a sample that has experienced a 90^0 RF pulse

Immediately following a 90^0 RF pulse all of the magnetisation that was aligned along the z-axis is tipped into the transverse plane (figure 1.6(b)). In an ideal sample (assuming there are no field inhomogeneities) all of the nuclei will

experience the same applied magnetic field. Thus, the multitude of individual magnetic moments will remain coherent, rotating at the Larmor frequency until T1 relaxation occurs. However in a real sample random tumbling of the neighbouring nuclei affect this coherence via low frequency random fluctuations in the local field. Each nucleus therefore experiences slightly different local magnetic fields, with some slightly larger and some slightly smaller than $\boldsymbol{B_0}$. This spread in local fields results in a related spread in rotational frequency, resulting in dephasing of the magnetic moments over time (see figure 1.6(c)) with the resulting decrease in transverse magnetisation. After a long enough time the phases will be completely dephased resulting in complete loss of measurable transverse magnetisation.

1.2.5 Signal in MRI – Bloch Equations

In section 1.2.3 the time dependence of $\boldsymbol{M}$ was described in terms of $\boldsymbol{B_0}$ and $\boldsymbol{B_1}$ (equations 1.18). However, these equations did not take into account the T1 and T2 relaxation processes. Remembering that the T1 relaxation relates to the longitudinal relaxation in the z-direction and that T2 relates to the transverse relaxation in the xy plane it is possible to derive the following:

$$\frac{dM_x}{dt} = -\frac{M_x}{T2}, \frac{dM_y}{dt} = -\frac{M_y}{T2}, \frac{dM_z}{dt} = -\frac{M_z - M_0}{T1} \qquad (1.19)$$

Superimposing the relaxation effects into equations described by 1.18 produces the Bloch equations, which relate to rate of change of magnetisation in the laboratory reference frame:

$$\begin{aligned}
\frac{dM_x}{dt} &= \gamma(M_y B_0 + M_z B_1 \sin\omega t) - \frac{M_x}{T2}, \\
\frac{dM_y}{dt} &= \gamma(M_z B_1 \cos\omega t - M_x B_0) - \frac{M_y}{T2}, \\
\frac{dM_z}{dt} &= -\gamma(M_x B_1 \sin\omega t + M_y B_1 \cos\omega t) - \frac{(M_z - M_0)}{T1}
\end{aligned} \tag{1.20}$$

These equations can also be derived in the rotating frame, resulting in the following equation:

$$\frac{d\boldsymbol{M}}{dt} = \gamma \boldsymbol{M} \times \boldsymbol{B}_{eff} - \boldsymbol{R}(\boldsymbol{M} - \boldsymbol{M}_0) \tag{1.21}$$

where, using matrix notation:

$$\boldsymbol{R} = \begin{bmatrix} \frac{1}{T1} & 0 & 0 \\ 0 & \frac{1}{T1} & 0 \\ 0 & 0 & \frac{1}{T2} \end{bmatrix} \text{ and } \boldsymbol{M}_0 = \begin{bmatrix} 0 \\ 0 \\ M_0 \end{bmatrix} \tag{1.22}$$

and $\boldsymbol{B}_{eff}$ is the effective field given by $\boldsymbol{B}_{eff} = \boldsymbol{B}_0 + \boldsymbol{B}_1 + \boldsymbol{\Omega}/\gamma$ (where $\boldsymbol{\Omega}$ is a vector pointing in the opposite direction to $\boldsymbol{B}_0$ with the value of the Larmor frequency)

These equations describe the transverse and longitudinal magnetisation. From these equations it is possible to develop pulse sequences that produce particular contrasts for different tissues, assuming that the T1 and T2 values for the tissues in question are known.

1.2.6 Signal in MRI – Signal development

If we assume a rotating reference frame (which simplifies the analysis), immediately following an RF pulse equation 1.21 can be solved as follows:

$$M_z(t) = M_0(1-\exp(-t/T1)) + M_z(t_0)\exp(-t/T1),$$
$$M_{xy}(t) = M_{xy}(t_0)\exp(-t/T2) \quad (1.23)$$

where $M_z(t_0)$ and $M_{xy}(t_0)$ are the longitudinal and transverse magnetisations just following the cessation of the RF pulse.

If a conductive coil is now placed close to the excited sample in an orthogonal orientation the relaxation and rotation of $\boldsymbol{M}_{xy}$ will induce an electric signal within the coil. This rotating magnetisation produces a sinusoidal signal within the coil. However, as has previously been discussed, relaxation occurs reducing the amplitude of the signal over time:

$$V_{induced} \propto \boldsymbol{M}_{xy}^{90} \cos \omega t \quad (1.24)$$

where $V_{induced}$ is the voltage induced in the coil and $\boldsymbol{M}_{xy}^{90}$ is the initial magnetisation in the xy plane following an RF pulse that flips the magnetisation into the xy plane (a 90^0 pulse). The signal induced and its decay is known as the free induction decay (FID) signal.

1.2.7 Signal in MRI – Pulse Sequences (2D)

Signal development is more complex when pulse sequences are run to generate MR images. The simplest imaging technique available is the spin echo (SE) sequence. In a basic SE sequence (see figure 1.7), signal from different tissues can be derived from the following equation:

$$S_{SE} \propto M_0\left[1 \cdot 2\exp\frac{-(TR-TE/2)}{T1} + \exp(-TR/T1)\right]\exp(TE/T2) \qquad (1.25)$$

where TR is the interval between two successive 90 degree pulses and TE is twice the time from the RF pulse to the 180 degree pulse, where the 180 degree pulse refocuses the signal at time TE as a spin echo.

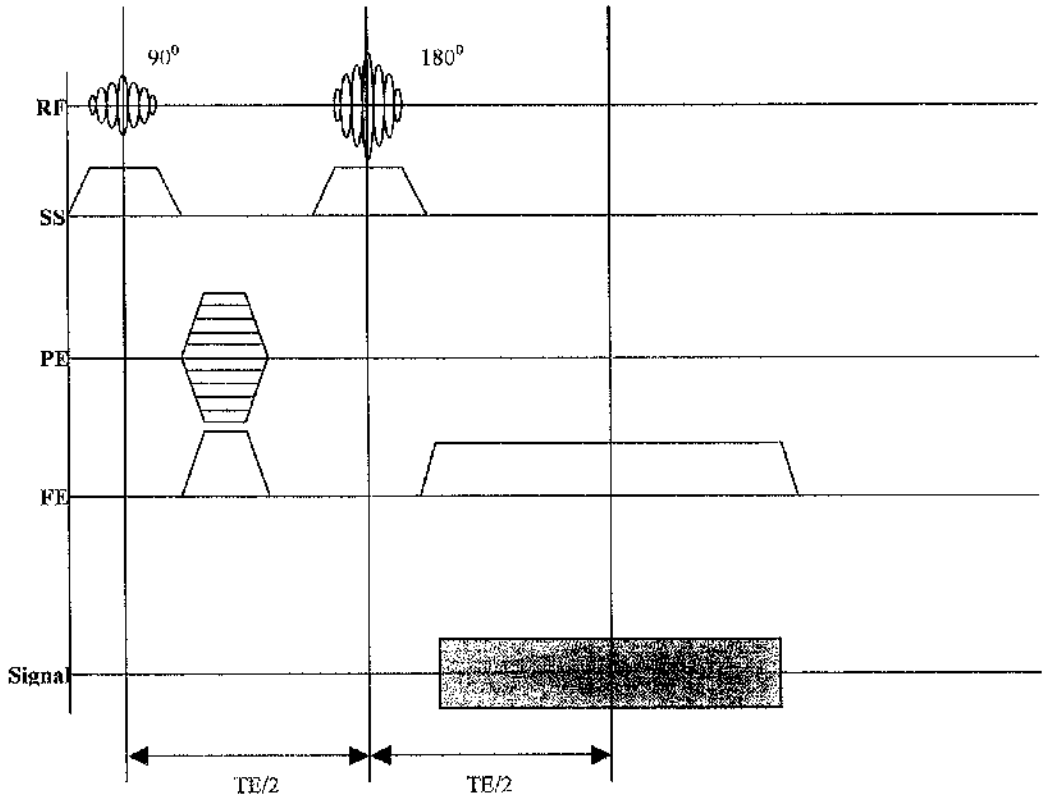

Figure 1.7: Pulse sequence diagram for a simple spin echo sequence
(RF represents the RF pulses, SS represents the slice-select gradients, PE represents the phase-encode gradients and FE represents the frequency-encoding gradients)

If it is assumed that TE is small compared to TR, which is often the case, equation (1.25) can be simplified to:

$$S_{SE} \propto M_0\left[1-\exp(-TR/T1)\right]\exp(TE/T2) \qquad (1.26)$$

To obtain good signal strength from SE sequences magnetisation needs to recover fully before the next RF pulse. Therefore, optimal SE sequences require long scan times. If TR is shortened the spin system become saturated resulting in weaker signal. One method of regaining signal is to reduce the flip angle from 90^0 to a smaller flip, thus reducing the time required for the magnetisation to recover. However, in SE the 180^0 refocusing pulse would invert the longitudinal magnetisation. As TR was shortened this would eventually drive the longitudinal magnetisation to zero. Thus to solve this problem a new type of pulse sequence was developed where the 180^0 RF pulse is replaced by a rephasing gradient in the frequency direction (see figure 1.8).

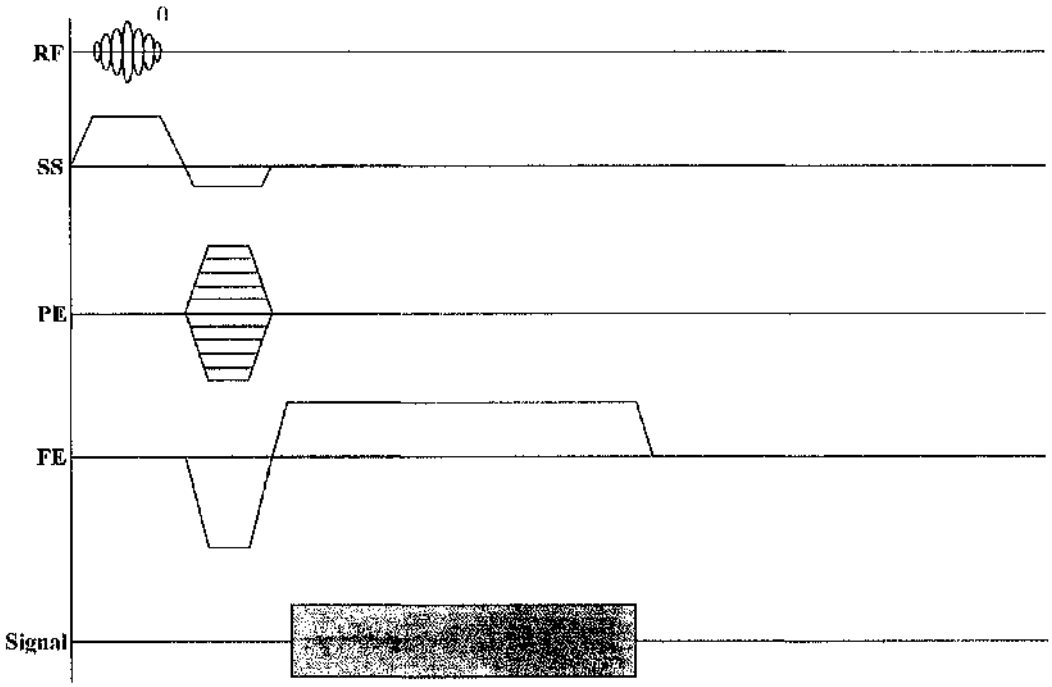

Figure 1.8: Pulse sequence diagram for a simple gradient echo sequence. θ is the flip angle of the RF pulse and is typically less than 90^0.

There are a large number of gradient echo (GE) sequences available with different characteristics. One simple GE sequence is the gradient-recalled acquisition

in the steady state (GRASS). In this sequence signal can be shown to vary as follows (Wehrli FW 1988):

$$S_{GRASS} \propto M_0 \frac{(1-\exp(-TR/T1))\sin\theta}{1-\exp(-TR/T1)\exp(-TR/T2)-\cos\theta(\exp(-TR/T1)-\exp(-TR/T2)} \cdot \exp(-TE/T2^*) \quad (1.27)$$

where T2* is the effective transverse relaxation which includes field inhomogeneity dephasing effects, and θ is the flip angle. If TR>>T2*, which is a reasonable assumption the equation can be simplified to:

$$S_{GRASS} \propto M_0 \frac{(1-\exp(-TR/T1))\sin\theta}{1-\cos\theta\exp(-TR/T1)} \cdot \exp(-TE/T2^*) \quad (1.28)$$

It can be seen from equation (1.28) that in GE sequences there is a strong T2* modulating effect on image contrast, thus gradient echo sequences are inherently T2* weighted imaging sequences.

However, there are a number of methods for reducing the T2* weighting to produce, for example sequences that are more T1 contrast weighted. For example the application of an inversion recovery pulse prior to a gradient echo sequence can introduce T1-weighting. These sequences typically employ a 180^0 magnetisation inversion pulse. This pulse reverses the equilibrium magnetisation, so that instead of being parallel to the main field it is anti-parallel. The inverted spins subsequently return to their equilibrium magnetisation during the subsequent delay between the inverting pulse and the low flip angle pulse (TI) at a rate depending upon their T1 value. The equation for this process is:

$$M_z = M_0(1-2\exp(-TI/T1)) \quad (1.29)$$

Tissue with a shorter T1 will recover faster towards its equilibrium than tissue with a longer T1. Therefore, if the TI delay, before the normal gradient echo sequence begins, is set to specific values it is possible to null the signal from certain tissues, as well as providing T1 weighting if using moderate values of TI. An

example of a simple inversion recovery sequence is shown in figure 1.9. Inversion recovery sequences will be discussed in more detail later.

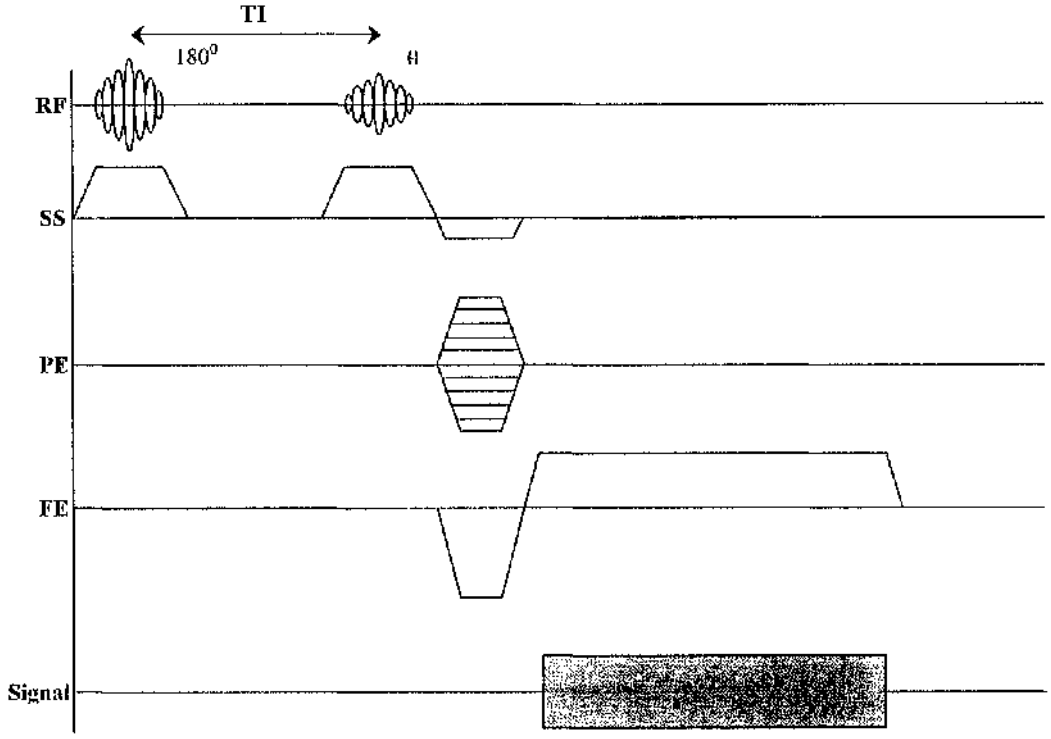

Figure 1.9: Pulse sequence diagram for a simple inversion recover sequence. TI is the time from the initial 180^0 inversion pulse to the imaging RF pulse.

1.2.8 3D Pulse Sequences

So far the sequences discussed have been 2D sequences, i.e., the data is collected in a slice by slice basis with each slice experiencing temporally separate RF pulses. However, in 3D pulse sequences every RF pulse excites the entire volume of tissue. The advantages of 3D imaging are the thinner contiguous slices (often referred to as partitions of a 3D data set) that can be produced due to the increased signal to noise available.

To enable slices to be separated in the slice select direction, phase encoding is applied in this direction as well as in the phase encode direction. If N_s slices are

required N_s phase encoding steps are acquired in the slice select direction. Each slice encoded gradient is applied for each of the phase encoding steps, before the next slice encode step is applied. Figure 1.10 shows a pulse sequence for a simple FLASH (Fast Low Angle SHot) 3D sequence.

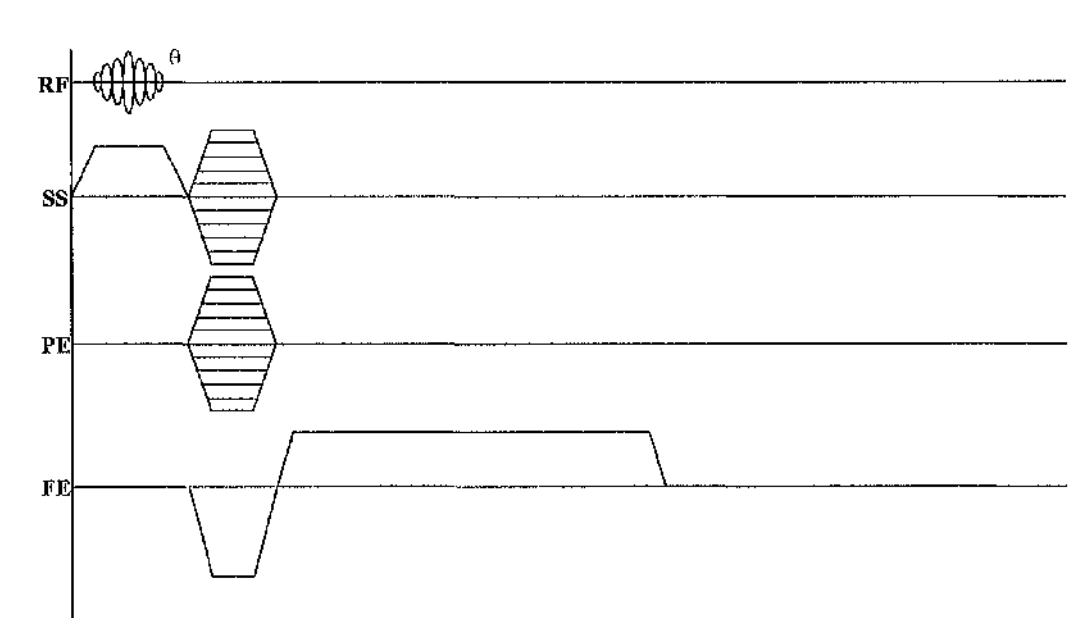

Figure 1.10: Pulse sequence for a simple FLASH 3D sequence.

It is possible to introduce T1 weighting to 3D sequences using the inversion recovery method described in 1.2.7. One such technique (MP-RAGE) will be described in more detail in the next chapter.

1.3 Chapter conclusions

Now that the basics of MR with specific reference to signal generation and pulse sequences have been introduced, the next chapter will introduce the concepts of angiography and venography with reference to previous and current methods. This

will include the use of contrast enhanced techniques in MR angiography. Focus will be placed on one particular venographic technique which utilises an inversion recovery 3D technique. The chapter will discuss whether there is a way of improving the technique and makes suggestions as to how this can be achieved.

Chapter 2

Improvement of Current Subtraction Venography Using Registration

2.1 Introduction

2.1.1 Overview

This chapter begins by introducing the technique of angiography and describes techniques currently used in MR angiography (MRA). Time of flight (TOF) and phase contrast (PC) MRA are described, paying particular attention to the advantages and disadvantages of each technique.

Two MRA techniques specifically designed to investigate the cerebral venous system are also described: a blood oxygenation level dependant (BOLD) venous contrast technique and an MP RAGE (Magnetization-Prepared RApid Gradient Echo) subtraction venography (MSV) technique. The MSV technique is described in detail and it is suggested that this technique is susceptible to inter-scan patient motion, as it requires two data sets to be collected serially: one pre-contrast injection and one post-contrast injection. If patient motion is a problem this would reduce the techniques capability of resolving small venous vessels, and would introduce artefacts into the resulting visualisation data.

To test if the technique was susceptible to such patient motion 20 patient data sets were collected and analysed using the MSV protocol, with and without inter-scan motion correction where the motion correction was achieved using a sub-voxel realignment algorithm (MATCH, Hammersmith Hospital, London). Analysis of motion over such short time scales using this technique is novel.

Following analysis of the results conclusions are reached on the requirements of inter-scan realignment in such studies. More general conclusions are also drawn on the requirements for realignment of pre and post-contrast data that are not

collected specifically for venous visualisation, and further work is suggested to test this hypothesis

All work described in this chapter has been conducted by the author, with the exception of the qualitative assessments conducted by the two trained observers, described in section 2.5.1.3 and the acquisitions which were performed by radiographic staff. Preliminary results from this chapter formed the basis for a presentation at the International Society of Magnetic Resonance in Medicine meeting in 1999 (Brennan *et al* 1999). The final data and results form the basis of a paper in preparation for journal submission.

2.1.2 Historical Context

It was shortly after the discovery of x-rays by Roentgen that the first angiograms were produced using cadavers in 1896. (Haschek and Lindenthal 1896) Live animal studies were not conducted until the 1900's (Franck and Alwens 1910). A mixture of Bismuth and oil was used as the contrast agent and was given via intravenous injection to observe blood flow in the heart.

The first arteriograms and venograms in humans were produced in 1923 using a contrast of 20% solution of strontium bromide (Berberich and Hirsch 1923). One year later iodine was first successfully used as a contrast agent by Brooks (Brooks 1924).

Since then iodine arteriograms have become the gold standard in x-ray based angiography (Setton *et al* 1996) offering high resolution (1024x1024 and greater) and good vessel contrast. It is also possible to acquire images in real time, allowing fluoroscopy to show the dynamic nature of the contrast flow.

There are however disadvantages with conventional angiographic techniques (Earnest *et al* 1984). Firstly, it is an invasive technique due to the requirement of intravenous injection. This can cause complications where the patient has vascular disease with associated thrombus. If there is thrombus at the injection site this can dislodge the thrombus which can cause stroke if it becomes lodged in the arteries of the brain. Cerebral angiography has been associated with a 1% transient deficit and 0.5% persistent neurological deficit in patients (Heiserman *et al* 1994).

The technique also involves the use of ionising radiation in the form of x-rays with associated dose risks. For example the typical dose received from a cerebral angiographic procedure has been quoted as 7.4mSv (McParland 1998) which translates to a fatal cancer risk of 3.7 per 10,000 procedures (ICRP Publication 60). There is also the risk of allergic reaction to the contrast medium which varies depending on the type of contrast medium used (0.2% - 0.7 %, (Cochran *et al* 2001)). As a result of the disadvantages in using conventional angiographic techniques there has been considerable interest in developing safer MR alternatives.

Before MRI was itself developed the effects of fluid and blood flow on nuclear magnetic resonance measurements had already been investigated (Surjan 1951, Singer 1959). Therefore, it was known during the early development of MRI that blood flow would have an effect on signal.

Early attempts to produce MRA sequences used spin echo pulse sequences which provided flow enhancement when unexcited spins entered the imaging slice. However, these techniques suffered from signal loss at higher velocities due to excited spins leaving the slice before the 180 degree refocusing pulse (Bradley & Waluch 1985).

2.2 Currently Applied MRA Methods

A number of methods have been developed to allow visualisation of the cerebral vessels using MRI. The two main methods currently used are time of flight (TOF) and phase contrast (PC).

2.2.1 The Time of Flight Technique

The TOF effect occurs in normal imaging sequences and generally results in flow related enhancement. In a typical sequence slices are excited repeatedly resulting in an equilibrium longitudinal magnetisation. However, if during the time between excitation and signal detection fresh blood flows into an excited slice this blood will not have reached this longitudinal equilibrium. If it has travelled from an unexcited region it will have full longitudinal magnetisation resulting in flow related enhancement. This is the TOF effect (see figure 2.1).

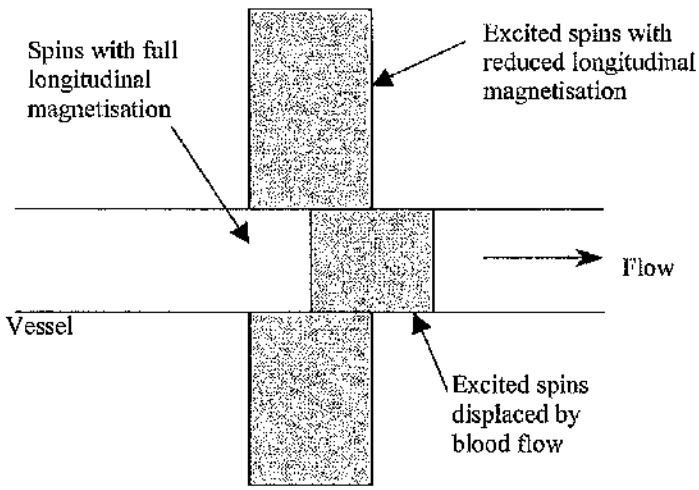

Figure 2.1: Blood flow resulting in inflow of longitudinally saturated spins into an imaging slice

The resulting signal strength is dependant on the fraction of saturated spins within the slice profile when the signal is sampled, the flip angle and the repetition time. It is possible to model this for any particular sequence. For example Gao *et al* (Gao *et al* 1998) modelled the flow induced signal changes in a spoiled FLASH sequence. This sequence differs from a normal FLASH sequence due to the presence of a spoiler gradient in the slice select axis, which destroys any remaining transverse magnetisation after signal readout. Gao initially assumed that flow within a vessel had a plug profile, i.e. all flow within the vessel had the same velocity. He also assumed that;

$$V_0 TR \geq L \tag{2.1}$$

where V_0 is the flow velocity, TR is the repetition time and L is the slice thickness. Thus the total signal from voxels within the vessel could be calculated;

$$S = M_0 \sin\theta \exp(-TE/T2)\pi a^2 L \tag{2.2}$$

where M_0 was the initial magnetisation , a was the radius of the vessel, and θ was the angle of the vessel in relation to the imaging slice.

More advanced modelling where more realistic assumptions are made, i.e. parabolic flow profiles (Gao *et al* 1988) are also possible. Using the TOF effect it is possible to measure flow velocities, however for the production of MR angiograms this is not required.

TOF angiography techniques are designed to use the TOF effect to increase signal from flowing spins whilst keeping the signal from stationary spins to a minimum. A number of 2D and 3D techniques have been developed utilising this effect for the production of MR angiograms. For example inversion spin labelling (Nishimura *et al* 1987) uses an 180^0 selective pulse to invert the magnetisation in a

slab of interest. After an inversion time (TI) uninverted blood flows into the slab before the normal spin echo sequence is run. The sequence is then repeated with a non-selective 180^0 pulse which inverts all of the spins. The complex data from both these sequences is then subtracted resulting in data that only contains signal from flowing spins.

Another method utilises pre-saturation pulses for spin labelling (Dumoulin *et al* 1989(a)). Here a 3D velocity compensated gradient echo sequence is used without any pre-saturation pulses. The velocity compensation results in high signal for the flowing spins. A second sequence is then run with a pre-saturation pulse placed down stream, effectively removing the signal from spins experiencing these pulses. Subtraction of the two image sets results in angiographic data. In this case they were displayed using maximum intensity projections (MIP).

Currently used methods of TOF angiography are designed to suppress the signal from stationary tissue by saturation of the longitudinal magnetisation. This can be achieved in both 2D and 3D techniques (Keller *et al* 1989,Ruggeri *et al* 1989). Short echo times are used with velocity compensation and partial flip angles. These parameters maximise the vascular signal whilst minimising the stationary tissue signal. Further techniques such as magnetisation transfer (Edelman *et al* 1992, Pike *et al* 1992), fat saturation (Lin *et al* 1993) and magnetisation preparation (Edelman *et al* 1991, Li *et al* 1994) can be used to reduce the signal from the stationary tissue.

2D TOF techniques are particularly good at providing high contrast between flowing spins and stationary tissue (Graves 1997), and are sensitive to slow flow. However, due to the use of relatively thin 2D slices signal to noise can be poor, and in-plane flow sensitivity can be low. The requirement for relatively long TE's results in intravoxel phase dispersion. This is a particular problem in areas of complex flow.

3D TOF techniques have higher signal to noise, due to the larger excitation volume and can provide thinner slices than 2D methods. TE's can also be shorter reducing intravoxel phase dispersion. However, due to the thickness of the slabs used areas of slow flow can suffer from saturation, leading to reductions in signal. Background suppression is also not as good as in 2D TOF. Both the 2D and 3D TOF techniques can also be sensitive to tissues with short T1's such as fat.

For the purposes of cerebral venous visualisation it has been suggested that 3D TOF is unsuitable, due to in-plane saturation effects. However, 2D TOF can still suffer from in-flow saturation problems relating to the choice of imaging plane. To avoid this problem 2D TOF can be acquired in three perpendicular planes, however, this requires significant increase in imaging time.

2.2.2 The Phase Contrast Technique

PC is another common technique used in the production of MR angiograms. Magnetic field gradients used during the image acquisition dephase the transverse magnetisation for stationary spins. To correct for this gradients are usually applied in equal and opposite pairs in order to restore the initial phase at TE. However, this is not applicable with moving spins. When such a bipolar gradient (see figure 2.2) is applied to a spin it acquires the following change in phase;

$$\phi(t) = \gamma \int_{t_0}^{t_1} \mathbf{G}(\tau)\mathbf{x}(\tau)d\tau + \gamma \int_{t_1}^{t_2} \mathbf{G}(\tau)\mathbf{x}(\tau)d\tau \qquad (2.3)$$

where $\boldsymbol{G}$ is the applied gradient at time τ, γ is the gyromagnetic ratio and x is the position of the spin, with respect to the gradient at time τ.

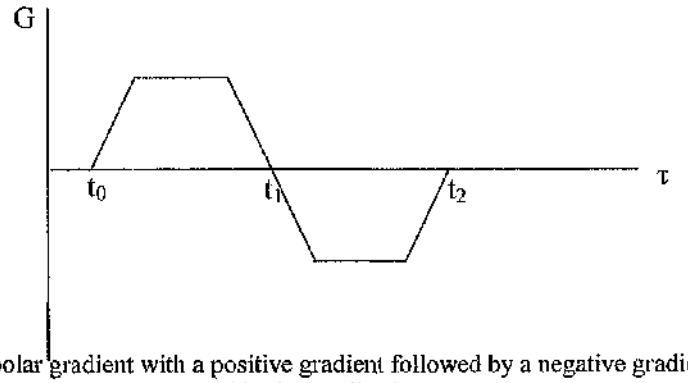

Figure 2.2: A bipolar gradient with a positive gradient followed by a negative gradient (positive bipolar gradient)

When a positive bipolar gradient (see figure 2.2) is applied to stationary spins the first and second term exactly cancel out in equation (2.3). However, if the spin is changing its position, the two terms will be different and an overall phase shift will occur. Therefore, the change in phase can be related to a velocity if the time of the phase change is known. For example for a bipolar gradient with each lobe having an area (in terms of its gradient and time) of A and the centre of the lobes being separated by time T, the induced phase shift relates to velocity by:

$$\phi(v) = \gamma v T A \tag{2.4}$$

It is possible to introduce bipolar gradients into conventional sequences and by producing phase maps from the raw complex data it is possible to determine flow velocities. However, a single bipolar gradient only imparts phase change on the moving spins which does not affect the magnitude images produced after the complex data has been Fourier transformed. To produce an angiogram we require a second sequence to be run with a negative bipolar gradient. Then after subtracting the complex data of the second sequence from the first sequence, signal from the stationary data will subtract out but will add for flowing spins. Taking the magnitude of the complex data results in an image of the flowing spins. Here the maximum

velocity spins would result in maximum signal, but only if the fastest flowing blood acquires a total phase shift of 180^0. Therefore, these sequences must be specifically tailored for particular flow velocities

If only one positive and negative bipolar data set is collected, then the sequence would only be sensitive to flow in the direction of the bipolar gradients. Therefore, PC angiography originally required this procedure to be repeated 3 times for 3D flow sensitivity (Dumoulin *et al* 1989(b)) resulting in 6 data sets. However, the scanning time can be reduced by collecting only 4 data sets where only the first set had no velocity sensitivity and the following three have sensitivities in the three orthogonal directions (Pelc *et al* 1991, Hausmann *et al* 1991). Subtraction of each velocity sensitive image from the reference image yields angiographic information for flows in that direction. The use of only one reference image, however, reduces signal to noise and more efficient subtraction schemes are often used (Pelc *et al* 1991, Dumoulin *et al* 1991).

2D phase contrast techniques have short acquisition times, good background suppression and are not particularly sensitive to saturation effects (Graves 1997). However 2D phase contrast angiography has been found to suffer from intravoxel dephasing within the relatively large voxels, and this suggests that it should not be used for venous visualisation (Liauw *et al* 2000). It also suffers from vessel overlap and requires good system stability.

3D PC techniques have thinner slices and good background suppression. However, acquisition times can be long and it is difficult to provide a sequence with full velocity compensation.

2.2.3 Other MR Angiography Techniques

There are a number of other less commonly used methods available for producing MR angiograms and more specifically of venous vessels. The BOLD method for visualising cerebral veins was introduced in 1998 (Reichenbach, *et al* 1997,1998) and is the newest method available. This technique uses the blood oxygenation level dependant (BOLD) effect (Ogawa *et al* 1992) to visualise and highlight venous structures. A strongly T2*-weighted FLASH 3D sequence is used in conjunction with phase mask filters, which are specifically designed to increase the phase induced signal reduction that occurs in voxels with both venous blood and brain tissue. This technique produces dark veins within a light background, therefore, minimum intensity projections are used to visualise the data instead of the normal maximum intensity projections.

The original technique suffered two major disadvantages. Firstly, the acquisition times were quite long (typically 10 minutes per acquisition) especially for the resolutions that they were recommending of 1024x1024. Thus there would be problems with patient motion artefacts. Secondly, mainly due to the long TE's required, the technique was sensitive to susceptibility artefacts especially at air tissue interfaces. In Essig *et al* 1999 the technique was being used to determine nidus size of arteriovenous malformations (AVMs). In 4 of 17 patients within the study nidus size was underestimated due to image as a result of the lesion being in close proximity to an air/tissue inteface, or being near a bony structure.

Lin *et al* 1999 investigated a solution to these problems. A T1 reducing agent, Omniscan, was injected to allow shorter TE's to be used. This would reduce image acquisition time and susceptibility artefacts. However, when this technique was used

in a study (Tan *et al* 2000), investigating the relationship of intracranial veins and multiple sclerosis (MS) lesions, it was found that there were still major problems with susceptibility artefects. Although this technique has further been expanded to 3T systems (Riechenbach *et al* 2000) and very fine detail has been displayed, as it currently stands it cannot display the whole intracranial venous system. Therefore, if a clinician requires such an overall picture with high resolution vessels a different technique is required.

Stevenson *et al* 1995 described another technique called MP RAGE subtraction venography (MSV). This technique uses the MP RAGE pulse sequence (Mugler and Brookeman 1991, Brant-Zawadzki *et al* 1992), which is a T1-weighted, small flip angle, 3D sequence with an 180^0 inversion recovery preparation pulse. Before this angiographic technique is described it is important to have an understanding of the MP RAGE sequence.

2.3 3D MP RAGE Pulse Sequence

In 1990 (Mugler and Brookeman 1990) developed the 3D MP RAGE sequence which followed on from work done by Haase *et al* (Haase *et al* 1989). At the core of this sequence is a FLASH sequence, similar to the one detailed in section 1.2.8 (figure 1.10). This sequence when modified by the addition of an 180^0 inversion pulse to introduce T1 weighting is called Turbo or snapshot FLASH (Atkinson *et al* 1990, Haase 1990). Similarly, it was possible to introduce T1 weighting to 3D imaging with the development of the MP RAGE sequence.

The MP RAGE sequence consists of an initial 180^0 inversion pulse (see figure 2.3) followed by a pause in the sequence, called the inversion time (TI), where

the inverted longitudinal magnetisation is allowed to recover (see figure 2.4). After TI the FLASH sequence runs through all of the depth encoding steps for one particular plane encoding gradient. There is then a further recovery time allowing longitudinal magnetisation recovery, before the next inversion pulse and FLASH loop is run with a slightly different plane encoding gradient.

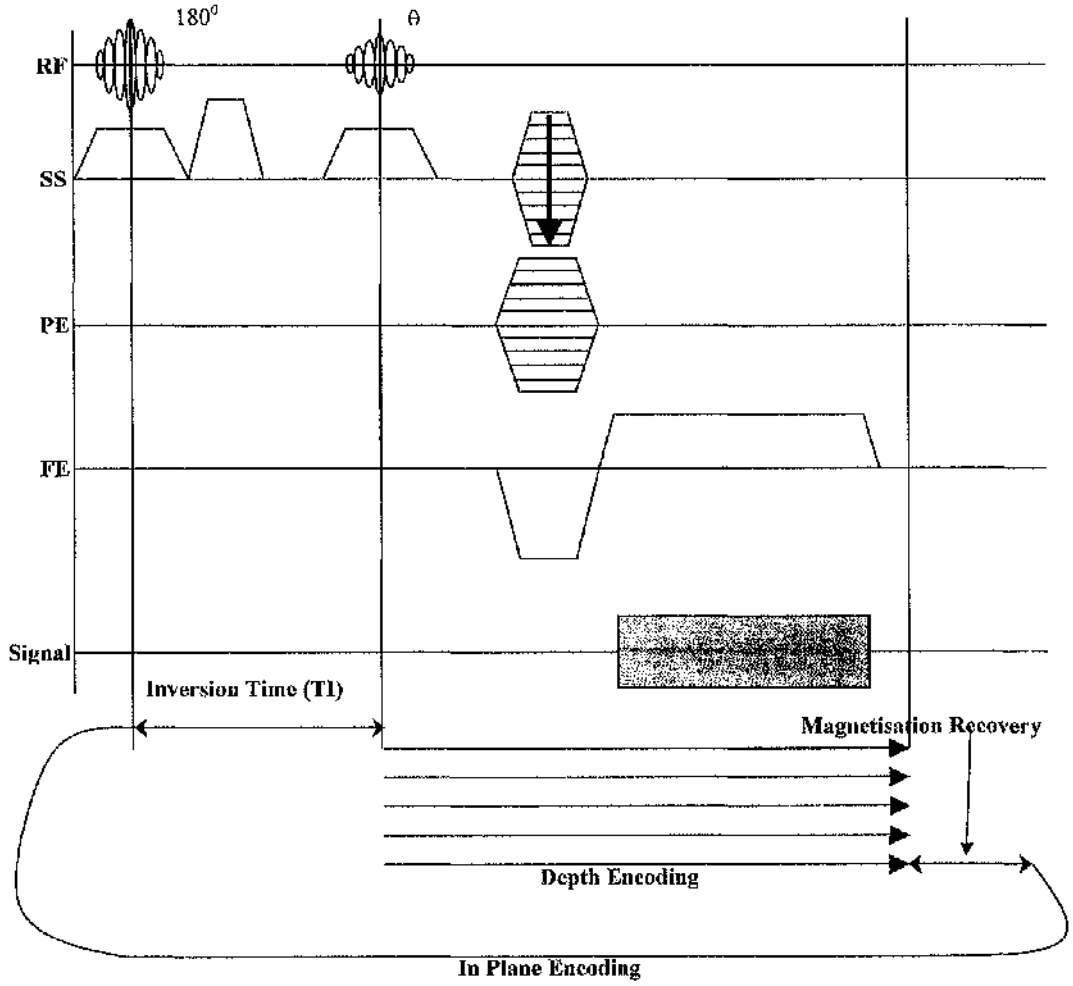

Figure 2.3: Pulse diagram of the MP RAGE sequence. The in plane loop consists of the 180^0 pulse followed by an inversion time (TI), the depth encoding loop, and magnetisation recovery time. The depth encoding loop is a FLASH sequence.

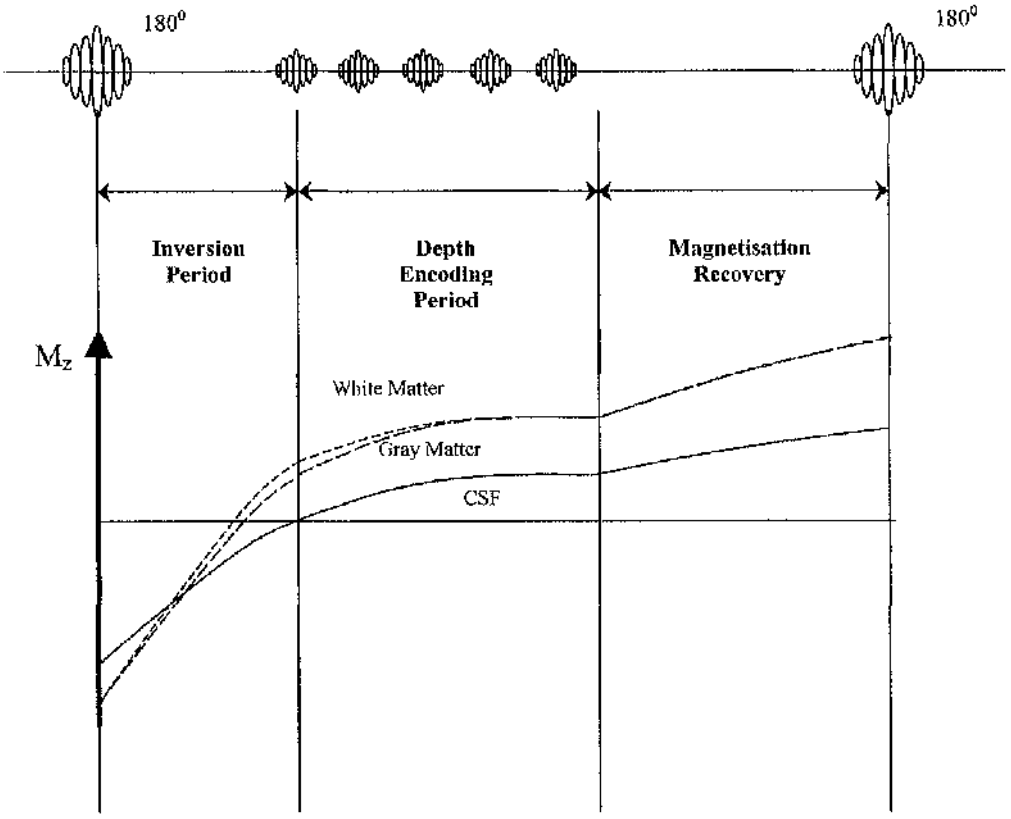

Figure 2.4: MP RAGE longitudinal magnetisation changes during the sequence. Tissue contrast does not remain constant during the depth encoding steps, thus the overall contrast is the result of complex averaging over all of the depth encoding steps.

Each depth encoding step within the FLASH sequence experiences a slightly different T1-weighting due to the variation in the longitudinal magnetisation over time (see figure 2.4). Therefore, the final tissue signal is a complex average of the depth encoding lines over each depth encoding period. Signal contributions from the in-plane encoding reach equilibrium within less than three depth encoding steps (Brant-Zawadzki *et al* 1992).

As applied in this thesis the depth encoding occurs sequentially. This results in an effective TI which is the average of the depth encoding period plus the inversion period. Therefore, when optimising the sequence for tissue contrast it is important to take into account the duration of the depth encoding period.

In a similar fashion to the other sequences described in chapter 1 it is possible to derive equations detailing the signal and magnetisation characteristics of this sequence. The average signal intensity achieved with an MP RAGE sequence is:

$$S_N = M_N \exp(-TE/T2^*)\sin\alpha \tag{2.5}$$

where S_N is the signal intensity for a sequence with N phase-encoding steps, M_N is the magnetisation and α is the depth encoding RF pulse angle. The longitudinal magnetisation can be defined by:

$$M_N = M_0(1-\exp(-TR/T1))\sum_{i=0}^{N/2-2}(\cos\alpha\exp(-TR/T1)^i + M_0(1-\exp(-TI/T1)) + M_{eq}\exp(TI/T1)(\cos\alpha\exp(-TR/T1))^{N/2-1} \tag{2.6}$$

where TR is the repetition time between readout pulses, TI is the inversion time and M_{eq} is the equilibrium magnetisation reached within a few Fourier loops. This is defined by:

$$M_{eq} = \frac{1}{1-\mathrm{X}\exp(-Trec/T1)} M_0(1-\exp(-Trec/T1)) \tag{2.7}$$

where Trec is the magnetisation recovery period as illustrated in figure 2.3. X is the fraction of magnetisation remaining from previous excitation loops due to the small angle excitation.

It is the 180^0 inversion pulses that are responsible for the T1-weighting of this sequence. As was described in chapter 1 (section 1.27) this T1-weighting is a result of the inverted spins returning to their magnetisation equilibrium at a rate determined by their T1 relaxation.

2.4 MP RAGE Subtraction Venography

2.4.1 Introduction

This particular venographic method requires the MP RAGE sequence to be run twice in quick succession with the second sequence shortly following injection of gadolinium (Gd). Due to the T1-reducing effect of Gd and the effect of flow on the MP-RAGE sequence, if the post-injection data set is subtracted from the pre-injection data set the venous system is highlighted in the output, due to the increased intensity of the veins in the post-injection sequence.

Due to the very short TE gradient-echo component the MP-RAGE sequence depicts normally flowing unsaturated arterial blood as bright. However, because of saturation effects venous blood flow is dark, due to its slow flow velocities. Therefore, after the T1 reducing agent has been injected the signal from veins increase but the signal from arteries does not. Therefore, the cerebral arteries are subtracted out in the final data.

However, it is not only the venous vessels that show contrast enhancement after Gd injection. Other structures within the normal human head also show some uptake on the MP-RAGE sequence, including the skin, nasal cavities and meninges, because they do not have the equivalent of a blood brain barier. After subtraction these structures are highlighted as well as the venous vessels.

There are several advantages to the MP RAGE subtraction technique. Firstly, it does not rely exclusively on time-of-flight effects to depict flow. Where TOF will only depict flow within a specific range of flow velocities dependant on the sequence parameters, the MSV technique only requires that the blood within the veins remains within the imaging region long enough to become saturated. This also has the

advantage of allowing small cortical veins to be depicted, as the flow within these vessels will be slowest. Therefore, it is theorised that the only limitations on small cortical vein visibility in the final subtraction data would be scan resolution, signal to noise (S/N) and the sufficient delivery of contrast medium.

Another advantage of this technique is that due to the short TE used in this technique there is very little artefact from susceptibility dephasing. As was previously discussed this can be a problem with the BOLD and PC techniques. Thus there are no areas of the brain that cannot be examined by this technique.

As with all the previous techniques there are disadvantages. The protocol requires Gd injection and is thus invasive. However, this is a minimally invasive technique only requiring intravenous injection, which can be delivered via long line. There are also problems with injecting Gd compounds such as Magnevist but these are very rare. In a survey-based study covering 687,255 gadopentetate dimeglumine injections 314 non-allergic reactions, 107 mild, 28 moderate and 5 severe allergic reactions were reported (Murphy *et al* 1999). Although these rates are low with only 0.001% of reactions being classed as severe, emergency medical treatment must always be close at hand.

Scan times for this protocol can be up to 6 minutes 30 seconds for each scan therefore patient motion is a problem. These motion problems can be reduced to a minimum by seeking patient co-operation and using head restraints to limit motion. It is also common procedure to insert an intravenous line before the study is started to negate the need for needle insertion half way through the procedure. However, none of these methods can guarantee the patient will remain still during the procedure. In fact, because there is a break in the imaging sequence, to allow the contrast agent to be delivered by long line, the patients often use this time to reposition themselves if

they feel discomfort (Brennan *et al* 1999). This motion results in misregistration of the pre and post-injection data, possibly reducing both the S/N and vessel resolution. It can also result in artefects appearing in the data either masking vessels of interest or masquerading as such vessels.

Various studies have been performed to examine motion correction during scanning. These include physiological gating (Runge *et al* 1984), reordered phase schemes (Bailes *et al* 1985) and the use of navigator pulses (Ehman *et al* 1989). However, in the MSV protocol, there is a pause during the scans were motion can occur and none of the correction algorithms can account for motion inter-scan. The gap between the two scans is the occasion during the protocol that motion is most likely to occur. Therefore it is important to determine if this motion does commonly occur and if so does correction improve the final subtraction data.

It is possible to correct for inter-scan motion using registration software to compare the pre and post-contrast data. Such software is designed to determine the best positional correction to account for the intervening motion. One such software package is MATCH which was designed and written by a group at Hammersmith Hospital, London (Hajnal *et al* 1995).

2.4.2 MATCH Registration Software

MATCH is a command line based program designed specifically to realign 3D T1-weighted serial data sets based on a chi-squared minimisation between the two data sets (Press *et al* 1992), where chi-square is calculated using:

$$\chi^2 = \sum_{voxels} \frac{(I_B - I_A)}{N_{voxels}} \tag{2.8}$$

where I_A and I_B are the intensities of corresponding voxels in the images A and B that are being positionally matched and N_{voxels} is the number of voxels used in the calculation. χ^2 is reduced by calculating new values for I_B as image B is moved relative to A using rigid body rotations and translations. The software applies 3 rigid body translations (x,y,z) and 3 rigid body rotations (Pitch, Roll, Yaw) to one of the data sets and for each set of rigid body parameters calculates a new χ^2. The software aims to produce a set of translation and rotation parameters that result in a minimum value for χ^2. Calculation time is reduced by only taking voxels into account when they are above a certain threshold in image A and where there are corresponding pixels in image B.

During optimisation of the alignment subvoxel shifts are required to enable high alignment accuracy. To minimise errors in χ^2 calculation, and thus improve the alignment accuracy, good quality interpolation is required.

To enable fractional pixel shifts in MRI data it is necessary to use an interpolation function appropriate to the nature of the data (Hajnal *et al* 1995). MRI data is collected using Fourier techniques with the data collected over a bounded region of k-space. Due to the existence of these boundaries the frequency of the data is strictly band limited. Thus for an MR image which has been Fourier transformed the equivalent point spread function would be a sinc function (Jain 1989). This is particularly true for 3D data sets that are collected with phase-encoding in two directions. These data sets are band limited in all directions. Therefore, theoretically it is possible to interpolate 3D MR images using sinc interpolation without introducing errors.

Sinc interpolation is, however, a computationally intensive technique, which if employed fully to large 3D data sets would result in prohibitively long

interpolation times. Therefore, a windowed sinc technique is employed with a Hanning window function, which is a compromise between accuracy and computational time (Hajnal *et al* 1995).

Hajnal *et al* also suggest that to ensure good registration accuracy, that structures that change between the two scans should be removed from the registration computations as local changes can introduce global errors in registration (Hajnal *et al* 1995). In the data presented here the main difference between the two data sets is the presence of the contrast enhancement. Certain structure's signal intensity significantly changes after contrast injection within the head, including venous vessels, skin and nasal tissues. Therefore these structures must be segmented out before the registration algorithm is applied. For the algorithm to ignore these tissues in the calculation they must be segmented from the post-contrast data, as it is not obvious from the pre-contrast data where these structures are.

It is also possible that if the patient moves their head that the brain can change position within the cranial vault, as it is not rigidly fixed in place. Therefore, the relationship between the brain and its attached structures can change with respect to the skull, muscle and other extracerebral structures. Therefore, as well as removing the enhancing structures from the calculation the remaining extracranial structures must also be segmented out.

2.4.3 Study Aim of This chapter

This study aims to determine the effects of using the MATCH registration software on the venograms produced using the MP RAGE subtraction technique. By subjectively and quantitatively assessing subtraction data quality it will determine if

the use of registration techniques improves the quality of the clinical information available to the radiologist.

2.5 Comparison of Registered and Non-Registered Subtraction Venograms

2.5.1 Methods

2.5.1.1 Imaging Protocol

Pre and post-contrast data were collected on 20 patients using a 3D MP RAGE sequence, after obtaining ethical approval. The imaging parameters varied during the study, reflecting the differing clinical imaging protocols required for the differing pathologies under investigation. The examinations included; 6 patients with meningiomas, 5 for suspected venous thrombosis, 3 with gliomas, 3 with adenomas, 1 with a cyst, 1 with a malignant neoplasm and 1 patient with normal imaging. The imaging parameters varied within the following constraints; TR=10 ms, TE= 4 ms, TI= 20-300 ms, flip angle = 10-15, equivalent slice thickness = 1.2-1.4 mm, matrix = 256x256, FOV = 250 mm. Slices were sagittal in orientation. The maximum acquisition time for each MP RAGE acquisition was 6 mins 46 seconds.

The imaging was conducted on a 1.5T imaging unit (Siemens Magnetom 63SP). Patients were asked to stay as still as possible throughout the imaging procedure with their head held in place with padding (see figure 2.5). The pads were secured at maximum pressure consistent with comfort, by two locking bars. A long IV line was inserted in the patient before the imaging protocol had begun. After initial scanning, including pilot scans, the first MP RAGE sequence was run before

contrast medium injection. The contrast medium (Magnevist) was administered as soon as the pre-contrast MP RAGE sequence had finished in the form of a 20 second bolus, via the IV line. This required a radiologist to enter and leave the room. The long line was used avoid having to slide the patient out of the magnet for the injection and then to slide them back in. Had this been required significant patient motion would be likely as well as introducing alignment errors. The post-contrast MP RAGE sequence was started as soon as the bolus delivery was complete and the radiologist had left the room. The data was transferred to a Sun Ultra 1 170MHz workstation where software (conv_analyze, written by Martin Connell, Department of Clinical Physics, Edinburgh University) was used to convert the ACR/NEMA (American College of Radiology- National Electrical Manufacturers Association) data format (Wang et al 1988) data to Analyze format.

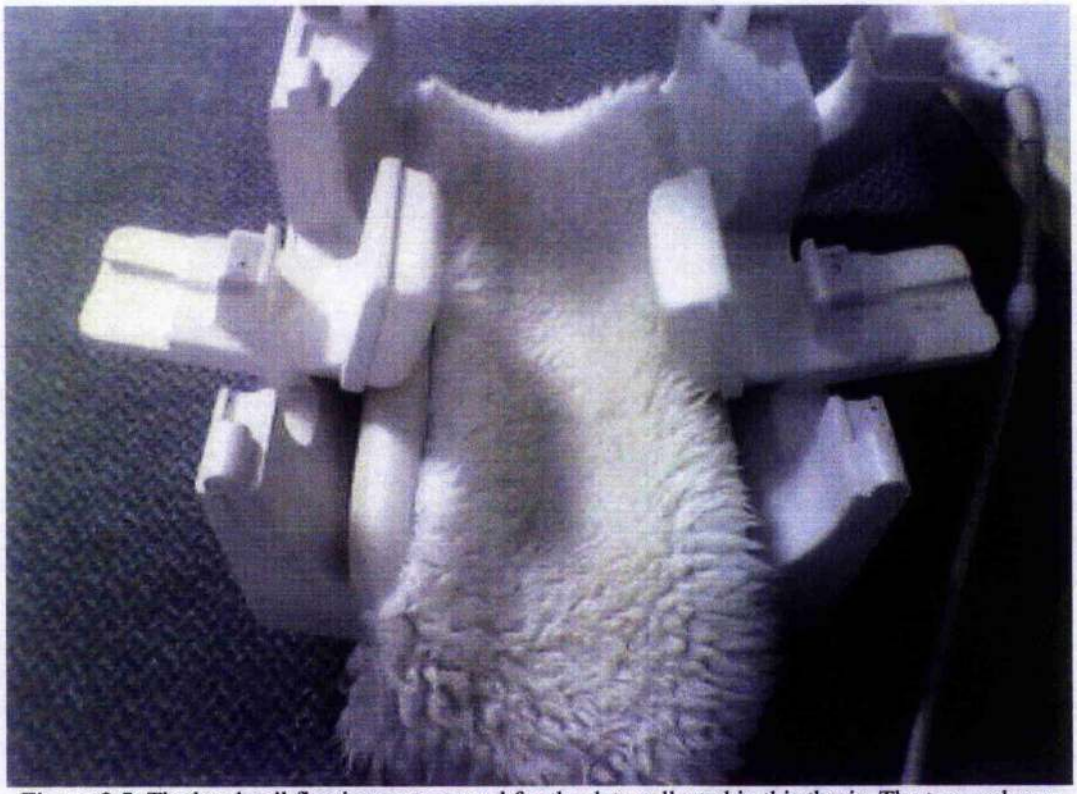

Figure 2.5: The head coil fixation system used for the data collected in this thesis. The two pads can be moved in and locked in the tightest position the patient can reasonably bear

2.5.1.2 Image Processing Procedure

Before using the MATCH software the post-contrast data was segmented in two stages. In stage one the extracerebral tissue was removed by manual segmentation, leaving only the brain parenchyma, including the brain stem down to the foramen magnum, the enhanced venous structures and the arteries. This segmentation was approximate and in all cases included some non-enhancing extra-parenchymal material (see figure 2.6)

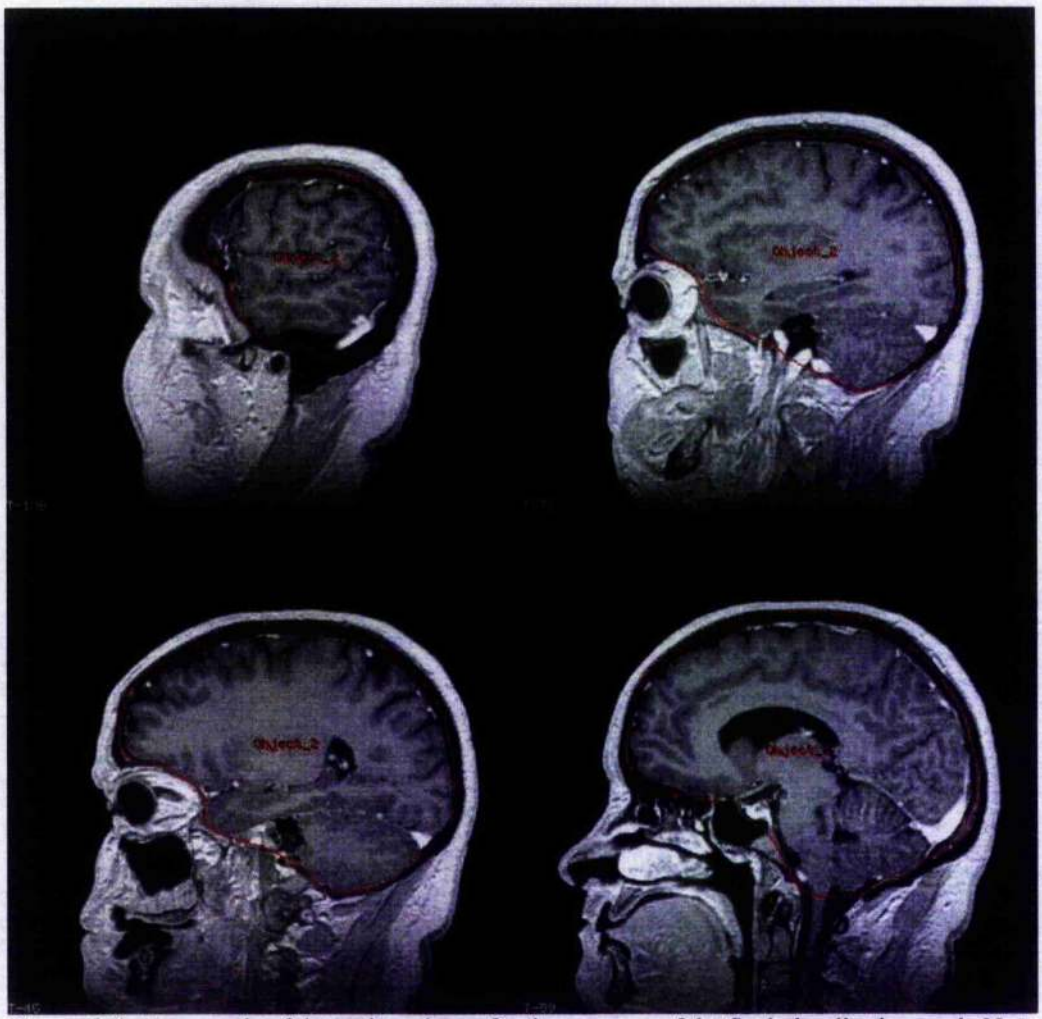

Figure 2.6: An example of the regions drawn for the purposes of the final visualisation mask. Note that the regions extend slightly beyond the brain and cerebral vessels.

This segmented data was used as a mask to define the data to be included in the final MIP visualisation. By restricting the data used for the MIP calculation to only the brain and the cerebral vessels this segmentation was achieved using software written by Martin Connell (3dMRI). On each sagittal slice regions were traced that contained the data to be retained. All data outside these regions was later removed. The regions were drawn on every slice until the brain and vessels to be retained had been fully enclosed within the regions. The regions required approximately 2 hours of operator time per subject to draw and were drawn by the author (see figure 2.6).

In the second stage the data was further segmented removing contrast-enhanced (high signal) data providing the MATCH software with a map of voxels to use in the realignment calculations (realignment mask). This was achieved using a seed growing technique. Initially large vessels were selected as a seed point and thresholds were set around the value of this pixel, by operator judgement, that would allow the seed point to grow into voxels containing high signal vessels. The thresholds were limited so that brain parenchyma was not included. All data connected to the initial seed point and within the determined thresholds were removed.

As all of the vessels within the brain do not appear connected in MR images, this did not remove all of the vessel data. Therefore, further seeds were used and grown in the same manner until the operator was satisfied that all enhancing vessel structures had been removed.

It should be noted that this technique also removed the high signal arteries. These vessels do not change in signal between the pre and post-contrast data sets, and therefore, these could be kept in the realignment mask. However, selectively

segmenting the venous vessels would have added considerably to the time required for the brain segmentation.

This fully segmented data had all the main structures that change between the two scans removed. Therefore the chi-squared minimisation algorithm applied by the MATCH software used this data to determine the best realignment of the brain parenchyma. The pre-contrast data was realigned to the post-contrast data using the MATCH algorithm.

Once the MATCH algorithm had calculated the 6 rigid body realignment parameters it used these parameters to realign the pre-contrast data to the post-contrast data. Therefore, if this data was subtracted from the post-contrast data it would produce a data set highlighting areas of contrast enhancement. However, this study is only interested in the contrast-enhancement within the brain vessels. Therefore, the extra-cranial enhancement had to be removed. This was achieved by producing a binary mask from the first segmented data which contained the enhancing vessels. In this binary mask any voxel that had not been segmented out was set to one with remaining voxels set to zero. This mask was multiplied with the pre and post-contrast data sets, before subtraction.

After subtraction a MIP algorithm was then applied to the subtracted data to produce MIP venograms. These venograms could be produced in any orientation, using the 3DMRI software.

To allow these realigned venograms to be compared to venograms that were produced without realignment, a second subtraction data set was produced. The pre contrast data set was subtracted from the post-contrast data without using the MATCH algorithm to realign them. The same mask used to segment the final subtractions in the realigned data was again used to allow the production of the non-

aligned subtraction venograms. These two sets of venograms could now be directly compared allowing the effects of the realignment software to be examined. From here in this chapter the data sets will be referred to as the matched and unmatched subtraction data.

All of the image processing in this chapter was conducted on a Sun Ultra 1 170 MHz workstation by the author.

2.5.1.3 Quantitative and Qualitative Assessment Protocol

The matched and unmatched subtraction data were compared in two ways. Firstly, for each set of data signal to noise (S/N) values were calculated (see equation 2.9). Three regions of interest (ROI's) were drawn in the matched subtraction data where there were no discernible veins present. The average pixel value within these three regions was representative of the noise within the matched data. The same three regions were used to produce noise data for the unmatched data sets.

$$SNR = \frac{S_{SS}}{|N_{sub}|} \tag{2.9}$$

where S_{ss} is the signal measured from the sagittal sinus and N_{sub} is the noise from the subtraction background.

ROI's were then drawn on, and contained within, a section of the sagittal sinus in the matched subtraction data. The mean pixel value within this ROI represents a value for the signal within the matched subtraction. Care was taken to avoid the superior aspect of the sagittal sinus. This was because in some patients the signal decreased close to the end of the coil and within the region of maximum

inhomogeneity. The same signal regions were used for the unmatched data. Student paired T-test statistics were then calculated comparing S/N values for matched and unmatched data with each patient acting as their own control. This resulted in quantitative comparison of the two data sets.

A second qualitative comparison was also conducted. For this comparison lateral MIP's were produced for each data set. The window levels were equalised for both the matched and unmatched data, allowing direct comparison of the images. Each patient's matched and unmatched MIP's were randomised and the images were presented to two experienced neuro-radiologists. They were asked to examine, in a blinded manner, the randomised matched and unmatched MIP data to determine which image was of the best quality. They were asked to take into account signal to noise, vessel resolution and the existence or non-existence of artefacts. This data was then compared to the signal to noise data.

2.5.2 Results

2.5.2.1 General Results

The time required to perform MATCH co-registration was on average 2½ hours. The majority of this time was spent reslicing the data using sinc interpolation. The manual segmentation took on average a further 2 hours for 128 slices. An example of a non-matched and matched subtraction are shown in figure 2.7.

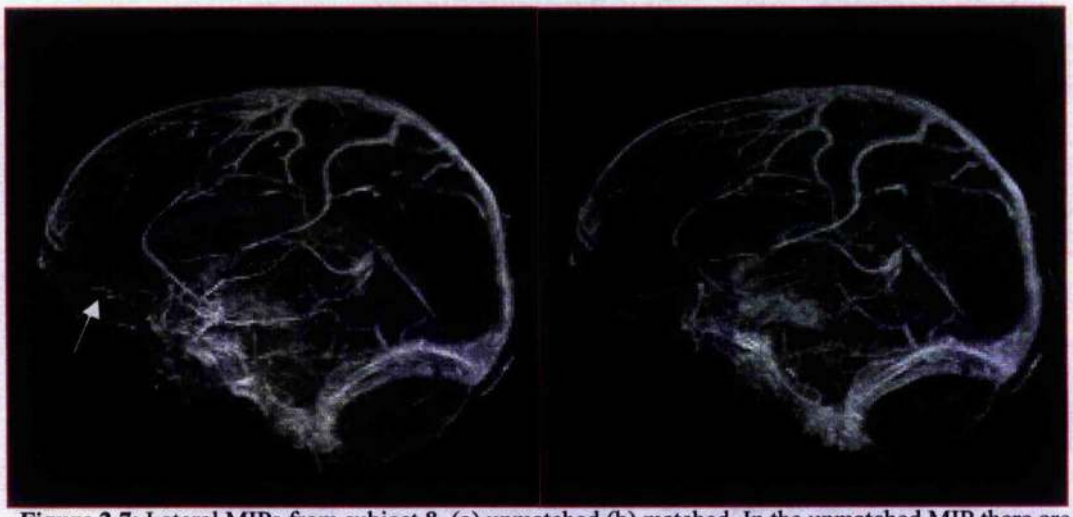

Figure 2.7: Lateral MIPs from subject 8. (a) unmatched (b) matched. In the unmatched MIP there are several artefacts due to miss-registration such as unsubtracted arteries. The shape of the corpus callosum can also be seen. The matched data has better vessel resolution and less artefacts. Here the corpus collosum has been correctly subtracted out. The arrow in (a) indicates an edge mis-registration artefact.

2.5.2.2 Quantitative Results

The S/N ratios are summarised in table 2.1. In 3 patients it was not possible to produce S/N data as the sagittal sinus was either occluded or was very close to the end of the imaging coil and thus non-uniform. The overall average S/N is higher for the matched data than for the non-matched data. This difference is statistically significant with p=0.003 and with a difference 95% confidence interval of 0.1354 - 0.5481.

Patient Number	Matched S/N	Matched S/N Standard Dev	Unmatched S/N	Unmatched S/N Standard Dev
1	2.72	1.21	2.47	0.96
2	2.83	1.39	2.83	1.36
3	2.24	0.98	2.25	0.99
4	2.05	0.88	1.93	0.81
5	3.25	1.36	2.94	1.39
6	Poor Sag Sinus		Poor Sag Sinus	
7	3.61	1.44	2.06	0.76
8	3.55	1.61	2.85	1.17
9	2.96	1.17	2.83	1.05
10	2.77	1.15	2.57	1.01
11	3.28	1.60	2.92	1.22
12	Poor Sag Sinus		Poor Sag Sinus	
13	2.67	1.29	2.60	1.23
14	2.86	1.33	2.10	0.82
15	3.24	1.47	3.09	1.35
16	2.91	1.53	2.82	1.38
17	Poor Sag Sinus		Poor Sag Sinus	
18	2.81	1.24	2.30	1.25
19	3.11	1.42	2.45	1.05
20	2.02	0.90	2.06	0.84
Average	2.88		2.53	

Table 2.1: Comparison of matched and unmatched signal to noise results

2.5.2.3 Qualitative Results

A summary of the result of the qualitative image assessments are shown in table 2.2. Observer 1 rated the matched data of better quality in 80% (16/20) of patients. In 15% (3/20) observer 1 could not observe any difference and in 5% (1/20) of cases observer 1 rated the unmatched data better. Observer 2 rated the matched data of better quality in 85% (17/20) of patients. In 15% (3/20) observer 2 could not observe any difference. In no cases did observer 2 consider the unmatched data was better. Both observers agreed in 75% of cases. Kappa statistics were not used to compare the inter-observer agreement. This was due to the high proportion of agreement between the observers when the matched data was better, 70% (14/20).

This high prevalence within one category can lead to misleading kappa values (Altman 1991). It is, however clear from the agreement data that the matched data were judged to be of higher quality.

Patient No.	Observer 1	Observer 2
1	M	M
2	M	ND
3	M	ND
4	NM	M
5	M	M
6	ND	M
7	M	M
8	M	M
9	M	M
10	M	M
11	M	M
12	ND	ND
13	M	M
14	M	M
15	M	M
16	ND	M
17	M	M
18	M	M
19	M	M
20	M	M

Table 2.2 : The qualitative results for matched and unmatched comparison
The entries for each observer correspond to the venogram that they deemed to be of higher quality
(M = matched MIP, NM = unmatched MIP, ND = no noticeable difference)

2.5.3 Discussion

It is often assumed when doing subtractions between two data sets within the same study, that there is little or no movement between the data sets. As far the author is aware no publication exists that examines the effects of such movement over such short periods of time in the MR scanner. Therefore, this study set out to investigate whether movement was a problem within inter-study data sets using a registration program to allow comparison between matched and unmatched data. This study also set out to investigate if by correcting any inter-scan motion that does occur, it was possible to improve the data quality when producing contrast enhanced subtraction venograms. If this was the case then it would be worth further investigating the methodology used to realign the data sets to optimise the technique for future use.

Two separate methods were used to determine the differences between data that had been realigned with data that had not. Quanititative measurement of S/N allowed rigorous assessment of any differences in the final subtraction data. This also allowed determination of the significance of any differences detected. It was expected that any difference in S/N would translate into detectable changes in the final MIP which might affect clinical diagnosis, therefore following the S/N results two observers were asked to compare side to side MIP outputs from both of the data sets for all of the subjects. To avoid any observer bias neither observer knew which images came from the matched and unmatched data sets, and neither observer had any information on the other's results. Both observers, however, had experience of looking at MIP venograms previously produced within the department.

The data from this study suggests that using registration software on pre and post-contrast data sets can improve the visualisation of the cerebral venous system. S/N did significantly improve after the data had been realigned using the MATCH algorithm. Also in the majority of cases the two trained observers determined the matched data sets of being of higher quality than the unmatched data sets. Therefore, it can be concluded that image realignment does indeed improve the data output from contrast-enhanced subtraction venograms. This also confirms that in many clinical imaging protocols of this nature that inter-scan motion is a problem that can significantly reduce the quality of subtraction data produced from it. For this study this is especially important clinically when the small cortical veins are involved in the disease process. It would also be important if higher resolution were used with smaller voxels or thinner partitions. Co-registering this higher resolution data would increase the visibility of very small vessels. This would allow determination of small vessel thrombosis as well as thrombosis of the larger vessels.

On only one occasion did an observer decide that the unmatched data was of better quality. On this occasion the observer stated that there were more vessels visible in the unmatched data. However, it is likely that these vessels were in fact artefacts due to the mis-registration of the data. The false veins could be created when an artery has been mis-registered and thus is not fully subtracted out or when a bright structure's edge is mis-registered and overlays a dark area when it has not been matched. This phenomenon is most common around the inferior surface of the frontal lobe where the brain interfaces CSF and bone (figure 2.6(a)). Motion artefacts are common here and are likely to occur due to the patient raising their head to look out of the magnet bore, towards their feet between the imaging sequences. This is despite express instructions to try and keep still throughout the procedure.

There are several possible uses for high quality MR venograms. Experience in this and other centres have demonstrated their usefulness in operative planning where the surgeon needs to know the relative position of the venous system with respect to the cortical structures and underlying pathology (Kikinis *et al* 1996). Such venous visualisations have been used in this department and an example of one is shown in figure 2.8.

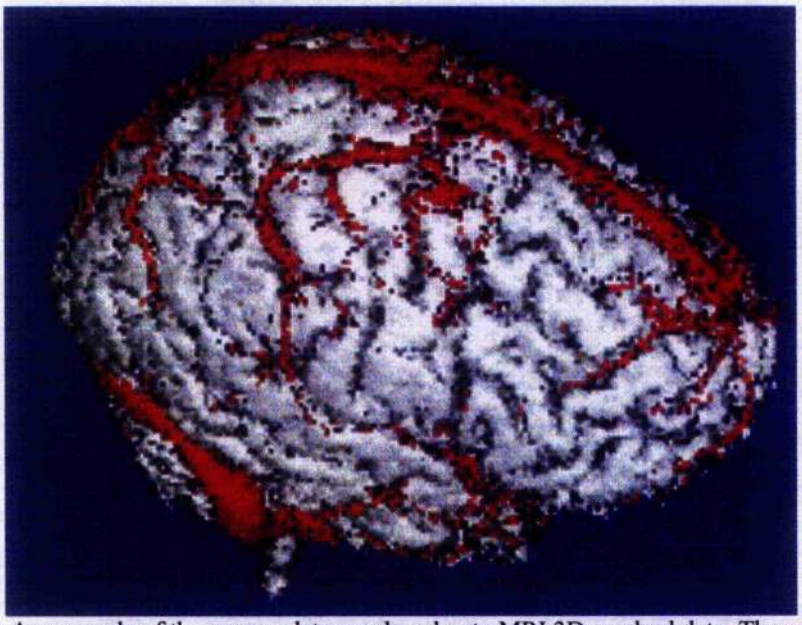

Figure 2.8: An example of the venous data overlayed onto MRI 3D cerebral data. The cerebral data was extracted from the pre-contrast data and displayed using Analyze (Mayo Foundation, Rochester, MN)

It is also important for visualising and delineating the extent of cerebral venous thrombosis. In this study patient 11 had previously been diagnosed with a cerebral venous thrombosis (CVT) using CT. This was present in the left transverse sinus. The MRV unmatched data also depicted the existence of the CVT, however, in the matched data the extent of the CVT is better defined (see figure 2.8). Being able to accurately depict the extent of CVT is important especially if serial studies are

examining the effects of thrombolysis or anticoagulant treatment. Co-registration should be used when examining such acute conditions.

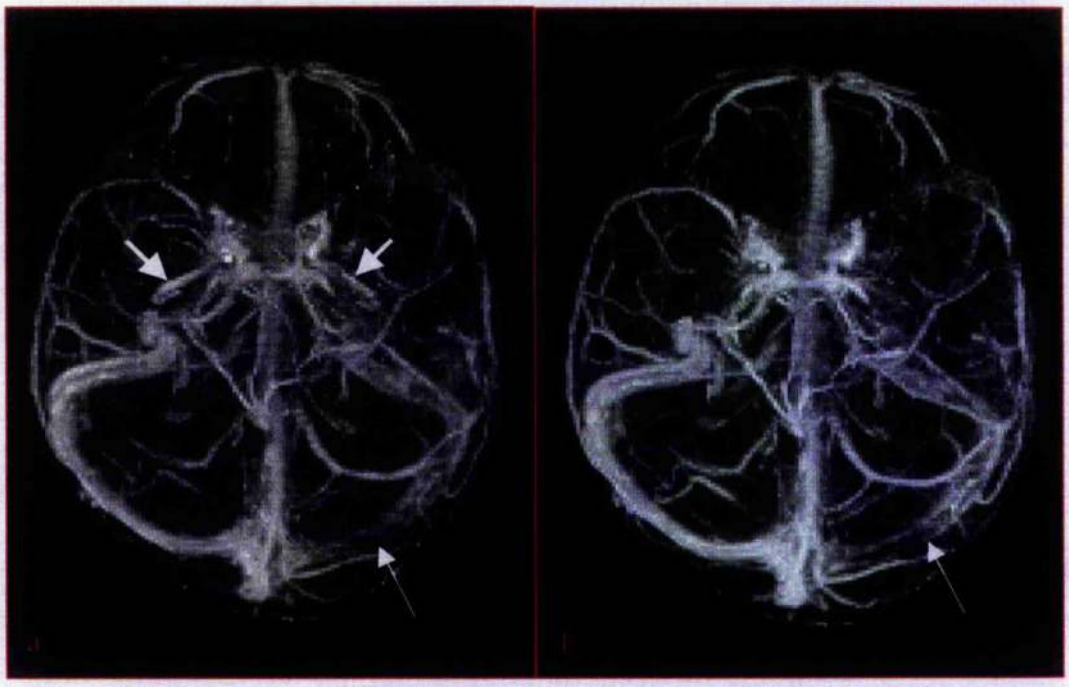

Figure 2.9: Inferior-superior MIP's from patient 11. (a) unmatched (b) matched. The long arrows show the area of thrombosis. The co-registered data delineates the thrombosis more clearly. The short arrows in (a) show arterial contamination of the unmatched data. This does not appear in the matched data.

Fig 2.9 also illustrates the possibility of arterial contamination if the data is not co-registered. The unmatched data contains what appear to be veins emerging from the posterior part of the cavernous sinus and travelling medially. However, these vessels are not visible on the matched data. After investigation of the subtraction and pre-contrast data, it emerged that the vessels were arterial contamination from the right and left internal carotid, as it entered the skull base at the foramen lacerum. Thus by using co-registration arterial contamination in the subtraction data can be kept to a minimum.

Currently, the co-registration processing time is lengthy at about 2 ½ hours. However, with increasing computing power this time will reduce. After this study was completed a new computer system was installed (Sun Ultra 10 440MHz). This was found to reduce the co-registration time to about 1 ½ hr.

Another way of reducing processing time is to use a less rigorous reslicing algorithm. Linear interpolation is often used as it is quicker to run and easy to implement (Woods *et al* 1992). However, as was discussed in section 2.4.2, sinc interpolation is the best suited method for reslicing MR images (Jain 1989, Hajnal *et al* 1995).

The manual segmentation in this protocol was also time consuming and required a trained operator throughout. There are several groups developing automatic segmentation algorithms for extraction of brain parenchyma. However, these algorithms have not yet been designed to provide correct segmentation of contrast-enhanced images which is required for this protocol (Lemieux *et al* 1999 and 2003 ,Saeed *et al* 1997,Lerski *et al* 1993,Cline *et al* 1987, Thacker & Jackson 2001). However, it may be possible to reduce segmentation time requirements by developing a new segmentation algorithm.

This chapter has focused on using pre and post-contrast subtraction data to visualise the cerebral vessels. This enabled subjective quality and signal to noise measurement to be made with respect to the effects of inter-scan patient motion on the subtraction data. However, there are other uses of contrast-enhanced 3D data sets that also depend on this type of subtraction technique. Therefore, the finding that alignment correction is necessary in one application may have more widespread implications. Chapter 3 will investigate the effects of inter-scan motion on a tumour volume measurement technique. This will enable the effects of inter-scan patient

motion to be quantified by examining the effects of alignment correction on the tumour volume measured.

Chapter 3

Tumour Volume Measurements in the Clinical Study of a Modified Herpes Simplex Virus in the Treatment of Glioma: The Effect of Registration on Volume Measurement

3.1 Introduction

3.1.1 Overview

This chapter investigates the effects of pre and post-contrast realignment on contrast-enhanced tumour volume measurements, using the subtraction data. Tumour volume measurements were previously measured using this technique in data sets that had been aligned visually using a manual technique (the author of this thesis made the tumour volume measurements in Rampling *et al* 2000). At the time of publication no technique existed that could automatically realign the pre and post-contrast data sets quickly and accurately. Therefore, to avoid the requirement for large amounts of manual segmentation the data sets were visually realigned. In the Rampling study this method was deemed sufficient as the main aim of the study was to determine toxicity of the agent, and not to determine treatment efficacy and tumour volume changes.

The results from chapter 2 suggest that accurate realignment using an algorithm such as MATCH may be required to ensure that tumour volume measurements are consistently accurate, in serial studies where changes in tumour volume are of specific interest. This chapter, therefore, investigates the hypothesis that tumour volume measurement from pre and post-contrast subtraction is most accurate when sub-voxel realignment is applied. Tumour volumes are compared for three different pre-processing protocols: no realignment, manual (visual) realignment (Rampling *et al* 2000), and sub-voxel (MATCH) realignment. As far as the author is aware this has not been previously investigated

The results from this study along with the results from chapter 2 suggest that inter-scan patient motion is a significant problem in scanning protocols of this nature.

All of the work in this chapter was conducted by the author with the exception of the data acquisitions which were performed by radiographic staff. This work resulted in two presentations at international conferences (Brennan *et al* 2000, 2001). The final data and results form the basis of a paper in preparation for journal submission.

3.1.2 Contrast-Enhanced Tumour Imaging

As was described in chapter 2 subtraction pre and post-contrast 3D T1-weighted imaging is a useful clinical tool for visualising the cerebral venous system in three dimensions. However, the Magnevist (gadopentetate dimeglumine) contrast agent used for this study is more often administered in cerebral imaging to allow visualisation and grading of intracranial tumours (Runge *et al* 1989, Runge *et al* 2001)

Magnevist is ideal for cerebral lesion imaging for two main reasons. Firstly, its paramagnetic properties significantly reduce T1 relaxation times in any tissue where the contrast agent is present. When T1-weighted sequences are acquired the presence of the Magnevist contrast agent within a tissue results in increased signal due to the T1 shortening. Secondly, due to the hydrophilic nature of the contrast agent it is unable to cross a fully intact blood brain barrier (BBB). Therefore, any area of contrast enhancement within the brain parenchyma, excluding vessels, indicates the presence of a local break down in the BBB, suggesting disease or injury (Månsson and Bjørnerud 2001).

A large number of studies have used this contrast agent (and similar agents) for investigations in to cerebral lesions and more specifically have used it to determine changes in lesion size and extent in serial MR studies (Markert *et al* (2000), Haney *et al* (2001), Schellinger *et al* (1999), Rampling *et al* (2000)).

BBB breakdown can occur in a number of clinical conditions, including MS (Powell 1983, Cotton 2003) and traumatic brain injury (Lenzlinger 2001), however, it is for tumour imaging that Magnevist is most commonly used in cerebral MRI.

BBB breakdown in tumours is most often a direct consequence of angiogenesis where the new tumour microvessels characteristically lose their blood brain barrier properties and leak fluid into the brain (Seitz & Wechsler 1987, Groothuis *et al* 1991). Investigations of the ultrastructure of human gliomas has revealed opening of the intermicrovessel endothelial cell tight junctions (Long 1970, Barr-Sella *et al* 1979, Nir *et al* 1986, Shibata 1989). These 'leaky' junctions result in increased permeability in the tumour region and hence an overall breakdown of the blood brain barrier.

Not all tumours, and not all grades of tumours results in 'leaky' microvasculature. A recent publication by the World Health Organisation (WHO 2000) describes the histological and radiological findings for tumours of the central nervous system and describes a number of cerebral tumours that do not result in significant BBB breakdown. However, BBB breakdown almost always occurs in glioblastoma multiforme (glioblastoma) which is a malignant form of glioma (astrocytoma grade IV) (Taveras 1996) and is the most common intracranial neoplasm in adults (Collins 1998, Salcman 1985).

Astrocytomas, and more specifically glioblastomas, are poorly circumscribed tumours and even if distinct borders are seen microscopically, close scrutiny may show that tumour cells extend beyond the apparent borders that represent the neoplasm (DeAngelis 2001). Tumour cells can be found several centimetres away from the tumour and in some cases can extend throughout the entire hemisphere or

large portions of the brain in a condition known as gliomosis cerebri (Jennings *et al* 1995, Kelly *et al* 1987).

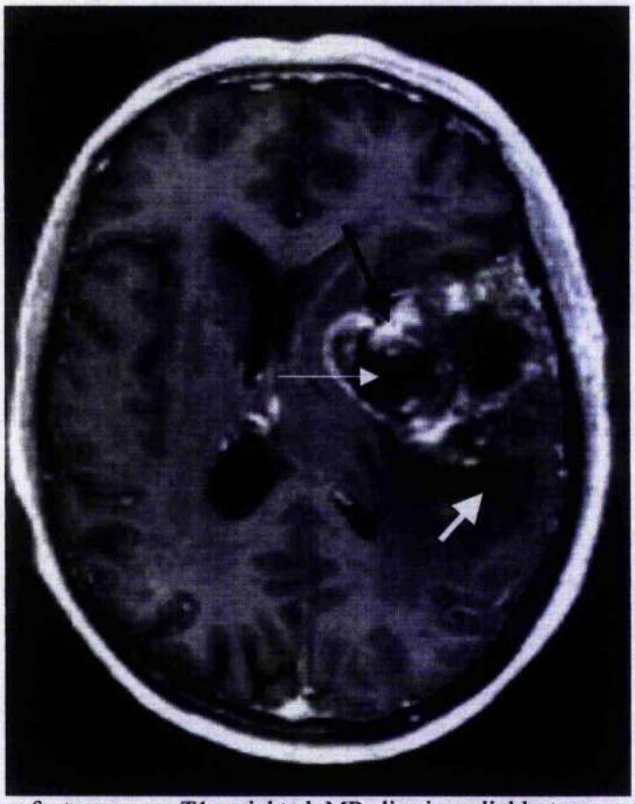

Figure 3.1: An example of a transverse, T1-weighted, MR slice in a glioblastoma patient following contrast injection. The enhancement pattern is typically ring-like (thick black arrow) suggesting active tumour surrounding a central area mainly consisting of necrotic tissue (long white arrow). There is often an area of edema closely associated with the tumour (thick white arrow)

Malignant astrocytomas, which include glioblastoma multiforme, have a typical appearance in MR images (See figure 3.1). Following contrast injection T1 weighted images typically display irregular contrast enhancement, which is often ring like. The lesion is also surrounded by edema, and mass effect can be severe enough to cause herniation. The tumour typically involves white matter and can spread across the corpus callosum (DeAngelis 2001). It is possible to use the changes in the volume of contrast enhancement to determine changes in tumour extent.

Glioblastoma remains a formidable problem in CNS cancer medicine (Rampling *et al* 2000). Following conventional therapy with surgery, radiotherapy

and chemotherapy the median survival, following diagnosis, is approximately 1 year (Scott *et al* 1999). Progression following primary therapy is associated with short-term survival (average 5 months) (Rajan *et al* 1994). Therefore, there are various ongoing studies attempting to develop more advanced treatments for this condition (Rampling *et al* 2000, Markert *et al* (2000), Hassenbusch *et al* (2003), Gariboldi *et al* (2003)).

3.1.3 Glioblastoma Treatment Measures

With the development of any new treatment agent, it is important to determine its treatment efficacy. In glioblastoma this will include determining various parameters at different time points within the treatment including immunological markers, histological markers, tumour perfusion, and tumour volume. Imaging, including MR imaging, can play a vital role in determining treatment efficacy and safety (Rampling *et al* 2000, Markert 2000), with tumour volume measurement playing a vital role in determining the effects of different treatments.

In Rampling *et al* (2000) tumour volume measurements were conducted as part of a phase 1 toxicity trial for a novel mutated herpes simplex virus treatment for glioblastoma. This replication competent virus is injected directly into the glioblastoma and has been specifically mutated to replicate in actively dividing but not terminally differentiated cells (Brown *et al* 1994). The aim of this study was to determine the safety of the virus when injecting it directly into the tumour. The virus was specifically designed to replicate in fast dividing tumour cells leaving brain cells unaffected. Therefore, the study observed the normal brain tissue surrounding the

injection site closely for any signs of infection or inflammation resulting directly from the virus agent.

As an integral part of this study tumour volumes were measured using both MRI and SPECT to help determine the effects of the virus agent. For the MRI tumour volume measurements the following protocol was applied.

The MRI data sets were acquired on a 1.5 T Siemens Magnetom MR scanner. Tumour enhancement volumes were measured using a threshold method applied to realigned pre and post-contrast MP RAGE 3D T1-weighted data sets. The data collection methods were the same as those described in chapter 2. The pre-contrast data was subtracted from the realigned post-contrast data resulting in a data set highlighting areas of enhancement such as veins, areas of BBB breakdown (tumour related), skin etc. To avoid the necessity of segmenting the brain tissue in these data sets, allowing automatic registration, the pre-contrast data was manually rotated and translated until a good visual registration was achieved

Before tumour related enhancement volumes could be measured other enhancing structures where excluded from the data. To achieve this an experienced neuro-radiologist (Prof Donald Hadley) drew regions of interest around the tumour related enhancement with the aim of excluding these structures. The regions were drawn using Analyze (version 3.5, Mayo Foundation, Rochester, MN) image processing software. Volume measurements were restricted to these regions of interest.

Background noise in the subtraction images was determined by drawing regions of interest in slices from the opposite hemisphere to the main body of the neoplasm (sagittal plane). These regions were drawn in areas where no contrast enhancement or subtracted structure could be visualised. A threshold for enhanced

tumour tissue was set to 2.5 standard deviations above the average noise level and this threshold was applied to the data within the tumour region of interest. The number of voxels within this threshold was counted and multiplied with the data voxel dimensions providing a measurement for the tumour related enhancing volume. These volumes were measured at the three time points required by the study, allowing comparison of volumes over time.

This method of tumour volume measurement is easier and quicker than full manual segmentation, which requires accurate regions of interest to be drawn. The regions of interest required for this method need only contain the data of interest and exclude unwanted enhancing data. Therefore, the regions can be drawn quickly reducing the requirement for skilled operator time. Also by registering the data sets manually, removing the requirement of segmenting the brain parenchyma, further time was saved in the analysis procedures

However, the threshold method of tumour volume measurement is likely to be affected by the accuracy of the registration between the pre and post-contrast data sets. Any structure visible in the background subtraction would affect the threshold level set to determine the tumour volume measurements. Poorly aligned data might also introduce artefacts into the tumour related enhancement resulting in incorrect volume measurements. Therefore, this chapter investigates the effects of using the MATCH realignment software on the resulting tumour volume measurements. It compares the volumes produced with and without realignment and concludes on the requirements for realignment in these data sets. It also compares the results with those determined by registering the data sets manually.

3.1.4 Measurement of Scanner Drift

When using this technique to determine changes in tumour volume over extended time-scales it must be assumed that the subtraction background characteristics remain invariant over these time scales. On the scanner used for this study, for each imaging sequence hardware gain settings are determined from initial tuning pulses before each sequence starts. Therefore, gain settings will be different after the injection of the contrast agent, due to the overall increased signal intensity within the patients head. This will result in different contrast characteristics for the pre and post-contrast data sets.

Differing contrast characteristics are not, however, a problem if the differences between the two data sets are similar at different imaging session. As has already been discussed measurements of contrast enhanced regions in MRI are not direct measurements of tumour volume. However, changes in contrast-enhanced volume over time are a good indication of tumour progression or regression (Nelson *et al* 1999). Therefore, the measurement of interest in these studies is not the absolute contrast-enhanced volume, but the change in contrast-enhanced volume over time. Thus, if the contrast differences, for individual patients, between the pre and post-contrast data sets are invariant over the long periods of time that encompass these studies then this method would provide a good method for measuring the extent of tumour progression.

To test the hypothesis that the differences do not vary over time, for each of the subjects detailed in this chapter the contrast to noise (CNR) of the original pre-surgical scans already analyzed were compared to the CNR post-surgical scans. As well as comparing the CNRs directly the changes in CNR from pre to post-contrast data were also compared.

3.2 Methods

3.2.1 Testing the Effects of Realignment on Tumour Volume Measurements

Nine patients following the phase 1 trial HSV protocol were scanned using the protocol displayed in table 3.1 This protocol contained pre and post-contrast 3D MP-RAGE data collected using a similar protocol to that described in chapter 2 (section 2.2.1.1). The main difference in the protocol occurs at step 7 where there is a five minute pause from the end of the injection to the start of the pos-contrast MP RAGE sequence. This was to allow for better tumour uptake of the contrast agent. The pre and post contrast data sets were realigned using the MATCH algorithm after the brain parenchyma had been manually segmented, ensuring no enhancement remained in the realignment mask.

Step in Protocol	Description of Scan/ Procedure
1	Transverse localised
2	Coronal Localiser
3	Sagittal Localiser
4	T2 Transverse sequence, 20 slices tilted to AC/PC line
5	Pre-contrast MP RAGE sagittal
6	Give contrast via long line
7	Wait 5 minutes from the end of the injection
8	Post-contrast MP RAGE sagittal

Table 3.1: The imaging protocol used for the HSV trial. The 5 minute wait at step 7 was to ensure good contrast uptake in the tumour

Following realignment the realigned pre contrast data was subtracted from the post contrast data, producing a realigned subtraction data set. For comparison a second subtraction data set was produced by subtracting the non-aligned pre-contrast data from the post-contrast data.

To allow tumour volumes to be measured for each of the subjects, the aligned subtraction data was loaded into the Analyze software package and an ROI was drawn around the tumour enhancement by the neuro-radiologist to ensure that contrast enhancement from within the ROI was from tumour only. Each subject's ROI was stored for use with both the non-aligned and aligned subtraction data sets. The ROI's for the manually realigned data sets had previously been drawn and used to calculate enhancement volumes. These regions were not available for use in this study as they had not been digitally stored. Therefore, there will be differences in the ROIs used for these measurements.

To enable thresholds to be set to determine the volume of tumour enhancement, ROIs were drawn on the aligned subtraction data set, in areas where little or no contrast enhancement was present. Care was taken to ensure that these areas were contained within the brain parenchyma. These regions would provide the mean and standard deviation of the background noise in the subtractions. The same regions were used to determine the mean and standard deviations of the noise in the non-aligned data sets.

Using the method described in the previous section, volumes were calculated for both the MATCH aligned and non-aligned data sets, using the corresponding noise results. This would determine the effect of misalignment on measuring tumour volumes using this method. Any differences between the aligned and non-aligned results would be a combination of two effects. Firstly, any differences in background noise will result in different thresholds being set for the corresponding data sets. This is likely to have a significant effect on the volumes measured. Secondly, due to poor alignment there will also be subtraction errors in the tumour data, possibly increasing or decreasing the apparent volume.

To investigate the tumour subtraction error separately the threshold value determined in the aligned data set was also used to threshold the non-aligned data in the repeat measurement. It is likely that any method using this subtraction technique for tumour volume measurement will be affected by the threshold and realignment errors.

3.2.2 Determining the CNR Drift

Contrast between two tissues A and B can be defined as:

$$C_{AB} = S_A - S_B \tag{3.1}$$

where S_A and S_B are signal values from tissues A and B.

Therefore, contrast to noise ratio can be defined as:

$$CNR_{AB} = \frac{C_{AB}}{\sigma_0} = \frac{S_A - S_B}{\sigma_0} \tag{3.2}$$

where σ_0 is the background noise in the image. In this thesis σ_0 was measured as the mean of magnitude data on a specified background region of interest.

As part of the HSV treatment protocol MRI scans were acquired at three time points during the study. The first scans were collected before the HSV agent was delivered to the tumour. Typically these scans occurred between 0 and 3 days before agent delivery. The HSV agent was then delivered to the tumour region using a sterotactic injection, which is a minimally invasive surgical technique.

The second set of MRI scans were collected between days 4 and 6 after the agent delivery. It has previously been shown by the author, in work closely related to this thesis (Brennan *et al* 2001), that post-surgical inflammation can result in increased uptake of Gd tracer in regions affected by operation, even after using such a

minimally invasive technique. Therefore, these scans were excluded from this study, due to possible changes in CNR as a result of surgical effects.

The third time-point where MRI scans were collected was between 27 and 66 days. At this time post surgical effects will be minimal with relation to Gd tracer uptake. Therefore, it is possible to determine changes in CNR over time differences varying between, 27 and 66 days. More importantly it is possible to determine if the differences in CNR between the pre and post-contrast data sets change significantly between sessions.

The data collection methods have been described previously (section 3.2.1) and were the same at all time points. Data was collected for the 9 patients in the study, however, for two patient's data the MPRAGE data at the later time point were erroneously collected in coronal slices instead of the normal protocol sagittal slices. These two patients were excluded from this study due to possible variability in contrast introduced by acquiring the slices in a different plane.

Four different sets of data required CNR measurements; the pre and post contrast data sets before surgery and the pre and post-contrast data sets after surgery. The pre contrast data used in both the before and after surgery measurements was the MATCH realigned pre-contrast data. Using the aligned data allowed the same regions of interest to be drawn for the pre and post-contrast data at the same time points.

Three sets of regions were required to determine CNR using the previously defined signal A, signal B and σ_0 (see equation 3.2) For this study signal A was defined as white matter signal, signal B was defined as CSF signal and σ_0 was defined as a background region outside the patients head (see figure 3.2).

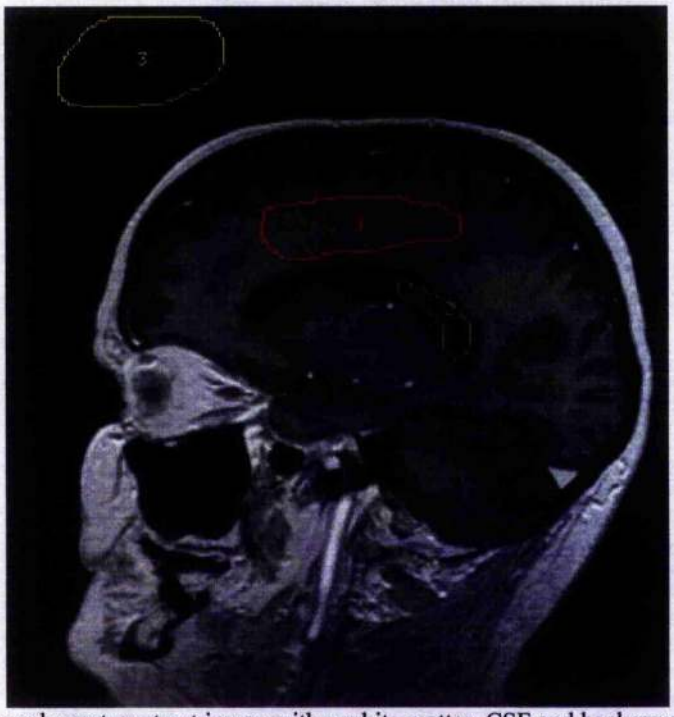

Figure 3.2: Example post-contrast image with a white matter, CSF and background noise region defined

White matter was a good tissue to use for measurement purposes in this study as normal brain white matter is not significantly enhanced by Magnavist injection. Therefore, signal differences detected before and after contrast injection, within white matter, should almost exclusively be due to differences in scanner signal gain with a random noise component. There are also large areas of white matter available for signal measurement which are homogenous and continuous. Thus white matter tissue is a good candidate for SNR and CNR measurements.

CSF signal was chosen as the second signal source for a number of reasons. In this study the realigned data sets are being used for the measurements, allowing the same ROI's to be used in the pre and post-contrast data sets. These data sets were aligned using only the brain parenchyma for the registration calculations. Therefore, it was not possible to guarantee that non-parenchymal structures outside the brain were correctly aligned. If signal B was measured from one of the non-parenchymal tissues

such as muscle, ROI's drawn on the pre-contrast data would not necessarily overly the same voxels or structures in the post-contrast data. Therefore the signal B measurements needed to be taken from somewhere within the brain itself.

The most obvious structure to measure in this instance would be the grey matter. However, the vast majority of the grey matter lies between white matter and CSF in thin, convoluted strips of tissue, leading to two problems. The first is partial volume effect. Due to the small thickness of the majority of the cortical grey matter (of the order of millimetres) if grey matter regions were drawn a significant number of voxels would be in volumes affected by white and CSF partial voluming unless care was taken to ensure such voxels were excluded. A more significant problem occurs where the patient has been unable to keep still during the scan.

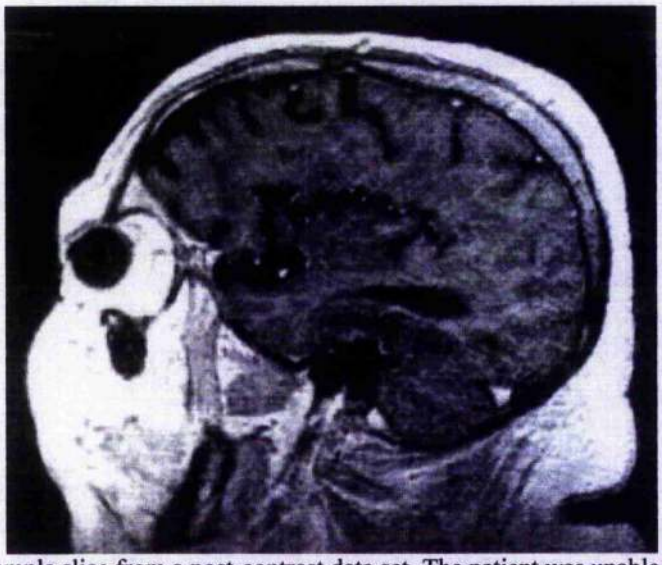

Figure 3.3: An example slice from a post-contrast data set. The patient was unable to keep still during the scan. This reduced the contrast between the grey and white matter making it difficult to define the grey and white matter borders.

As figure 3.3 illustrates patient movement results in difficulty in separating the grey matter from the adjacent white matter, due to blurring and signal contamination. As the motion is occurring during the scanning as well as between the scans, this

limits the accuracy of the alignment. Therefore, this would result in difficulty when drawing regions for both the pre and post-contrast data sets.

To avoid these problems CSF signal from the cerebral ventricles was measured and compared to the white matter signal. Although the ventricles themselves are not brain parenchyma, they were included in the realignment data sets for this study, as the location of these structures are physically linked to the location of the brain itself. The larger dimensions of the CSF within the ventricles, when compared to the grey matter enable the regions to be drawn with greater confidence, avoiding the boundaries with brain matter where signal blurring may occur.

The noise regions were drawn in the superior/anterior corner on slices where CSF and white matter regions were drawn. Placing the regions in these locations avoided contamination from the vast majority of motion artefacts (phase direction was in the anterior/posterior direction).

All regions were produced using Analyze software's trace tool within the ROI module. The corresponding pre and post-contrast data from before surgery were loaded into the same ROI module allowing the regions to be drawn with respect to both data sets. The post surgery data sets were then loaded into a separate ROI module with the aim of reproducing the same ROI's by hand, so that the regions were in the same areas before and after surgery. This would allow comparison of the CNR figures at both time points. The statistics tool was then used to sample the data within each region supplying the mean voxel values for the corresponding regions. Using this information from each data set, it was possible to calculate the appropriate CNR results. CNR was compared at both time points. The effect of contrast injection on CNR was also investigated.

3.3 Results

3.3.1 Tumour Volume Measurements

Table 3.2 displays the tumour volume measurement results from the MATCH aligned and un-aligned and the manually aligned data sets.

Patient	Aligned Volume (cm^3)	Non-Aligned Volume (cm^3)	Non-Aligned (Aligned Thresh) Volume (cm^3)	Manually Aligned Volume (cm^3)
1	60.16	51.02	61.89	60.13
2	142.10	115.52	144.18	129.02
3	19.48	15.52	20.68	19.47
4	12.10	11.36	12.84	11.38
5	46.55	46.74	46.74	39.27
6	62.32	52.77	63.87	53.67
7	23.65	27.72	25.21	24.50
8	9.07	4.10	9.3	8.56
9	32.39	28.68	33.19	31.43

Table 3.2: Tumour volume results from aligned and non-aligned data

When the aligned and non-aligned tumour volumes are compared using a two tailed paired T statistical test which assumes normality of the data, $p = 0.074$, which is a non-significant result. If it is assumed that overall there is a reduction in tumour volume measured, as would be expected due to the increase in threshold values used, and a 1 tailed test was used, $p=0.037$ which indicates a significant difference between the groups. In all but two patients (patient 5 and 7) the tumours volumes measured with the non-aligned data are smaller than the aligned data measurements.

If the MATCH aligned is compared to the manually aligned data again using a paired T test, $p=0.076$ in a two tailed test. Once again the significance is significant if using a one tailed test ($p=0.038$), which again can be accepted as manual alignment was not expected to be of as good quality as the MATCH alignment, once again

resulting in increased thresholds and smaller volume measurements. When the manually aligned data is compared to the non-aligned data there is no significant difference detectable (p=0.23, two-tail). However, the overall average volume for the manually aligned data is marginally larger (41.94cm^3 compared to 39.27cm^3) suggesting a slight improvement in measurement accuracy if we assume the trend towards the MATCH volumes is increasing accuracy.

When the aligned and the non-aligned data are compared, when the same threshold values are used with both data sets, the two tailed paired t-test significance is $p = 0.001$. Here there is no requirement to assume the overall direction of change in tumour volume between the two sets of data and as there was no a priori information to suggest the direction of the difference in this statistic is not relevant. However, from viewing the data in table 3.2 it is clear that in all cases the tumour volume measured is greater when the non-aligned data is used with the aligned data threshold.

It should be noted that although the data here were assumed to be normal this may not be the case. For any future work where larger data sets are collected normality should be tested and appropriate statistical tests used.

3.3.2 CNR Variations

Table 3.3 displays the CNR results from all of the patients data sets at both time points.

	Before Surgery			After Surgery		
Patient	Pre CNR	Post CNR	Difference	Pre CNR	Post CNR	Difference
1	8.18	7.81	0.37	9.78	9.20	0.58
2		No Calculation			No Calculation	
3	12.92	12.48	0.44	12.81	11.05	1.76
4	7.40	5.68	1.72	7.49	5.08	2.41
5	11.51	7.28	4.24	11.85	9.26	2.58
6	11.06	10.47	0.59	10.11	8.23	1.88
7	7.92	7.61	0.32	10.75	9.75	1.00
8		No Calculation			No Calculation	
9	8.51	5.93	2.58	7.53	5.66	1.87

Table 3.3: CNR results of pre and post-contrast data before and after surgery

To determine if there was any detectable scanner drift over time, the pre surgical pre and post-contrast data sets were compared with the corresponding post-surgical data sets. The data sets are paired, therefore to determine if there was any significant difference a paired sample T-test was used. No significant difference was detected (p(two-tailed)=0.52). However, there is a linear relationship between CNR before and after surgery (see graph 3.1). This relationship has a Pearson correlation of 0.783 (p=0.001).

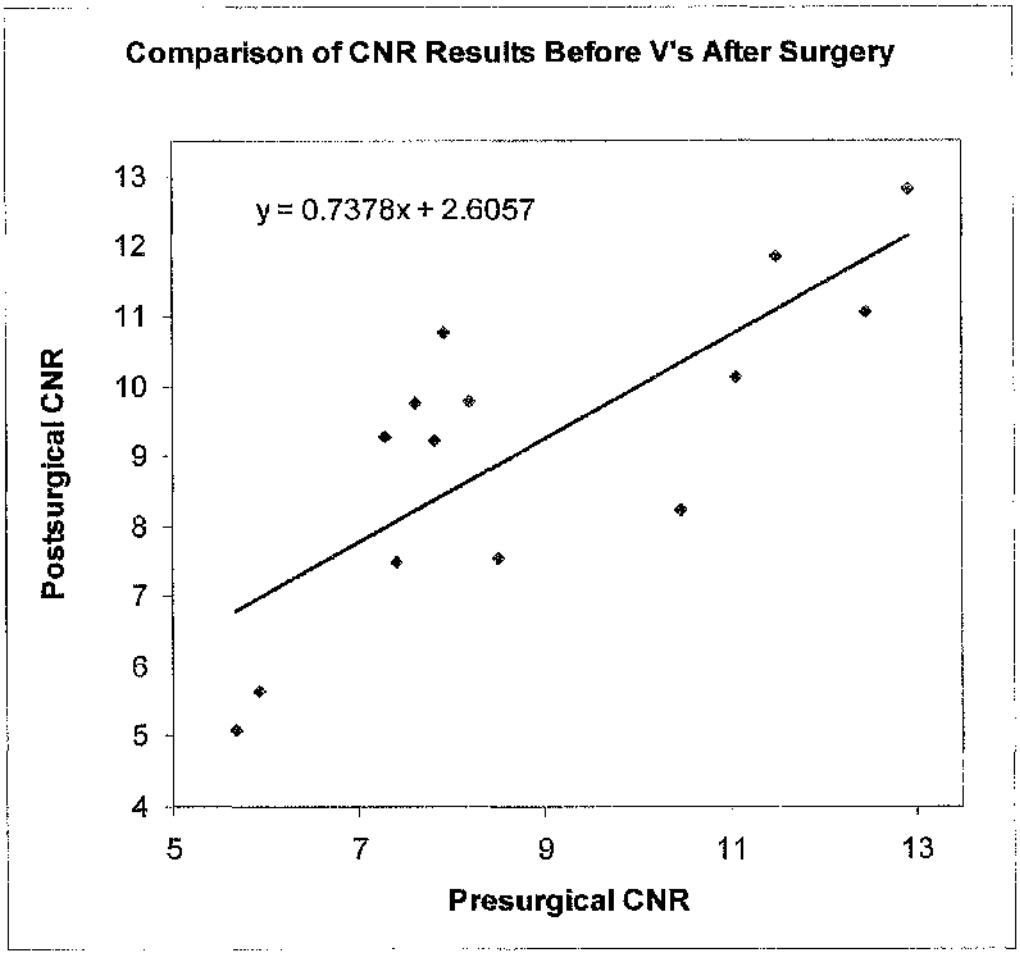

Graph 3.1: Comparison of CNR before and after surgery

It should be noted that the before and after surgery scans were conducted at different times for different patients. Graph 3.1 has a gradient of below 1 and crosses the after surgery axis significantly above zero. This may suggest that CNR does change over time. However, due to the large amount of variability in CNR from patient to patient, it is difficult to provide any firm conclusions from this result. Tumour volume also increases for all but two patients over the course of this study (Rampling *et al* 2000), therefore this may have an effect on the CNR and CNR differences. Larger areas of enhancement would most likely lead to a decrease in the CNR measured here.

To further understand the effects of contrast injection on CNR pre-contrast CNR values were compared to post-contrast CNR values. Here there was a significant difference with an expected drop in CNR (p(one-tailed)<0.001). The drop in CNR was consistent for all measurements as can be demonstrated in graph 3.2.

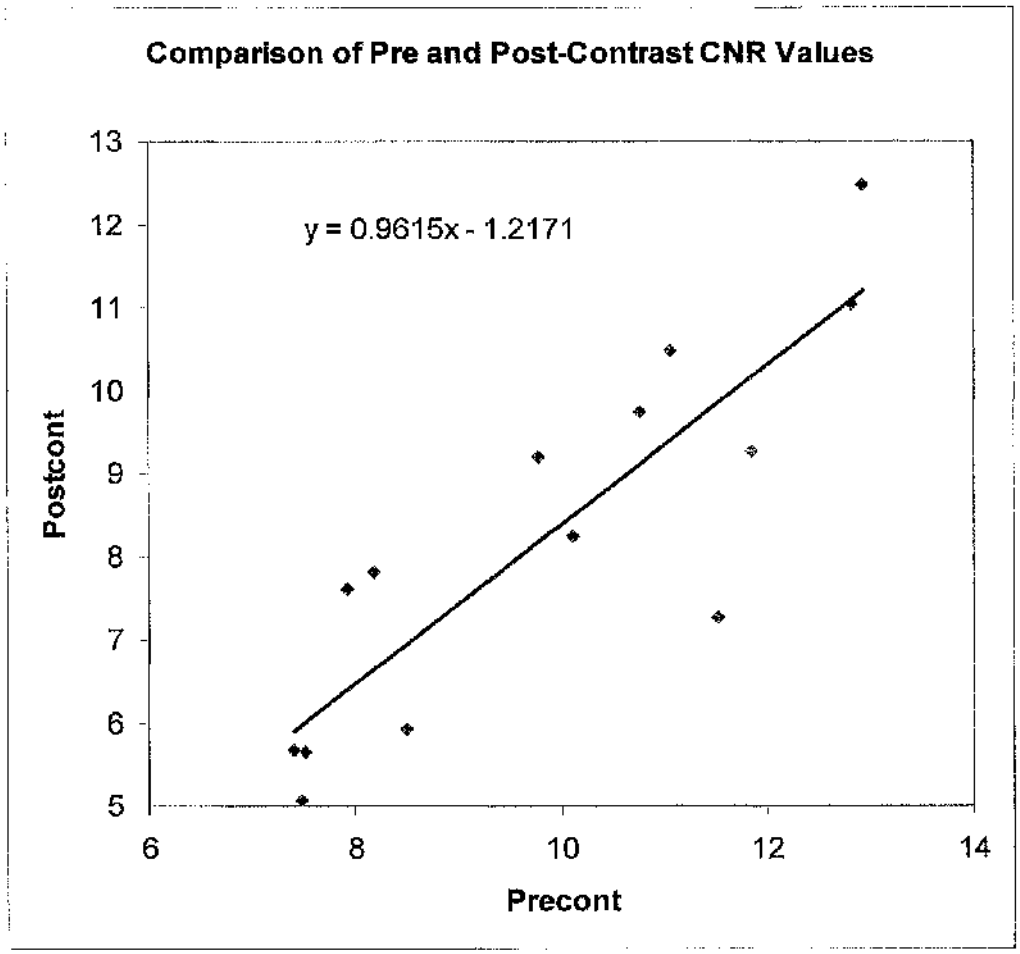

Graph 3.2: Comparison of pre and post-contrast CNR values at both study time points

The graph has a gradient very close to 1 suggesting a one to one correlation between pre and post-contrast CNR. The intersection of the graph is at –1.22. This would appear to confirm the prediction that post contrast injection, the scanner compensates for the increased signal within the brain by reducing the signal gain.

However, once again there was a significant amount of variation in the data from patient to patient.

There was found to be no significant difference in the CNR differences (pre minus post) before and after surgery. However, due to the variable nature of the CNR results there was a significant amount of variation in the differences calculated with a before surgery mean of 1.47 ±1.49 and an after surgery mean of 1.73 ±0.72. The large standard deviations would reduce the likelihood of detecting significant differences (this was also a result of the small sample). There may be a linear correlation between the before and after surgery differences (see graph 3.3) , however once again the sample is too small to assume such a relationship exists.

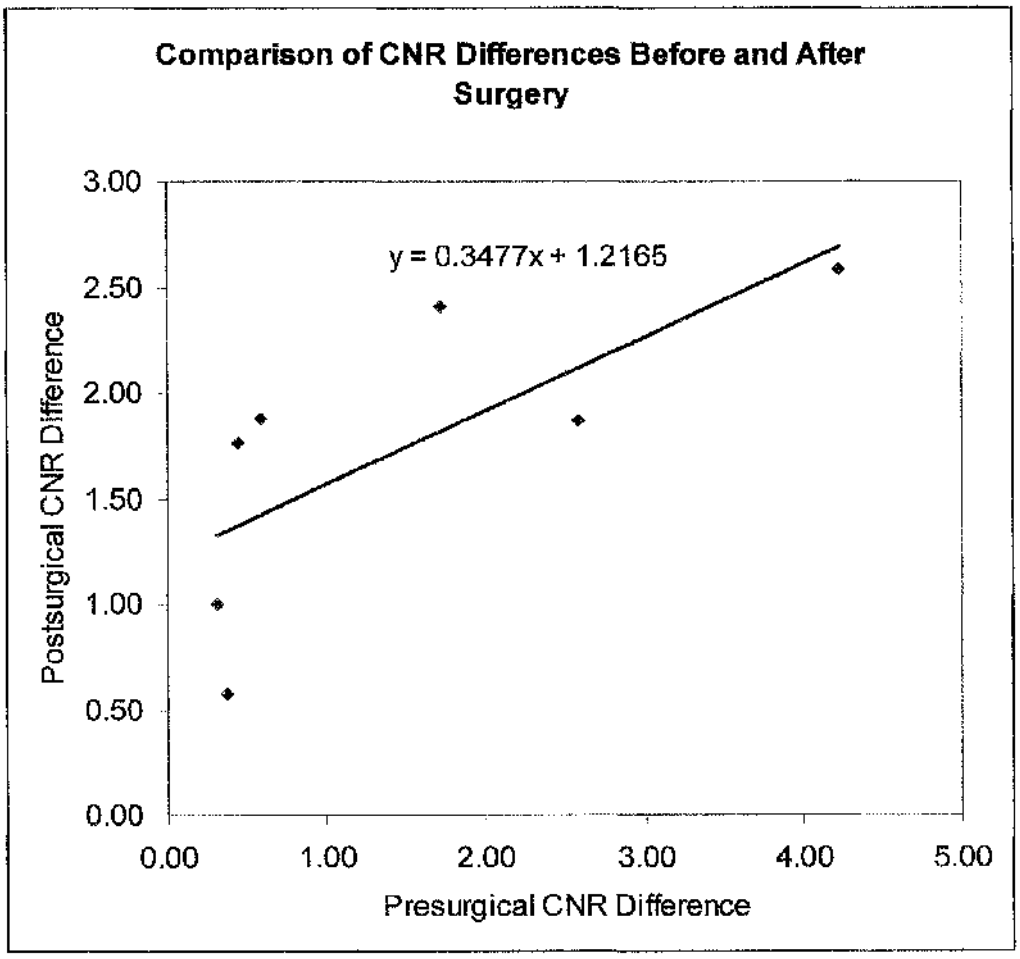

Graph 3.3: Comparison of the CNR differences before and after surgery

Despite the small numbers and lack of significance it should be noted that there are large differences in CNR for paired data sets.

3.4 Discussion

The main aim of this chapter was to determine the effects of realignment on pre and post-contrast data sets when the subtracted data is used to determine tumour volume. As with any method of determining tumour volume there are advantages and disadvantages in using particular techniques. The threshold technique used in this study does have several disadvantages.

As this study has shown the requirement for thresholding introduces errors into the volume measurement due to the uncertainty in setting the value of the threshold. By determining the threshold from the background subtraction noise the tumour volume measured carries some dependence on any changes in the background subtraction data. It has been shown that this background variation can be minimised by ensuring the pre and the post-contrast data sets are correctly aligned resulting in an accurate subtraction and therefore an accurate measurement of the subtraction background noise. Data sets that are not fully realigned often have structure visible in the subtraction data. Figure 3.4(a & b) illustrates this, showing the same slice from a non-aligned and MATCH aligned data set. The presence of unwanted structure within the subtraction data would result in incorrect background noise measurements resulting in incorrect tumour volume measurements.

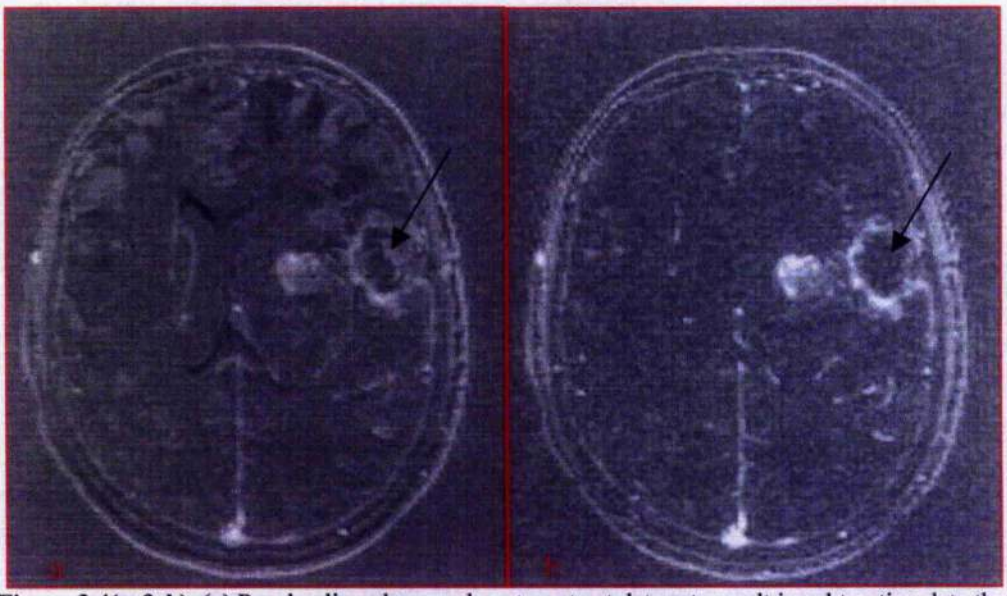

Figure 3.4(a & b): (a) Poorly aligned pre and post-contrast data sets result in subtraction data that displays unwanted anatomical structure compared to (b) realigned data from the same subject The two arrows indicate an area within the tumour that appears to contrast-enhance on the unaligned data but does not appear contrast-enhanced on the realigned data.

Following alignment of the pre and post-contrast data, there are still problems using the threshold technique. When using this technique to determine changes in tumour volume over extended time-scales it must be assumed that the subtraction background characteristics remain invariant over these time scales. On the scanner used for this study, for each imaging sequence hardware gain settings are determined from initial tuning pulses before each sequence starts. Therefore, gain settings will be different after the injection of the contrast agent, due to the overall increased signal intensity within the patient's head. This will result in different contrast characteristics for the pre and post-contrast data sets.

Differing contrast characteristics are not, however, a problem if the differences between the two data sets are similar at different imaging session. As has already been discussed measurements of contrast enhanced regions in MRI are not direct measurements of tumour volume. However, changes in contrast-enhanced volume

over time are a good indication of tumour progression or regression (Nelson *et al* 1999). Therefore, the measurement of interest in these studies is not the absolute contrast-enhanced volume, but the change in contrast-enhanced volume over time. Thus, if the contrast differences between the pre and post-contrast data sets are invariant over the long periods of time that encompass these studies then this method would provide a good indication of tumour progression.

To test the hypothesis that the CNR differences do not vary over time, for each of the subjects detailed in this chapter the CNR of the original pre-surgical scans already analyzed were compared to the CNR post-surgical scans. As well as comparing the CNRs directly the changes in CNR from pre to post-contrast data were also compared. From this work it was found that following contrast injection CNR did change in a predictable way. However, it remains unclear if CNR and the difference in CNR between pre and post-contrast CNR remains invariant over time.

It was difficult to reach conclusions regarding CNR changes using the available data. The data for each patient was collected at different times during an approximately one year period. Therefore, this analysis would only detect if there was a trend that remained consistent over this time period and that the change was large enough to be measured between the before and after surgery scans. It is possible that there could be drifts that do not follow this linear pattern. For example the gain electronics could be susceptible to weather conditions, such as temperature, pressure and humidity, although variations in temperature at least should be moderated by air conditioning. If this were the case then there would be variations in the gain characteristics either with a period of 1 year relating to seasonal weather variations or with periods of a day relating to variations in temperature over the course of a day.

It is also possible that the variations in CNR between patients would be greater than the effect being measured. Therefore, it is suggested when using the pre and post-contrast tumour measurement technique (such as in chapter 3) that some form of test of the scanner gain characteristics should be devised. Results from these measurements could be used to improve the reliability of the tumour measurements using the pre and post-contrast technique.

Despite these problems it would appear that CNR at two separate time points is linearly related (see graph 3.1). This suggest that scanner gain, although not predictable from a previous gain result, is strongly associated with the patients anatomy (i.e. size of head, amount of grey/white matter etc). Although there is not a direct one to one equivalence of the CNR values before and after surgery this may be a reflection of the general increase in tumour volumes at the second time point (Rampling *et al* 2000) and not a result of scanner drift. As a result of the linear relationship it may be possible for future studies to develop a protocol using the initial scan information for a patient to set subsequent gain setting on the scanner for subsequent scanning sessions.

Despite these problems the region drawing threshold technique can be quickly applied to studies with a large amount of data sets, such as was required by a gene therapy agent trial (Rampling *et al* 2000). For example, as a direct consequence of this work the corrected MRI tumour volume measurements were compared to the SPECT tumour volume measurements at the three time-points in the Rampling study (Brennan *et al* 2000, 2001). It was found that post-surgical enhancement effects resulted in artefactually large tumour volume measurements in scans collected shortly after minimally invasive surgery. Therefore, it was suggested that for future studies

where serial tumour volume measurement are required shortly after surgery, that SPECT should be used for tumour volume measurement.

It might be possible in the future to automate the tumour volume measurement procedure by amending algorithms such as those developed by Haney (Haney *et al* 2001) to work with the subtraction data sets. Not only would this speed up the measurement process, it might also improve overall accuracy and reproducibility.

Despite the errors inherent in the technique described here, the errors are likely to be small compared to the effect that is being investigated. When measuring tumour volume changes in treatment studies, it is necessary to determine criteria under which tumour progression or regression can be measured. The most recent guidelines for tumour response criteria were published by Therasse *et al* (Therasse *et al* 2000) who developed the RECIST (Response Evaluation Criteria in Solid Tumours) and was based on work by James *et al* (James *et al* 1999). The suggested definition for tumour volume progression using these RECIST criteria is an increase in the sum of the longest diameters of the tumour of 20%, which according to Therasse would suggest a volume increase of 73%. A partial response to treatment is defined as a 30% decrease in the sum of the diameters suggesting a decrease in volume of 65%. These figures suggest that accuracy of this technique developed within this chapter is well within the required accuracy to detect these changes reproducibly.

The report by Therasse and others before it (WHO 1979, Miller *et al* 1981) are currently the only published guidelines for determining tumour response to treatment. However, the guidelines are based on solid tumours with well defined edges. As has been discussed previously (section 3.1.2) glioblastoma type tumours have poorly defined edges and are far from solid. Despite these differences the response guidelines

are often used in clinical practice. However as tumour size measurement improves it is likely that new guidelines will be devised with particular reference to new 3D tumour volume measurement techniques.

The comparison between aligned and non-aligned data sets using the same threshold value indicated that the errors in not aligning these data sets are not confined to the threshold values calculated. The different volumes calculated for the tumour enhancement suggest that the accuracy of the tumour subtraction itself is sensitive to patient movement between data collection of the pre and post-contrast data. In general when the thresholds are set to the same value the use of the non-aligned data results in a larger contrast volume. Therefore, poor alignment results in subtraction data that appears to have contrast enhancement where in reality there is none. An example of this is shown on figure 3.4. However, it is also likely that misaligned data will also result in voxels that have lower subtraction signal, and will therefore fall below the contrast-subtraction threshold. The overall increase in volume in the realigned data sets suggests that more voxels increase in value and move into the threshold value range, than fall below the threshold value range. This is a consistent finding for all of the patients in this study and is a statistically significant result.

The increase in contrast volume for non-aligned data can be explained by assuming that for contrast to be present there must be an underlying structure for the contrast material to be present in. If this assumption is correct, and when the data is correctly aligned, where there is contrast enhancement in the post-contrast data there will be some corresponding tissue signal in the pre-contrast data. Contrast enhancement is not uniform in all tissues and likewise in the pre-contrast data sets, different tissues have varying voxel signals. Therefore, there will be voxels with

intermediate pre-contrast signal and intermediate amounts of contrast enhancement. Subtraction of the data sets would result in a number of such voxels falling below the threshold levels set and below levels of operator perception. In this situation these voxels would not be included in the volume measurements.

However, if the pre and post-contrast data were not correctly aligned and the voxels described above are close to non-enhancing structures where the signal was low in the pre-contrast data set, it is possible that the realignment might result in enhancing post-contrast voxels overlying voxels with little or no pre-contrast signal. These voxels are likely to occur at the edges of the tumour enhancement, particularly where the edges are close to regions of low signal. Some increase in the volume of the contrast edges is visible in figure 3.4. In resulting subtraction data these voxels would have values greater than the threshold value and would be included in the final volume measurement.

This suggests that the non-aligned data sets might subtract to produce a more accurate measurement of the true tumour enhancement volume as moderately enhancing voxels are also being included in the final measurements where they were not before. However, as has been shown previously pre and post-contrast alignment is an uncontrollable variable, and would thus lead to uncontrollable variations in the amount of 'extra' voxels included in the final analysis. This extra error would decrease the ability to legitimately compare volume results collected in different sessions. Also as illustrated by figure 3.4 if gross motion occurs between the pre and post-contrast data artefactual enhancement can occur away from the edges of the tumour suggesting that this signal is due to the incorrect alignment of tissue boundaries. Therefore, for the purposes of measurement repeatability in tumour

studies using the subtracted pre and post-contrast data a good method of registration should be employed.

3.5 Conclusions

Any technique of measurement that requires subtraction of pre and post-contrast data sets must ensure that the data sets are aligned as well as possible before subtraction takes place. This study has shown that if this step is not taken erroneous results for tumour volume are derived from the data measurements. Manual methods of determining tumour volumes from these subtracted images are also likely to be affected by alignment errors.

As has been discussed in the previous chapter good registration of these pre and post-contrast data sets requires segmentation of the brain parenchyma from the surrounding tissue, especially enhancing structures. This would be of particular importance in this study due to the presence of large enhancing tumours, which would likely introduce realignment errors if they were not removed from the data analysed by the MATCH software.

Most segmentation algorithms are designed to accurately segment brain tissue sometimes separating them into finer components such as grey matter, white matter and cerebro spinal fluid (Thacker & Jackson 2001, Lemieux *et al* 2003). This segmentation is often used to determine ratios of different brain components or to determine changes in volumes over time. This requires that the segmentation is as accurate and repeatable as possible to enable trends to be determined. However, it is not certain how accurate the segmentation needs to be to enable accurate registration of the pre and post-contrast data sets.

It is likely that the removal of structures that change between successive scans is important. It is also likely that the existence of contrast enhancing veins that exist on one scan but not the other will introduce errors in the comparison algorithm. Therefore, it is reasonable to assume that such structures should be removed. However, how important is it that all the remaining brain is correctly segmented. For example if 5% of the brain is removed will this noticeably affect registration? Or will errors only occur when 15% of the brain is missing from the segmentation.

Having justified the requirement for realignment with subtraction of pre-and post-contrast data sets, it is now important to determine the best method of preparing the data for realignment. Therefore, chapter 4 will investigate the effects of segmentation accuracy on the realignment of pre and post-contrast data. Having this information will later allow design and implementation of automated or semi-automated procedures for segmenting such data sets, reducing the amount of skilled operator time required.

Chapter 4

Segmentation Accuracy : Review and Phantom Data Set Construction

4.1 Introduction

4.1.1 Overview

Chapter 2 described the need for realignment of pre and post-contrast data when producing subtraction venograms from 3D MP RAGE MR data sets. Chapter 3 went further and quantified the effect of applying alignment correction on tumour volume measurements using a similar technique. Both chapters achieved the realignment following manual segmentation of the post-contrast data set. However, manual segmentation is a process that requires large amounts of skilled operator time to accomplish. Therefore, it is preferable to implement an automatic or semi-automatic segmentation algorithm that would both simplify and speed up this process.

As described in chapter 2 (section 2.5.3) there are currently no segmentation algorithms available that are designed to segment contrast enhanced 3D data sets. However, there are a number of segmentation algorithms available that could segment the pre-contrast data. Therefore there are two possible protocols that could be followed to accurately realign the pre and post-contrast data without the requirement for manual segmentation.

Firstly it might be possible to segment the pre-contrast data, for which there are algorithms available that could accurately segment the brain. However, in pre-contrast data it is not always obvious what structures will enhance post-contrast. For example, in a patient with a tumour that enhances post-contrast, the corresponding pre-contrast data can be iso-intense with the surrounding normal brain tissue. This would make it very hard for segmentation algorithms to be certain of removing all

contrast-enhancement. Nevertheless, if realignment is not adversely affected by the presence of contrast-enhancement it may be acceptable to segment the pre-contrast data.

If, however, contrast-enhanced data does affect realignment adversely then the only way of ensuring that contrast-enhanced data is not contained in the realignment process is to segment the post-contrast data. Thus a new segmentation algorithm would be required.

Within the cranium, the largest enhancing structure following contrast injection, in a normal subject, is the venous system. The cerebral venous system can vary significantly from person to person (Curé *et al* 1994, Meder *et al* 1994, Morris and Choi 1996). Thus, even when there is no contrast-enhancing abnormal pathology present accurate modelling of the contrast-enhancement would be difficult to achieve.

Therefore, it is important to determine what accuracy of segmentation is required to produce good quality registration. If the post-contrast data set must be segmented and if good registration is possible without the requirement for high accuracy segmentation then a more simple and robust method of segmentation could be used. By keeping the segmentation algorithm as simple as possible it should be easier to transfer the methodology to other data sets from different scanning protocols where contrast between tissues may be different from those achieved using the MP RAGE technique.

However, before any measurements can be made a new data set is required where the pre and the post-contrast data differ from each other by known amounts of spatial transformation and tissue contrast. Therefore, before the next two chapters

investigate the effects of segmentation accuracy on segmentation accuracy, a phantom data set must be produced to fulfil the above criteria.

As far as the author is aware there have been no previous attempts to produce such a pre and post-contrast phantom, therefore, a novel method of producing one was devised by the author. This chapter as well as introducing the concept of segmentation, describes the production of the novel phantom data.

The work in this chapter (and chapter 5) led to an international conference presentation (Brennan 2002). All of the work described in this chapter was conducted by the author, with the exception of the data acquisition which was performed by radiographic staff.

4.1.2 Background

Serial investigations in MRI have been conducted since the introduction of the technique. For example Maruyama *et al* (1984) investigated the effects of neutron brachytherapy on cerebral malignant gliomas, with specific reference to the dimensional extent of the tumours. Kovanen *et al* (1985) looked at cerebral atrophy rates in patients with Creutzfeldt-Jakob disease and compared them to clinical deterioration. Single patient serial studies were also performed, one example being the study by Pomeranz *et al* (1985), where the brain of a lung cancer patient was serially scanned to detect metastatic growth. In this study MR detected the metastasis before CT. Such serial studies allowed the morphological changes over time to be assessed which could be associated with disease progression and treatment and could be compared to other modalities such as CT. Serial studies remain in prevalent use especially in MR research into disease progression (Takeoka *et al* 2003, Schott *et al*

2003, Giovannoni 2001) and treatment outcome studies (Rao *et al* 2002, Kwon *et al* 2001, Rampling *et al* 2000)

As was discussed in chapters 2 and 3 registration is not only required when serial studies are carried out over days, weeks or months, but it is also required when the patient remains within the scanner between the serial scans. This is especially true when there is some form of intervention occurring during the inter-scan interval.

Chapter 2 (section 2.4.2) also discussed the importance of conducting image segmentation to ensure the most accurate registration between the serially acquired data sets. Ideally, for the purposes of image registration, the human body would be a rigid structure in which the 3D positional relationships of every structure would remain constant over time. Thus, if one structure within an MR image was correctly registered with a previously acquired image then all other structures within the area of interest would also be correctly registered. However this is far from the case, with the human body consisting to a large extent of deformable soft tissue and movable joints. Thus, the spatial relationships of the various structures within the body change over time and so it does not follow that if you realign one structure then all other structures will also be correctly aligned even when the structures are spatially close.

When conducting studies over the course of weeks and months it is also possible for body shape to change due to increased or decreased fat or muscle, however, this is not a problem over the course of a normal scanning session and thus would not impact on pre and post contrast injection studies.

Further problems exist when attempting to realign structures contained within the head. The brain is not firmly fixed within the skull cavity and floats semi-freely in a cerebro spinal fluid (CSF) (Martini 2001), therefore, if a patient moves their head slightly it is possible for the brain to shift within the cranial cavity in relation to

all of the other cranial structures. Thus, for a study investigating changes in brain volume only the brain should be used for realignment purposes as the inclusion of other structures such as skin, muscle etc would introduce realignment errors. Consequently, if the brain is segmented from the other structures within the head it can then be used to register subsequent images of the brain as accurately as possible without introducing errors from its movement in relation to the rest of the head.

However, in this current study it is not the brain itself that is of interest, it is the cerebral veins or other contrast enhancing structures. It might seem obvious that these structures should be segmented and aligned for the serial data sets. However, there are several problems with this approach. Firstly this study acquires one 3D data set followed by a second, which includes signal from contrast enhancement. The reason the subtraction technique works is because of the changing signal from the venous system following this contrast enhancement. The MATCH algorithm that was used in the previous chapter attempts to minimise differences in the segmented data in the serial data sets, however, if the contrast-enhanced structures were used as the segmented volume errors in registration would result. It is likely that an ideal structure for registration should not change significantly in signal or shape. Therefore, another structure that is fixed in 3D space relative to the contrast-enhanced structures is required. In the case of enhancing cerebral tumours and veins the best structure to use is the brain itself.

The vast majority of the cerebral veins are either contained in or on the surface of the brain parenchyma, so it should be reasonable to assume that the cerebral veins are rigidly connected to the brain parenchyma, and any change in position of the cerebral veins is mirrored by a similar change in the position of the

brain parenchyma. This is also likely to be true of many cerebral tumours, especially those whose origin is from the brain itself.

As was discussed in chapter 3 (section 3.1.2) Magnavist does not cross the intact BBB. Therefore, in an intact brain there should be little or no contrast enhancement of the brain parenchyma. Due to this lack of contrast enhancement, the brain parenchyma does not significantly change between the pre and post-contrast data sets allowing it to be used as the segmented volume.

4.1.3 Segmentation

4.1.3.1 Introduction

3D segmentation involves the grouping of similar voxels into coherent volumetric structures either for visualisation or for volumetric or structural analysis. There are a number of clinical and research applications that require the brain to be segmented. For example it is possible to use a segmented brain for quantitative analysis of anatomical and functional structures (Kohn *et al* 1991, Kikinis *et al* 1992, Dale *et al* 1999, Joshi *et al* 1999), for surgical planning (Xu *et al* 1999, Roux *et al* 2001), and for providing an anatomical reference in fMRI studies (Ogawa *et al* 1992, Logothetis *et al* 2001).

There are a large number of brain segmentation techniques which can be broadly summarised as being manual, semi-automated or fully automated methods. Of these methods manual segmentation is the computationally simplest.

4.1.3.2 Manual Segmentation

Manual segmentation requires a skilled operator using image processing software to define the region containing brain tissue by tracing around the brain with a drawing tool (Suetens 1993, Smith 2002). The accuracy and reproducibility of this technique very heavily depends on the skills of the operator, requiring a high level of expertise in neuroanatomy. However, even under ideal conditions and with a very skilled practitioner applying segmentation the technique is subjective and therefore not reproducible resulting in significant inter and intra-observer variability.

Jack *et al* (Jack *et al* 1990) investigated accuracy and variability using manual segmentation on phantom and patient data. Phantom data sets were segmented with an average error of 3%, despite using a simple phantom consisting of contrasting classes in an homogenous background. Intra and inter-variability when segmenting the anterior temporal lobe was found to be 3% and 6% respectively.

Another concern with the manual segmentation method is the time required. Within this department, for example, it was found that a typical MP RAGE data set (256x256 matrix with 128 slices in the sagittal orientation) could take more than 2½ hours of skilled operator time to complete. The time required varies depending on the operator's skill and experience, the integrity of the data and the required segmentation accuracy required for a particular study. Thus a number of techniques have been developed to either semi or fully automate the process.

4.1.3.3 Semi-Automatic Segmentation

One of the first recorded attempts at producing a semi-automatic segmentation algorithm can be attributed to Cline *et al* (Cline *et al* 1987). They wrote an algorithm designed to detect the external surface of the brain allowing it to be displayed in 3D, using a seed growing technique. This technique required an operator to select seed points within the brain parenchyma. By then varying threshold values pixels around the seed were examined and included within the regions if they were within the threshold. Each added pixel then became a new seed whose neighbours were then inspected using the same method and if they too were within the threshold they would also be included within the growing region. They found that the best type of data to collect for brain extraction was T1 data due to the good contrast between the brain tissue and CSF. Later work found that seed growing techniques were still dependant on operator settings (Clarke *et al* 1995).

Around the same time another technique was being developed based on multispectral analysis (Vannier *et al* 1985). Multispectral analysis involves the collection of two or more data sets during a single scanning session. Each data set is collected with different imaging parameters and/or pulse sequences varying the contrast from the tissue of interest. Pixel intensity values from the different data sets can then be plotted against one another in feature space and if the correct sequences have been run different tissues can be separated by assigning particular areas of feature space to particular tissue types. Vannier papers (Vannier *et al* 1985 & 1998) described the maximum likelihood method which assumes multivariate Gaussian distributions. This particular method was not fully automatic and required user intervention in the form of user supplied training sets. Several later papers further

developed this technique and developed different statistical methods for analysing the training sets (Just & Thelen 1988, Peck *et al* 1992, Fletcher *et al* 1993, Kao *et al* 1994), however, the requirement for user intervention and the variability in the results due to inter and intra-operator variability limited its use (Gerig *et al* 1992, Clarke *et al* 1993).

4.1.3.4 Automatic Segmentation

Automatic or unsupervised multispectral segmentation methods have been developed to counter the problems associated with user intervention. These unsupervised methods attempt to find structure within the data with the aim of producing clusters within the feature space. This has been achieved using a variety of mathematical methods such as k-means and fuzzy c-means (Taxt *et al* 1992, Ardekani *et al* 1994, Brandt *et al* 1994, Phillips *et al* 1995). More recently new variations have been developed such as the Adaptive Fuzzy C-Method (AFCM) (Pham & Prince 1999) and the Orthogonal Subspace Projection technique (OSP) (Wang *et al* 2001).

These methods continue to be used today with several studies using multispectral segmentation to demonstrate changes over time in different clinical conditions, such as HIV (Patel *et al* 2002), and brain tumours (Moonis *et al* 2002).

The main disadvantage of multispectral methods is the requirement to collect more than one data set per imaging session with particular sequence parameters determined by the requirements of the algorithms used and the tissue requiring segmentation. It is therefore impossible to apply these segmentation techniques to

routine high resolution T1 weighted 3D data sets, such as those used in the chapter 2 for examination of contrast enhancement.

There are a number of automatic methods that have been applied to T1-weighted 3D data sets. Some of the more recent methods described in the literature include morphological methods (Stokking *et al* 2000, Shan *et al* 2002), methods that use prior knowledge of likely brain structures (Lemieux *et al* 1999, 2003), deformable model techniques (MacDonald *et al* 2000, Smith 2002), and probabilistic tissue clustering methods (Barra & Boire 2000, Fischl *et al* 2002). As these techniques are all fully automatic they do not suffer from inter or intra-observer variability. One recent study suggested that the reduction in variability may be offset by an overall reduction in accuracy (Lee *et al* 2003), however this study was limited to only two freely available fully automated segmentation algorithms, and did not examine some of the more recent algorithms that are claiming good segmentation accuracy. For example Lemieux *et al* claim that automatic segmentation algorithm can segment brain volumes, when compared to the Montreal Neurological Institute (MNI) digital phantom scan, to an accuracy of 98% (Lemieux *et al* 2003, Collins *et al* 1998) and Stokking *et al* achieved an average similarity index rating (Zijdenbos *et al* 1994) of 0.98 when compared to a supervised method (Stokking *et al* 2000). These studies suggest that it is possible to develop automatic segmentation techniques that can reliably and accurately segment 3D T1-weighted data sets.

4.1.3.5 Segmenting Post-Contrast Data

Despite the availability of good quality segmentation techniques there are currently no algorithms available that have been designed to segment contrast

enhanced 3D T1-weighted data sets. As has been described in chapter 2, segmentation of the post-contrast data sets is required in two stages. Firstly, voxels that do not contain brain parenchyma need to be removed. This segmented data set would then be used to realign the pre and post-contrast data sets using the MATCH software. The second segmentation would provide a mask for the final visualisation of the data. This would include the enhancing structures of interest, such as the enhancing veins, but exclude other enhancing structures that would interfere with final 3D visualisations.

As there is no technique available to achieve this, a new segmentation algorithm is required. However, due to the variability of the enhancing cerebral venous system, and the possible presence of enhancing lesions it may be difficult to accurately segment the brain parenchyma reliably and accurately. Therefore, before an algorithm is designed it is important to determine the effects of segmentation accuracy on registration accuracy.

Before segmentation accuracy can be determined a phantom data set is required upon which the different segmentation accuracies can be simulated and the resulting effects on registration determined. This phantom would consist of pre and post-contrast data that when subtracted would produce a perfect subtraction with no alignment errors. This data set could be rotated and translated by known amounts so that for different segmentation accuracies the accuracy of the MATCH realignment could be assessed. Noise could also be added to the phantom to simulate realistic data sets.

Several segmentation studies have used phantom data sets to test the accuracy of their segmentation algorithms (Stokking *et al* 2000, Shan *et al* 2002, Lee *et al* 2003, Lemieux *et al* 2003) all use the MNI digital head phantom (Collins *et al*

1998). However, there are no reports in the literature of the use of a contrast enhanced brain phantom. Therefore, before it was possible to test the effects of segmentation on registration accuracy in the pre and post-contrast data sets a pre and post-contrast phantom was developed.

The phantom data was produced using real pre and post-contrast 3D MP RAGE data. The following sections describe in detail the production of the phantom data.

4.2 Construction of Pre and Post-Contrast Phantom

4.2.1 Methods

One patient data set was collected using a pre and post contrast protocol. The patient had a long IV line inserted prior to the imaging protocol allowing the contrast agent to be administered with the minimum disturbance to the patient. The patient's head was held in position with pads secured at the maximum pressure consistent with comfort and they were asked to keep as still as possible during the procedure (see figure 2.5 in chapter 2). The Magnevist contrast agent was administered via the long line by a radiologist within the room. It was administered in a 20 second bolus and the post-contrast sequence was started within 20 seconds of finishing the contrast injection. The imaging parameters for the 3D MPRAGE sequences were TR=10 msec, TE=4 msec, TI= 300 msec, flip angle=10 equivalent slice thickness= 1.4 mm, FOV=250 mm with a matrix size of 256x256.

An artificial pre-contrast data set was produced using the original real pre and post-contrast data collected. The artificial pre-contrast data set was based on the post-

contrast data set from which contrast-enhanced characteristics were removed. The original pre-contrast data set was used to identify the areas of contrast-enhancement on the post-contrast data.

The new artificial pre-contrast data set differed from the original pre-contrast data by being perfectly aligned to the post-contrast data set. The only difference between the phantom pre-contrast data and the post-contrast data was the presence of contrast.

It took the author several steps to produce the phantom data. The first step in the process was to accurately segment the post-contrast data set using the manual method described in chapter 2 (see section 2.5.1.2), removing all the voxels not containing any brain parenchyma. All of the enhancing structures were removed as a result of this process. This segmented data was used to register the real pre-contrast data to the real post-contrast data using the MATCH algorithm (Hajnal *et al* 1995). Following realignment the realigned pre-contrast data was subtracted from the post-contrast data, producing a subtracted data set for the patient. Contrast-enhancing structures were highlighted in this data set.

For the next stage of analysis all of the voxels within the subtraction data that were not considered to be contrast-enhancing were removed from the data. This was achieved using a manual threshold technique. The threshold level was determined using the Analyze software package (Mayo Foundation, Rochester, MN). Using the morphology tool a threshold was subjectively determined such that all of the enhancing structures were within the determined threshold. This threshold was further set such that whilst it contained the maximum amount of contrast-enhanced voxels, it also contained the minimum amount of background subtraction noise. Once the threshold had been set to fulfil these requirements the threshold was applied,

resulting in a binary map (mask), where data voxels within the threshold were set to a value of one and all other data voxels were set to zero.

The mask represented data within the post-contrast data set that significantly changed between the pre and post-contrast scans. Therefore, by modifying all of the voxels in the post-contrast data that coincided with the mask voxels of value one, and keeping the remaining data from the post-contrast data unchanged, it was possible to create a phantom pre-contrast data set.

To select the voxels requiring modification the post-contrast data set was multiplied with the mask. The resulting data only contained voxel values above zero for the contrast-enhancing voxels. This new data was subtracted from the post-contrast data. In effect this reduced the signal in the contrast-enhanced structures without affecting the data within non-enhancing structures, such as the brain parenchyma, resulting in phantom pre-contrast data that was perfectly aligned to the post-contrast data.

Once the pseudo pre-contrast data set had been produced it was subtracted from the post-contrast data set using the Analyze algebraic module. The data was then visually inspected to ensure that the methodology had correctly produced the required phantom.

4.2.2 Results

Examples of the pseudo pre-contrast and post-contrast data sets are shown in figure 4.1.

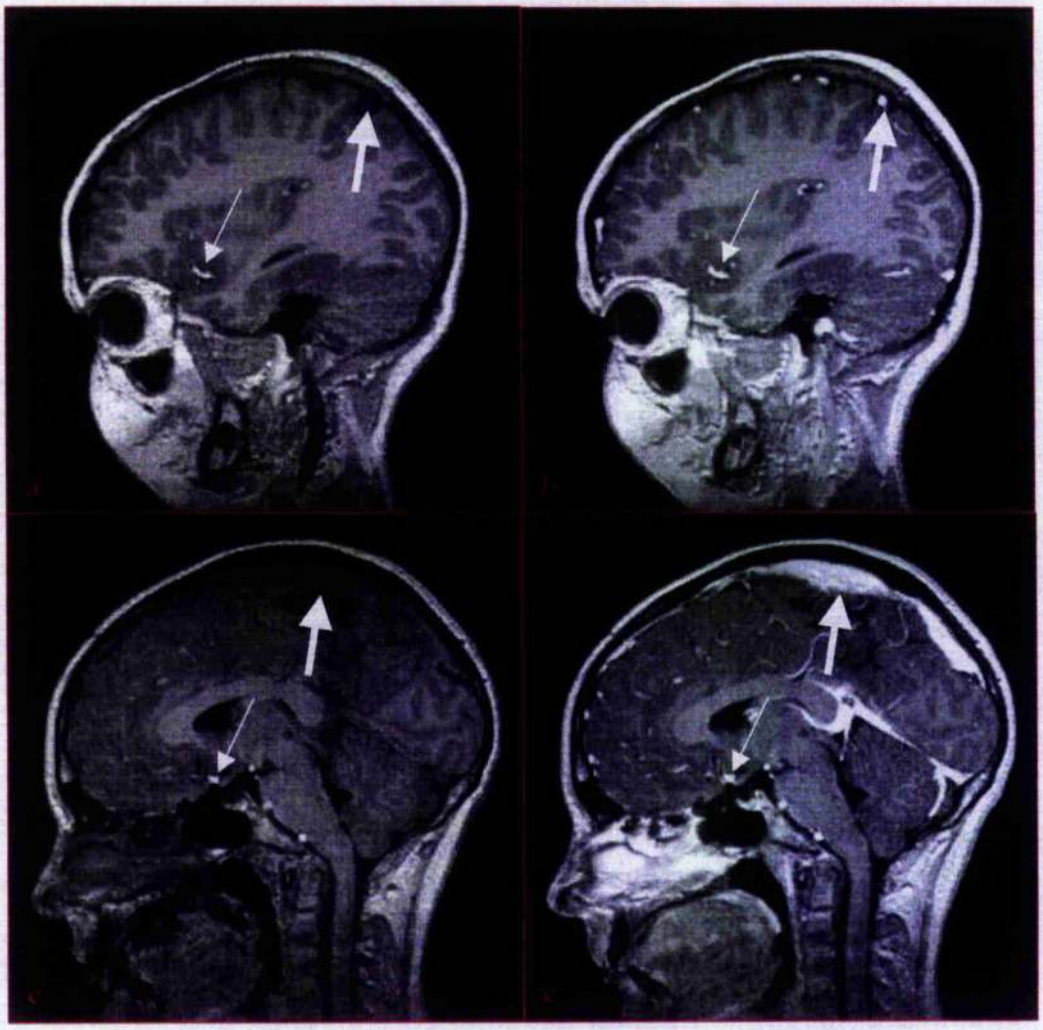

Figure 4.1 (a-d): Both of the 3D slices on the left (a & c) are from the pseudo pre-contrast data set. The images on the right (b & d) are the equivalent post-contrast slices from which the pseudo data set was created. The thin arrows highlight arteries that do not increase in signal and the thick arrows highlight veins that do increase in signal.

It is clear from figure 4.1 that the signal from the venous vessels in the pseudo data set had been removed reducing the signal to pre-contrast values. The arterial

enhancement inherent in this pulse sequence remained and was evident in both slices displayed in figure 4.1.

Other enhancing structures such as the skin and muscles also demonstrated reduced signal intensity in the pseudo pre-contrast data set as was expected. To demonstrate this figure 4.2 displays the subtraction data from these two slices.

Figure 4.2: Example slices from the subtraction data where pseudo pre-contrast data has been subtracted from the post-contrast data. Slice (a) contains some artefactual enhancement from outside the head (arrow)

There was no background noise in the subtraction images, only signal from the enhancing structures. There were, however, some erroneously enhancing pixels outside the head. These were produced in areas where the original data was affected by ghosting or phase wrap by different amounts in the pre and post-contrast data sets. The resulting subtraction data for these voxels had values within the threshold range, resulting in their inclusion in the mask.

For comparison it is possible to compare the new pseudo pre-contrast data set with the real pre-contrast data set that had been realigned to the post-contrast data set. The simplest and most informative way of comparing the data was to subtract the real

from the pseudo data. This subtraction highlighted the differences between the phantom, and real-realigned data. Two example slices are displayed in figure 4.3.

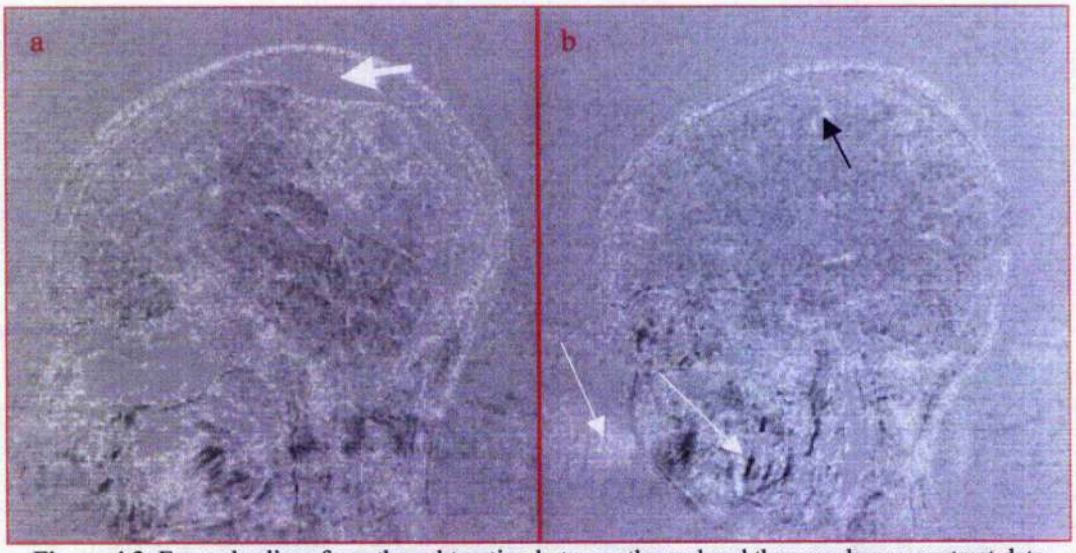

Figure 4.3: Example slices from the subtraction between the real and the pseudo pre-contrast data sets.(Black voxels are negative and white voxels are positive) The thick arrow in (a) shows an homogeneous grey area suggesting good subtraction (contrast-enhanced area). The thin arrows in (b) show areas affected by pulsatile artefacts resulting from a carotid artery. The back arrow shows a cortical edge enhancement.

There were a number of significant features visible in the subtraction data. The effects of ghosting were apparent in the phase encoding direction (anterior/posterior direction), especially in figure 4.3(b). These artefacts were a result of pulsatile blood flow, especially within the carotid arteries and eye movement during the scanning. The existence of these artefacts on the subtraction, suggests that the position and the signal from these ghosts varied between the pre and the post-contrast scans. It should be noted that the ghosting artefacts will be the same in the pseudo pre and post-contrast data, although this is not the case in real data sets.

Areas of enhancement show up as homogeneous grey areas on the subtraction (i.e. in the subtraction they have a value of zero). This confirms that these regions in the pre and phantom pre-contrast data have the same values and position.

The edges of some of the cortical structures could be visualised in the subtraction data. This is especially obvious in figure 4.3(b). This was a result of the imperfect realignment of the real pre and post-contrast data sets.

The final difference to note between the data sets is the differences that occur between the enhancing structures not contained within the brain parenchyma and the enhancing venous structure. Structure such as the skin and muscles are visible in the subtraction of the phantom pre and real pre-contrast data. The differences in signal pre and post-contrast in these structures is smaller than that found in the cortical veins. Therefore, when the threshold was applied these structures were not included within the resulting mask.

4.2.3 Discussion

This chapter has followed on from the previous chapter by describing the need for an automatic segmentation and registration protocol for pre and post-contrast data, where subtraction data sets are required. However, before this can be achieved a new method of segmenting post-contrast data is required to both allow accurate registration of the data and to allow maximum intensity projection (MIPs) to be produced from the cerebral enhancement without being obscured by other overlying enhancing structures.

Segmentation of these data sets is complicated by the fact that the enhancing venous system varies markedly from person to person (Curé *et al* 1994, Meder *et al*

1994, Morris and Choi 1996), thus, it would be difficult to achieve high accuracy in segmenting these structures. Therefore, this chapter introduces the concept of segmentation accuracy, where a truly accurate segmentation would include all of the brain parenchyma and no other tissue. Using this segmentation volume as a reference the following chapters investigate the effects of varying the segmented volume on the realignment. Using the information gained from these experiments it should be possible to determine the segmentation accuracy required to ensure good realignment of the data.

Before the effects of segmentation accuracy and it effects on realignment could be investigated a pre and post-contrast data set was required where there was a known spatial alignment between the pre and post-contrast data. Therefore, using real patient data a phantom pre-contrast data set was produced where the contrast-enhanced data was derived from the pre-contrast data and the remainder of the phantom pre-contrast data was derived from the post-contrast data.

The phantom pre-contrast data when subtracted from the post-contrast data resulted in a subtraction data set that contained only the contrast-enhanced difference between the two data sets, with no other differences, such as noise or artefacts.

4.2.3.1 Discussion of Potential Errors and Limitations of the Phantom Data Set

The phantom pre-contrast data does not represent a perfect pre-contrast phantom as a number of assumptions were made in its production. It was assumed that the real pre and post-contrast data sets were perfectly aligned when they were used to produce the phantom data. This was not the case as illustrated by figure 4.3, when the phantom and real pre-contrast data were compared. As some edge structure

of the cortical folds are visible, this suggests that alignment was not perfect, although the alignment does not appear to be grossly incorrect.

If there had been gross misalignment between the real data sets this would have resulted in errors in the thresholded mask. For example misaligned structures could produce false high intensity signals in the subtraction data that would be included in the threshold mask. Due to their erroneous inclusion within the mask these voxels would then be derived from the pre-contrast data when they should have been derived from the post-contrast data.

It was however, unlikely that these threshold errors if present were significant. Although there was an apparent error in realignment, it was not gross and so errors are likely to be small (see figure 3.3). More significantly, however, these errors are most likely to occur at tissue boundaries, where the differences could be large enough to include these voxels in the threshold. However, in the mask data no boundary structures were found suggesting that little or no voxels had been erroneously included in the threshold mask due to misalignment of non-enhancing structures.

At the edge of contrast-enhanced structures these errors would be undetectable by visualising the data, as these voxels would appear to be part of the larger area of contrast-enhancement. However, it was unlikely that this effect was significant when compared with errors introduced by the threshold technique itself. Thresholding the data was a compromise between including all of the contrast-enhancement within the threshold and not including unwanted noise data within the threshold. The optimum threshold value selected for this study will have inevitably resulted in some of the contrast data not being included within the mask. It will also have resulted in some of the subtraction noise data being included within the mask.

Therefore, in this situation it was reasonable to assume that errors due to misalignment of the real pre and post-contrast data sets were negligible with respect to the thresholding errors.

The thresholding errors could have been removed by manually segmenting the contrast enhancing structures. However, this would be time consuming but more importantly would introduce the normal manual segmentation operator errors. For example for every voxel the operator would have made a subjective decision for its inclusion in the mask. It is very unlikely that these decisions could have been applied consistently throughout the procedure.

The most significant result of the misalignment and threshold errors on the phantom itself will be the inclusion of small amounts of contrast-enhanced data in the phantom pre-contrast data set. When the MATCH software is used to compare the phantom pre and post-contrast these enhancing voxels, when present within a particular segmentation, would improve the realignment accuracy due to the similarity of the voxels in the two data sets. It is, however, unlikely that this effect will be significant, as the number of voxels involved will be small when compared to the total number of voxels in the segmented volume. For example if there were significant areas of contrast-enhancement in the phantom pre-contrast data, when the real pre-contrast data was subtracted from it the contrast-enhanced voxels would be visible. Little, if any, are visible in figure 4.3.

A further assumption that this technique made was that the receiver gain in the scanner did not change significantly between the acquisition of the pre and post-contrast data. It is likely that the gain (which was not accessible to the scan operator) was reduced whilst collecting the post-contrast data compared to the pre-contrast gain. This would result in a reduced range of values for the post-contrast data.

Therefore, using post-contrast data in the real pre-contrast data would result in a phantom that had a reduced data range compared to a real data set. This was tested by carefully segmenting the brain on the pre-contrast data to produce a brain mask using the Analyze software. The phantom data set was subtracted from the post-contrast data set and the mean value for the subtraction should, if there was no difference in gain, equal zero. The mean of the subtraction was found to be 0.2 with a standard deviation of 5.91. This value, although not zero, was well within the range of noise, therefore, it was reasonable to assume that there was little or no effect due to receiver gain.

One final problem with the phantom data was the inclusion of ghosting artefacts in the data. Ghosting artefacts vary from scan to scan as they depend upon the physiological motion present, which varies over time (Wood and Ehman 1992), however, the phantom pre-contrast data has the same ghosting artefacts as the post-contrast data. It is feasible that these ghosts are consistently different in post-contrast scans compared to pre-contrast scans. For instance after the injection of contrast agent it is possible that there are consistent changes in pulse rate, which would affect the carotid ghosting artefacts. However, for the studies that follow, where it is the registration algorithm's ability to realign pre and post-contrast data sets with varying degrees of segmentation accuracy, it is desirable to remove errors introduced due to physiological variability. Therefore, although the artefact is present it is desirable that it remains consistent between the phantom pre and post-contrast data.

Despite these problems the phantom is the first of its kind. The cortical structures on the phantom pre-contrast data set are identical to those on the post-contrast data set. Therefore, using this phantom it is possible to compare the effects of segmentation on a post-contrast data set on registration to a pre-contrast data set,

knowing the exact spatial relationship of the two data sets. The phantom can also be used to determine the effect of including contrast-enhancing structures in the alignment calculations, knowing that all other structures remain the same. This will have consequences for any segmentation algorithm that is later designed to segment these data sets.

4.3 Conclusions

This chapter has discussed the segmentation methods that have been previously developed, including a number of techniques that have been designed to segment the brain on 3D T1-weighted data sets. However, there were no algorithms available for segmenting 3D T1-weighted contrast enhanced data sets. Therefore, a new algorithm is required.

However, due to the variable nature of contrast enhancement it is likely that it will be difficult to accurately segment these data sets using automatic techniques. Therefore, to test the effects of segmentation accuracy on registration accuracy a phantom was required. This chapter described the production of such a phantom and discussed the advantages and disadvantages of the techniques used to produce it.

Chapter 5

Realignment of Phantom Pre and Post Contrast Data: The Effect of Segmentation Accuracy on Realignment

5.1 Introduction

As was described in chapter 3 this chapter investigates accuracy of realignment of the phantom pre-contrast data set with the post-contrast data. In this chapter no further changes were made to the phantom except for the addition of rotations and translations to the phantom pre-contrast data. There was no attempt to add noise to the data sets to simulate the differences that would be present in normal imaging situations. Therefore, the only difference between the phantom pre and post-contrast data remains the addition of contrast enhancement.

Due to the similarity between the data sets it should be possible, when the data has been segmented correctly, to perfectly realign the pre and post data. However, the MATCH software is not expected to produce such results. The main reason for this is the iterative nature of the algorithm and the requirement to terminate the iterations in a finite and reasonable time (Hajnal *et al* 1995). The longer that the algorithm attempts to correctly realign the data sets the more accurate the realignment will be. This iterative process would not, however, tend towards the correct parameters in a linear fashion. It is more likely to do so in an approximately exponential trend, which would require a large amount of time to arrive at the desired result. Therefore, when designing the algorithm the program writers introduced a termination condition. This is where the differences between iterations become small enough such that there is little gain in realignment quality for further calculations. Due to this termination there will always be a realignment error despite the lack of noise differences or movement between the phantom pre and post-contrast data set.

Before attempting to realign a rotated and translated phantom pre-contrast data set it was important to determine the effects of the algorithm's iterative

procedure on the realignment process. To do this the perfectly aligned data sets were input into the algorithm using the various segmentation volumes as the realignment masks. Even though the data was perfectly aligned to begin with the algorithm would initially introduce rotations and translations in its attempt to determine the correct alignment. The process would then continue to iteratively test different alignments tending towards the correct alignment. However, it would never reach the correct values because of the termination protocol used. This is unlikely to be critical because the data was originally aligned perfectly so the resulting realignment error will be the minimal error that could be computed for this data set. It would then be possible to compare these baseline realignment parameters with the parameters for the artificially translated and rotated data. This would in turn allow an estimate of the error introduced by the segmentation volumes and a comparison of these errors with the errors inherent in the realignment algorithm.

As far as the author is aware no one has previously attempted to determine the effects of segmentation accuracy on realignment accuracy. Therefore, despite this work focusing on pre and post-contrast data, some of the results will provide more general conclusions. The work in this chapter (and chapter 4) led to a presentation at an international conference (Brennan *et al* 2002). The final data and results form the basis of a paper in preparation for journal submission.

All work in this chapter has been conducted by the author with the exception of the data acquisition which was performed by radiographic staff.

5.2 Methods

5.2.1 With and Without Rigid Body Rotations and Translations

This study was conducted in two parts. Part one of the study investigated the effects of segmentation accuracy of the post-contrast data on realignment of the phantom data where no rotations or translations were applied to it. Thus the phantom pre and post-contrast data were perfectly aligned when input into the MATCH algorithm. The second part of this study investigated the effects of segmentation accuracy of the post-contrast data on realignment of the phantom data when a relative rotation and translation had been applied to the phantom pre-contrast data.

However, before the effects of segmentation accuracy could be determined (in chapter 6), a gold standard segmentation of the brain parenchyma was required, allowing a set of relative segmentations of varying accuracies compared to the standard to be produced. This gold standard segmentation is referred to as the 100% segmentation volume from here on in this thesis.

5.2.2 Production of the 100% Segmentation Volume

The post-contrast data set was loaded into Analyze AVW 3.0 image analysis software, where the image edit module was used to edit the data series. Contrast settings were set to ensure that good grey and white matter contrast was obtained and to ensure that brain matter was distinguishable from other structures.

An approximate 3D region outlining the brain parenchyma was drawn separately on each slice of the data in the sagittal plane using the freehand region drawing facility. The data was then zoomed to three times its normal viewing size,

with interpolation switched off. At this level of zoom it was possible to easily visualise separate voxels within each slice. The region was adjusted one slice at a time using the region edit tool to accurately outline the brain surface. This resulted in a 3D region outlining the brain surface with a high level of accuracy.

On each slice new regions were drawn around structures that were to be excluded from the final brain region, such as the ventricles, veins, arteries, and any other enhancing structures. Any voxels contained within these regions were excluded from the final brain region.

To further improve the accuracy of the 3D brain region each data slice was checked twice to ensure that all the brain voxels were contained within the main region and all other voxels were either outside this region or contained within separate non-brain regions. The aim of iterating the process in this way was to achieve the greatest accuracy possible for the brain region.

The regions were then saved and converted to a 3D binary map, where voxels within the brain region were set to one and all other voxels, including those within the other regions, were set to zero. This binary map was multiplied with the post-contrast data resulting in segmented data that within the errors of manual segmentation contained only the brain structures within the post-contrast data. (See figure 5.1). This segmented volume will be referred to as the 100% segmentation volume. However, it should be noted that this designation does not imply 100% accuracy in the segmentation process. The 100% segmentation volume was created by a manual segmentation method, which despite the care taken to produce it is still likely to contain segmentation errors. The segmented data along with the binary mask were saved to disk.

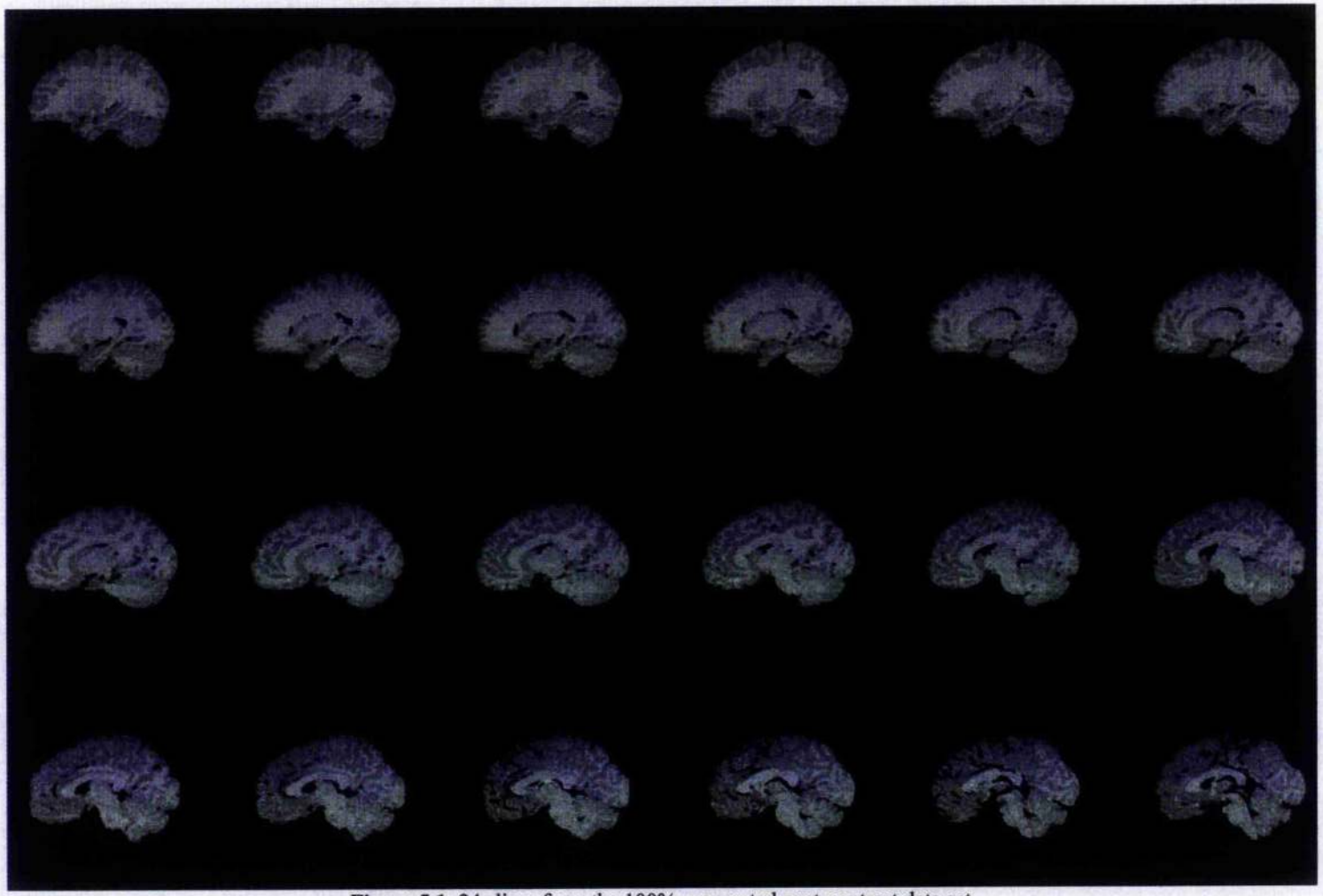

Figure 5.1: 24 slices from the 100% segmented post-contrast data set.

5.2.3 Production of the Variable Segmentation Volumes

To test the alignment capabilities of the MATCH algorithm a variety of segmented volumes were required which contained either more or less of the original post-contrast data in the segmented data. These volumes would simulate the effects of both over-segmentation and under segmentation. Over-segmentation would occur where an algorithm removes too much data, i.e. it would erroneously classify voxels within the brain as non-brain voxels. Under-segmentation would occur where an algorithm erroneously classifies non-brain voxels as brain voxels resulting in a larger volume than required. Under segmented voxels could also include contrast-enhanced data.

It is very likely that any applied segmentation algorithm would over and under-segment at the same time, i.e. some areas of the volume would contain non-brain data and in other areas of the volume would exclude brain data. However for simplicity this study will investigate these phenomenon separately. Also by separating over and under-segmentation, it will be possible to better determine the required capabilities of any segmentation algorithm developed for this and similar data sets.

To produce the varying segmentation volumes the 100% segmentation volume binary mask was loaded into the morphological module within Analyze. Three binary morphological operators were used to produce the various segmentation data sets: erode, dilate, and conditional dilate.

Morphological operators are image processing algorithms that work at pixel level on binary data sets (although this is not exclusively so). A detailed description of these morphological operators is provided in appendix 1. The erode and dilate operators as utilised by the Analyze software package use N x N x N convolution

matrices as defined by the user. Erode is used to remove binary voxels that are not fully surrounded by other similar binary voxels in the surrounding N x N x N space. In binary image analysis operations this generally reduces the size of a binary volume. Dilate, which is the morphological dual to erosion, generally expands a binary volume. A new voxel is included within a binary mask if within the surrounding N x N x N space there are voxels already included in the binary mask.

The conditional dilate operator as used by the Analyze software package allows the definition of a conditional mask into which the dilation of the binary mask is allowed. It does not allow dilation of the binary mask where it does not coincide with the conditional mask. This operation allows a large number of dilate operations to be applied whilst limiting the expansion of the binary volume.

Using the erode, dilate and conditional dilate operators it was possible to produce larger and smaller segmentation volumes with the minimum of observer bias in their production.

The over-segmented data sets were produced by using both the erode and conditional dilate operators with a 3 x 3 x 3 convolution kernel. By the variable application of erode and conditional dilation operations, where the condition was the 100% binary mask, ensuring that no under-segmented voxels were included in the masks, a set of over segmented binary masks were produced. To increase the number of data sets produced this procedure was repeated using a mixture of 3 x 3 x 3 kernels and 5 x 5 x 5 kernels. After these masks were produced they were multiplied with the original post-contrast data resulting in the various over-segmented data sets.

The under-segmented data sets were produced by dilating the accurately segmented data set by varying amounts and with different kernels. However, a threshold was set so that no voxels were be added that were below the noise, user

determined threshold of the image. These voxels were excluded on the assumption that any method of brain segmentation would at the very least remove background noise from the image, as these have very different voxel values from that of brain parenchyma.

To label these data sets the number of voxels within each mask were compared to the number of voxels within the original 100% binary mask. The resulting volume labels are shown in table 5.1 and figure 5.2 shows an equivalent slice from several of the segmentation volumes.

Over-Segmentation	Under-Segmentation
97%	103%
92%	117%
88%	126%
80%	135%
73%	145%
70%	153%
65%	169%
59%	
56%	

Table 5.1: The relative volumes (as a percentage of the 100% binary volume) of the artificially produced over and under-segmentation masks

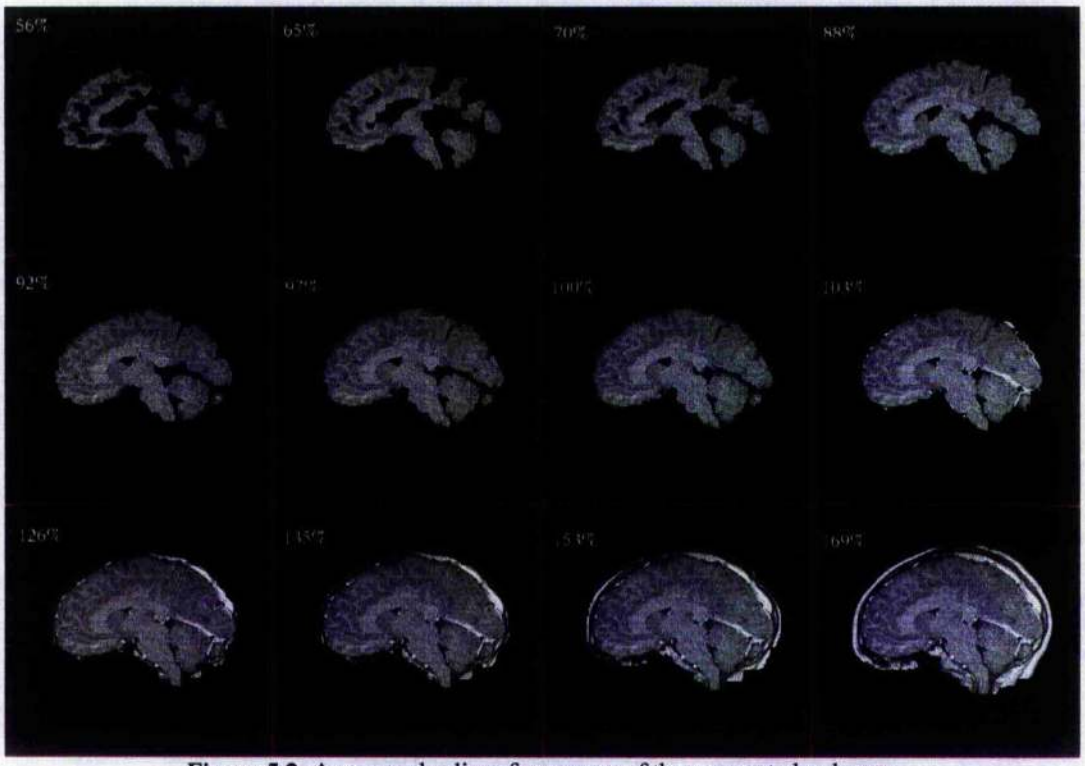

Figure 5.2: An example slices from some of the segmented volumes.

5.2.4 Quantitative Assessment of Realignment

For the following studies a direct and an indirect measure of realignment quality were assessed. Each time the MATCH algorithm was applied to a pre and post-contrast data set it produced a text file containing the realignment parameters. These parameters were calculated by comparing the segmented post-contrast data volume to the phantom pre-contrast data. The parameters were the translations p,q, and r which were stored as half pixel values, and the rotational parameters pitch, roll and yaw, which were stored as radians (although they were later translated into degrees for easier interpretation). Figure 5.3 shows how these rigid body translations and rotations related to the 3D MRI data.

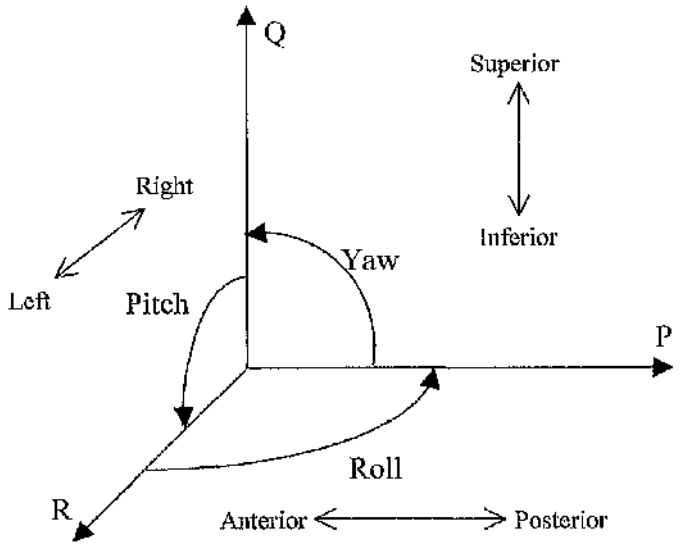

Figure 5.3: The relationship between the rotational and translational parameters output by the MATCH algorithm and the 3D data.

From these text file outputs it was possible to record and plot the effects of segmentation volume on the various registration parameters using software such as Excel (Microsoft). In both the following studies the spatial transformations required to correctly align the phantom pre and post-contrast data are known, therefore the variation in actual realignment parameters calculated using the different segmentation volumes could be compared to actual parameters required. The known rotations and translations were subtracted from the MATCH results, producing values that represented the errors in the realignment.

As well as individually comparing the six rigid body parameters it was possible to determine a single measure of overall translation and of overall rotation. Once again, by subtracting the known rotations and translations these overall measures of rotation and translation represented the overall realignment errors. To calculate the magnitude of the translational error the following equation was used:

$$T_{error} = \sqrt{(r_p - m_p)^2 + (r_q - m_q)^2 + (r_r - m_r)^2} \qquad (5.1)$$

where r_p, r_q, r_r are the magnitude of the known P, Q and R translations required to correctly align the data sets, and m_p, m_q, m_r are the magnitude of the P, Q, and R translations calculated using the MATCH algorithm.

To calculate the magnitude of the rotational error, the yaw pitch and roll rotations, which are equivalent to Euler (Ojeda et al 2002) angles can be converted to an axis-angle. An axis-angle is another method of defining a 3D rotation, which is defined as a rotation of θ degrees around a unit vector. For the purposes of this study it is the magnitude of the rotation that is of interest. It is possible to convert the Euler rotations to this magnitude using the following equation (Baker 1998):

$$\theta_{error} = 2\cos^{-1}(c_y c_p c_r + s_y s_p s_r) \tag{5.2}$$

where,

$$c_y = \cos(yaw/2),\ c_p = \cos(pitch/2),\ c_r = \cos(roll/2)$$

and

$$s_y = \sin(yaw/2),\ s_p = \sin(pitch/2),\ s_r = \sin(roll/2)$$

T_{error} and θ_{error} were compared for the non-transformed and transformed data sets.

As an indirect measurement of the quality of the realignment signal to noise (S/N) measurement were made on the subtraction data produced for each segmentation volume. To produce these S/N values regions of interest were required for both the signal and noise measurements. These regions were used for the signal and noise measurements on all of the subtracted data sets, allowing direct comparison of the S/N results.

The region used to determine the noise was defined as the area of brain segmented in the 100% volume data set. The 100% binary mask was loaded into the Analyze software and converted to a region of interest for this purpose. An example of this region overlaid on one of the subtraction data sets is shown in figure 5.4.

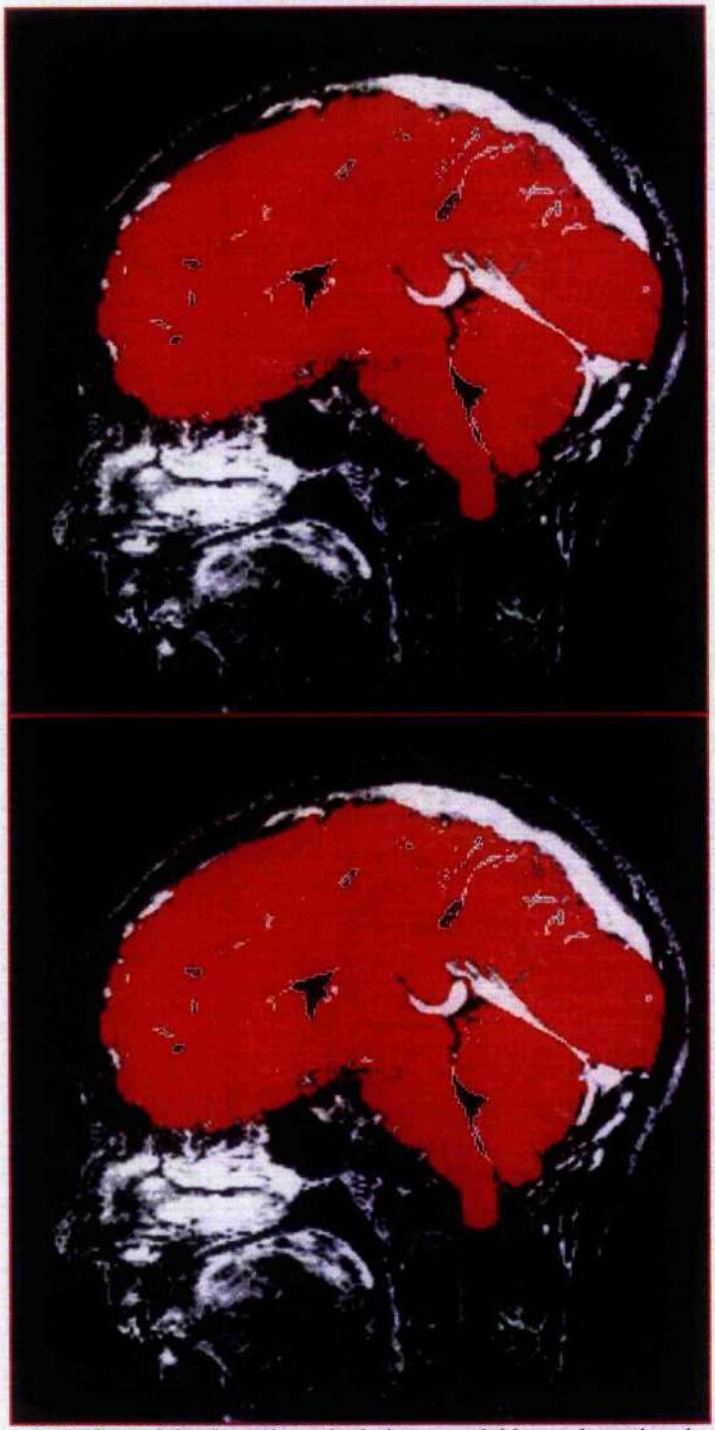

Figure 5.4: The ROI (red) used for the noise calculations overlaid on subtraction data produced using the 135% segmentation volume in realignment calculations. (Upon close inspection background subtraction noise is visible in this subtraction)

The region used to determine the signal was defined as all significantly enhancing voxels within or on the surface of the brain. In the phantom the majority of these voxels would relate to enhancing venous structures. To produce the correct region the post-contrast brain was manually segmented approximately, such that it contained only structures within the brain parenchyma and the surface veins. This region was then converted to a binary mask using the Analyze morphology module. This mask was multiplied with the 100% subtraction data resulting in a segmented subtraction data set only containing information within the masked regions. A threshold was applied at the same level used in chapter 4 (section 4.2.1) resulting in a mask for the enhancing cerebral structures. This mask was saved and converted to a region of interest file to enable it to be used to determine signal strength. An example of this region overlaid on one of the subtraction data sets is shown in figure 5.5.

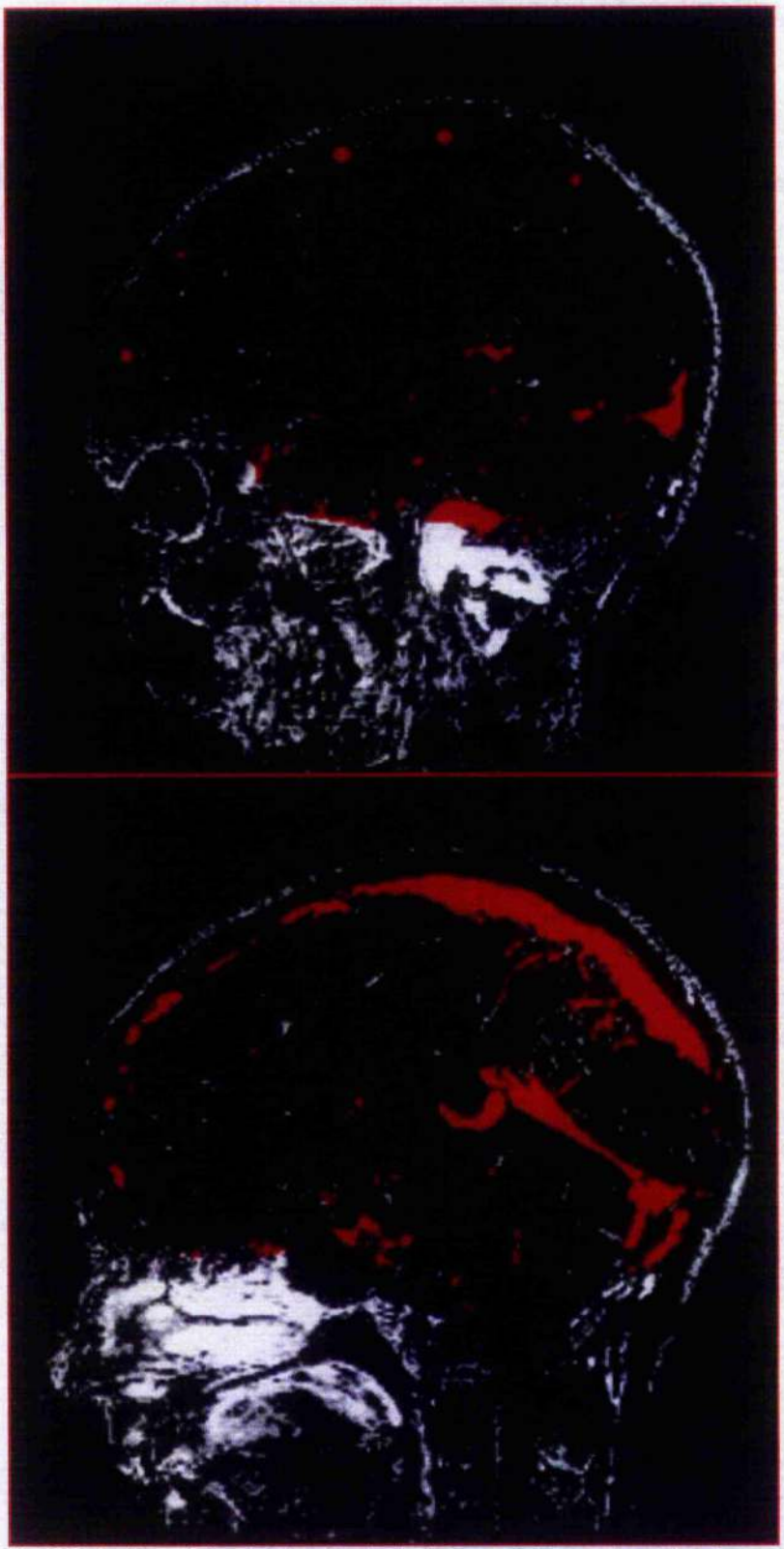

Figure 5.5: The ROI (red) used for the signal calculations overlaid on subtraction data produced using the 135% segmentation volume in realignment calculations.

5.2.5 Application of the MATCH Algorithm to Non-Transformed Data

The aim of this study was to measure the effects of segmentation accuracy on the realignment parameters calculated using the MATCH realignment algorithm. However, the phantom pre-contrast data produced in chapter 2 was already perfectly realigned to the post-contrast data and the post-contrast segmented volumes. Therefore, before assessing the realignment capabilities on the spatially translated and rotated phantom pre-contrast data, the MATCH algorithm was applied to the phantom pre and post-contrast data set that were perfectly aligned.

For the over-segmented data sets the MATCH algorithm would be comparing voxels that exactly matched between the phantom pre and post-contrast data. Therefore, if the MATCH algorithm was functioning correctly it was expected that the transformations applied should all be close to zero within the experimental error for the algorithm. Therefore, these results would provide information on the overall accuracy of the algorithm.

For the under-segmented data sets the MATCH algorithm would be comparing data that contained a majority of exactly matching voxels. However, the segmented post-contrast data would also contain enhancing voxels that would contain equivalent non-contrast enhancing voxels in the phantom pre-contrast data. It was expected that the resulting effect of these differences on the chi-square algorithm used by MATCH would result in larger realignment errors, confirming the assumption that for contrast enhanced data sets segmenting out these structures was vital for accurate alignment.

The MATCH algorithm was run on the phantom data set once for each segmentation volume created. Upon completion the MATCH software produced a new pre-contrast data set that had been resliced using the realignment parameters

determined by the algorithm. This new data set was subtracted from the post-contrast data resulting in a new subtraction data set relating to each segmentation volume.

5.2.6 Application of the MATCH Algorithm to Transformed Data

The same tests as those described in section 5.2.5 were also applied to the phantom pre and post-contrast data after the phantom pre data had been transformed to simulate inter-scan motion. The transformation consisted of a translation and rotation of known amounts, which could be subtracted from the realignment parameters calculated by the MATCH algorithm. The effects of segmentation volume on these transformation error measurements were examined. It was also possible to compare these results for the transformed and non-transformed data.

To apply the rigid body translation and rotation, the phantom pre-contrast data was loaded into the Analyze software package within the 3D fusion module. Within this module it was possible to define rotations and translations and apply them to the data. The artificial pre-contrast data set was rotated 1 degree (YAW direction, backward head tilt) and moved 1 pixel in the posterior direction (P). Only one translation and rotation was applied. Therefore, it was expected that no correction would be necessary in the other rotations and translations. Therefore, any corrections applied in these directions could be attributed to realignment error. A YAW rotation of 1 degree and P translation of 1 pixel were applied as this represented a possible movement of the head where the patient had lifted their head to look down the bore and rested it back down.

After applying the rotation and translation the data required to be resliced and the voxels interpolated. There are several methods of interpolation available within the software, however, the most appropriate was the sinc interpolation method. As was previously described in chapter 2 (section 2.4.2) sinc interpolation is the most robust method for resampling and interpolating 3D MRI data and introduces the minimum of sampling errors.

Figure 5.6 demonstrates the resulting misalignment between the transformed phantom pre and post-contrast data by displaying some slices from a subtraction. The misalignment results in an increase in the background noise in the subtraction.

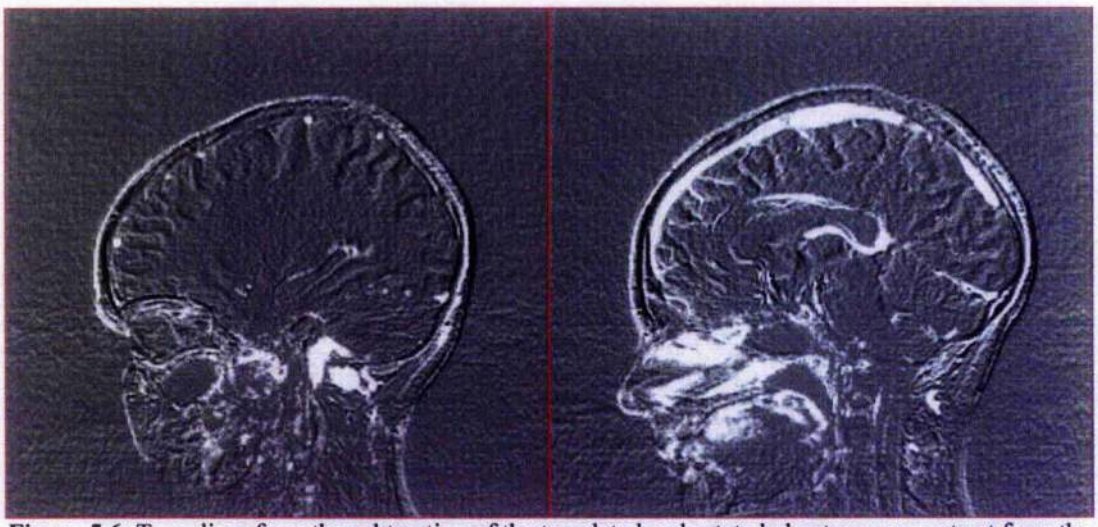

Figure 5.6: Two slices from the subtraction of the translated and rotated phantom pre-contrast from the post-contrast data. The misalignment results in increased noise in the subtraction. The outline of the misaligned cortical folds can also be seen.

The results of the MATCH realignment using the transformed data were analysed using the same protocol as in section 5.2.5.

5.3 Results

5.3.1 Non-Transformed Phantom Data Results

Graph 5.1(a-f) displays the realignment parameters produced when the perfectly aligned phantom pre-contrast data set was realigned to the post-contrast data set using the MATCH software. The resulting rotations and translations are a result of the iterative processes used to determine the parameters and the effect of segmentation volume on this process. Error bars have been included using the parameter error estimates derived by the MATCH software.

The most apparent effect on realignment accuracy is whether the segmentation volume is above or below approximately the 100% value. For the three rotation parameters there should have been no rotation applied, and likewise for the translation parameters there should have been no translations applied. All of the parameters vary around or close to these optimum values for segmentation volumes of less than and equal to approximately 100%.

For segmentation volumes not containing contrast (<100%) the largest rotational deviation from zero degrees occurs at the 100% segmentation volume with the YAW rotation parameter with a rotation applied of 0.0121 degrees. The largest translational deviation from zero half pixels occurs at the 97% segmentation volume for rotational parameter Q with a value of 0.0212 half pixels. In all of the rotational and translational parameters below and inclusive of the 100% segmentation volume there is no observable trend towards or away from the optimum values.

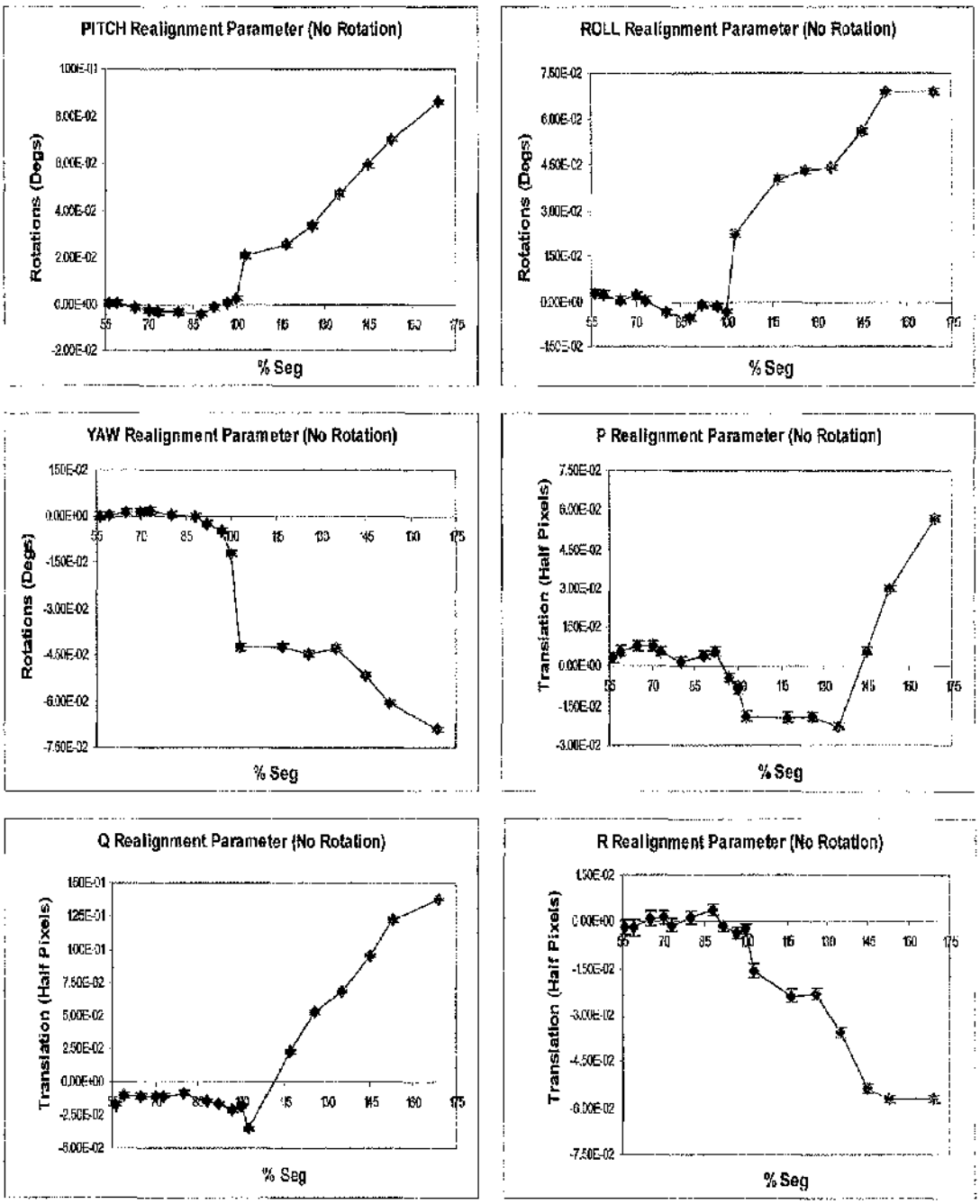

Graphs 5.1(a-f): The realignment parameters determined by the MATCH software when attempting to realign the non rotated and translated data

Above the 100% segmentation volume, where contrast enhanced data is included in the segmentation mask, there are much larger deviations from the optimum values in both the rotational and translational parameters. Both PITCH and

ROLL follow linear increasing trends away from the optimum value with R^2 equal to 0.974 and 0.855 respectively. YAW also follows a linear trend (R^2=0.755) however, in this case it tends away from the optimum value in the opposite direction.

P can be described by a linear trend, although with a poorer linear fit. Overall there is an increasing trend over the range with R^2=0.6582. Q and R also both follow linear trends away from the optimum value, in opposite directions, both with strong correlations (R^2=0.969, 0.912 respectively).

For all parameters except R the largest deviations from the optimum values occur at the largest segmentation volume of 169%. The largest deviation in R occurs at 153%. Overall the largest deviation in rotation occurs for the PITCH parameter and has a value of 0.0858 degrees. The largest deviation in translation occurs for Q and has a value of 0.138 half pixels.

These results suggest that increasing the volume of contrast enhancing structures within the registration mask increases the algorithm's error in realigning data sets, i.e. when segmenting a contrast enhanced brain for realignment to a non-contrast enhanced brain all contrast enhancement should be removed from the registration mask. The data also suggest there is little increasing error in realignment with increasing over-segmentation.

Graph 5.2 displays the signal to noise (S/N) characteristics for the subtraction data produced when the realigned phantom pre-contrast data was subtracted from the post-contrast data.

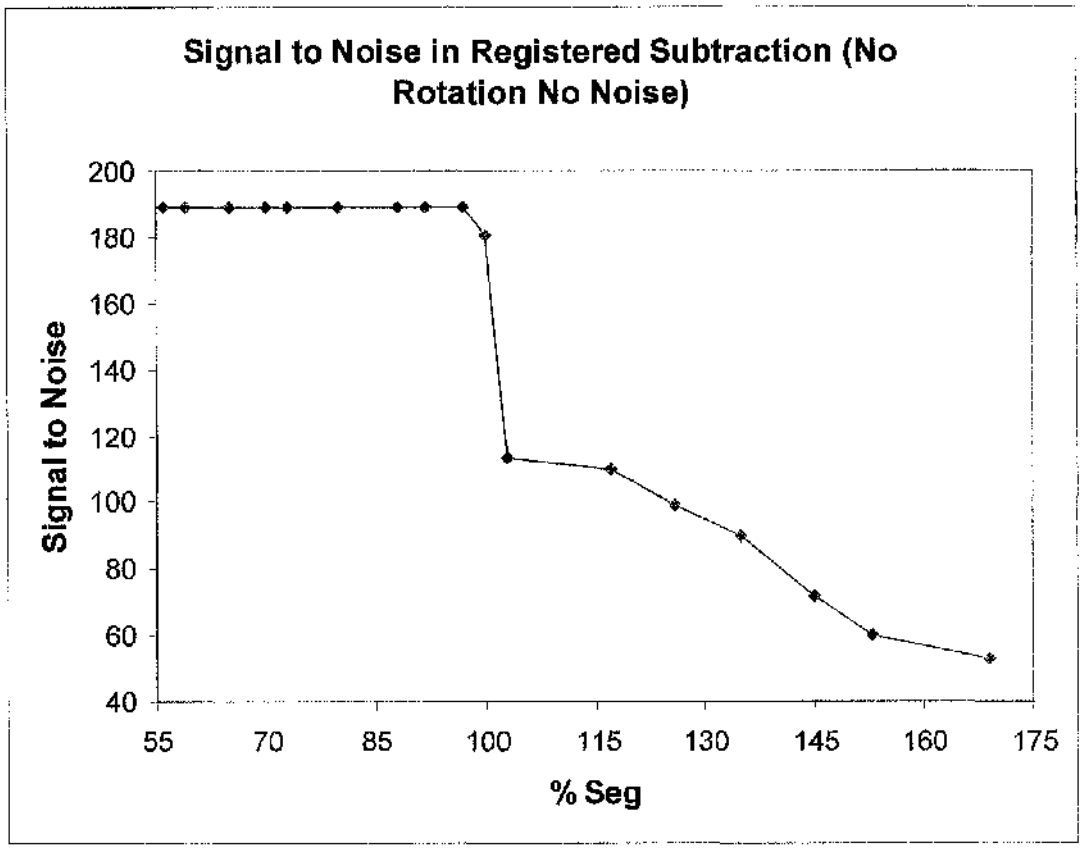

Graph 5.2: Signal to noise changes in the modulus of the subtraction image for the no movement data

Signal to noise does not vary significantly for segmentation volumes below 100% and remains at its highest value of 188.8. This is consistent with the data displayed in graphs 5.1(a-f) where the realignment parameters remain close to the optimum value. For segmentation volumes above 100% there is a rapid drop in signal to noise with the minimum value found at segmentation volume of 175% with a value of 52.7. Once again this is consistent with the realignment parameters in graphs 5.1(a-f), where they tend away from the optimum values at higher segmentation volumes.

It was also noted that the signal to noise was lower for the 100% segmentation volume than for all of the smaller segmentations volumes. At the 100% segmentation volume the signal to noise is 180.2.

5.3.2 Transformed Phantom Data Results

Displayed in graphs 5.3(a-f) are the realignment results for the rotated and translated data. This data has been plotted along with the previous non-rotated/translated results so that comparisons can easily be made. To allow direct comparison of the YAW and P data (which contained the rotation and translation), 1 degree was subtracted from the moved YAW data and 1 pixel from the P data. These graphs represent the realignment errors for both the transformed and non-transformed data.

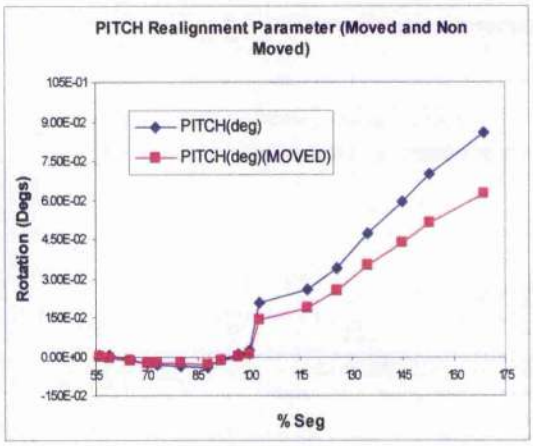

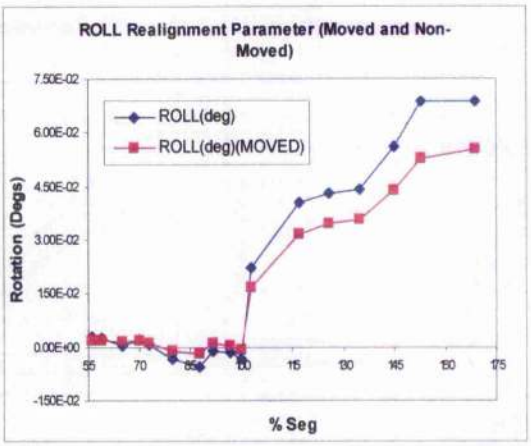

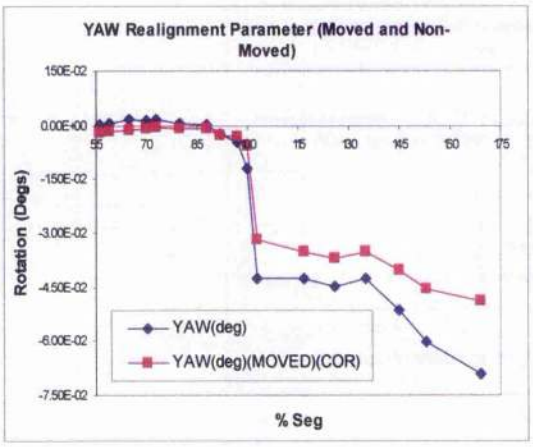

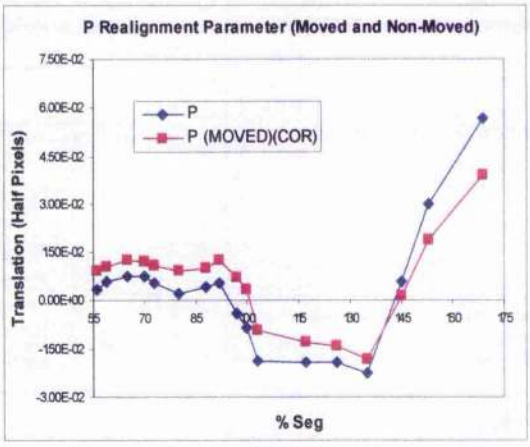

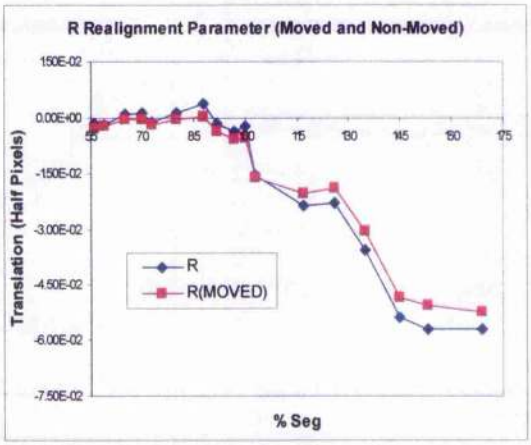

Graph 5.3(a-f): The realignment parameters (errors) determined by the MATCH software when attempting to realign the rotated and translated data (compared to the non-rotated and translated data)

Graphs 5.3(a-f) clearly show that the overall trends in the realignment parameters remain similar for all parameters after the phantom pre-contrast data set has been moved. Once again the most accurate realignments occur for segmentation

volumes below the 100% value, i.e. when there is no contrast-enhanced data contained within the registration mask. However, there are detectable differences in the realignment parameters between the transformed and non-transformed data sets. To demonstrate these differences more clearly the moved results, with the translation and rotation corrected P and YAW parameters were subtracted from the non-moved results. The subtracted results are displayed in graphs 5.4(a-f). These subtractions display the differences in the realignment parameters produced purely due to the presence of transformation between the phantom pre and post-contrast data sets.

The movement induced errors displayed in graphs 5.4(a-f) appear to follow similar trends to those in graphs 5.1(a-f). This suggests that where there is increasing error due to a poor registration mask used for the MATCH realignment, the error in correcting for movement also increases. To examine this a further a set of graphs were produced displaying the relationships between the realignment parameters produced when there was no introduced movement (segmentation and algorithm errors), and the errors introduced by introducing movement (see graphs 5.5(a-f)).

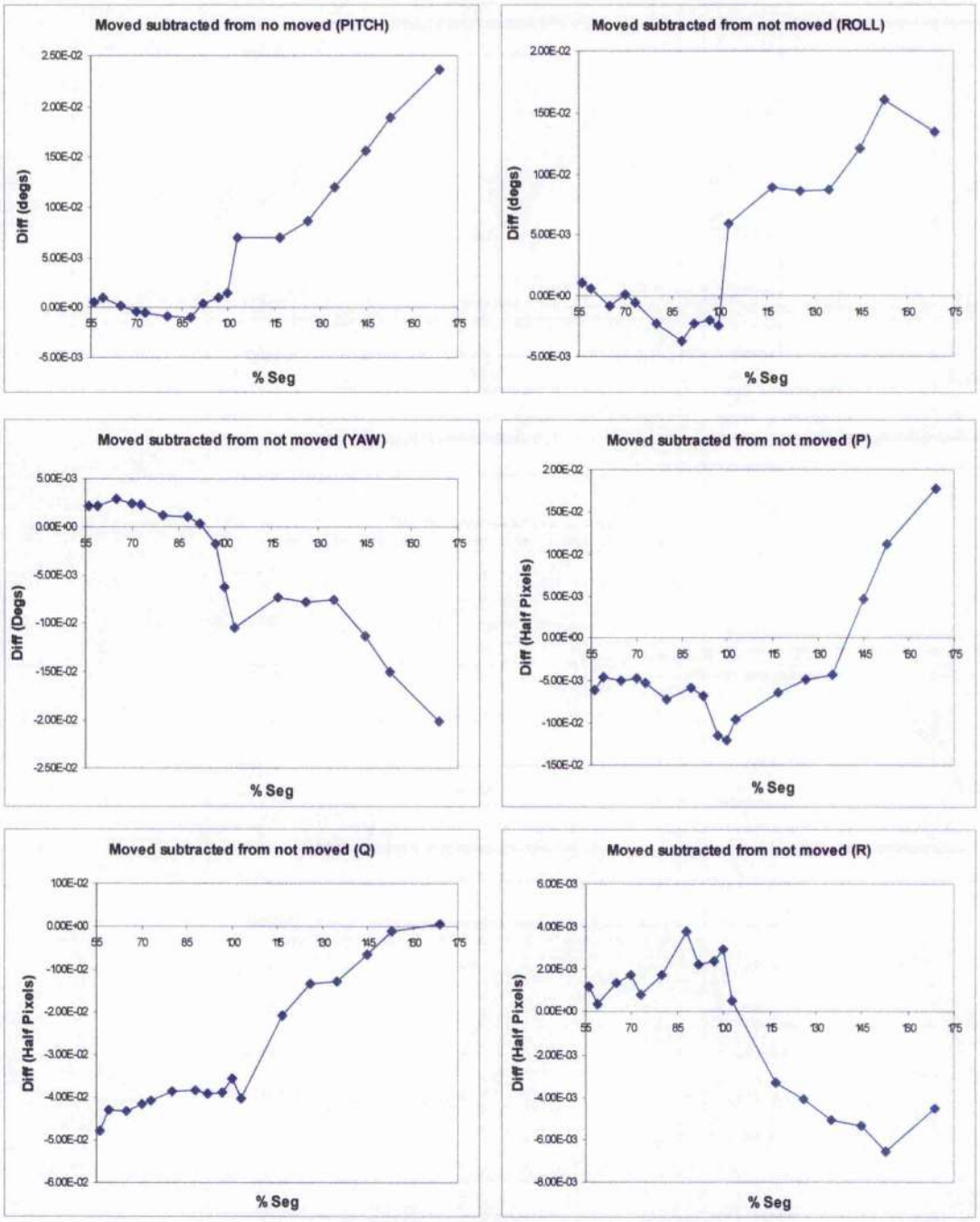

Graphs 5.4(a-f): Moved data translation and rotation parameters subtracted from the non-moved rotation and translation parameters.

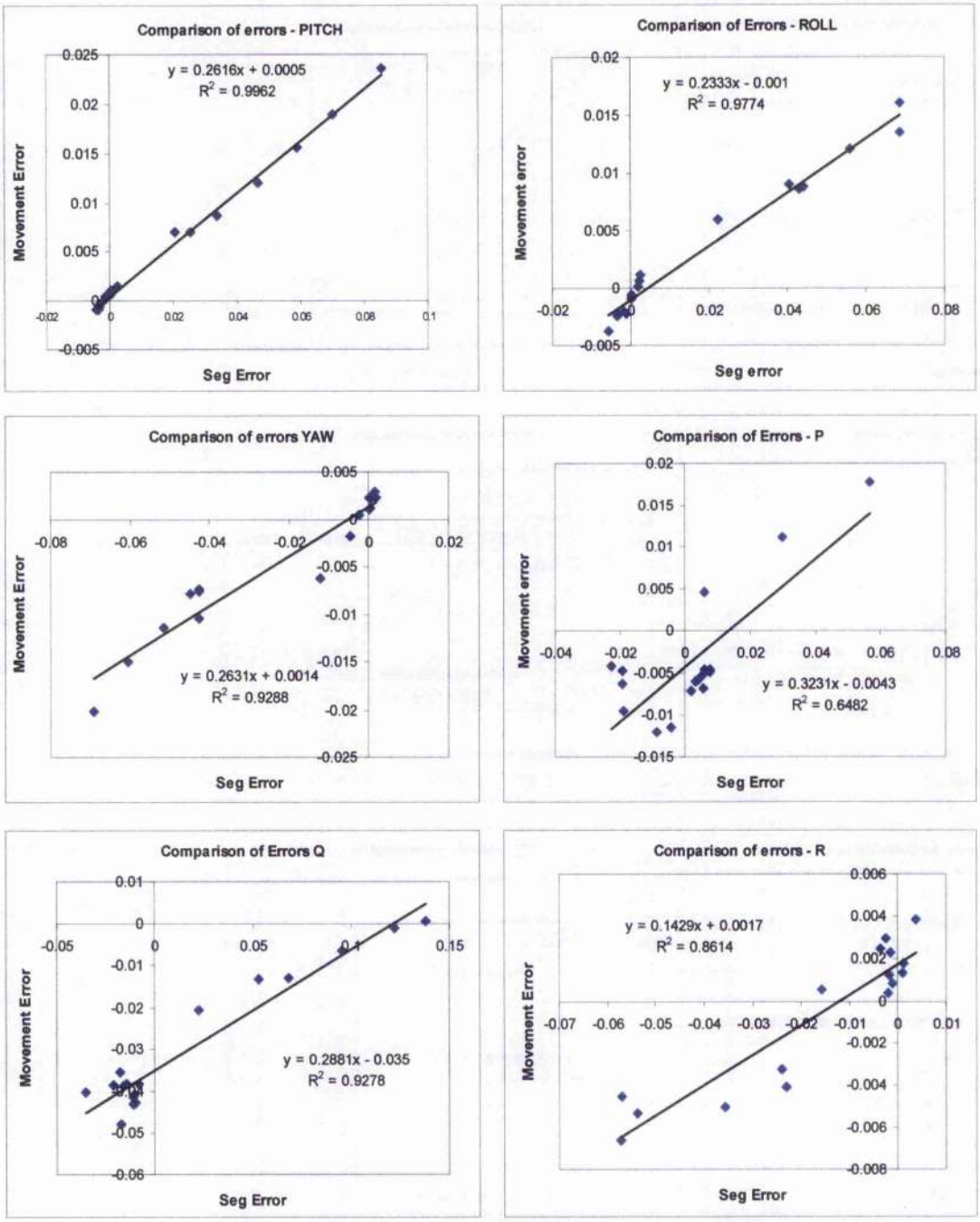

Graphs 5.5(a-e): Relationships between segmentation/algorithm errors and the errors introduced by movement of the phantom pre-contrast data set

All of the comparison of error graphs can be described by linear trends with four having a very good linear correlation of $R^2 > 0.9$ (PITCH, ROLL, YAW and Q). These 4 graphs also display very similar linear gradients varying between 0.2333 and

0.2631. P and R also follow linear trends, however, the linear fit is not as accurate (R^2= 0.6482 and 0.8614 respectively).

These linear trends suggest that there is a relationship between the inherent errors for the algorithm for each segmentation volume and its ability to correct for rotations and translations. Therefore, where the segmentation volumes contain enhancing structures large inherent errors will also lead to large realignment errors.

For this data set it should be noted that the inherent algorithm errors are larger than the movement errors by a factor of about 4 overall, i.e., the average linear gradient for the realignment graphs in graphs 5.5(a-f) is 0.252 with a mean deviation of $x_{\sigma n-1}$= 0.0614. The majority of the variation in this figure results from the two graphs where the linear fits were not as highly correlated.

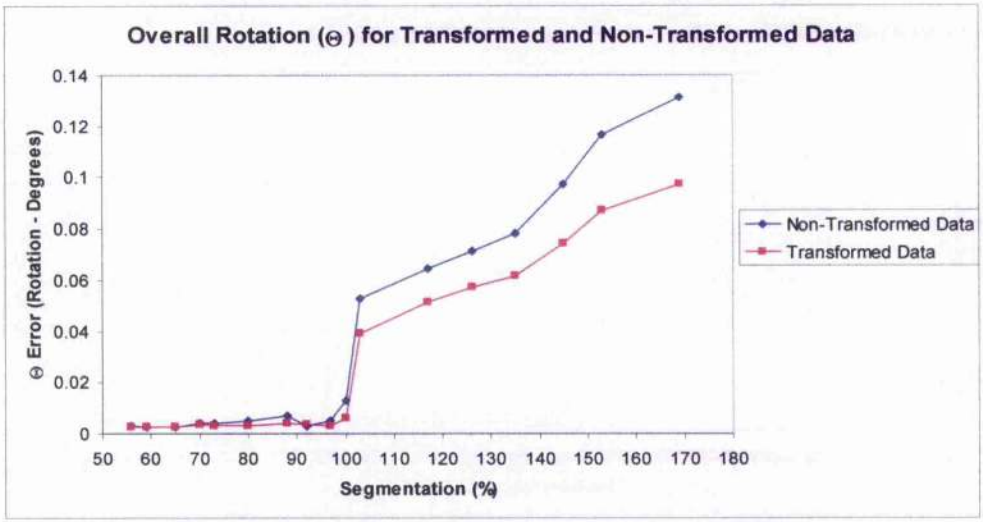

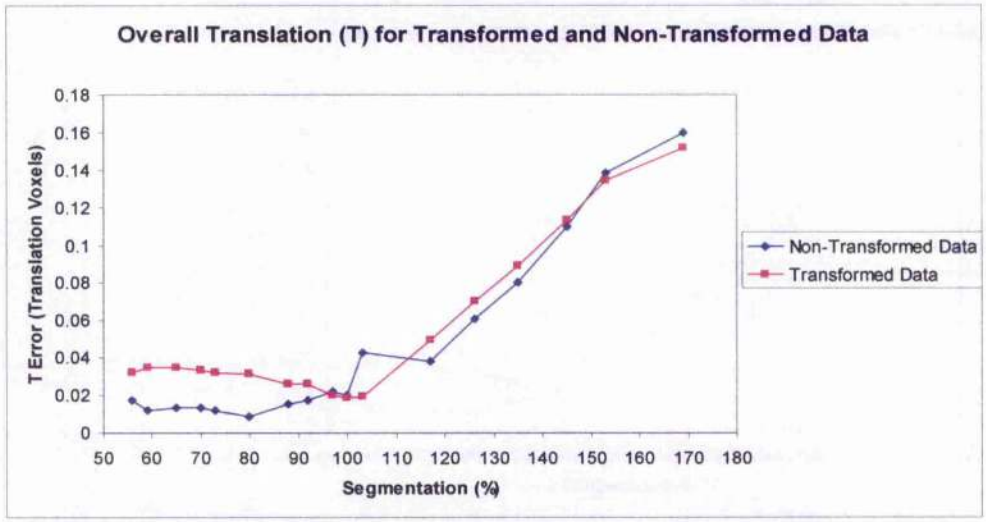

Graph 5.6 (a & b): The calculated overall rotation and translations are compared for the non-transformed and transformed data (the values for translation and rotation relate to the errors when compared to the known rotations and translations)

As described in section 5.2.4 it was possible to generalise the comparison for the translations and rotation see graphs 5.6 (a & b). Looking at graph 5.6(a) it was apparent that there were no significant differences in the rotations applied for the non-transformed and transformed data at segmentation volumes below 100%. However, for all segmentation volumes above 100% there were larger rotation alignment errors in the non-transformed data than there were in the transformed data, for all data points. This would suggest that the transformed data realigned better than the non-

transformed data. It was also found that the correlation between the transformed and non-transformed rotation data was excellent with $r=0.999$ and $p<0.01$.

When translation was examined (see figure 5.6(b)) the transformed data contained larger errors for data below the 100% segmentation volume, with the errors becoming more comparable in value for the larger segmentations above 100%. These results suggested the opposite of the rotation results. Here the correlation was also excellent with $r=0.968$ and $p<0.01$.

It was unclear from these results whether the transformed or non-transformed data realigned more accurately. However, it appeared that the non-transformed data realigned more accurately, for all segmentation volumes when the signal to noise results were examined and compared (see graph 5.2 and 5.7).

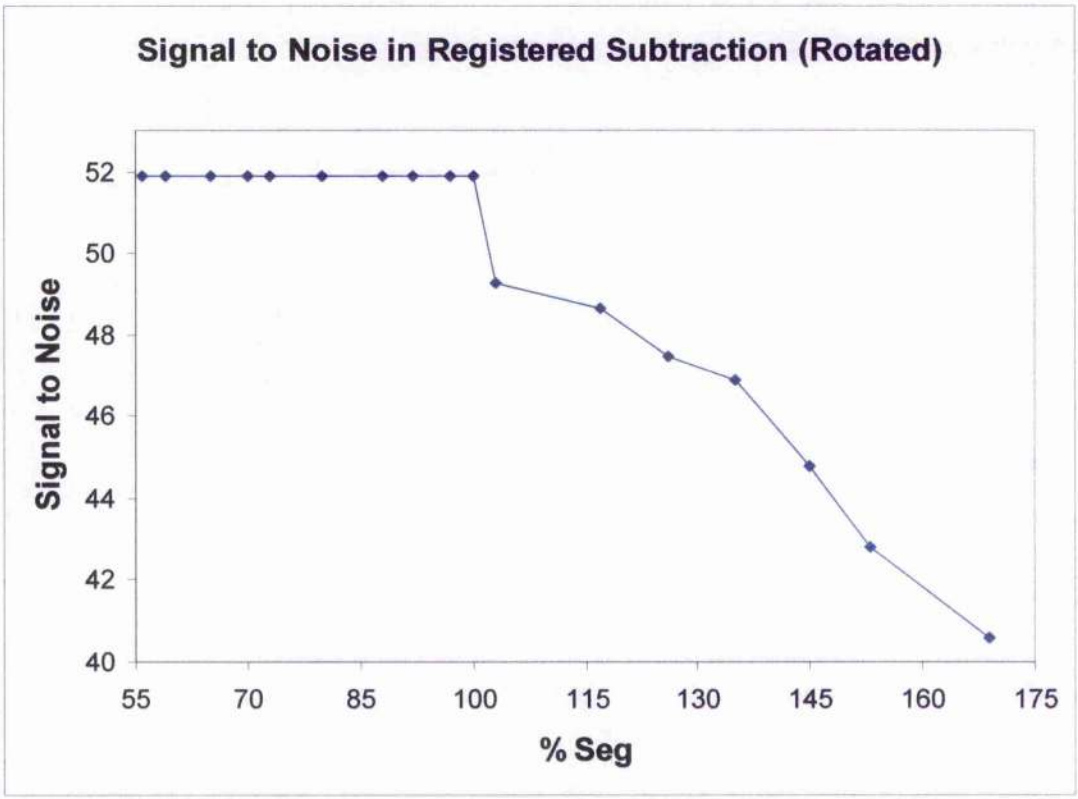

Graph 5.7: Signal to noise changes in the modulus of the subtraction image for the movement data

The transformed data signal to noise graph was very similar to graph 5.2 in shape and trends. The main differences were the much lower starting signal to noise, due to larger errors in the realignment parameters (see graphs 5.3(a-f)) and the smaller percentage drop in signal to noise over the segmentation volume range (72% for graph 5.5, and 22% for graph 5.6). For all segmentation volumes the non-transformed data had higher signal to noise results, however, the difference reduces for the larger segmentation volumes.

5.4 Discussion

5.4.1 Overview of Chapter Aims

This chapter set out to investigate the registration capabilities of the MATCH algorithm, which is a sub-voxel sinc based alignment technique, on a phantom pre and post-contrast data set. Two separated studies were conducted. The first study examined the effect of the algorithm on a perfectly aligned phantom pre and post contrast data set. The only difference between the two data sets was the contrast enhancement in the post-contrast data set. Under ideal conditions the algorithm would introduce no translations and rotations when attempting to register the data sets. The algorithm was run with varying volumes of a realignment mask to determine the effects that segmentation would have upon the realignment results and on the signal to noise of the final subtraction data.

The second study investigated the same data sets but with a rotation and translation introduced into the phantom pre-contrast data set. The ability of the algorithm to correct for these rigid body motions was investigated by comparing the

algorithms realignment parameters with the known rotation and translation. These results provided an indication of the registration limits of this algorithm where the data had exactly the same noise structure for both data sets and only differed in areas that contain contrast enhancement.

The aim of these two studies was to determine the effects of segmentation volume on ideal data, and to determine the source of the realignment errors that would result. It was also an aim to determine how the realignment errors would affect signal to noise on the subtraction data output. This would provide underlying knowledge of the realignment principles that could be applied to more realistic phantom and patient data sets.

5.4.2 Realignment of the Non-Transformed Data

Realignment of the non-rotated and translated data was expected to provide a measure of the underlying errors inherent with the realignment algorithm with respect the pre and post-contrast data and the segmentation volumes used. It was expected that minimal errors should be introduced for segmentation volumes where the volume contained no data differences between the two sets. This was indeed found to be the case (see graphs 5.1(a-f)).

Segmentations of 100% and below contained voxels of exactly the same values in both the phantom pre and post-contrast data sets. For these segmentation volumes all of the realignment parameters remained very close to the expected values of zero degrees rotation and zero pixels translation. There was some variation, however, this remained within or close to the rigid body errors determined by the

algorithm itself. Therefore, for these data sets the algorithm introduced no significant errors.

The related signal to noise data is displayed in graph 5.2. Segmentation volumes below 100% displayed the maximal signal to noise value of 188.8. The 100% segmentation volume had a slightly lower signal to noise of 180.2. This suggests that the 100% segmentation volume might have contained a small number of incorrectly assigned voxels, i.e., CSF, enhanced vessels etc. In producing a 97% volume it is possible that the majority of these voxels were removed resulting in more accurate alignment of the data sets. This would suggest a classification error of about 3% or less which agrees with expected manual segmentation errors from the literature (Jack *et al* 1990). Figure 5.7 highlights some of the voxels that were removed from in the 100% segmentation volume to produce the 97% segmentation volume.

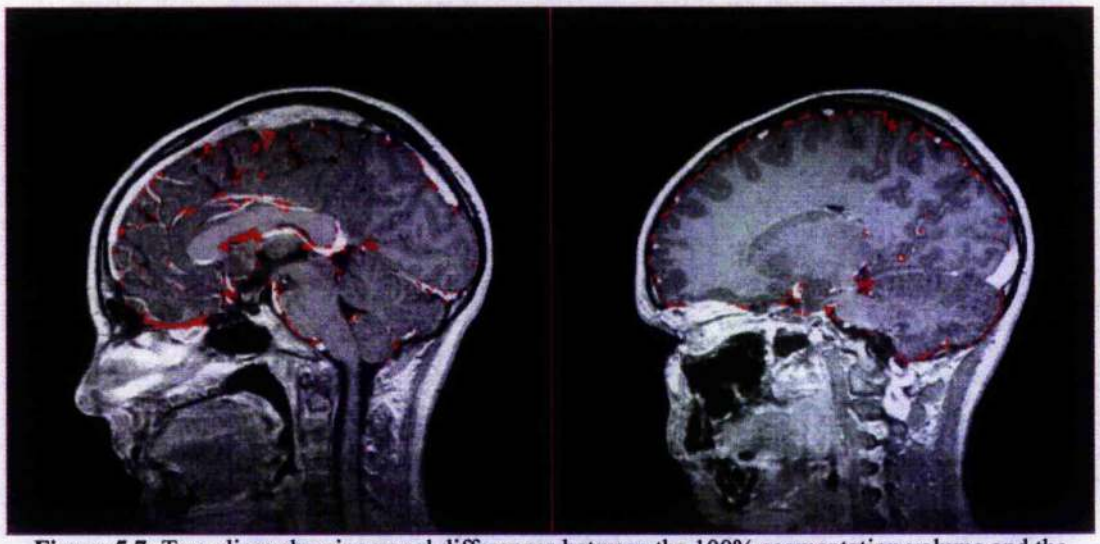

Figure 5.7: Two slices showing voxel differences between the 100% segmentation volume and the 97% volume (Indicated by voxels on the post-contrast data)

The highlighted voxels displayed in figure 5.7 almost exclusively belong to data from brain parenchyma boundaries, and would thus be prone to operator segmentation error. It is therefore possible that the 97% segmentation volume

represented a more accurate segmentation of the brain parenchyma. This would account for the reduction in signal to noise when the 100% segmentation volume was used for realignment purposes.

More significant realignment errors occurred for segmentation volumes above 100% (See graphs 5.1(a-f)). For these volumes contrast-enhanced data was contained within the segmentation volumes as well as brain parenchyma and other non brain structures (in general the CSF is excluded due to noise level thresholding). For segmentation volumes just above 100% a significant proportion of the voxels added to the segmentation volume were from contrast enhancing structures, including the veins (see figure 5.8).

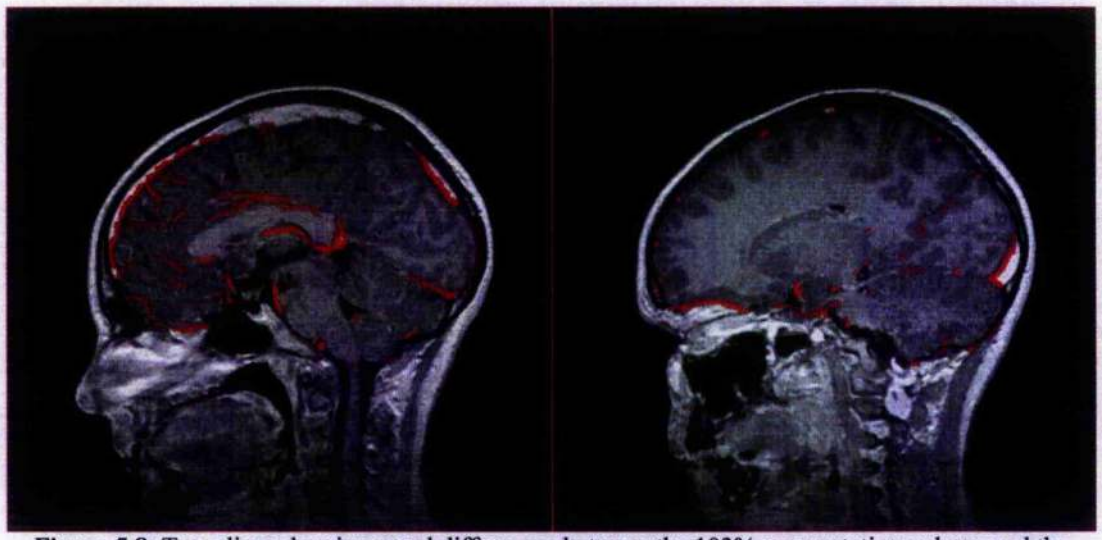

Figure 5.8: Two slices showing voxel differences between the 103% segmentation volume and the 100% volume (Indicated by voxels on the post-contrast data)

Figure 5.8 suggests that any errors introduced into the realignment and signal to noise parameters for this segmentation volume were mainly due to contrast enhanced structures being included in the volume. However, it should be noted that there were also voxels in this and larger segmentation volumes that were not contrast

enhancing. For the volumes close to 100% the additional voxels mainly belonged to structures close or contained within the brain parenchyma, including the arterial vessels. For the larger segmentation volumes other structures such as muscle, connective tissue, and skin were also included.

In nearly all of the realignment parameters in graphs 5.1(a-f) there is a large step away from the optimum values for the 103% segmentation. This suggests that a large part of the realignment errors above 100% were due to the inclusion of the contrast-enhanced data in the segmentation volumes. A large reduction in signal to noise is also seen at the 103% segmentation volume in graph 5.2. Therefore, it was evident that a large proportion of the error in registration above 100% was due to the presence of the contrast-enhanced structures. With increasing segmentation volumes and increasing amounts of enhanced data, the errors in realignment increased.

This first study only investigated realignment of already perfectly realigned data sets with exactly matching signal to noise characteristics. Restricting the study in this way allowed the effects of contrast-enhanced inclusion within the segmentation volumes to be estimated separately. The inclusions of such voxels introduced significant errors to all of the realignment parameters resulting in reduced signal to noise in the final output subtraction. This leads to the conclusion that any new segmentation algorithm, designed for the realignment of similar data sets, must remove all contrast-enhanced data from the realignment volume. However, the phantom data used for this test was perfectly aligned. Therefore, it was important to extend the work to include data that was not perfectly realigned, as would be the case in a real scanning session.

5.4.3 Realignment of the Transformed Data

When the rotation and translation errors for the transformed data are compared to the non-transformed results, it is clear that segmentation accuracy affects these data sets in very similar ways. All of the parameters follow very similar trends with increasing segmentation volume. From these parameters it is very difficult to assess if the transformed data has been aligned to a similar accuracy as the non-transformed data. However, signal to noise is significantly reduced in the transformed case, suggesting that overall alignment is less accurate.

There were two possible sources of the additional errors in the realignment parameters and of the overall reduction in signal to noise. The first was a result of the realignment errors within the algorithm itself, i.e. its inherent ability to correctly determine the realignment parameters for data where there is a significant misalignment. If the algorithm were unable to fully correct for rotations and translations then this would result in the overall reduction in signal to noise. Although from the realignment data there was no overall trend for the realignment parameters to contain larger errors in the transformed data, it was likely that a combination of incorrect rotations and translations, although individually small, resulted in the reduced signal to noise detected.

The second possible source of error would be from the interpolation used and the requirement for re-slicing. For this study re-slicing and realignment occurred on two separate occasions. Firstly, the data was re-sliced to add the offset rotation of 1 degree and translation of 1 pixel. The interpolation in this situation was windowed sinc (Analyze). The second re-slice will have occurred within the MATCH algorithm, where the phantom pre-contrast data was realigned with the post-contrast data set.

Once again this used windowed sinc interpolation. Therefore, to investigate if this would introduce noise to the data the phantom pre-contrast data set that was already offset was realigned, with the known correct parameters of 1 degree YAW and 1 pixel P using the MATCH re-slice algorithm. If any difference in signal to noise was then evident in the resulting subtraction data then this could be attributed purely to the re-slicing and interpolation used.

It was found that the signal to noise of this subtracted data set was 51.20. This value was very similar to the best signal to noise achieved for the transformed data of 51.89. It can therefore be concluded that the majority, if not all, of the reduction in signal to noise for the more accurately aligned data sets (segmentation volume <100%), is due to the reslicing and interpolation used. It is also likely that the variation in the realignment errors are due to reduced signal to noise in the realigned phantom pre-contrast data set which the realignment algorithm then tries to correct for. This is highlighted by the fact that the data that has been analysed by the MATCH algorithm has a slightly higher signal to noise, indicating that the algorithm has moved the data set to try and compensate for the decreased signal to noise.

5.4.4 Overall Conclusions

Therefore, in conclusion it appears that when realigning the phantom pre and post-contrast data any segmentation volumes used for realignment purposes should not include contrast-enhanced voxels. The inclusions of even a small amount of contrast-enhancement results in detectable realignment errors. It can also be concluded that for the phantom data the MATCH algorithm corrects the artificially

induced rotation and translation with excellent accuracy, despite the errors introduced by the two stages of sinc interpolation.

However, this study was conducted on idealised data, where there were no differences in the noise structure of the pre and post-contrast data. Therefore, the next chapter extends this study to determine the effects of additional image noise on the realignment of the phantom data using the various segmentation volumes. Extending the work in this way should allow firm conclusions to be drawn on the effects of segmentation accuracy on real pre and post-contrast data sets.

Chapter 6

Assessing the Effects of Segmentation Accuracy on Patient Data Sets

6.1 Introduction

6.1.1 Overview

Chapter 5 investigated the effects of segmentation accuracy on a phantom data set. Using the phantom data set allowed the MATCH algorithm's realignment capabilities to be assessed on data with known differences in alignment, and known differences in contrast. It discussed the effects of segmentation accuracy on the realignment parameters determined by the MATCH software and on the resulting signal to noise in the final subtraction data. However, due to the artificial nature of the phantom it was uncertain exactly what additional errors would relate to the application of the MATCH algorithm on real patient pre and post contrast data sets.

As discussed in chapter 5 real patient data sets would differ from the phantom data in a number of ways. The most significant difference being the variation in noise and artefacts between the pre and the post-contrast data, which is difficult to model artificially. Therefore, this chapter investigates the effects of segmentation accuracy on realignment parameters calculated by the MATCH algorithm on two real patient data sets. Both data sets are segmented to a high level of accuracy and, using similar methods to chapter 5, the effect of differing segmentation accuracy on realignment are investigated. The results collected for each patient data set are similar to those collected in chapter 5. The only difference in the results is that no prior rotation and translation information is available for the MATCH alignment parameters to be compared with.

The two patient data sets used in this chapter are chosen because they have differing contrast-enhanced properties. The patient 1 data used in this chapter

corresponds to the same patient data used to develop the phantom data in the previous chapter. This allows direct comparison between the results here and in chapter 5. This patient has normal contrast-enhanced anatomy. The second patient has a large contrast-enhanced space occupying lesion, which could have a large effect on the relationship between realignment and segmentation accuracy.

These results in conjunction with the results from chapter 5 enable firm conclusions to be drawn on the segmentation accuracy required in realigning pre and post-contrast data accurately, allowing an automatic segmentation algorithm to be developed later in this thesis.

All of the work in this chapter is original and is currently being prepared for paper submission and all work was conducted by the author, with the exception of the data acquisition which was performed by radiographic staff.

6.1.2 Potential Differences Between Patient and Phantom Data

Real patient data sets will differ from the phantom data in a number of ways. In a real pre and post-contrast data set there will be noise differences within the data. Noise in MRI is produced by a number of connected and unconnected sources. There are, however, two main types of noise present: inherent and non-inherent noise. Inherent noise comes from various sources such as thermal vibrations within the body, quantisation noise in the analogue to digital conversion hardware, preamplification electronic noise and thermal noise in the RF coil. It may be possible to limit the hardware noise by careful design and construction of the components, however, it is impossible to completely eliminate this noise. The thermal noise within

the patient's body is obviously impossible to reduce or eliminate (Redpath 1998). The overall signal to noise resulting from the inherent noise for an MRI data set can be shown to be proportional to the following variables:

$$SNR \propto \frac{signal}{\sigma_n} = m_0 V \sqrt{T_{A/D}} \qquad (6.1)$$

where, m_0 is proportional to the number of hydrogen nuclei , B_0 and magnetic susceptibility (λ), V is the voxel volume, and $T_{A/D}$ is the total time that the MRI systems analogue to digital converter is sampling.

Using the relationship described by equation (6.1) it is possible to increase the signal to noise in MR imaging. For example we know that increasing B_0 increases m_0 resulting in increased signal and thus signal to noise. Another way of increasing the signal to noise would be to increase the sampling time, reducing the noise.

However, there are sources of noise in MRI that cannot be described in such a simple manner. These sources are know as non-inherent noise sources. For example patient motion, external interference, blood and organ pulsation can all affect the overall image signal to noise. Moreover, these noise sources can vary from patient to patient and from session to session and do not necessarily affect all of the data to the same extent. It is possible, though, to limit the effects from these sources under certain circumstances.

Head fixation could correct for the majority of head motion during the scans in co-operative patients, however, motion artefacts would still be present in the data especially in less co-operative patients and in patients who due to illness would find it difficult to keep still.

Pulsation artefacts (ghosting) which can significantly degrade data quality (Wood and Henkelman 1985, Ehman *et al* 1986) can be reduced by the application of

k-space ordered acquisition or scan gating or by utilising specific imaging schemes (Mitchell *et al* 1994, Haacke and Lenz 1987, Hinks *et al* 1993, Kruger *et al* 1997) however, none of these techniques are applied in MP RAGE sequences. Therefore, pulsation artefacts, especially as a result of pulsatile blood flow within the internal carotid arteries, would be present in these data sets. To minimise the contribution of these effects the phase encode direction was set to anterior/posterior so the majority of the pulsation artefacts would remain outside the brain parenchyma.

Non-inherent noise can also result from external noise sources. External interference should not result in significant image noise due to the Faraday shielding surrounding modern scanners and the restrictions concerning their operation. However, if electrical equipment, which is not properly shielded, is brought into the room, interference artefacts can affect the overall signal to noise of the data. However for this study no significant external interference was detected in any of the data collected.

Differences between the pre and post-contrast data will also result from changes in transmitter and receiver gain. The phantom data sets used in the previous chapter assumed that transmitter and receiver gains remained the same. In an ideal situation this would be the case, however, transmitter and receiver tuning occurs at the beginning of each sequence and would be affected by the presence of the contrast medium (See chapter 3). This could result in differing contrast characteristics between the two data sets. It is possible to override the automatic receiver gain setting, however, this could lead to voxel overload in the contrast scans.

Patient motion during the scanning sequences could also introduce further differences between the data sets. The post-contrast data set is serially acquired following the pre-contrast data set and the contrast injection. It is possible due to the

injection or prolonged time within the scanner that the patient might become more agitated during the acquisition of the post-contrast data set. This might lead to the patient moving more during the post-contrast data set, resulting in image blurring and ghosting artefacts. Conversely, it is also possible that with time the patient becomes more accustomed to the MR environment and that the pre-contrast data is more affected by motion than the post-contrast data set.

The realignment software is designed to correct for rigid body rotation and translation between the two scans, however it is unable to correct for partial volume effects. Voxels in MR imaging have a finite and well defined size that is usually measured in cubic millimetres. Due to the finite size of the voxels it is possible for a single voxel to contain signal from two or more structures with differing MR contrast properties. This results in an overall voxel signal that is an average of the different signals contained within it. These voxel intensities would change if the patient moves between the scans, and would be especially significant in the slice direction due to the slightly thicker slices collected in this direction using the MP RAGE technique. In chapter 5 the phantom data set was rotated and translated using sinc interpolation, which would not correctly model difference in the partial volume effect if the subject had in reality moved before the scan. Sinc interpolation would also introduce interpolation errors of its own (see section 5.4.3). Therefore, due to the requirement for interpolation in this technique the data will differ slightly from real data.

Furthermore there could be physiological changes occurring in the patient between the pre and post contrast data collection. For example changes in the patient blood pressure during the two data collection periods might result in more or less vessel pulsation within the brain resulting in more or less pulsation and ghost artefacts. Changes such as these are possible due to the injection of the contrast agent

before the second scan. Although Magnevist's physiological effects are limited or non-existent in the majority of patients, it can induce significant physiological perturbations in a small minority of patients. In extreme cases Magnavist can induce anaphylactic reactions, however this is a rare side effect (Murphy *et al* 1999).

Due to all of these contributing factors it is important to determine if data from real data sets display the same sensitivity to segmentation accuracy as data produced artificially. If similar patterns of realignment accuracy and signal to noise occur then it could be concluded that the phantom data results were a good reflection of results from real data sets, with the phantom data set's advantage being the ability to introduce known rotations and translations. If it transpires that the phantom data sets do represent real pre and post-contrast data sets well then it would be possible in future to use similar data sets for assessment of realignment accuracy of different registration algorithms.

To test these ideas real patient data sets will be investigated using the same procedures as in chapter 5. Two patient data sets will be investigated in detail.

6.2 Patient Study Methods

6.2.1 Data Collection

Two patient data sets were analysed as part of this study. The data sets were collected utilising normal departmental imaging protocols. A description of the imaging protocols used for both patients is described in table 6.1.

Patient 1's data was the same data used to produce the phantom pre-contrast data in the previous chapters. However, in this study the real pre-contrast data set was used rather than the phantom data used previously. Using this same data as before would allow direct comparison of the results from the phantom data and the actual patient data. This patient had normal venous anatomy with no abnormal enhancing structures as determined by a neuroradiologist.

For comparison a second patient data set was examined (patient 2). To test the effects of segmentation accuracy on an abnormal patient data set, patient 2 was selected due to the presence of a large enhancing intra-orbital menigioma (see figure 6.1). It was expected that for segmentation volumes above 100% the presence of a large enhancing volume would affect the realignment and signal to noise parameters to a greater degree than data without such an enhancing tumour.

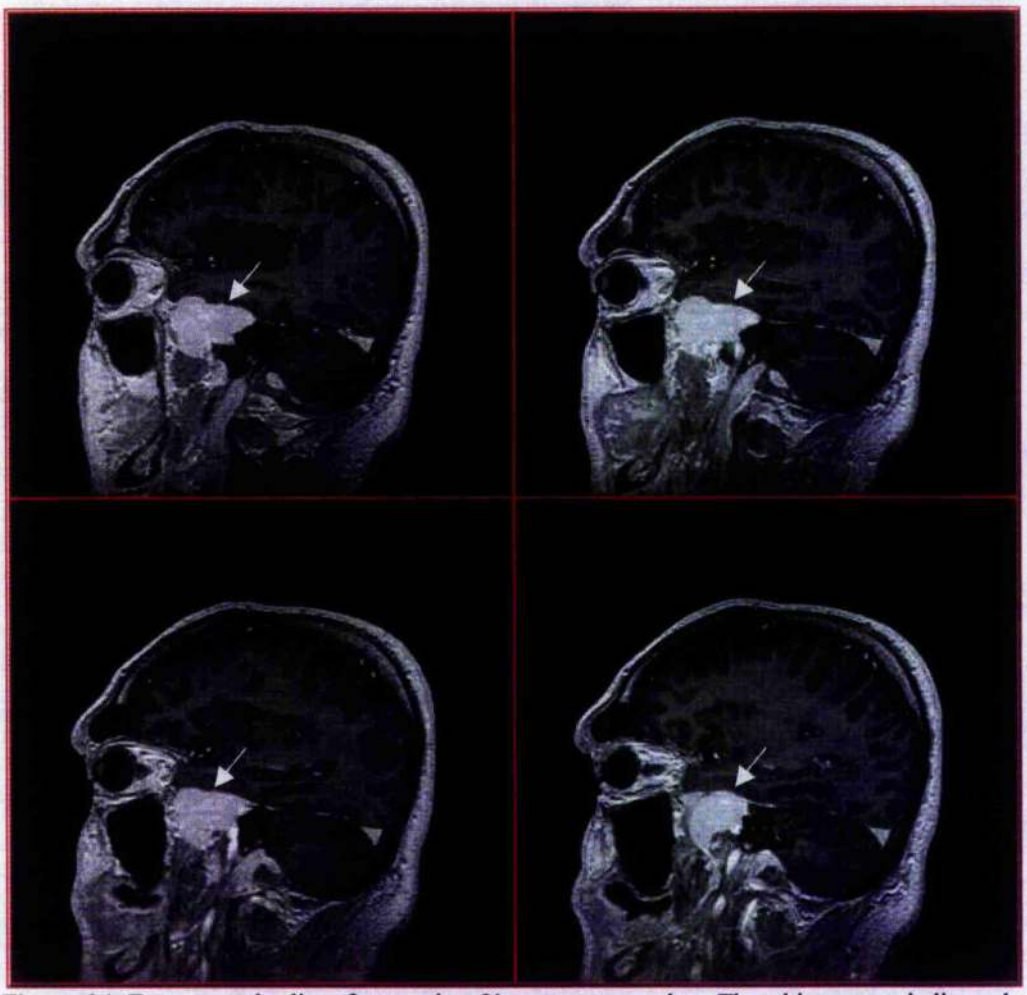

Figure 6.1: Four example slices from patient 2's post-contrast data. The white arrows indicate the location of the large enhancing lesion

The patients had a long IV line inserted prior to the imaging protocol allowing the contrast agent to be administered with the minimum disturbance to the patient. The patient's head was held in position with pads and they were asked to keep as still as possible during the procedure. The Magnevist contrast agent was administered via the long line in a 20 second bolus and the post-contrast sequence was started within 20 seconds of finishing the contrast injection. The imaging parameters for the 3D MP RAGE sequences were TR=10 msec, TE=4 msec, TI=300 msec, flip angle=10 degrees, equivalent slice thickness= 1.4 mm, FOV=250 mm,

with a matrix size of 256x256. Scanning time for each 3D MP RAGE sequence was 6 minutes 46 seconds.

Patient 1	Patient 2
3-Plane Localiser	Sagittal Localiser
2D T1/T2 Multi-echo SE sequence	Pre-Contrast 3D MPRAGE sequence
Pre-Contrast 3D MPRAGE sequence	Magnevist injection (13mls)
Magnevist injection (8mls)	Post-Contrast 3D MPRAGE sequence
Post-Contrast 3D MPRAGE sequence	

Table 6.1: Imaging protocols for study patients

After scanning was completed the data sets were archived and transferred to a sun Ultra 10 workstation. Here they were converted from ACR/NEMA 2.0 format to Analyze format using a conversion tool (conv_analyze , courtesy of Martin Connell) to allow the data to be loaded and processed in a commercial software package.

6.2.2 Image Analysis

Patient 1's post-contrast data was already accurately segmented for the work carried out in chapter 4. However, patient 2's post-contrast data set required accurate segmentation of the brain parenchyma using the methods described in chapter 4. Extra care was required when segmenting the data from patient 2 due to the space occupying lesion which affected the shape of the patients brain (see figure 6.1).

For patient 1 it was also possible to reuse the segmentation volumes created in chapter 5. This allowed direct comparison of the results from the two studies. Similar segmentation volume data sets were produced for patient 2.

The image analysis methods were the same as those used in chapter 5, where both the transformation and signal to noise parameters were examined. However, for these two data sets the rotational and translational parameters required to correctly align the pre and post-contrast data were not known. Therefore, the trends in the transformation and signal to noise parameters were examined and compared to those determined for the phantom data.

6.3 Patient Study Results

6.3.1 Patient 1

Graphs 6.1(a-f) display the alignment parameters produced when registering patient 1's pre and post-contrast data sets. These graphs include both under and over-segmentations.

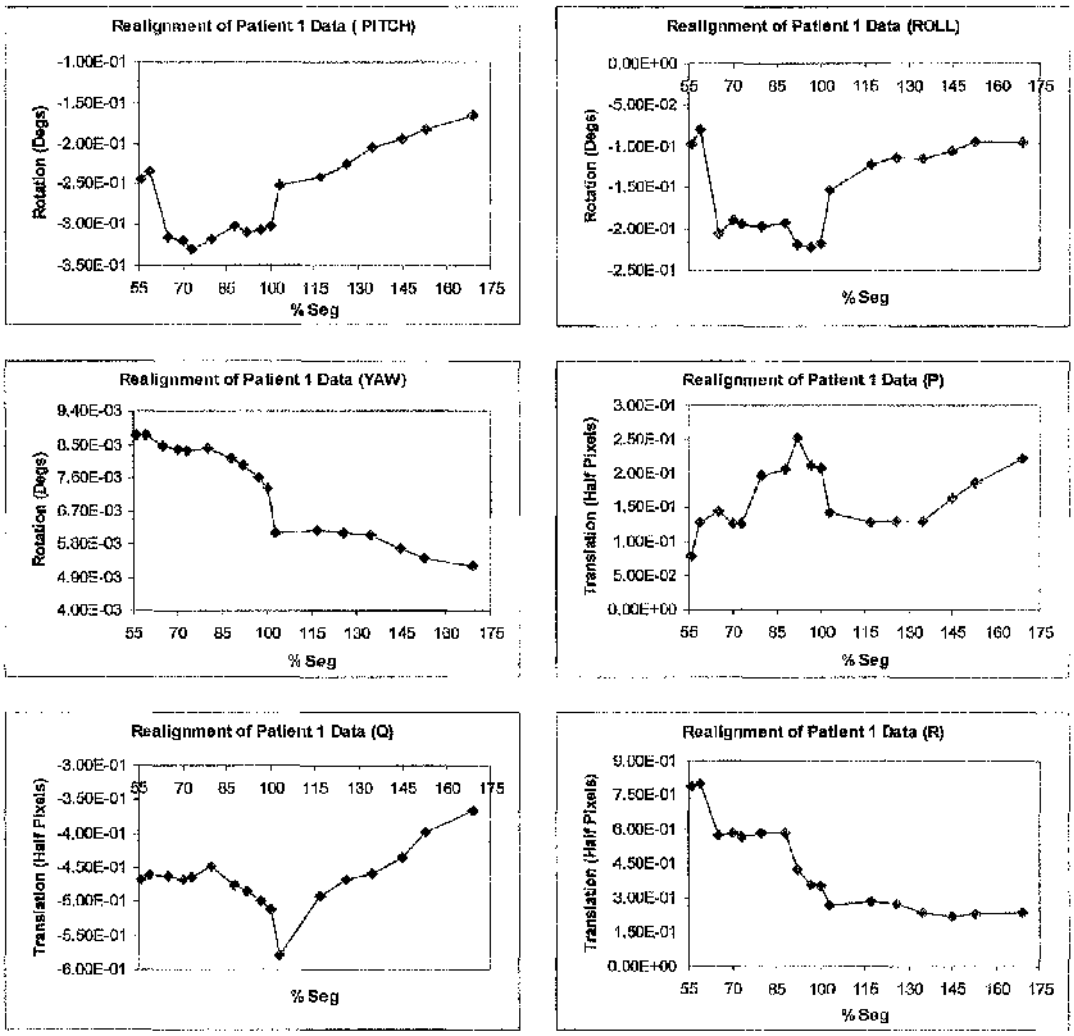

Graphs 6.1(a-f): Rigid body rotation and translation parameters for alignment of the pseudo pre-contrast data with the post-contrast data (Patient 1).

The rotations and translations estimated by the MATCH algorithm attempt to correct for the unknown rotations and translations that occurred with the patients' head during the inter-scan period. It is not possible to relate these to true values as they were unknown, however, it is still instructive to note any features of the graphs produced. It should also be noted that the overall trends in graphs 6.1(a-f) are very similar to those found in the phantom graphs 5.1(a-f).

The graphs of PITCH and ROLL are of similar shapes and dimensions. At 100% segmentation PITCH has a rotation of 0.303 degrees and ROLL has a rotation

of 0.218 degrees. PITCH has a maximum rotation of 0.33 degrees (73%) and a minimum of 0.16 degrees (169%). ROLL has a maximum rotation of 0.223 degrees (97%) and a minimum of 0.08 degrees (59%).

YAW displays a decreasing trend with increasing segmentation volume. All rotations are smaller than for PITCH and ROLL with a rotation of 0.007 degrees at 100% segmentation volume, and a maximum rotation of 0.009 degrees (56%) and a minimum rotation of 0.005degrees (169%).

Translation P shows no overall trend with segmentation volume. The 100% segmentation volume has a translation of 0.104 pixels with the maximum and minimum being 0.126 (92%) and 0.039 respectively. Translation Q varies to a greater extent with segmentation volumes above 100% in what appears to be a linear trend. Below 100% the rotations are more stable. The 100% Q translation is 0.256 pixels with the maximum and minimum being 0.290 pixels (103%) and 0.184 pixels (169%) respectively.

R displays the greatest range of translations over the segmentation volume range. The 100% R translation is 0.178 pixels with the maximum and minimum being 0.401 pixels and 0.119 pixels respectively. The variations in translation are larger below 100% segmentation volume with an overall trend for decreasing translation for larger segmentation volumes.

As was discussed in chapter 5 it is difficult to comprehend the overall effect of the segmentation accuracy upon visual inspection of the individual rotations and translations. Therefore, using the methods described in section 5.2.4 the overall rotations and translations were calculated.

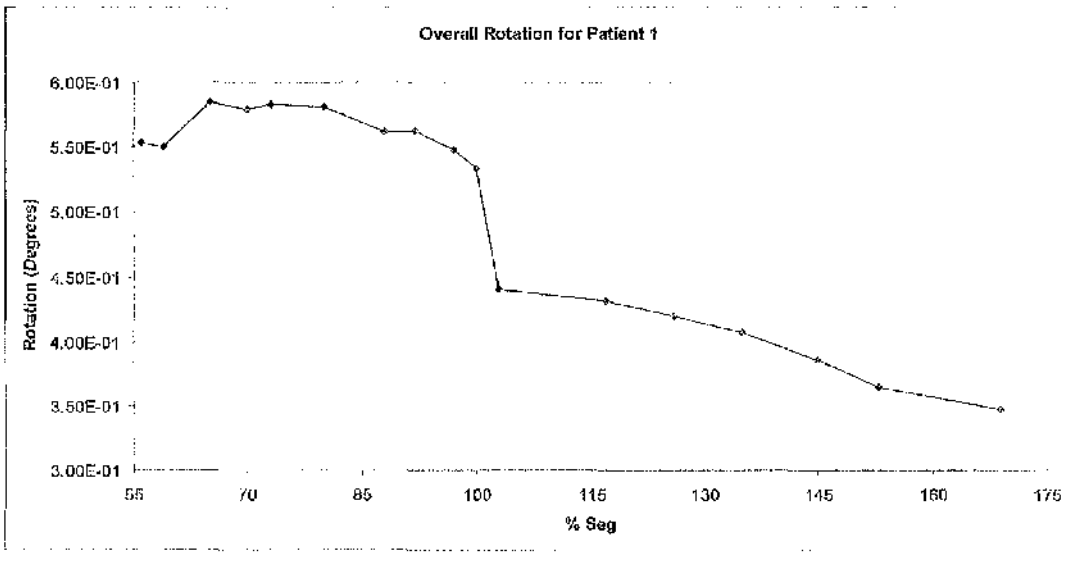

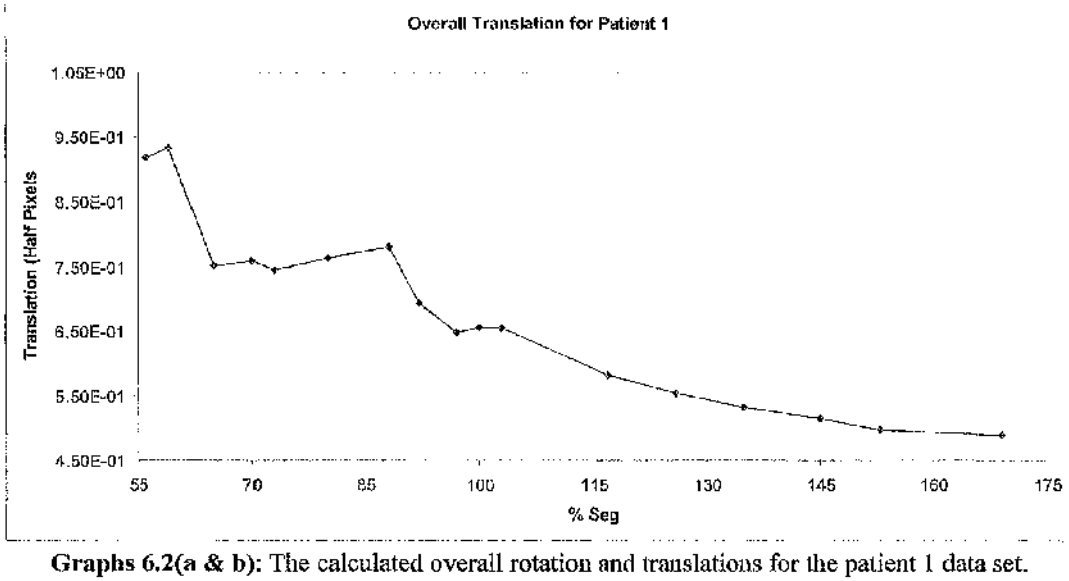

Graphs 6.2(a & b): The calculated overall rotation and translations for the patient 1 data set.

Graphs 6.2(a & b) display the results for both rotation and translation. Graph 6.2(a) shows the overall rotations applied to patient 1's data for different segmentation volumes. For segmentation volumes of 100% and below, the overall rotation varied between 0.534 degrees at the 100% segmentation volume, and 0.585 degrees at the 65% segmentation volume. The largest variation within this region represented a difference of 9.5% with respect to the 100% segmentation volume. Above the 100% segmentation volume there was a trend for decreasing rotation with the maximum rotation being 0.441 at the 103% segmentation volume and the

minimum being 0.347 at the 169% segmentation volume. The smallest variation from respect to the 100% segmentation volume was 17.4%. Therefore, the greatest variation in overall rotation occurred for segmentation volumes greater than 100%. This concurs with the conclusions of chapter 5.

In contrast the overall translation (graph 6.2(b)) is more variable for segmentation volumes of 100% and below than for segmentation volumes above 100%. For segmentation volumes of 100% and below the overall translation varied between 0.649 half pixels at the 97% segmentation volume and 0.934 half pixels at the 59% segmentation volume. The largest variation from the 100% segmentation volume translation (0.656) represents a difference of 42% with respect to the 100% segmentation volume.

As described in section 6.2.2 these overall rotations and translations could be directly compared to the rotations and translations in the phantom data from chapter 5. Comparing these results would provide information on the effects of noise differences between the real pre and post-contrast data (graphs 5.6(a & b) and 6.2 (a & b).

On inspection of the results it was obvious that patient 1 did move a significant amount between the pre and the post-contrast scans. Ideally, therefore the patient data would be compared to the phantom transformed data. However, as was discussed in section 5.4.3 the overall signal to noise in the transformed phantom data was reduced by the extra SINC transformation required to produce this data, therefore, the data was of reduced quality. This suggests that the patient data should be compared to the non-transformed phantom data. Conversely, it could be assumed that the extra interpolation introduced noise into the phantom data, and thus the transformed data results would be more closely related to the results for the patient

data, which contain significant noise differences between the pre and post-contrast data. Therefore, for completeness the overall rotations and translations were compared for both the transformed and non-transformed data sets.

Graphs 6.3(a & b) display the relationship between patient 1's overall rotation and translation parameters with the non-transformed phantom data. Graphs 6.3(a & b) display the relationship with the transformed data.

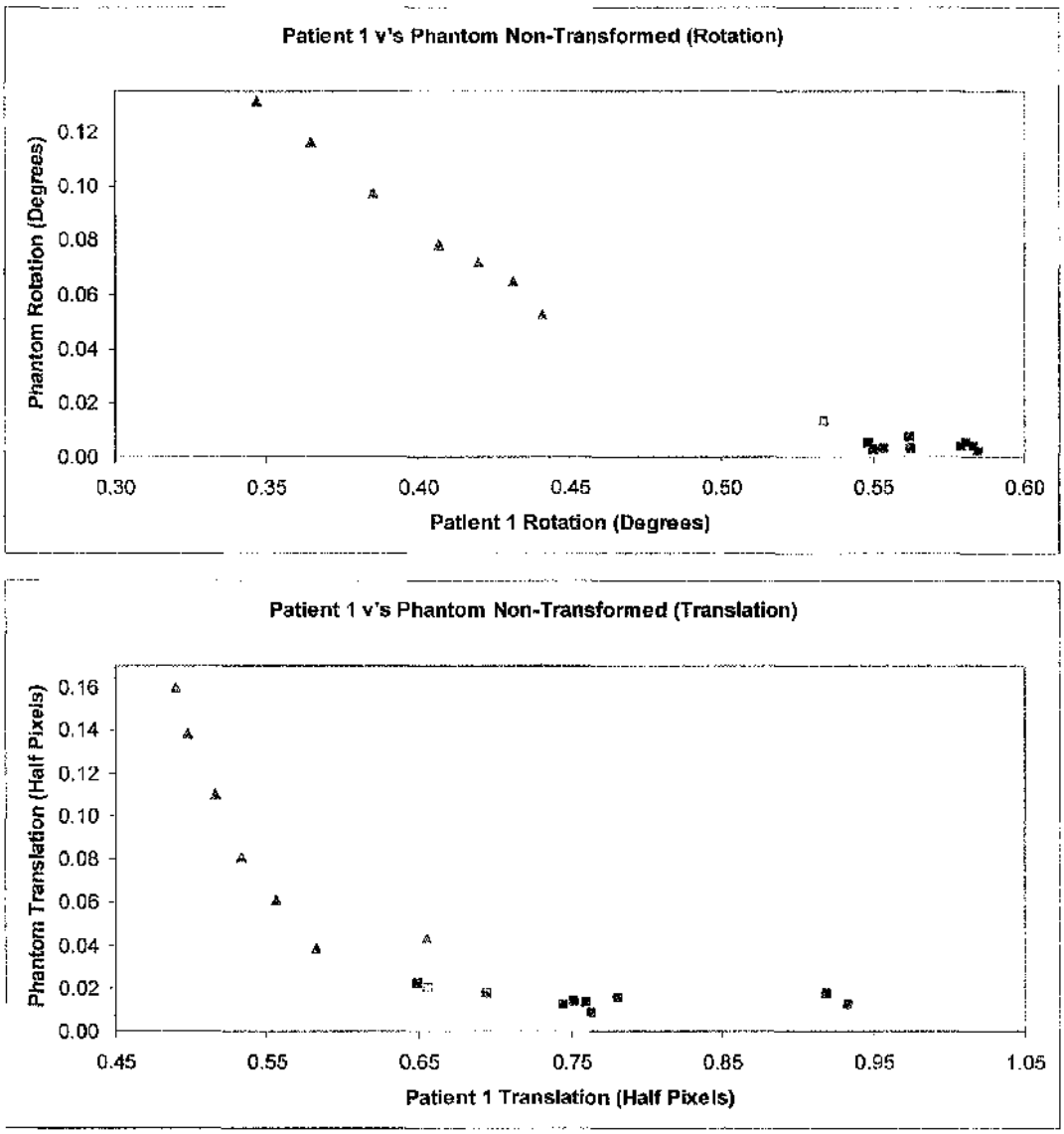

Graphs 6.3(a & b): The relationship between patient 1's overall rotation and translation with the non-transformed phantoms rotation and translation
(The triangles represent data from segmentation volumes >100%. The blue squares represent data from <100% and the red square is the 100% data point)

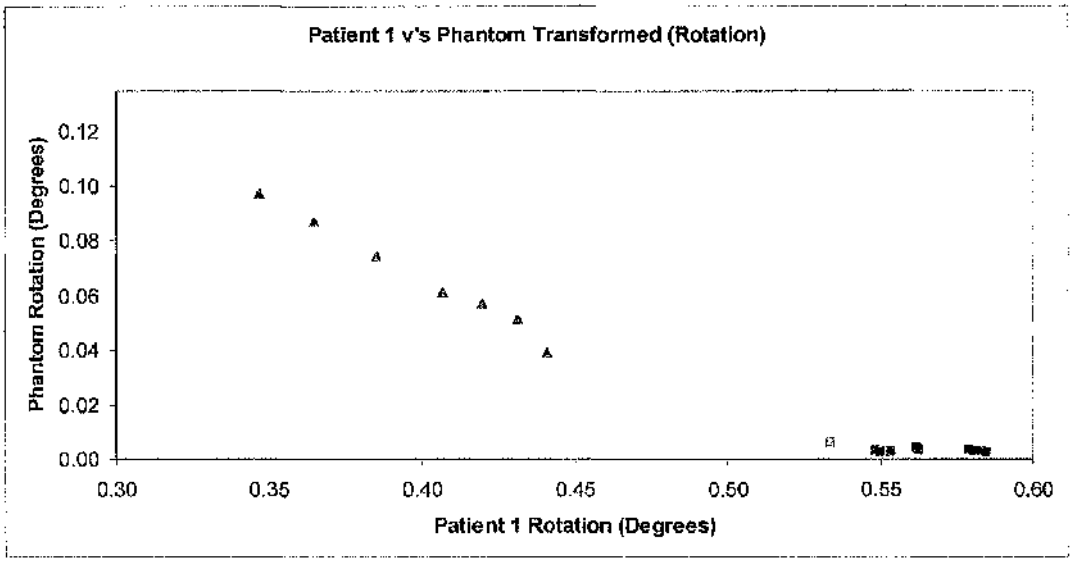

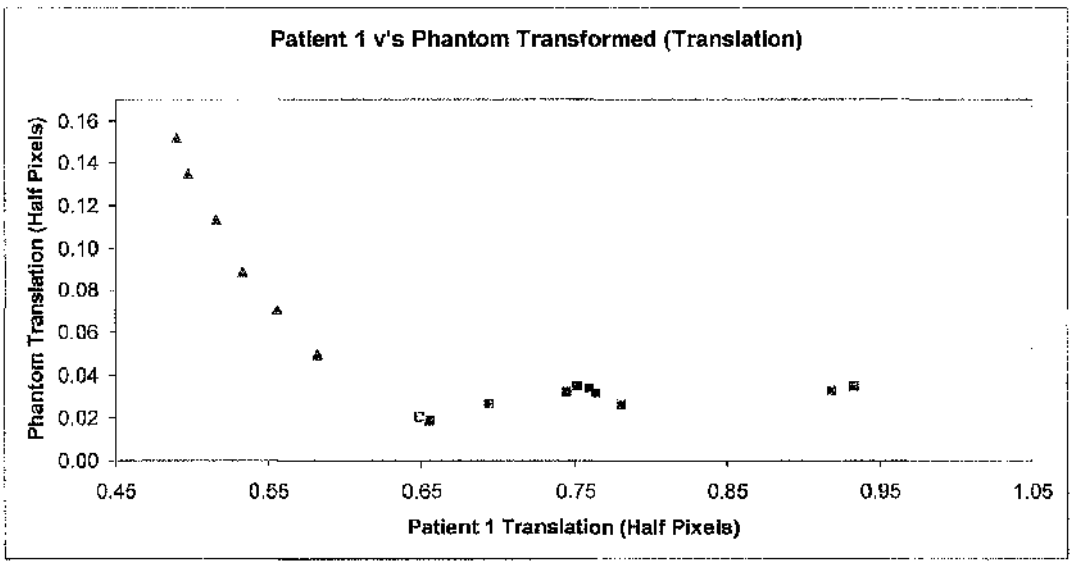

Graphs 6.4(a & b): The relationship between patient 1's overall rotation and translation with the transformed phantoms rotation and translation
(The triangles represent data from segmentation volumes >100%. The blue squares represent data from <100% and the red square is the 100% data point)

Graphs 6.3(a & b) and 6.4(a & b) suggest that for segmentation volumes larger than 100% that the overall rotational and translational parameters follow the same trends for the phantom data as for the patient data. This can be quantified by calculating the correlation coefficients for this data (see table 6.2)

Data comparison	Pearson Correlation	Statistical Significance
Patient 1 v's Non-transformed (Rotation)	-0.997	<0.001
Patient 1 v's Non-transformed (Translation)	-0.858	0.013
Patient 1 v's Transformed (Rotation)	-0.994	<0.001
Patient 1 v's Transformed (Translation)	-0.962	0.001

Table 6.2: Pearson correlation coefficients and statistical significance when comparing segmentation volumes > 100% segmentation volume

All correlations are significant at the $p<0.05$ level with only the transformed rotation comparison not significant at the $p<0.01$ level. These results suggest that for segmentation volumes above 100%, where the volume contains contrast-enhanced data, that the overall trends in rotational and translational correction are very similar for both the phantom data and for the patient data. Therefore, because the chapter 5 results suggest that contrast-enhanced data inclusion within the segmentation mask is undesirable, then it appears that these results confirm this conclusion.

Data comparison	Pearson Correlation	Statistical Significance
Patient 1 v's Non-transformed (Rotation)	-0.541	0.107
Patient 1 v's Non-transformed (Translation)	-0.443	0.200
Patient 1 v's Transformed (Rotation)	-0.519	0.124
Patient 1 v's Transformed (Translation)	0.706	0.022

Table 6.3: Pearson correlation coefficients and statistical significance when comparing segmentation volumes =< 100% segmentation volume

For segmentation volumes of 100% and below this is not the case as is illustrated by table 6.3. Only translation is significantly correlated and only then with the transformed data.

The differences in correlation and in the shape of the graphs above and below the 100% segmentation suggest that the noise differences present in the patient data affect the realignments to a greater extent at segmentation volumes below 100%.

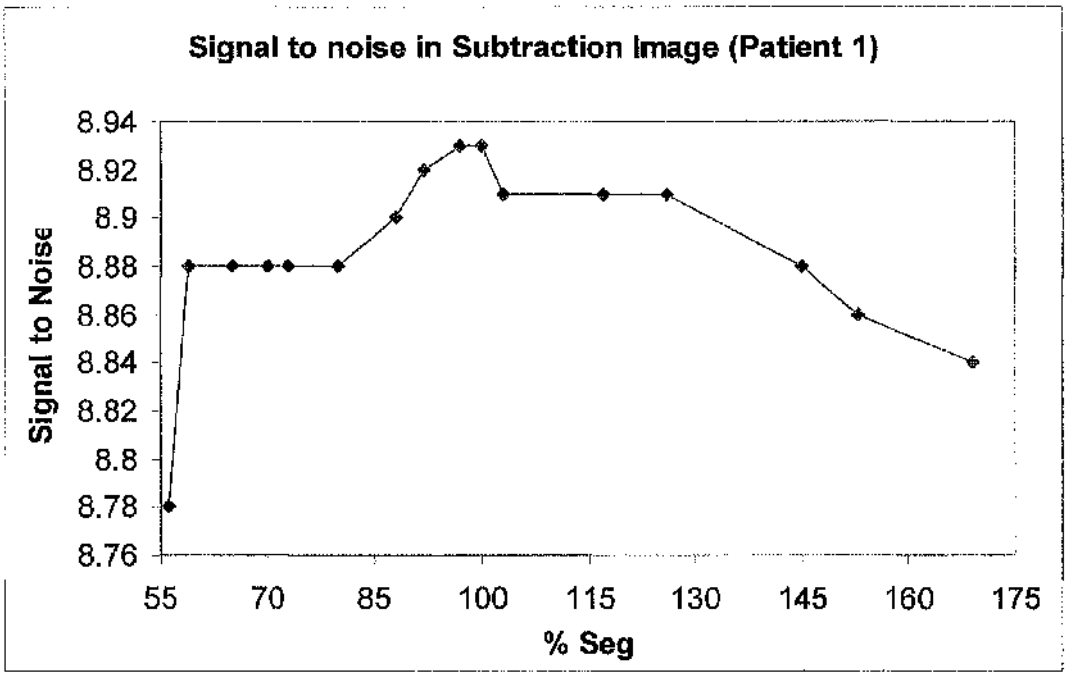

Graph 6.5: Signal to noise variations with respect to the segmentation volume applied during the registration process (Patient 1)

The signal to noise data for this patient is displayed in graph 6.5. The highest signal to noise occurs at two segmentation volumes, 100% and 97%. Segmentation volumes between 88% and 126% all have signal to noise values within 1.5% of this value. Below 100% segmentation volume signal to noise levels off at 8.88 between 80-59% before dropping of considerably to 8.78% at segmentation volume 55%. Signal to noise drops in a more linear fashion above the 100% segmentation volume. If we compare this graph to the equivalent graphs in chapter 5 (5.2 and 5.7) it would appear that the increased variability of the translational parameters at different segmentation accuracies below 100% result in reductions in the signal to noise. These results will be discussed in more detail later.

6.3.2 Patient 2

Graphs 6.6(a-f) display the alignment parameters produced when registering patient 2's pre and post-contrast data sets. These graphs include both under and over segmentations.

Only two of the graphs can be described by a linear trend over the whole range investigated, PITCH (R^2= 0.9391) and ROLL (R^2= 0.9832). Both of these parameters tend toward smaller required rotations with increasing segmentation volume. The 100% segmentation volume has a value of 0.450 degrees for PITCH and 0.428 degrees for ROLL. PITCH has a maximum rotation of 0.481 (70%) and a minimum rotation of 0.363 degrees (155%). ROLL has a maximum rotation of 0.465 (59%) and a minimum rotation of 0.351 (155%).

Overall the whole range YAW displays no overall rotation trend, although there is more variability in this parameter at segmentation volumes above 100% than below 100%. The 100% segmentation volume has a value of 0.477 degrees. The maximum rotation occurs at a segmentation volume of 124% with a value of 0.544 degrees. The minimum rotation occurs at a segmentation volume of 0.474% with a value of 97%.

Translation parameter P shows no overall trend over the whole range of segmentation volume values, although there is more variability above 100%. The 100% segmentation volume has a value of 0.1825 pixels. The maximum translation of 0.196 pixels occurs at 118% with the minimum of 0.171 occurring at 155%.

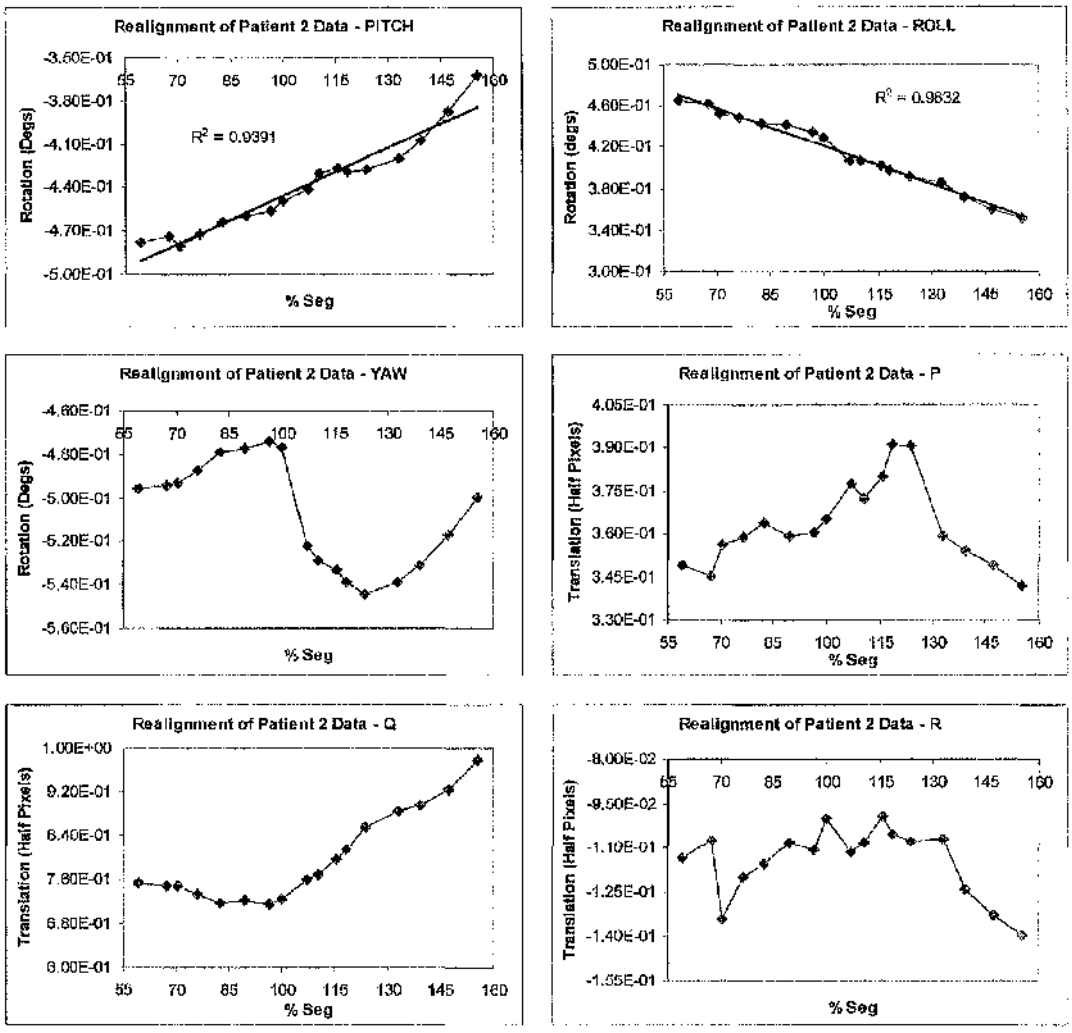

Graphs 6.6(a-f): Rigid body rotation and translation parameters for alignment of the pseudo pre-contrast data with the post-contrast data (Patient 2).

Translation parameter Q appears to display a trend to reducing translation below 100% and an increasing trend above 100%. Once again the values above 100% tend to be further away from the 100% value of 0.362 pixels. The maximum translation of 0.489 pixels occurs at 155% with the minimum translation occurring at 97% with a value of 0.358.

Translation parameter R displays no overall trend over the whole range of segmentation volumes. Variability appears to be similar above and below the 100%

segmentation volume. The 100% segmentation volume translation value is 0.050 pixels. The maximum translation of 0.070 occurs at a segmentation volume of 155% and a minimum translation of 0.049 at a segmentation volume of 116%.

Once again to simplify the analysis the individual rotations and translations were converted to overall rotations and translations (see section 5.2.4) and are displayed in graphs 6.7 (a & b).

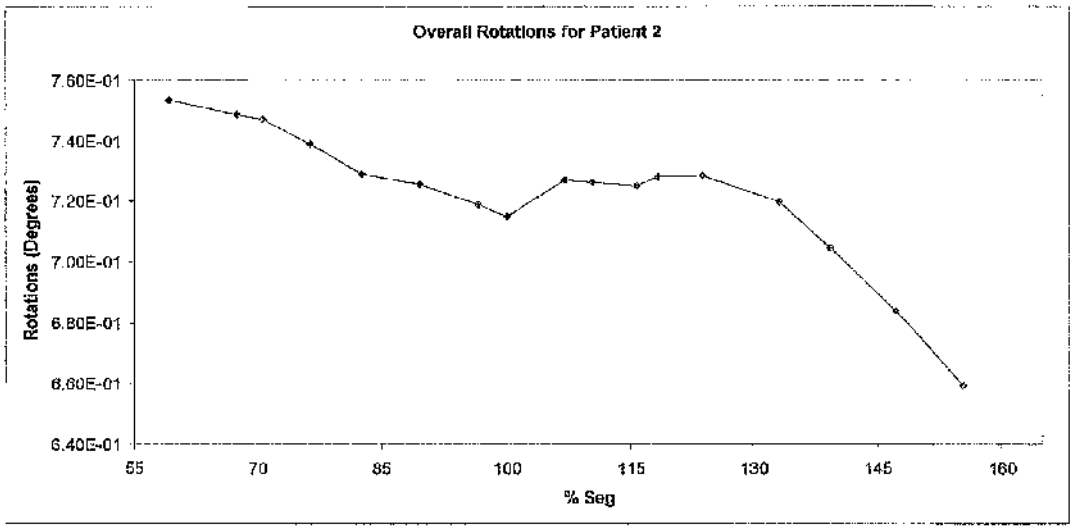

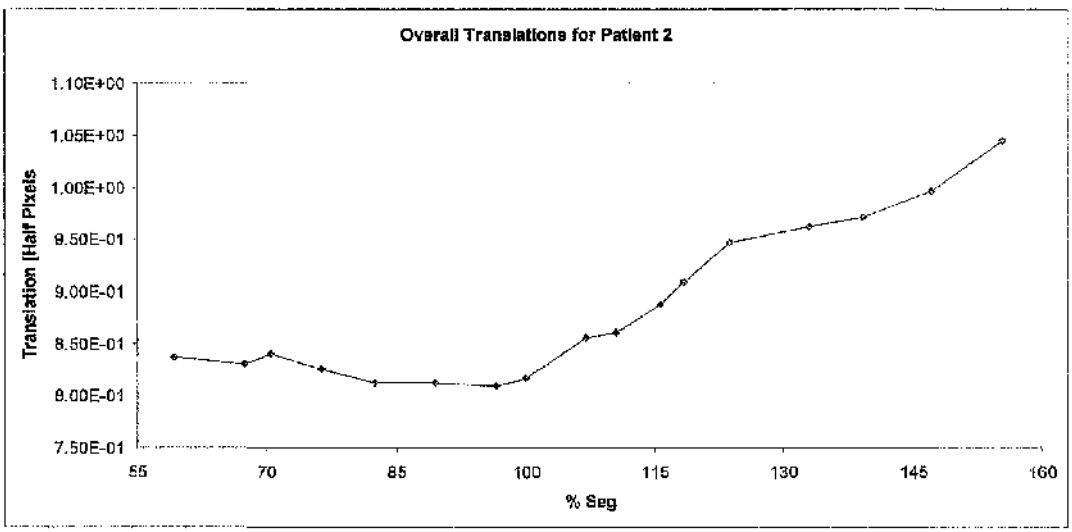

Graphs 6.7(a & b): The calculated overall rotation and translations for the patient 1 data set.

In the 100% segmentation volume and below range the overall rotation parameter (graph 6.7(a)) varied between 0.715 degrees at the 100% segmentation volume to 0.753 degrees at the 59% segmentation volume. This represented an overall variation of 5.3% with respect to the 100% segmentation volume rotation. Above 100% the overall rotation varied between 0.728 degrees at the 107% segmentation volume to 0.659 at the 155% segmentation volume. This represented a largest variation of 7.8% with respect to the 100% volume rotation. However, it should be noted that for segmentation volumes between 83% and 139% the rotations remain within 2% of the 100% volume rotation.

Graph 6.7(b) shows the overall translation applied to patient 1's data for different segmentation volumes. For the segmentation volumes of 100% and below the overall rotation varied between 0.809 half pixels at the 97% segmentation volume and 0.837 at the 55% segmentation volume. With respect to the 100% segmentation volume (0.816 half pixels) this represents a largest variation of 2.6%. Above 100% the overall translation varied between 0.816 half pixels at the 107% segmentation volume and 1.045 half pixels at the 155% segmentation volume. This represents a largest variation of 28.1%.

Graph 6.7(b) in particular supports the hypothesis that there is smaller amount of variation on the realignment with differing segmentation volumes when there is no contrast enhancement present in the realignment segmentation volume. It follows a very similar trend to the phantom data translation results in chapter 5 (graph 5.6(b)). This, however, is not the case for the rotation parameters (see graphs 6.7(a) and 5.6(a)). For larger segmentation volumes the graph does indeed tend away from the 100% segmentation value, however, for segmentation volumes closer to the 100%

volume the variability appears to be smaller for segmentation volumes above the 100% volume.

To appreciate the effects of these rotations and translations on the resulting alignment data it is important to inspect the signal to noise results (see graph 6.8)

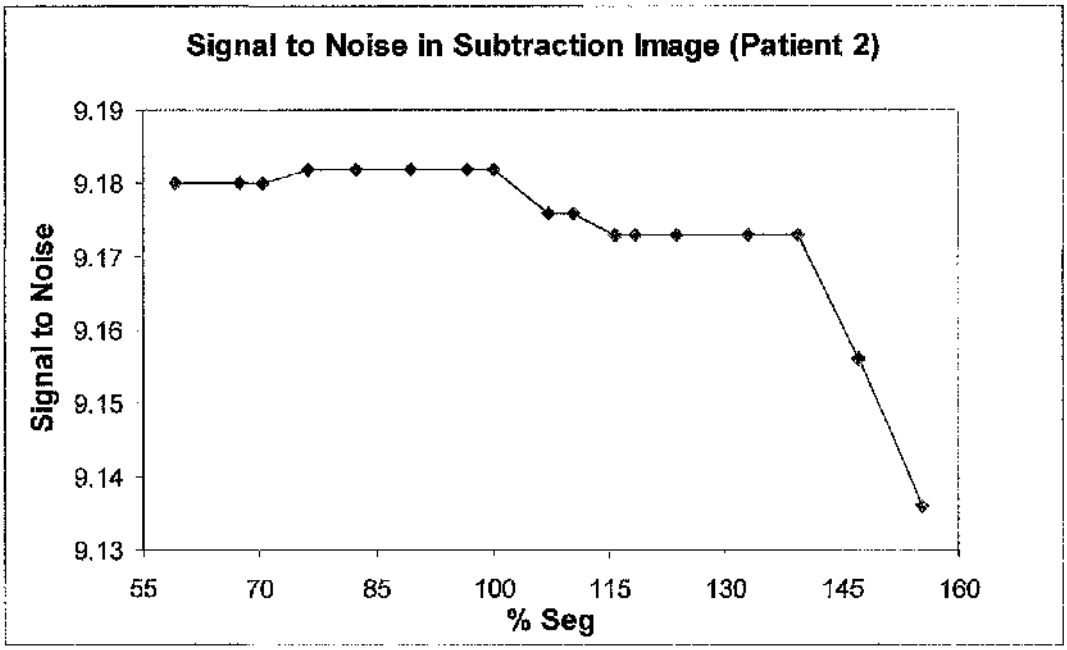

Graph 6.8: Signal to noise variations with respect to the segmentation volume applied during the registration process (Patient 2)

Graph 6.8 displays the signal to noise ratio for the subtraction data for this patient. Below the 100% segmentation volume signal to noise changed very little. It remains close to 9.180 which is higher than the signal to noise measurements for patient 1 (see graph 6.5). Above 100% however, there is more variation in signal to noise with an overall decrease in signal to noise with increasing segmentation volume. The drop is signal to noise is most significant for segmentation volumes above 139.3% where the signal to noise falls to 9.136.

The signal to noise results suggest that despite the variability of the overall rotation below the 100% segmentation volume (see graph 6.7(a)) that segmentations below 100% produce better overall alignment results than for segmentation volumes above 100%. It was for these over 100% segmentation volumes, where there was increased variation in the overall translation, that signal to noise falls significantly. Therefore, for patient 2 it would appear that the realignment is of better quality when using segmentation volumes of 100% and below. These results therefore support the conclusions of chapter 5 despite the presence of the large enhancing lesion.

6.4 Discussion

The patient 1 data is the same data from which the phantom was derived in chapter 3. Therefore, by determining the differences between the two data sets it was possible to determine the effects that real noise differences have on realignment accuracies for different segmentation volumes. The realignment parameters for patient 1 have similar graph characteristics and trends to those determined for the transformed and non-transformed phantom data in chapter 5 (comparing graphs 5.1(a-f) and 6.1(a-f)).

The most noticeable difference between the two data sets is the increased variability for all of the realignment parameters, compared to the moved phantom data, for segmentation volumes below 100%. It is possible to illustrate this by displaying the variation of these parameters around their average value (below 100%) for both data sets whilst keeping the graph scales the same (compare graphs 6.9(a,b)

and (c,d)). It is obvious from these graphs that the variations are greater for the patient data set.

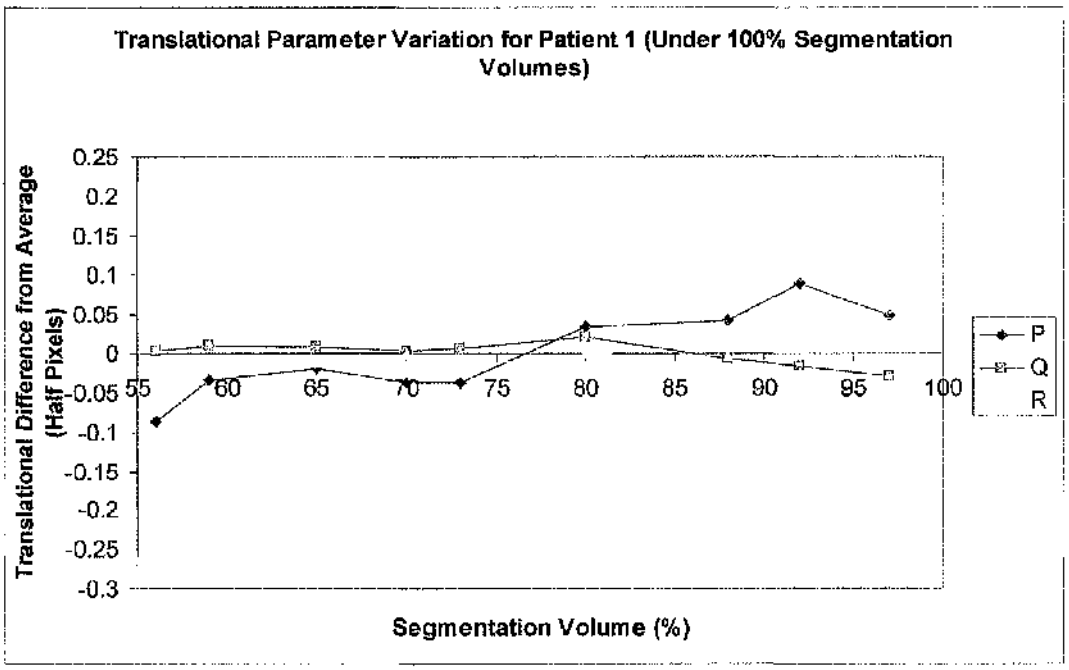

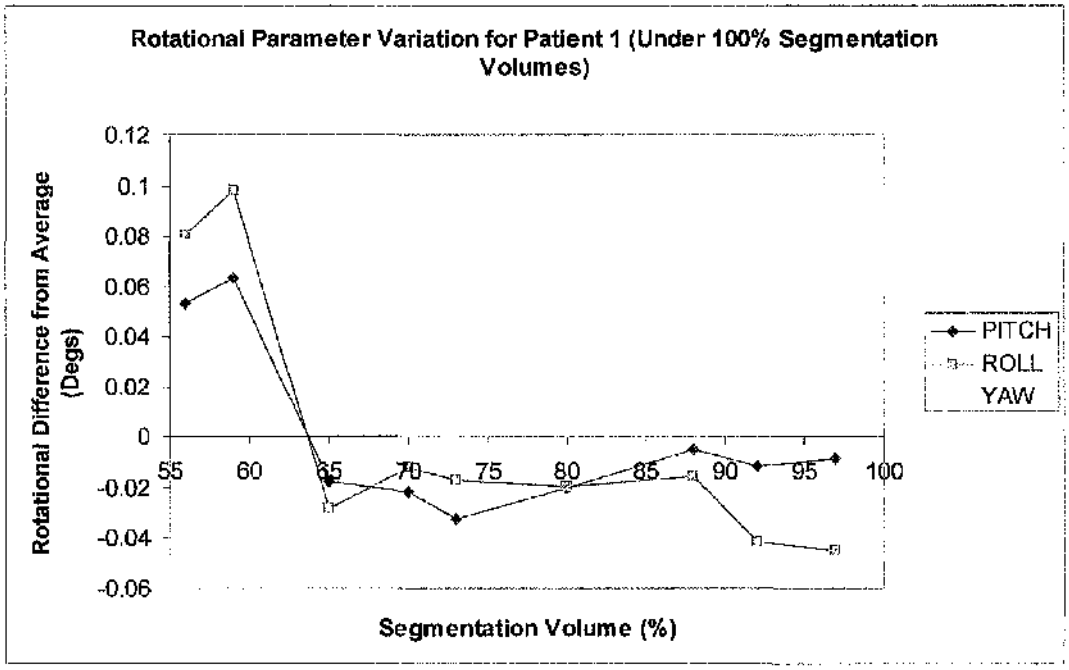

Graphs 6.9(a,b): Patient 1 variations from the average rotational value for segmentation volumes below 100%

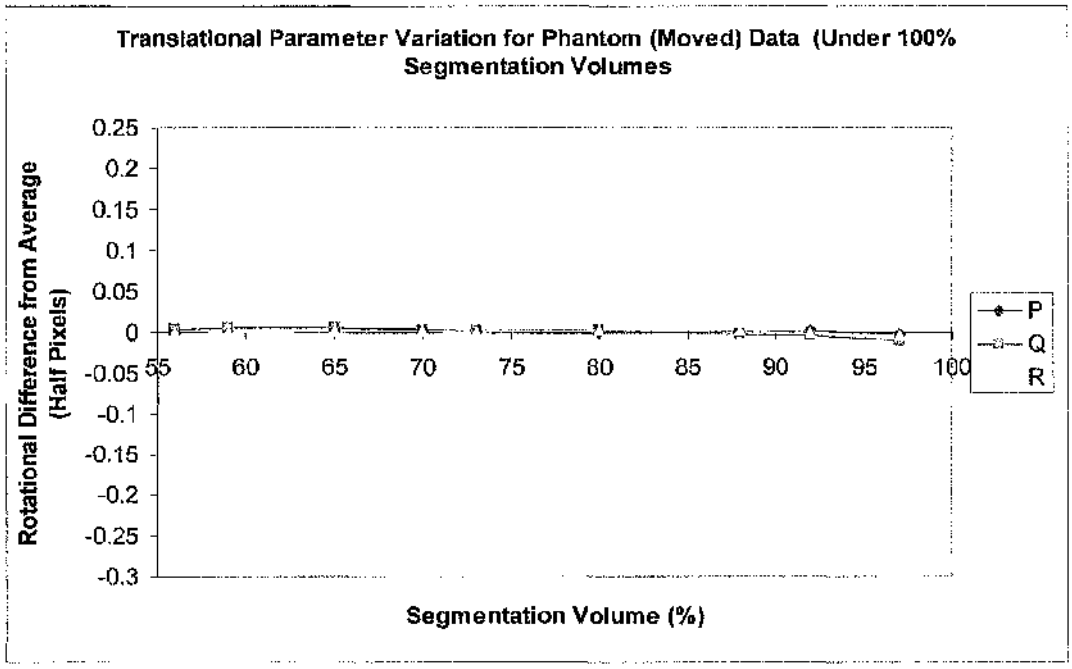

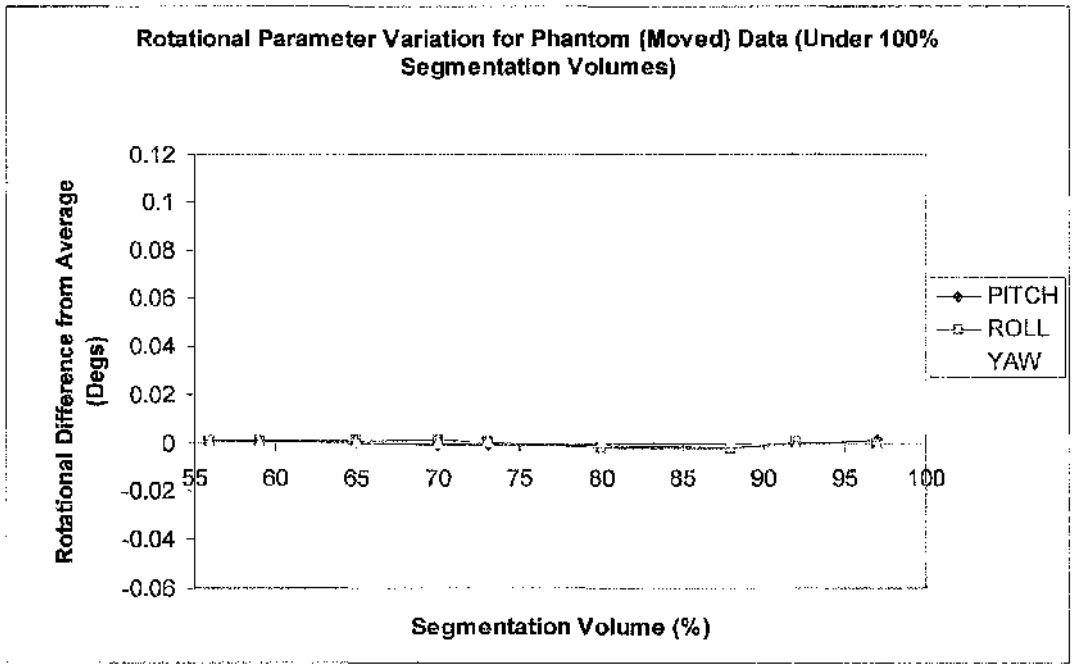

Graphs 6.9(c,d): Phantom (moved) translational variations from the average rotational value for segmentation volumes below 100%

These results can be explained due to the presence of noise differences in the pre- and post-contrast data sets that was not present in the original phantom study in chapter 5. The noise introduces random variations in the realignment parameters when compared to data with no such noise differences. The variations are larger for

the smaller segmentation volumes (below 65%). This suggests that the noise differences have a greater effect when the volumes are smaller, however, the noise differences do not appear to be linearly related to segmentation volume. It is likely that local noise characteristics within the data sets will contribute to the overall variations. Local variations might occur for example if there is arterial ghosting affecting part of the images.

When the data equal to and above the 100% segmentation volume is compared it is found that corresponding parameters from the phantom and patient data set vary linearly with respect to one another (see graphs 6.10 (a-f)). All of the translation and rotation parameters have linear least squares fits (R^2) of greater than 0.7 with four (PITCH, ROLL, YAW and Q) producing linear fits of greater than 0.9. For all of the parameters the rotations and translations required are larger for the patient data set than for the phantom data set, due to the real patient motion present. More significantly the best-fit line gradients are all larger than 1. This suggests that there are larger errors in the realignment parameters for the patient data set than for the phantom data set, i.e. each increase in segmentation volume over 100% increases the error in the patient data by a larger amount. Therefore, despite the preservation of a linear relationship between the phantom and patient data set for these segmentation volumes it remains the case that the segmentation volumes containing contrast-enhanced data introduce significant errors into the realignment.

The comparisons of overall rotation and translation for the phantom and patient data strengthen these conclusions (see graphs 6.3(a & b) and 6.4(a & b)). For segmentation volumes above 100% the phantom and patient 1 data correlate significantly (table 6.2) but correlate poorly for segmentation volumes below 100% (table 6.3).

The signal to noise graphs for patient 1 and the phantom data sets also display similar differences. For example for the phantom data set with rotation and translation added, signal to noise does not vary for segmentation volumes below 100% (See graph 5.7). However, for the same segmentation volumes the patient 1 signal to noise does vary to a larger degree, and remains below the optimum signal to noise measured at the segmentation volume of 100% (see graph 6.5). There is a more significant fall at segmentation volume 56%. The reductions in signal to noise will result from the variable nature of the realignment parameters, which themselves are a result of the noise differences between the pre and post-contrast data sets. The larger variations in the realignment parameters would also explain the large drop in signal to noise at the 56% segmentation volume.

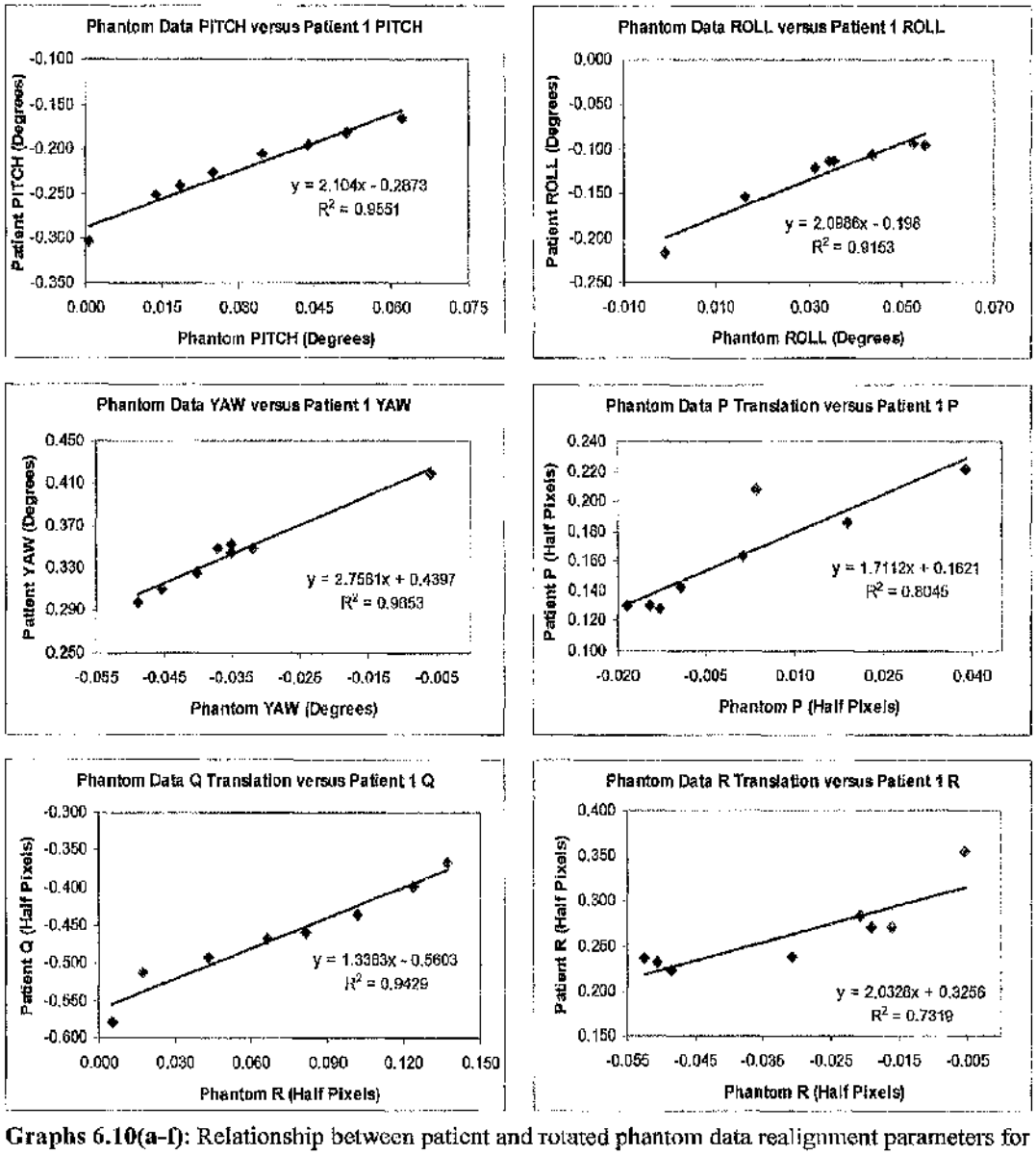

Graphs 6.10(a-f): Relationship between patient and rotated phantom data realignment parameters for segmentation volumes above 100%

Above 100% the shape of phantom graph is similar to the shape of the graph for patient 1. The signal to noise falls with increasing segmentation volume. This fall is a result of the realignment errors produced due to the presence of the contrast enhancement in the segmentation volumes.

From comparing the phantom data set with the patient data set it is possible to determine the effect that real noise differences have on realigning pre and post-

contrast data sets. From the above analysis it can be concluded that noise differences play an important role when realigning data with sub optimal segmentation volumes by increasing the overall error in the realignment parameters by a random amount. The error appears to remain random although larger errors are introduced for the smaller segmentation volumes.

Despite the extra realignment error introduced for segmentation volumes <100%, the realignments for this range of segmentation volumes are still more accurate than the realignments calculated for volumes greater than 100%. Therefore, it can still be concluded that when segmenting pre and post-contrast data sets, that care must be taken to ensure that contrast enhanced data is not contained within the segmented volume.

The inclusion of a second patient data set in this study allowed segmentation accuracy to be investigated on a sub-optimal data set. Patient 2 had a large enhancing, space occupying lesion, which would be expected to affect the realignment accuracy in a different way to the previous data sets. However, to be able to make general conclusions about segmentation accuracy for pre and post contrast data sets, all of the conclusions previously reached should remain consistent with the realignment results for this sub-optimal data set.

For two of the parameters (YAW and Q) distinct changes in the realignment parameters occurs at the 100% segmentation volume similar to those described in patient 1, with YAW displaying a large discontinuity and Q displaying a reversal of the line gradient. (See graphs c and e). Graphs P and R are more generally variable over the whole range, however, this is similar to P in patient 1 (graph 5.1(c)). The two parameters that display unusual characteristics for patient 2 in comparison to patient 1 and the phantom data are the PITCH and ROLL parameters. Both of these

parameters display linear trends over the whole range of segmentation volumes. (See graphs 5.6 (a and b). Linear trends such as these were not produced for any of the other data sets.

In trying to describe the processes that produced these linear trends note should be made of the overall rotations and translations calculated and the signal to noise changes in the final subtraction image (See graphs 6.7(a and b) and 6.8).

The linear trends in these rotational parameters did not translate to a linear trend in rotation. As was described in section 6.3.2 the overall rotation appears to remain closer to the 100% segmentation rotation value for segmentation volumes above the 100% segmentation volume than those below it, at least until segmentation volume 139%. This suggests that under-segmented volumes were aligning more accurately. However, the overall translation parameter suggests the opposite. Thus, the accuracy of the realignments were not obvious from the realignment parameters. Therefore, it was important to examine the signal to noise results.

The overall shape of the signal to noise graph is very similar to those produced in chapter 5 (see graphs 5.2 and 5.7), with very little variation in signal to noise for segmentation volumes below 100% but with falling signal to noise above 100%. The lack of variation in the signal to noise below 100% suggests the changes in the realignment parameters within this range of segmentation volumes do not affect the subtraction image to any significant degree. The fall in signal to noise above 100% suggests that the inclusion of contrast-enhanced data within the realignment volume reduced the realignment accuracy. The more significant fall in signal to noise above 139% is likely to be due to increasing inclusion of the enhancing tumour within the realignment volume.

Therefore, despite the lack of cohesive conclusions from the translation data for patient 2, when the signal to noise data is included in the analysis, this patients results appear to confirm the previous conclusions on the realignment accuracy in relation to the segmentation accuracy of the post-contrast data sets.

6.5 Segmentation Accuracy Conclusions

One of the main aims for this chapter and for chapter 5 was to determine the effect of segmentation accuracy on realignment accuracy. More specifically it was intended to use this data to determine the segmentation accuracy required to accurately correct for patient head motion between pre and post-contrast 3D scanning. Chapter 5 investigated this by producing an idealised phantom data set which could be rotated and translated by known amounts allowing the accuracy of the realignments to be compared to a gold standard. This chapter continued these investigations but on real pre and post-contrast data, which despite the data sets differing by unknown rotations and translations, allowed real world effects on realignment accuracy to be examined.

The first overall conclusion that could be drawn from these two studies was that varying segmentation volume and thus segmentation accuracy did indeed have a measurable effect on the resulting realignment parameters. In some cases, as has been displayed in the resulting graphs, small changes in segmentation volume resulted in large changes in realignment parameters. This is especially true for the patient data where noise appears to introduce random errors into the realignments. The exact

nature of the noise effects is likely to vary from patient to patient and from study to study, due to the varying nature of noise in MRI.

The results from chapter 5 indicated that the realignment accuracy reduced for data sets that were under-segmented (>100%), suggesting that the presence of contrast-enhanced data in the segmented realignment volume was contraindicated for optimal alignment of pre and post-contrast data. Therefore, any segmentation algorithm applied to these data sets will be required to remove as much of the contrast-enhancement as possible.

Ensuring the segmentation volume does not contain contrast-enhanced structures is non-trivial. The pre-contrast data set is a simpler data set to segment due to the lack of confounding contrast enhancing structures. Chapter 4 (section 4.1.3.4) described some of the algorithms capable of segmenting such data sets. The segmentation algorithms typically have segmentation errors of about 2% (Lemieux *et al* 2003, Stokking *et al* 2000). Due to the close proximity of the veins to the brain parenchyma, and the similarity of the venous signal to grey matter signal in the pre-contrast data, a significant amount of these segmentation errors are likely to result in venous inclusion within the segmented data. It is impossible to use the post-contrast data set to determine the venous voxels as it is not correctly aligned to the pre-contrast data. Therefore to ensure that the volume used for the realignment does not contain any regions of contrast enhancement the post-contrast data set must be used.

Currently there are no segmentation algorithms designed to segment brain parenchyma from contrast-enhanced 3D data sets. It is therefore important for any segmentation algorithm that is to be developed for, and applied to the post-contrast data, to ensure that it fully removes the contrast enhanced data. Ensuring that all

contrast-enhanced voxels are removed is likely to result in over-segmentation of the post-contrast data.

The level of accuracy required would affect the method of automatic segmentation used to produce the realignment volumes. For example if a high level of segmentation accuracy was required, i.e. within 2 or 3% of trained observer estimates, this would require very accurate modelling of the data using complicated segmentation algorithms. Such methods were described in chapter 3 (section 4.1.3.4). However, with increasing accuracy there would also tend to be a higher segmentation failure rate due to any large variations from the expected brain model. For example if there was a large enhancing tumour (such as in patient 2), which is a space occupying lesion, this may confound the model resulting in poorly segmented data.

If segmentation accuracy was not required to be as accurate as 2-3% then it might be possible to devise a segmentation algorithm that would cope better with unusual data sets. The ability to process a wider range of data sets would be advantageous, removing the requirement to assess image data sets for suitability prior to attempting the segmentation and realignment protocol. This improved applicability would likely be offset against poorer registration accuracy, however, if accuracy was only slightly affected then the benefits would outweigh the cost.

Examining the signal to noise parameters first, for the phantom data and for the two patient data sets, signal to noise is at its highest value at 100% except for graph 5.2. This confirms that the observer based segmentations are at or very close to the optimum segmentation volume for realigning the data sets. Signal to noise below 100% remains steady for both patient 2 and for both the transformed and non-transformed phantom data sets with only a very slight drop in signal to noise for

patient 2 for the smaller segmentation volumes. There are more significant falls in signal to noise for patient 1 especially at the very smallest volume used.

Due to the same post-contrast data set being used for patient 1 and the phantom data it is possible to assign the drop in signal to noise detected for the lower segmentation volumes to noise differences between the pre and post-contrast data. These noise differences have a strong local effect that dominates at the lower segmentation volumes. Therefore, it can be concluded that very small realignment volumes should not be used due to the increased influence of data noise differences. This conclusion is also strengthened when the realignment parameters are examined in the patient data sets, especially those demonstrated in graphs 6.9(a & b), where larger variations are detected at the smaller segmentation volumes.

However, for segmentation volumes of more than 80%, in all cases the signal to noise remained within 0.5% of the maximum signal to noise value. From the signal to noise data alone it would appear that segmentation volumes that contain no contrast enhancement and contain not less than 80% of the brain parenchyma would produce sufficiently accurate final subtraction data sets. This suggests that good quality realignments can be achieved when segmentations of 80% to 100% accuracy are used in conjunction with the MATCH algorithm

The phantom data realignment parameters are consistent with this conclusion, however, it is not obvious from viewing the patient data realignment parameters on their own that this is the case. For both patient 1 and 2 there were more significant variation in the realignment parameters for segmentation volumes of 100% and less (see graphs 6.2 (a & b) and 6.7 (a & b).

However, by comparing the phantom and patient 1 results it was shown that the variations were almost exclusively due to the noise differences between the pre

and post-contrast data sets. As has been previously discussed these noise differences cannot be simply modelled and corrected for. The differences will also vary from subject to subject and from scan session to scan session. It is therefore likely that for the majority of patient data sets that the underlying trend of realignment accuracy is similar to the phantom data results with further modulation of the realignment parameters as a result of the noise differences between the pre and post-contrast data. It was likely, therefore, that the patient 2 data was modulated by the noise differences in the same manner. Despite this the overall translation parameter (graph 5.7(b)) did follow the expected trend with translation varying little for segmentation volumes below 100%.

It should be further noted that the scanner used in this thesis was installed in 1993. Signal to noise from this scanner is significantly lower than for the newest generation of scanner. For example a typical signal to noise (white matter to background noise) value for a good MP-RAGE scan from the scanner used for this study was 17. This compares poorly for an equivalent sequence from a newer scanner within the department using a similar type of sequence (IR FSPGR) which has a typical signal to noise around 44. Therefore, due to the improvements in signal to noise in modern scanners it is likely that the modulation of the realignment at segmentation volumes below 100% will not be as significant as it was in this study. However, some noise sources cannot be reduced by improved technology alone, and will continue to modulate the data.

The results discussed here are specific to cerebral imaging and to one particular contrast agent. However, these results and conclusions have implications in any situation where data sets, which are collected within the same imaging session, are used to compute an overall result data set. Such realignment corrections are

common in areas such as fMRI where a large number of data sets are collected and realigned using simple and fast realignment algorithms (Jenkinson *et al* 2002, Ashburner & Friston 1997). These algorithms do not attempt to segment the brain parenchyma for realignment purposes due to processing time constraints. Also despite the changing signal from brain parenchyma itself in the T2* sequences used to detect the BOLD signal, the algorithms do not attempt to remove realignment accuracy modulation due to these fluctuating signals. It has been shown in this thesis that where signal varies significantly between data sets significant errors in realignment can result. FMRI techniques are constantly being improved and it is likely that over time signal to noise will increase, resulting in more significant contrast differences between the scans requiring realignment. Significant errors in realignment may result.

Currently the simple realignment algorithms are acceptable due to the typically low resolution of these data sets and the small size of the BOLD signal changes. Voxel dimensions are of the order of 3mm cubed and the data is commonly smoothed by Gaussian filters of about 6mm. Therefore, small errors in realignment are unlikely to be significant. However, as fMRI resolution increases with advances in technology and technique these issues will need to be addressed.

6.6 Implications in Designing an Automatic Segmentation Algorithm

The next chapter aims to design an automatic segmentation algorithm that enables pre and post-contrast data to be accurately aligned whilst remaining robust enough to work with real clinical data sets that will vary significantly in their nature.

This algorithm must completely remove contrast enhanced data and should also remove extra-parenchymal data to keep the errors in the realignment to a minimum. The segmentation of the brain should be as accurate as possible, although it is acceptable to over-segment to ensure that all of the contrast-enhancement is removed. Therefore, the next chapter aims to design a segmentation algorithm taking into account the findings of this chapter.

Chapter 7

Development of Automatic Segmentation Realignment and Subtraction Algorithm

7.1 Introduction

7.1.1 Overview

Previous chapters have investigated the segmentation requirements for the accurate realignment of pre and post-contrast 3D data sets. The aim of this chapter is to use this information to develop an automated segmentation algorithm for these data sets. This chapter also aims to produce a fully automated algorithm that can produce subtraction venogram data when supplied with the raw pre and post-contrast data sets. Following production of these data sets it would be possible to view the cerebral venous structures using maximum intensity projection (MIP) software in 3 dimensions.

To determine the effectiveness of this algorithm in producing correctly aligned and segmented data sets, in chapter 8 the outputs from the automatic algorithm will be compared to subtraction data sets produced using manual segmentation. This will determine the effectiveness of the algorithm using clinically relevant data sets.

Therefore, a method will be developed that is specifically designed for these contrast enhancing data sets but based on the morphological techniques described by Höhne & Hanson 1992.

As well as requiring a segmentation volume for realignment purposes, a second volume is required to define the subtraction data that should be used for the final MIP visualisation. The production of this secondary volume will also be addressed.

The algorithm in this chapter has been written by the author and is being used to segment post-contrast data which is a novel application. The automatic production venograms using this technique is also, as far as the author is aware novel. The data acquisition was performed by radiographic staff.

7.1.2 Rational For a New Algorithm

As has been described previously (see section 4.1.3) there are a number of possible methods of segmenting the brain from surrounding tissue. However, a number of these are likely to fail where there is significant enhancing pathology or significant variation in normal anatomical enhancement. For example probabilistic clustering methods (Barra & Boire 2000, Fischl *et al* 2002) require the brain to be normal or close to normal in its morphology. With contrast enhancing lesions present these techniques are unlikely to be able to take account of such variations. Methods that depend on modelling of the brain (Lemieux et al 1999, 2003) are also likely to fail where the anatomy is grossly affected by enhancing lesions.

However, morphological techniques such as those based on the work of Höhne & Hanson (1992) have enough flexibility to enable them to be developed for the purposes of this study. Recently these techniques have been extended to produce an automatic segmentation technique (Stokking 1998). Both techniques use a seed point and threshold followed by morphological operations to separate the linkages of the brain from the surrounding tissue. Stokking devised a method of determining the seed point and thresholds automatically (CACTUS). The seed point was detected by first examining the data histogram to find a reasonable signal value for grey matter

and thresholding all data above this value. This was then eroded twice and using a spherical search from the middle of the data set the first encountered point within the seed volume is set as the seed point. Following this Stokking devised an algorithm to detect the lower and upper bounds of the threshold to apply the morphological operators on.

Although the CACTUS technique works well on typical 3D T1 data, the technique would run into problems when used on post-contrast data. For example, it is the aim of this study to produce a segmentation procedure that can segment data sets that have enhancing abnormalities as well as those that have normal enhancing anatomy. Large enhancing tumours could, depending on their size and position, confound the algorithm resulting in poorly defined threshold values. It also likely this technique would result in contrast-enhanced data remaining within the segmented volume. Therefore a new protocol was required.

Before a protocol could be devised it was important to determine what was required from it. Therefore, an overview was devised detailing the requirements for the final automatic procedure. The protocol was divided up into a number of sections:

1) Load the pre and post-contrast data sets
2) Segment the post-contrast data set to a good accuracy ensuring that no enhancing structures are contained within the final segmentation mask
3) Produce a second mask containing all structure of interest (e.g. brain and enhancing vessels) but excluding unwanted structures (e.g. skin and muscle) to enable good quality MIP visualistion after final subtraction.
4) Use the segmented volume within the MATCH algorithm to determine the realignment parameters to best align the pre and post-contrast data sets.

5) Apply the realignment parameters to the pre-contrast data set and reslice using SINC interpolation
6) Subtract the pre and post-contrast data contained within the mask produced in section 3.
7) Use generic MIP visualisation software to allow the cerebral venous system to be visualised in 3D.

The aim of this chapter is to devise a step by step protocol following the above overview steps using Analyze (Mayo Clinic) software. Having achieved this, this study then attempts to devise a fully automated algorithm using the IDL (Interactive Display Language, Research Systems, CO, USA) image processing language.

The two most important sections within this plan, with regard to this study, are sections 2 and 3. Section 2 aims to segment the post-contrast data set to a standard described in the previous chapter. This segmented data set will allow the realignment to be made with respect to structures that do no change between the pre and post-contrast data sets.

Section 3 aims to produce second mask. This mask is required to enable good quality visualisation of the venous structures. This is achieved by producing a mask that contains all of the required venous structures within it. If this mask was not produced this would result in reduced signal to noise in the final MIP visualisations.

As has been previously described contrast enhancement occurs in structures other than those of interest within the head. These include skin and bone marrow. The realigned pre-contrast data set contains all of the structures within the head that were present in the original pre-contrast data set. Thus, if this were subtracted from the post-contrast data set (which also contains all of these structures, along with any

enhancement) and is viewed using a MIP, the overlying structures, such as the skin would obscure the structures of interest. In this respect this extracranial enhancement introduces noise into the MIPs.

Further problems would arise from venous vessels contained within the head, but not contained within the brain parenchyma. When investigating cerebral venous disease these vessels are often of little or no interest for clinical diagnosis. However, if no mask were used to determine the MIPs area of interest these vessels would be included in the final MIPs. Due to the varying nature of the venous system it is possible that these structure could be misinterpreted as cerebral vessels, especially when single view MIPs were used. With access to 3D rotateable MIPs overlying vessels become more distinguishable from cerebral vessels, however, it is still possible that these vessels would obscure areas of interest and would introduce unnecessary difficulty into the reporting process.

Therefore, it was important to produce a second mask that would only contain cerebral parenchyma and cerebral vessels serving the cerebral parenchyma, thus simplifying the reporting procedure and improving the quality of the final MIP data.

The following sections describe the design of an algorithm that fulfils the requirements for automatically producing MPRAGE subtraction venograms.

7.2 Methods - Analyze Protocol

7.2.1 Introduction

Before the IDL algorithm could be developed a protocol was devised using the Analyze software package. This software package provided a user friendly graphical interface that contained a number of image analysis modules, including filtering and morphology. It was possible using this software package to devise and develop the techniques required for correctly segmenting the post-contrast data for realignment purposes and also to create the mask used to produce the final subtraction image. The following sections describe the procedures used to determine the best protocol for achieving the automatic production of good quality subtraction venograms. Testing and designing the algorithm protocol with a software package such as Analyze enabled faster evolution of the design at the macro programming level without the initial requirement for time consuming programming and debugging.

7.2.2 Devising the Paradigm Protocol

As described earlier in this chapter the most important aspect of the new algorithm is its ability to segment the brain parenchyma and to produce the final subtraction mask. Often segmentation algorithms are devised with very specific MRI data sets in mind. Some algorithms are also specific to particular scanner characteristics (see section 4.1.3). However, it is the intention of this study to

produce a segmentation algorithm that can be easily adapted for use on other scanners with different methods for producing 3D T1 data.

Despite the differences in scanner characteristics and pulse sequences available, there are always a core set of sequences that are common to all scanners. These include T1-weighted spin echo , T2-weighted spin echo, gradient recalled and more recently echo planar sequences. All currently available neurological MR scanners also have access to T1-weighted 3D sequences which are often the sequence of choice for high resolution 3D structural imaging. For example the scanner used in this study is a Seimens 1.5T scanner which uses the MP-RAGE (Brant-Zawadzki *et al* 1992) pulse sequence. GE scanners use a different sequence called IR Fast- SPGR. This sequence is very similar to the MP-RAGE sequence in its use of an inversion recovery pulse to produce the T1 weighting. However, due to the different core sequences used (FLASH v's SPGR) there are differences in overall contrast characteristics and signal to noise. These sequences also require different inversion recovery times to produce similar grey and white matter contrast

There are similar sequences available for other makes of scanner and these are displayed in table 7.1.

Manufacturer	Magnetisation Prepared GRE
Generic	snapshot FLASH
Elscint	V-SHORT/ Turbo-SHORT
GE	IR-SPRG/ IR-FSPRG
Hitachi	RS (Rapid Scan)
Philips	Turbo (T)FE
Picker	RAM-FAST
Shimadzu	SMASH
Siemens	Turbo-FLASH/ MP RAGE

Table 7.1: Examples of similar magnetisation prepared GRE sequences from different manufacturers

Despite the differences between the sequences there are a number of consistent properties of these sequences that can be exploited to accomplish good quality segmentation for all of them.

The following protocol and algorithm were devised using five pre and post-contrast data sets that were selected at random from a list of available data sets that did not contain significant motion artefacts.

7.2.3 Inhomogeneity Correction and Histogram Operations

Before any post processing analysis is conducted on the data it is important to remove inhomogeneities from the MR images. Signal inhomogeneities are likely to result in poor tissue segmentation (Zhou *et al* 2001). Inhomogeneities can be caused by radio frequency (RF) pulse attenuation in tissue, non-uniform RF coil transmission and sensitivity, non-uniformity in the MR scanner's main magnetic field, gradient-induced eddy currents, RF standing waves, magnetic susceptibility of tissue and interslice cross talk (Condon *et al* 1987, Simmons *et al* 1994).

There are a number of post-processing approaches to correcting for such inhomogeneities (Studholme *et al* 2004). However, these are often complex or model based techniques and it remains uncertain as to how these methods would be affected by the presence of contrast enhancement. As far as the author is aware there is no published data on the applicability of inhomogeneity correction in post-contrast data.

Homomorphic unsharp masking (HUM) is a technique that functions to a first approximation as a band notch filter, where a certain spatial frequency range in the data is removed, and was first proposed by Axel *et al* (1987). This method assumes that the majority of RF inhomogeneity within the data results in low frequency signal

variation. Thus by convolving the data with an appropriately sized mean kernel, it is possible to remove the low frequency RF variation. It is a simple method to apply and if used with the correct filter size (Brinkmann *et al* 1998) produces good results with a variety of sequences.

Brinkmann showed that so long as the mean in a local window matches the global mean of the overall image that the HUM technique results in good inhomogeneity correction. This was found to be approximately true for large kernel sizes which would enclose a representative sample of tissues, where different tissues were found to intertwine in close proximity. This is true for pre-contrast data and is also true of post-contrast data where the enhancing vessels or lesions are contained within or close to the brain parenchyma. It has also been shown that using this technique results in mean histogram values for each tissue component that are not significantly altered following correction.

Therefore, the first post-processing step applied to the data was an inhomogeneity correction based on the techniques described by Brinkmann. For all of the following work the kernel size was set to 65 x 65 and was applied before any histogram operations.

One of the most important consistent properties between the sequences described in section 7.2.2 is the overall shape of the data's histogram of voxel intensity values. If it is assumed that all histograms have the same shape characteristics, and from these characteristics it is possible to determine parameters that describe the voxel values of the various features of the histograms, it should be possible to determine initial segmentation thresholds that will allow further segmentation procedures to be utilised.

There are a number of features that are present in T1-weighted post-contrast histograms that will allow the initial stage of segmentation processing to occur automatically. Graph 7.1 demonstrates a typical histogram from the Siemens Magnetom running a post-contrast MP RAGE sequence for a patient with normal contrast-enhanced MR anatomy.

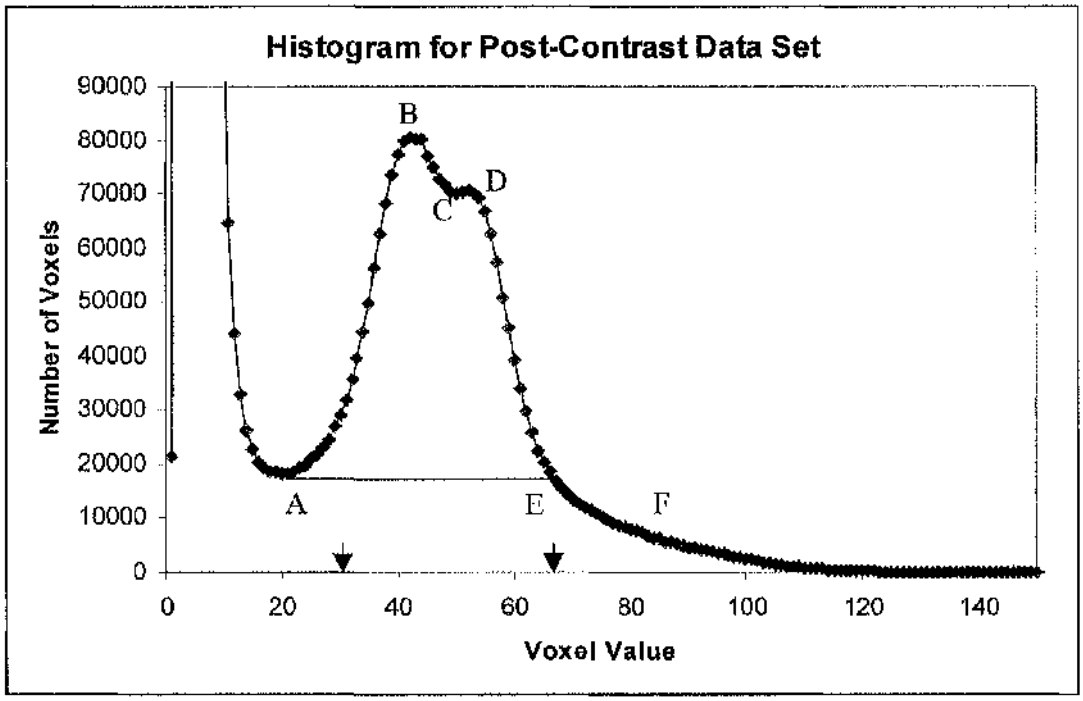

Graph 7.1: Example histogram for a post-contrast data set. (Siemens Magnetom MP RAGE). The minima and maxima of interest have been labelled and the calculated thresholds have been labelled with arrows.

The first feature of this histogram is the high pixel count for low voxel values. This area of the histogram almost exclusively originates from voxels outside the patients head, i.e. from the surrounding air. There are no materials here to produce any contrast with the MP RAGE sequence and so this part of the histogram relates purely to scanner noise.

The second feature is the drop from the large number of voxels to a much smaller number for higher voxel values. This produces a minimum (A) in the histogram data. This region contains a much smaller contribution from pure noise voxels and will consist mainly of voxels within the CSF and other low signal structures such as bone.

With increasing voxel signal values the number of voxels increases to the first maxima (B). The vast majority of voxel data here will originate from structures with low to intermediate signal. These structures will include muscle and other connective tissues, skin, non-enhancing veins, and parenchymal grey matter. With increasing signal values the voxel count decreases until there is second minimum (C). This minimum occurs at the overlap between grey and white matter voxel values. Voxel values contained within the second peak (D) mainly represent the parenchymal white matter with some contribution from skin, muscle, and connective tissue.

At higher values (above voxel value of 70 for this example) there is a tail to the histogram (E). This tail result from voxels containing high flow vessels (arteries), fat and the contrast-enhanced vessels.

The exact range and separation of these features will vary from system to system and from subject to subject. There will also be slight variations in the flow characteristics of the sequences depending on the pulse sequence parameters, however, the overall shape of the histogram will remain the same. Therefore, it should be possible to use these features to determine threshold parameters, allowing an initial stage of image segmentation to be conducted on the post-contrast data sets. Graph 7.2 shows equivalent histogram result from a General Electric IR-FSPGR sequence. The General Electric histograms do show some different characteristics, such as higher signal values for the grey and white matter. However, it is very likely

that these changes form a particular signature depending on the sequence and type of scanner used. Therefore, histograms operations applied to the MP RAGE data sets in this thesis will require some tuning for each system and sequence used.

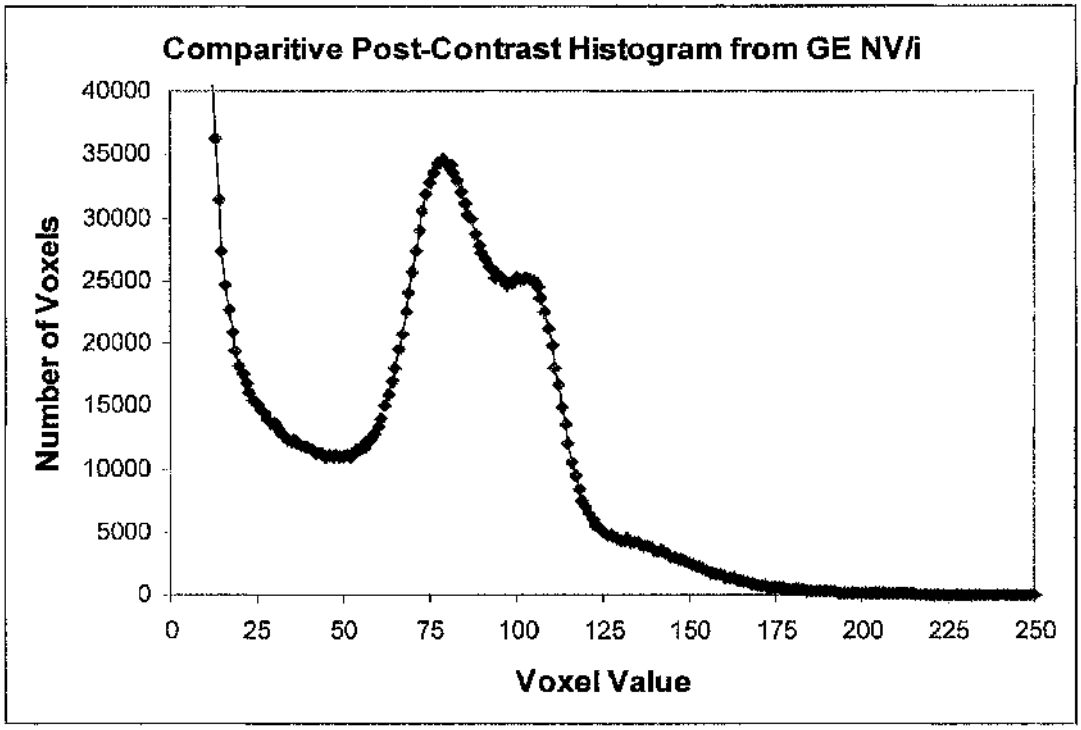

Graph 7.2: Comparison post-contrast histogram for a General Electric acquired 3D volume (IR-FSPGR)

For each of the training data sets appropriate thresholds were determined to correctly threshold the grey and white matter in the brain, whilst avoiding the inclusion of contrast-enhanced vessels. However, in all cases a compromises was required due to the overlap in signal intensities of the white matter and enhancing vessels. Due to the requirement to remove contrast-enhancement the thresholds were set such that little or no such vessels were included. This inevitably resulted in some loss of white matter.

Having determined the optimal threshold levels for these data sets their histograms, following inhomogeneity correction, were examined to determine if the

thresholds set could be related to histogram features, thus providing a means for calculating the thresholds automatically.

After examining all of the data sets, it was determined that acceptable threshold levels (max and min) could be set for the brain parenchyma using the following algorithms:

$$T_{\min} = 1.5 * V_{\min} \tag{7.1}$$

$$T_{max} = V_{fmin} + V_{fmax} \tag{7.2}$$

where T_{min} and T_{max} are the minimum and maximum thresholds respectively, V_{fmin} is the first minimum in graph 7.1 (A) and V_{fmax} is the first maximum in graph 7.1 (B).

For four of the data sets used for training purposes equations 7.1 and 7.2 resulted in good brain parenchyma thresholds. However, for one data set significant numbers of white matter voxels would have values beyond the threshold maximum calculated in this way. To account for this the protocol was adjusted.

The data set used to produce the histogram in graph 7.1 required this revision. In this data set equations 7.1 and 7.2 would provide thresholds of $T_{min} = 30$ and $T_{max} = 62$. T_{max} was increased until the related voxel count was below the voxel count at point (A) providing the new threshold at point E ($T_{max} = 67$). Figure 7.1 shows some example slices from the related threshold mask.

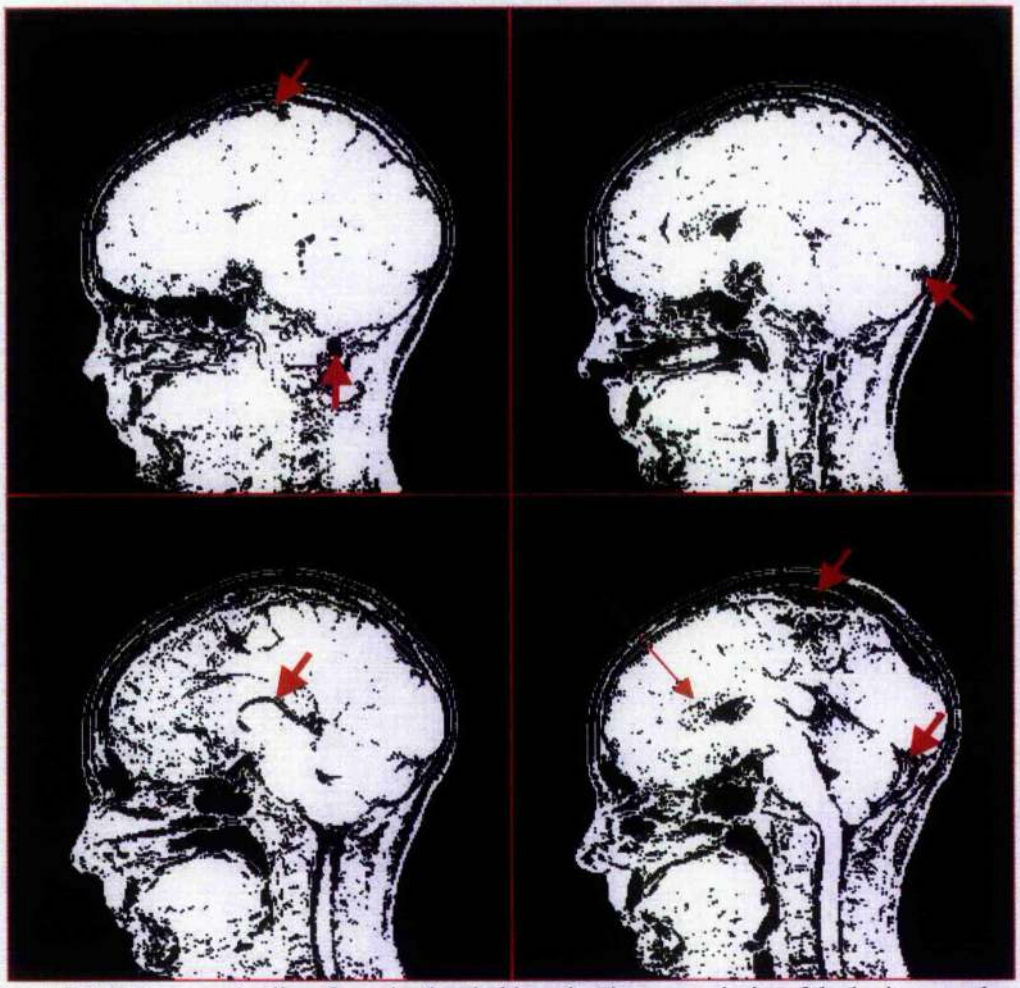

Figure 7.1: Four example slices from the threshold mask. The vast majority of the brain parenchyma is included in the mask with the exception of some white matter (thin red arrows, corpus callosum). The mask excluded contrast enhancement (thick red arrows)

Therefore, the final protocol would first apply equations 7.1 and 7.2, it would then compare the voxel count at point A with the voxel count at T_{max} and if point A had a lower voxel count, T_{max} would be increased until its voxel count fell below the voxel count at A. In all cases this produced a good threshold that excluded contrast enhancement.

7.2.4 Morphological Operations – Separating the Brain

Threshold segmentation is very poor at separating brain parenchyma from other structures when used on its own. Therefore, the binary mask produced was used as an initial approximation upon which further processing could occur.

After the data had been thresholded it was necessary to separate the grey/white matter structures from the remaining data that was included within the threshold segmentation. A simple, yet robust method for achieving this is by using morphological operators (Höhne & Hanson 1992).

In attempting to separate large connected binary structures there are a number of fundamental morphological operators that are required. These are ERODE, DILATE and CONNECT. The effect of these operators on binary data sets are described in Höhne & Hanson.

The first step in separating structures is to apply a 3D ERODE operator to the data set. This operator works by erasing voxels that have few surrounding voxels in any of the three dimensions. Therefore, if two structures are connected only by a thin 3D bridge of voxels, using the erode command would remove this bridge, separating the structures. When the data has been thresholded, connections will remain between the brain parenchyma and other tissues. So long as the connections have fewer connected voxels than the brain parenchyma then the connections would be eroded more efficiently than the brain voxels thus disconnecting the brain from the surrounding tissue.

To further improve the likelihood of separating the brain and other structures it is possible to apply a LOW PASS FILTER using a 3x3x3 kernel. This filter removes voxels within areas where the rate of change of voxel values is larger than a

predetermined value. In the case of binary data it determines the number of surrounding voxels with value 1 and if the number of these voxels is above a particular threshold the central voxel is set to 1. This operation first involves convolving the binary data with a 3x3x3 kernal of voxels with each element having a value of 1, and thresholding the resulting data set. For a 3x3x3 kernal the threshold would lie between 0 and 27.

Setting the threshold to a low value, for example 3 would set the central value to 1 when more than 3 of the voxels of the thresholded binary map from the previous section, had values of 1. Otherwise the central voxel would be set to zero. Such a value would remove only very thin connections and would increase the overall size of the output binary mask. Likewise setting the kernel threshold to a large value close to 27 would result in a significant amount of the original binary mask being set to zero. Therefore, a more central value (for example 15) would result in little change in overall size of the binary mask but connections, where voxels have less than 15 surrounding voxels with the value of 1, would be set to zero thus removing such connecting structures.

Despite the efficiency of the two operators at removing connections some thicker connections will remain in certain data sets. To remove these thicker connections it is possible to apply a second ERODE operation to the data to ensure disconnection.

One major problem with using ERODE is that it does not leave the connected objects unchanged. Due to the nature of the ERODE operator the objects themselves will shrink in size and any large holes within the eroded object increase in size. Therefore, further operations need to be applied to regain the original shape and size of the object after the objects have been successfully separated. The FILTER

operation also has an effect on the size of the connected objects, however, if the FILTER threshold is selected carefully then this effect is minimal.

Before the reshaping operations are applied the CONNECT operator can be used to give the objects that have been disconnected different voxel values, allowing the objects to be described separately. For example one object would be given a value of 1, another 2 and so on resulting in an object map. By producing this object map it is possible to compare the sizes of the various objects produced and to make decisions based on the outcome of these measurements.

It was described previously that thresholded head data sets contain structures other than the brain parenchyma which is of interest. After thresholding the T1 weighted 3D data sets, the brain parenchyma almost inevitably remains connected to other structures such as muscle, orbits etc, due to the similarity in signal from these structures when using such a T1 weighted sequence, and the close proximity to the brain parenchyma. Thus as described previously the ERODE operator must be applied until the brain has been separated from the remaining tissue. However, due to its effects on the shape and size of the binary object, it is preferable to apply ERODE a minimum number of times and indeed only once, where possible. Therefore, a method of determining the number of ERODEs necessary to separate the structures is required.

Due to the nature of T1-weighted 3D imaging there are two large areas of similar signal characteristics; the brain parenchyma and inferior to this a large area of muscle, tongue, and skin within the region of the neck. Following erosion to separate the brain from other structures this second region often remains as a slightly smaller connected object.

Initially following the thresholding of the data, one ERODE/FILTER operation is applied. A CONNECT operation is then applied to the data giving each separate object different voxel values. The two largest objects are selected and the relative size of these objects is compared. If the ERODE/FILTER operation has separated the brain correctly the two objects should be of similar volume, with the larger being the brain parenchyma and the smaller object consisting of muscle etc from the subjects neck (see figure 7.2).

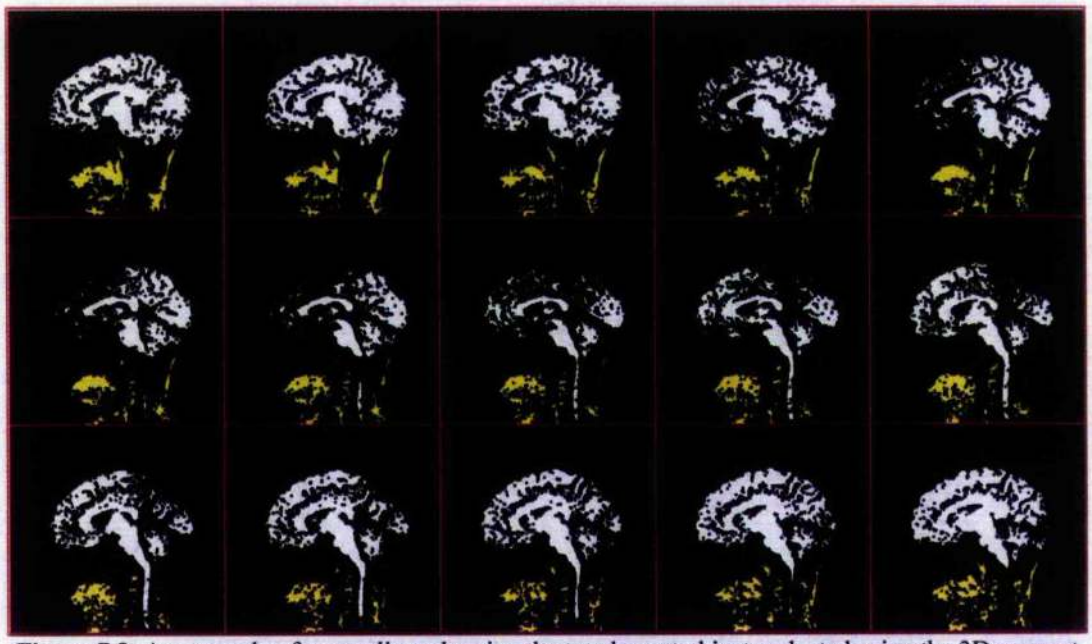

Figure 7.2: An example of some slices showing the two largest objects selected using the 3D connect operation. The brain (white) is the larger if the two objects. The second object is a mixture of tissues inferior to the brain (yellow)

If the difference in size between the largest and second largest object is large this suggests that the first ERODE/FILTER was not sufficient to separate the brain from the remainder of the head tissue. The smaller object in this case would be an unspecified area of extracranial tissue that was only slightly connected to the remaining extracranial tissue. Thus, a second ERODE is applied to the data set and the same procedure of checking is reapplied.

In the vast majority of cases this procedure would allow the brain parenchyma to be separated and correctly identified. However, the assumption that the brain object will always be larger than the extra-cranial object does not always hold true. In general this assumption is correct due to the less contiguous nature of the thresholded data outside the brain parenchyma. When an erode is applied to such data with a large number of holes the volume of the output is greatly reduced due to the increasing size of the holes. The brain parenchyma, on the other hand has a more uniform signal intensity and thus after thresholding does not contain as large a number of holes.

Due to the conservative thresholds used in this protocol some white matter holes will exist and therefore it cannot be guaranteed that this assumption is always true which was indeed discovered when applying early versions of this protocol to test data sets. In certain data sets there was an object comprising of neck muscle, tongue, skin and bone marrow, inferior to the real brain object that was larger than the brain object itself. If object selection was purely based on object size then the neck object would on occasion be selected instead of the brain object. Therefore, it was important to account for this possibility and correct for it.

The correct selection of the brain object can be achieved by analysing the overall voxel positions within the two largest objects. The brain object would have an average pixel position superior to the neck object. Therefore, when designing the algorithm it would be possible to test for this. Using Analyze it was possible to accomplish this visually, however, in the final IDL algorithm this test could be fully coded and so automated.

7.2.5 Morphological Operators – Producing the Final Brain Mask

After the brain object has successfully been separated from the rest of the thresholded data, the object must be 'reshaped' back to the original shape of the brain parenchyma. The morphological operator used to achieve this is the DILATE operator. It has been previously been determined, through experience (Stokking 1998) that when using DILATE operators following EROSION that one extra DILATE operations should be used when compared to the number of ERODES. However, for this study due to the stringent application of histogram thresholds it was found from testing that two additional DILATES were required. An example of a shape that has been eroded and dilated the required amount of times is displayed in figure 7.3.

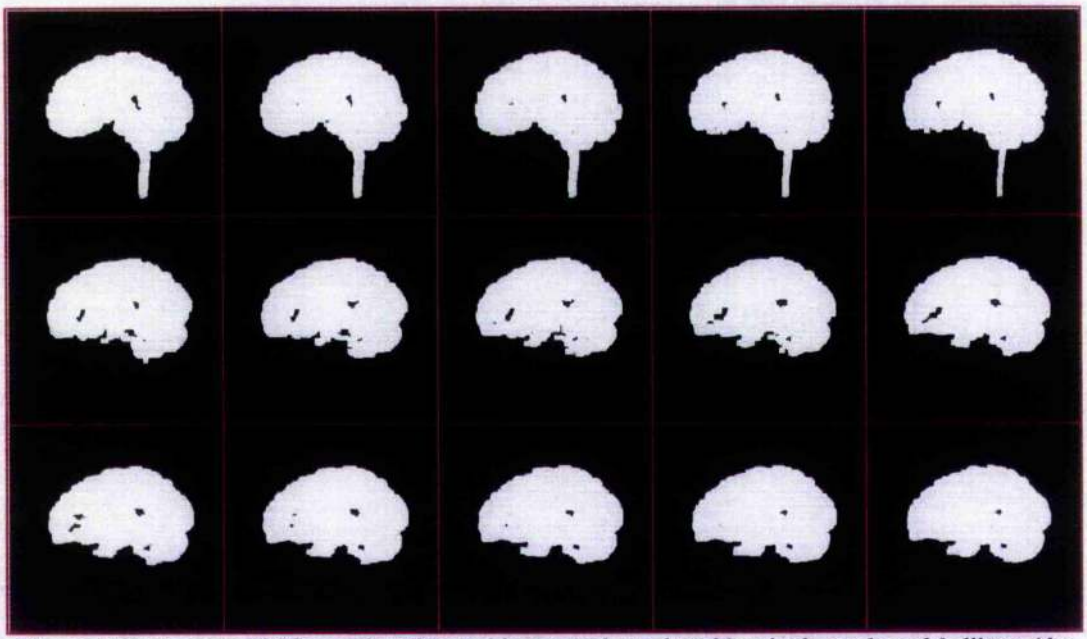

Figure 7.3: Example of fifteen slices from a binary mask produced by single erode and 3 dilates (the brain has been separated).

Figure 7.3 illustrates that although the overall volume associated with the object is restored the outline is poorly reproduced. This is due to information loss during the ERODE operations. To compensate for this the DILATE operator can be adjusted to take account of the original threshold mask. This CONDITIONAL DILATE does a normal DILATE on the data and then multiplies the result with the thresholded output. Therefore, any data that was not originally thresholded but was contained within the DILATED data result is removed. This ensures that the final DILATED data reflects the overall outline of the brain parenchyma in the thresholded data. It also ensures that none of the enhancing voxels are included in the realignment mask which is important to ensure accurate realignment.

One problem with this approach is that it is possible to DILATE into data that is not part of the brain parenchyma, but is within the threshold mask. This occurs at points where the brain parenchyma is connected to the other objects in the threshold data (the data bridges). However, if the number of DILATES are kept low (which can be achieved by keeping it limited to two plus the number of erodes) then the amount of extra parenchymal tissue included would be minimal.

Once the data has been CONDITIONALLY DILATED the required number of times the resulting mask is a representation of the brain parenchyma. This mask is saved and is called the realignment mask as it can now be used to define the area that the MATCH software uses for its realignment.

This mask would then be multiplied with the post contrast data set producing the segmented brain required in the MATCH software to determine the volume used for calculating the realignment. As has been described previously this protocol would not produce a 100% accurate segmentation of the brain parenchyma, but importantly it should contain little or no contrast enhanced data, and should be of high enough

quality that a good quality realignment would occur. This quality of the realignment will be investigated in chapter 8.

7.2.6 Production of MIP Visualisation Mask

As was described in section 7.1.2 a second mask is required to allow the final MIP to be produced. This mask should ideally contain brain parenchyma and its associated veins and arteries only. Therefore the second mask will be larger than the first mask, although care must be taken to ensure that as little extracranial tissue as possible is included within it to keep the final signal to noise of the resulting MIPs as large as possible.

The first step to producing this mask is to construct a data set that maps the distribution of the CSF within the head. This is achieved in a number of steps. Firstly the original data is re-thresholded. The minimum threshold is set to 1 and the maximum threshold is set to twice the minimum threshold previously calculated. This thresholded data set will contain data from noise outside the head, from CSF, and from other low signal structures within the head such as bone, the sinuses and the eyes. Importantly the data directly surrounding the brain parenchyma is almost exclusively CSF. The thresholded data is complimented, that is any voxel with the value 1 becomes zero and vice versa. This is then morphologically filled so that all voxels contained within the mapped region are set to a value of 1 and all those outside are set to zero. This data is then multiplied with the thresholded CSF/noise data to produce a map of CSF and other structures (see figure 7.4). For simplicity this mask is called the CSF mask.

Figure 7.4: Fifteen example slices from a CSF mask. It should be noted that the mask contains other highlighted structures such as the sinuses, bone and the eyes.

The segmentation mask produced earlier is then dilated using the CSF mask as a condition 12 times (this value was derived empirically using the 5 training data sets). This allows the dilation to spread to the surrounding CSF but not significantly to other structures such as the bone and sinuses. To finish the mask it is once again morphologically FILLED so that all the voxels contained within the brain parenchyma and the surrounding CSF are included in the final mask. This will also include the venous vessels on the surface of the brain and any vessels within the brain parenchyma itself. Using this method also ensures that any venous vessels not in direct contact with the brain are included within the mask. This was important as the superior sagittal sinus was found in some subjects to not always be adjacent to brain tissue. This technique also ensures that no data beyond the CSF that contains contrast enhancement is contained within the final subtraction data set.

Once the MATCH software has realigned the data using the brain segmented volume, the visualisation mask can now be multiplied with the realigned pre and

post-contrast data. The mask prevents the inclusion of extracranial enhancement from being included in the final subtraction data thus improving the resulting signal to noise and removing structures that might otherwise obscure the structures of interest.

Following subtraction the data can be viewed using any 3D software package with the ability to display maximum intensity projections (MIP's). Due to the 3D nature of the data sets it is possible to use software to rotate these MIP's in real time to allow the data to be viewed from a number of angles.

The individual Analyze based steps of the constructed protocol are listed in Appendix 2. Figure 7.5 displays a flow diagram highlighting the main features of the protocol.

Having devised these steps it was now possible to start developing a program to conduct these step and prove the concept that it was possible to achieve the segmentation of these data sets in an automatic manor. There are a number of programming languages available which could be used to write the appropriate segmentation algorithm. One very common language used to produce similar algorithms is C or C++. It is possible with the use of optimised compilers to produce executable code for a number of computing platforms. This language is very good at producing fast and reliable code. However, programming in C can be cumbersome with a large amount of programming required even for relatively simple tasks.

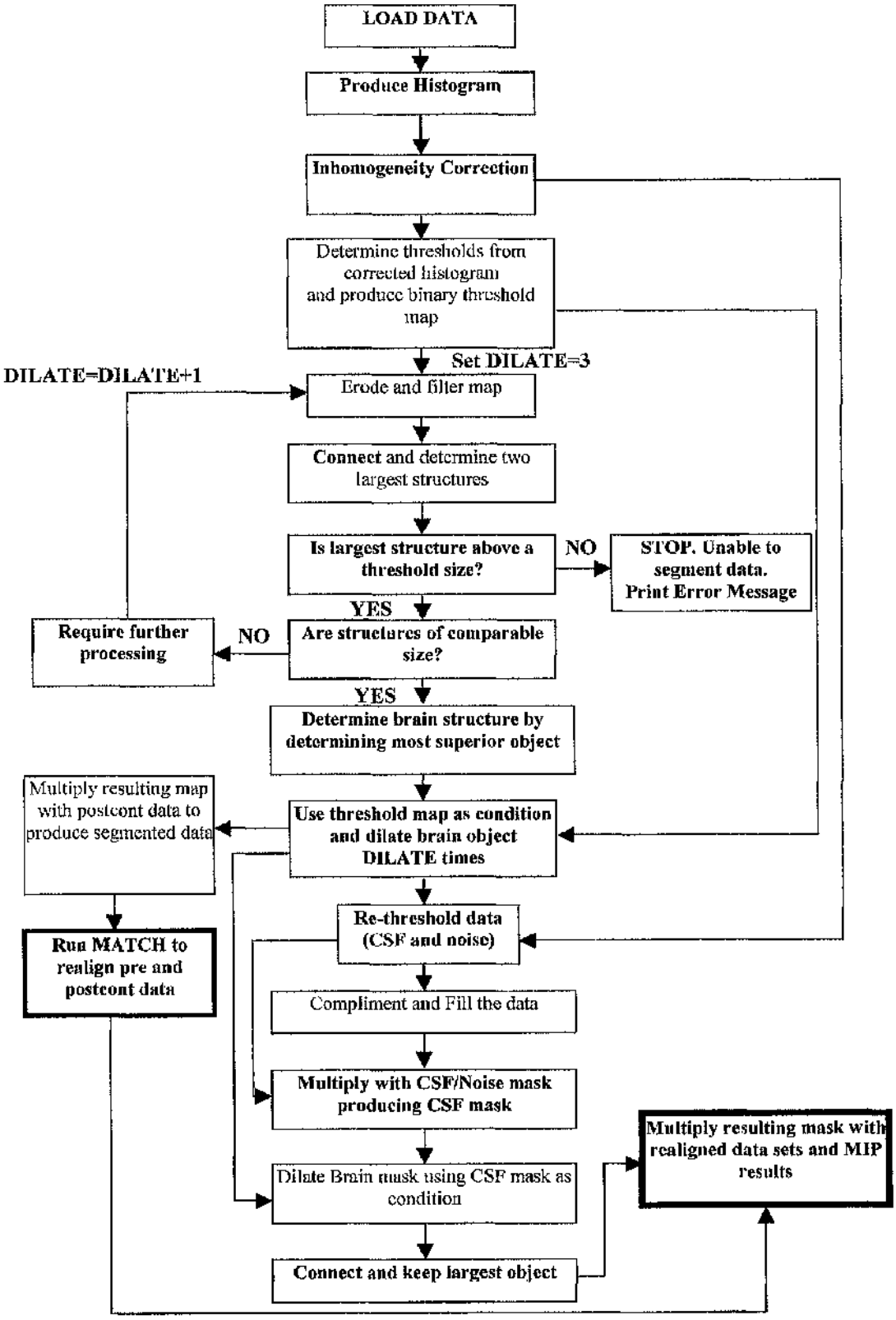

Figure 7.5: Flow diagram of segmentation protocol determined using Analyze

More recently new programming languages have been developed with image processing in mind, these include Matlab (with the Image Processing module installed) and IDL (Interactive Display Language, Research Systems, CO, USA). Both of these languages contain commands that simplify programming for image processing tasks, with special routines developed for processing large image arrays. These specialist commands and routines simplify the programming requirements producing less cumbersome code. However, with the improved code efficiency comes a reduction in algorithm speed. IDL code will not run as fast as code produced in C which has been compiled with optimised compilers.

This study, however, has the aim of proving the concept of automatic segmentation of pre and post-contrast data sets. It is beyond the scope of this work to develop algorithms designed with optimal computational speed in mind. Therefore, to develop the algorithm for this study IDL was used. The software version used was IDL 5.1.

Based on the devised protocol an algorithm was written using IDL by the author. The code for this software is displayed in appendix 3. The basic structure of the software remains faithful to the original protocol, however, in developing the software a number changes were required and a number of problems arose. The following section describes the code in detail and describes the changes and problems.

7.3 Description of Algorithm Code

The code was written with one main module and two separately programmed functions. The two functions were separated from the main program to reduce the number of code lines, i.e. both functions are used more than once in the code, and by separating them the overall code length is shorter. The functions are 'auto_fill', which is written to fill in holes in a binary data set, and 'postcont_max_min' which calculates the histogram of the post contrast data set and determines where the maximum and minimum values occur within the histogram. These functions are called from the main code 'auto_veno'.

The first section of the auto_veno code allows the user to inform the algorithm of the location of the pre and post-contrast files and it utilises a UNIX command 'readspacing' to determine the data dimensions for both data sets. To allow the analysis to continue both data sets should have the same matrix dimensions. The operator is also asked to determine a file name for the final output data set.

The next section opens the post-contrast data set, on which much of the image processing occurs. Care is taken to ensure that the data is loaded correctly, i.e. it determines if the data is stored in 8 bit or 16 bit format.

The next section attempts to correct for inhomogeneities using the method described in section 7.2.3 (Brinkmann *et al* 1996, 1998). This method of inhomogeneity correction requires a minimum threshold to be set, where data below this threshold is excluded from the calculations. A minimum threshold is required to exclude errors being introduced by the noise from outside the patient's head. The data is therefore passed to the 'postcont_max_min' function, which can provide this

minimum value from the data histogram. The minimum is calculated within the module along with the maximum (the voxel value of the grey matter peak) by examining the data histogram. The search for the minimum within this algorithm is confined to values above the background noise, but below the grey matter peak. The inhomogeneity section takes the minimum value calculated and calculates the inhomogeneity correction for all data above this value.

The inhomogeneity corrected data is now passed back to the 'postcont_min_max function'. This is to allow calculation of the initial threshold values for the corrected data set. The thresholds are set using the method described in the previous section. The morphological segmentation can now begin.

Two parameters require to be set for the first section of the morphology, where the data is eroded and filtered. Firstly, an erode kernel is required to determine the extent of the erode calculations. The erode kernel is a 3-dimensional matrix with matrix values of 1 defining the extent. This kernel can be varied to suit the data being segmented, however for the data used in this study a kernel matrix of dimensions 3x3x3 suffices. The kernel size will mainly depend on the resolution of the data, therefore the kernel size might need to be increased for higher resolution data. The second parameter required relates to the low pass filtering. The low pass filtering is achieved using the technique described in section 7.2.4.

The code now uses the label_region command to separate out the two largest regions. This is achieved by counting the number of pixels in all of the regions detected by the label_regions algorithm and keeping only the two largest. The program now compares the sizes of the two regions to determine the required number of erodes. Figure 7.6 illustrates the decisions made by the program.

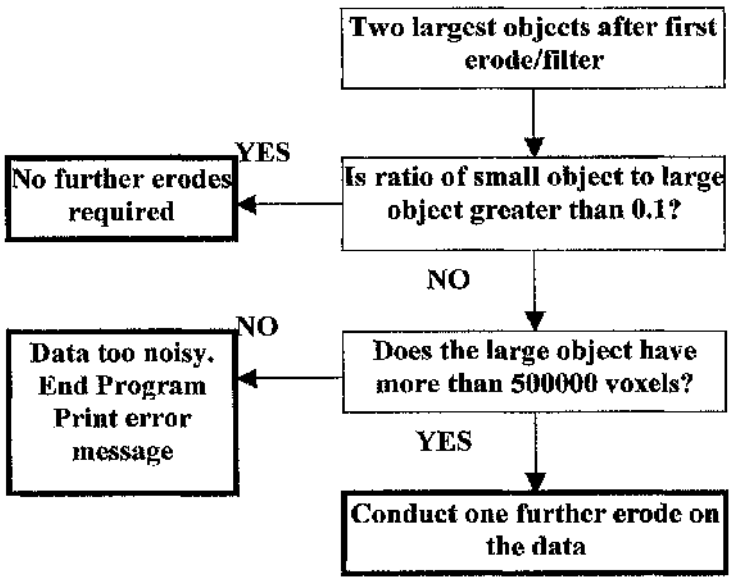

Figure 7.6: A flow chart visualising the decision process used by *auto_veno* to determine the number of morphological erodes required

This section makes a number of assumptions about the size of the brain object and the non-brain object. The brain object is expected to contain at least 500,000 voxels after the erode and filter have been applied. If voxel sizes are assumed to be approximately $1mm^3$ this would relate to a volume of approximately $500cm^3$. It is known from previous studies that the average brain volume is $1200cm^3$ (Martini 2001) and normally varies between 1000-$1500cm^3$. Therefore even after two erodes and low-pass filters the remaining object should have a volume greater than $500cm^3$ which would represent a drop in volume of between 50-66% for a normal brain. However, this figure is conservatively low because this program will not always be segmenting a normal brain.

For example venography may be required in a patient with a space occupying tumour. It is possible in such patients that the overall brain volume is reduced below that of the normal range. Therefore, by having a low volume requirement following erosion and filtering these data sets can still be segmented.

There will be occasions where after erosion and filtering that the brain object will not contain more than 500,000 pixels. The main cause of this is expected to be poor signal to noise in the data set. For example if the patient is unable to keep still during the MR exam the resulting data set is blurred and would likely contain a number of phase ghost artefacts. These artefacts would results in a poor signal to noise which when thresholded using the previous techniques described would result in a poorly defined brain mask with a large number of holes within the brain parenchyma. After erosion and filtering the holes would grow in size and reduce the number of voxels within the brain considerably resulting in the final number of pixels decreasing and thus falling below 500,000 voxels.

In data sets with very poor signal to noise there are likely to be a number of motion artefacts that might take on the appearance of venous vessels. It is also possible that due to the motion blurring vessels are not visualised despite their existence. Therefore, it is desirable that the software highlights these data sets and does not attempt to segment and realign them, as spurious output may result.

The second assumption in this section is that further erosion is required if the second largest object is less than 10% of the size of the first object. This is a reasonable assumption to make due to the nature of the signal in T1 imaging from the brain and its surrounding tissue. The signal amplitude in T1 imaging of muscle and skin is similar to that of grey matter. Therefore, when the data is initially thresholded the large area of muscle and tongue inferior to the brain is included in the data. After

one erosion, if the brain has been successfully separated from the thresholded neck tissue, the two largest objects should consist of the brain and a second object consisting of the inferior muscle. In this situation the second object is never less than 10% of the size of the first.

If an erosion is applied and the brain and neck tissue are not separated another region of mask will however be separated, specifically an area of bone marrow and skin from the skull region, which will become the second largest object. However, this region will always be much smaller than the largest object (which in this situation would contain both brain and neck tissue). Therefore, it is safe to assume that a further erode is required. The 10% threshold is a reasonable threshold as the combined volume of the brain and neck tissue is likely to exceed the volume of the average human brain (i.e. greater than $1200cm^3$). In this situation the second object would need to have a volume of greater than $120cm^3$, which is unlikely to occur due to the lack of any other large structures within the threshold mask.

Using these two assumptions it is possible to determine the number of erodes required and the overall suitability of the data for segmentation and realignment. In the majority of cases it is also now possible to determine which object is the brain parenchyma as the brain object is often the largest. However, as was described previously this is not always the case. Therefore, the next section of the code determines the average voxel location within each object and defines the brain object as having the most superior location.

Following selection of the brain object the dilation process can begin with the number of dilations being related to the number of erosions required. This dilation is conditional, using the original threshold data as the condition. The realignment mask

is now multiplied with the post-contrast data to produce a data set that MATCH can use to base its realignment calculations on.

Before running the MATCH algorithm the program produces the visualisation mask required to produce the final subtraction data. The venogram mask is produced in much the same way as was previously described in section 7.2.6, however, one variable needs to be set for this section.

After the CSF mask has been produced the segmentation mask is conditionally dilated using the CSF mask as its condition. However, it is not certain how many conditional dilates are required to ensure all of the vessels are contained within the final mask without extending the mask too far and decreasing the overall signal to noise of the final subtracted data. For the data from this particular scanner 12 dilations was found to be a good compromise, ensuring that all of the required vessels were contained in the final output data, when applied to the training data sets. However, for different scanners with different signal to noise and contrast characteristics the ideal value for this parameter may be different.

With both the masks completed, the pre and post-contrast data sets, along with the segmentation mask are passed to the MATCH software algorithm for registration. This part of the procedure is significantly longer than the post processing required to produce the mask, with the MATCH software requiring approximately 2hours 30 minutes to complete and the post processing requiring approximately 10-15 minutes.

Apart from some disk tidying the only remaining section within the program is the final multiplication of the registered pre and post-contrast data sets with the final mask and the subtraction of the resulting data. This data set is then saved and is ready to be displayed as a MIP using image analysis or image display software.

7.4 Testing the Algorithm

Having developed an automatic software algorithm it was necessary to test this on real patient data. Chapter 2 described 20 clinical data sets that had been previously collected with the required 3D pre and post-contrast images. This set of patients represented a wide cross-section of the clinical conditions with distinct contrast-enhanced characteristics The clinical range of this data set therefore constituted a stringent test of the algorithm.

The following chapter describes this process and concludes on its effectiveness.

Chapter 8

Assessment of the Algorithm with 20 Patient Data Sets

8.1 Introduction

Having previously devised an automatic algorithm for the production of realigned pre and post-contrast subtraction data this chapter aims to test the algorithms capabilities by running it on the patient data set described in chapter 2.

Several performance parameters will be examined. The segmentation accuracy of the brain parenchyma will be compared to both the accurately segmented data from patients 1 and 2 (see chapters 5 and 6) and the less rigorously segmented data in chapter 2 which were prepared by the author of this thesis. As has been previously discussed, reasonable quality segmentation is required if the data are to be realigned with good accuracy.

The final subtraction data will be analysed in the MIP format, as would be the case in the clinical setting. Most importantly the MIPs will be compared to those produced in chapter 2 to ensure that all of the vessels visualised in the manually segmented data are present in the automatically produced data.

As a final check, the signal to noise of the MIPs will be compared to those measured in chapter 2. The signal to noise will be affected by the accuracy of the visualisation mask. The inclusion of too much extraneous tissue could result in a significant reduction in signal to noise.

The algorithm being tested is novel and is applied to pre and post-contrast with the aim of automatically producing subtraction venograms.

All of the work contained in this chapter was conducted by the author with the exception of the data acquisition, which was performed by radiographic staff.

8.2 Methods

To test the ability of the algorithm to automatically produce good quality subtraction venograms 20 patient data sets were collected, having been scanned on the Siemens Magnetom SP scanner using a pre and post-contrast 3D MP-RAGE protocol. These were the same patients that have been processed manually in chapter 2. The patients were scanned using the contrast-enhanced protocol for differing pathologies under investigation. The examinations included: 6 patients with meningiomas, 5 for suspected venous thrombosis, 3 with gliomas, 3 with adenomas, 1 with a cyst, 1 with a malignant neoplasm and 1 normal patient. Due to the wide variety of conditions being included in this study this patient group was expected to be a good indicator of the different conditions that the algorithm would have to deal with in real clinical circumstances.

The imaging parameters varied within the following constraints; TR=10 ms, TE= 4 ms, TI= 20-300 ms, flip angle = 10-15, equivalent slice thickness = 1.3-1.4 mm, matrix = 256x256, FOV = 250 mm. Slices were sagittal in orientation. The maximum acquisition time for each MP RAGE acquisition was 6 mins 46 seconds. The imaging was conducted on a 1.5T imaging unit (Siemens Magnetom 1.5 T). Patients were asked to stay as still as possible throughout the imaging procedure with their heads held in place with padding (see section 2.5.1.1, figure 2.5). A long IV line was inserted in the patient before the imaging protocol had begun. After initial scanning, including pilot scans, the first MP RAGE sequence was run before contrast medium injection. The contrast medium (Magnevist) was administered as soon as the pre-contrast MP RAGE sequence had finished as a 20 second bolus, via the IV line. This required a radiologist to enter and leave the room. The long line

was used to reduce the patient motion due to the injection. The post-contrast MP RAGE sequence was started as soon as the bolus delivery was complete and the radiologist had left the room. The data was transferred to an Sun Ultra 1 170MHz workstation where in-house software (conv_analyze, courtesy of Martin Connell) was used to convert the ACR/NEMA 2 data to Analyze format.

The algorithm was run on the pre and post-contrast data. When the algorithm was successful it produced the realigned- subtracted data sets. These output data sets were loaded into Analyze and MIPs were produced.

Segmentation accuracy was determined for the automatic algorithm by comparing the brain segmentation volumes produced with manually produced brain segmentation volumes from earlier in this thesis. In chapters 5 and 6 two patient data sets had accurate manual segmentations produced. Both of these patients were included in the 20 patient assessed in this study. Therefore, for these subjects it was possible to accurately determine the brain parenchyma segmentation accuracy of this algorithm with respect to this standard. The two subjects were patient 1, who had normal enhancing anatomy and patient 2 who had a space occupying enhancing lesion.

In chapter 2 all 20 subjects in this study had a lower quality manual segmentation applied to them (these data sets were in general under-segmented). Therefore, by comparing these low quality and the high quality manual segmentations with those derived from the software, it should be possible to assess if the algorithm is segmenting the data to an acceptable quality.

To assess the quality of the MIPs produced they were compared to the manually produced MIP's from chapter 2. These MIPs were produced from post-contrast data that had been manually segmented for the purposes of realignment and

for final MIP display. The manual segmentation procedures have been described in detail in chapter 2.

The first method of MIP assessment was to determine the integrity of the MIPs produced using the algorithm when compared to the manually produced MIPs from chapter 2. Assuming that the manually segmented MIPs represented the gold standard, then the automatically produced MIPs should not exclude any vessels that were included in the manually segmented data set. Exclusions of veins, especially within the cortex could lead to misdiagnosis or poor interpretation. Therefore, the automatically produced MIPs were visually compared with the manually produced MIPs by the author to determine if any vessels had been excluded.

As well as totally excluding particular vessels it was possible that the automatic algorithm would exclude particular sections of individual veins. This might lead to misdiagnosis of cerebral venous thrombosis where the continuity of the vessels is investigated. Therefore, it was important for the observer to look for these features as well.

Signal to noise was measured for lateral projections for corresponding manually and automatically produced MIPs. To determine the signal to noise four regions were drawn on the manually prepared data set, with three areas containing no discernable vessels (noise) and one drawn on an enhancing area of the Superior Sagittal Sinus. These regions were drawn using the Analyze region of interest module using the freehand drawing tool. Average pixel values were determined and used to calculate the signal to noise. These same regions were used to determine the signal to noise on the automatically produced MIP. Therefore it was possible to directly determine the effects on the signal to noise of the automatic algorithm relative to the manually produced data.

8.3 Results

The algorithm was successful in producing venograms in 18 of the 20 patients when compared to manually produced venograms. Figure 8.1 displays some comparisons of the MIPs produced.

Both data sets that failed contained gross patient motion artefacts, which resulted in reduced signal to noise in the original data. Example slices from the post-contrast data for these patients are displayed in figure 8.2. The algorithm stopped at the section where it compared the object sizes after the first erode. Therefore, the algorithm correctly determined that these data sets were of poor diagnostic quality. Manually produced venograms from these patients were of little clinical value.

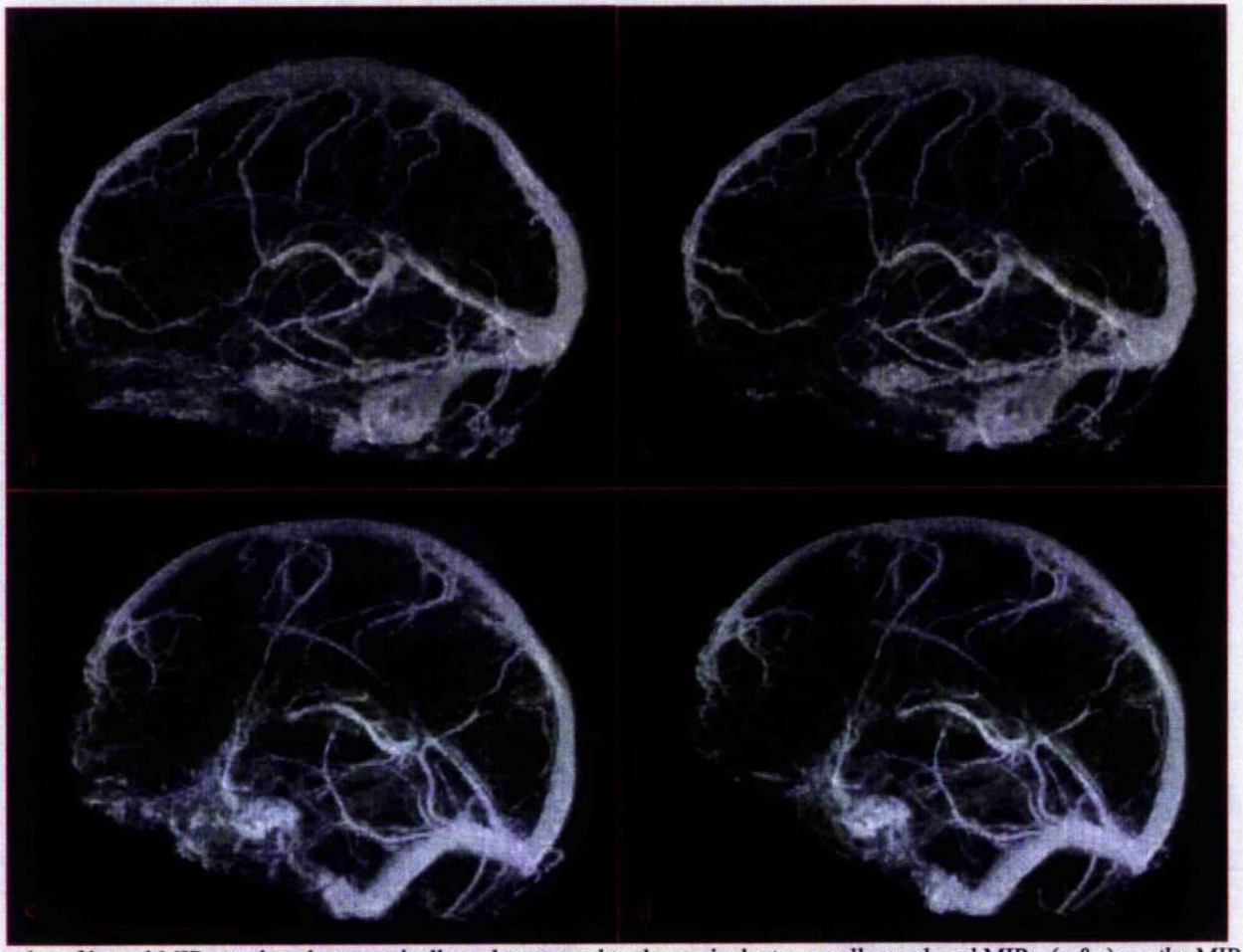

Figure 8.1: Two examples of lateral MIPs produced automatically and compared to the equivalent manually produced MIPs. (a &c) are the MIPs produced from the automatically produced data and (b & d) are produced from the manually segmented data

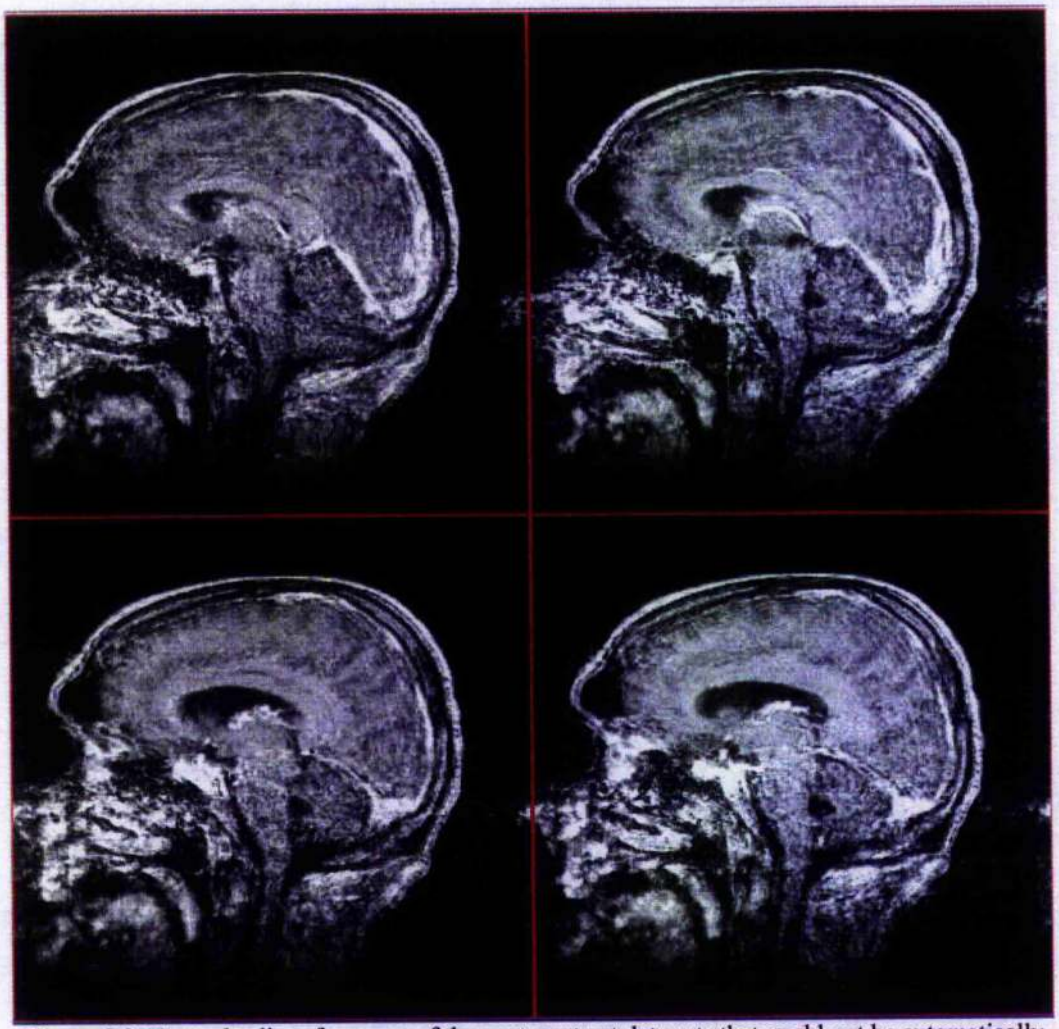

Figure 8.2: Example slices from one of the post-contrast data sets that could not be automatically segmented due to poor signal to noise

When the brain parenchyma segmentation volumes produced by the IDL algorithm were compared to the accurate manual segmentation volumes, patient 1's IDL segmentation contained 91% of the manual segmentation voxels. Patient 2's IDL segmentation contained 83% of the manual segmentation voxels. As was discussed in chapter 6 segmentation volumes of 80% and above are deemed acceptable for the purposes of realignment.

For these patients when the IDL segmentation was compared to the under-segmented volumes used in chapter 2 (section 2.5.1.2), the percentages were 73% and 63% respectively. It would therefore appear that using the lower quality

segmentations from chapter 2 would require setting an acceptable segmentation threshold of about 60%. Using this threshold results in the results table 8.1.

Patient Number	IDL Segmentation Compared to Low Quality Segmentation	Acceptable?
1	73%	YES
2	63%	YES
3	72%	YES
4	71%	YES
5	68%	YES
6	78%	YES
7	POOR DATA	
8	POOR DATA	
9	50%	NO
10	68%	YES
11	57%	NO
12	58%	NO
13	72%	YES
14	64%	YES
15	79%	YES
16	49%	NO
17	61%	YES
18	82%	YES
19	76%	YES
20	64%	YES

Table 8.1: Results comparing the IDL segmentation to the lower quality manual segmentations from chapter 2 (section 2.5.1.2)

Acceptable segmentation was achieved in 14 of the 18 (78%) of the analysed data sets. Patients 11 and 12 were close to the acceptable threshold and it is likely that they would have benefited from a further conditional dilate in the production of the realignment mask. Patients 9 and 16 were significantly below the acceptable threshold, suggesting the algorithm faced more significant problems in segmenting these data sets. On closer inspection of the threshold values calculated it was discovered that the maximum value of the threshold in both cases was inappropriately low, with the threshold masks containing little white matter material in both cases. The poor segmentations could be attributed to the algorithm method used to determine the maximum threshold.

As was described in section 7.2.3 an empirical equation had been derived for the calculation of the maximum threshold (equation 7.2). It was also discussed that on certain occasions this calculation was not sufficient to determine the maximum threshold and a further step was applied in these cases based on the level of the first minima (grey matter). From experience the second step ensured that an acceptable maximum threshold was set. However, for the two patient data sets in question, the histogram minimums used for this calculation had significantly more voxels than for the majority of the other data sets examined (see graph 8.1)

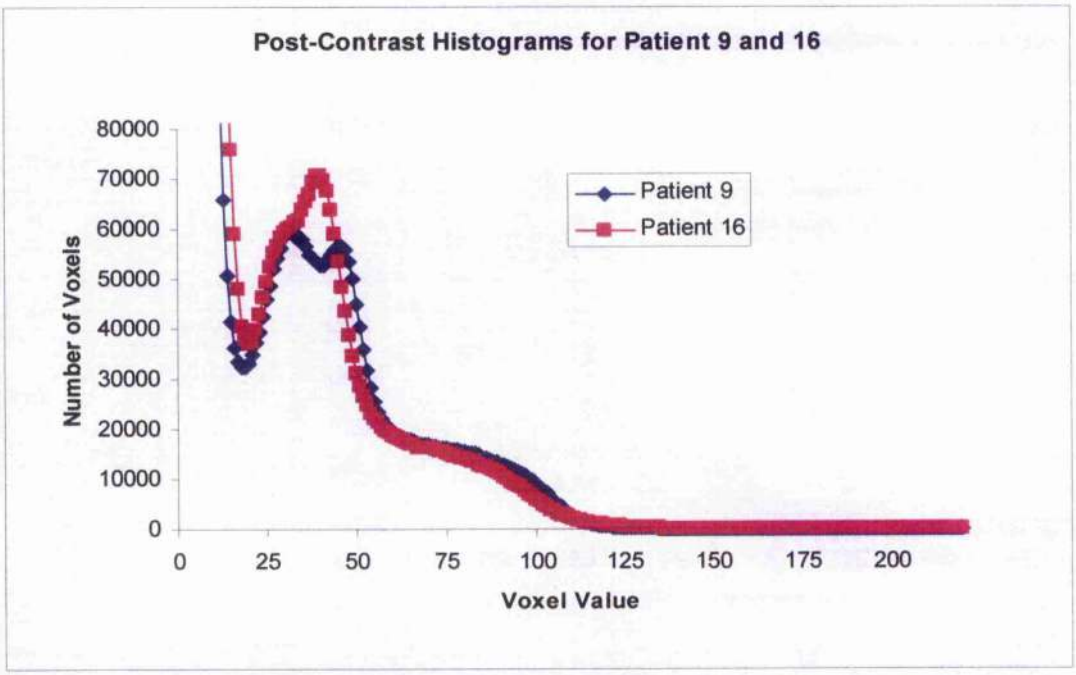

Graph 8.1: The post-contrast histogram from patient 9 and 16. Special attention should be paid to the voxel count of the first minima which is 32570 for patient 9 and 36738 for patient 16. In other post-contrast histograms this is typically 25000 and below

The data that contributes to the voxel count close to and at the minimum in these data sets will mainly consist of CSF voxels. Therefore, higher voxel counts in this part of the histogram will be a result of a larger volume of CSF. Therefore, due to variations in CSF volume from patient to patient, the threshold correction will occasionally encounter data sets, such as those described here, that have significantly

more CSF. Thus the algorithm as it stands will not work for all patient data sets. Either a new automatic method of determining the threshold or a manual threshold stage is required. These issues will be discussed in more detail in the conclusions.

Of the 18 MIP venograms produced, 12 upon visualisation were found to contain all of the vessels visualised in the manually segmented subtraction MIPs produced in chapter 2. There were 6 automatically segmented data sets that either fully excluded a vein that was present in the manually segmented data or contained discontinuities in the veins that were not present in the manually segmented data. Table 8.2 list the data sets that differed and the veins that were not correctly visualised and figure 8.3 displays an example of manually and automatically produced MIPs from the same patient.

Patient Number	All Veins Visualised?	Differences
1	YES	
2	YES	
3	YES	
4	NO	Cavernous Sinus
5	YES	
6	NO	Spheno Parietal Sinus
7	N/A	
8	N/A	
9	YES	
10	NO	Tumour draining veins
11	NO	Superior Petrosal Sinus
12	YES	
13	NO	Superior Petrosal Sinus
14	YES	
15	YES	
16	YES	
17	YES	
18	NO	Spheno Parietal Sinus,Cavernous Sinus, Cortical Veins
19	YES	
20	YES	

Table 8.2: A comparison of the manually produced venograms and the automatically produced venograms. This table lists the veins excluded from the automatically produced MIPs.

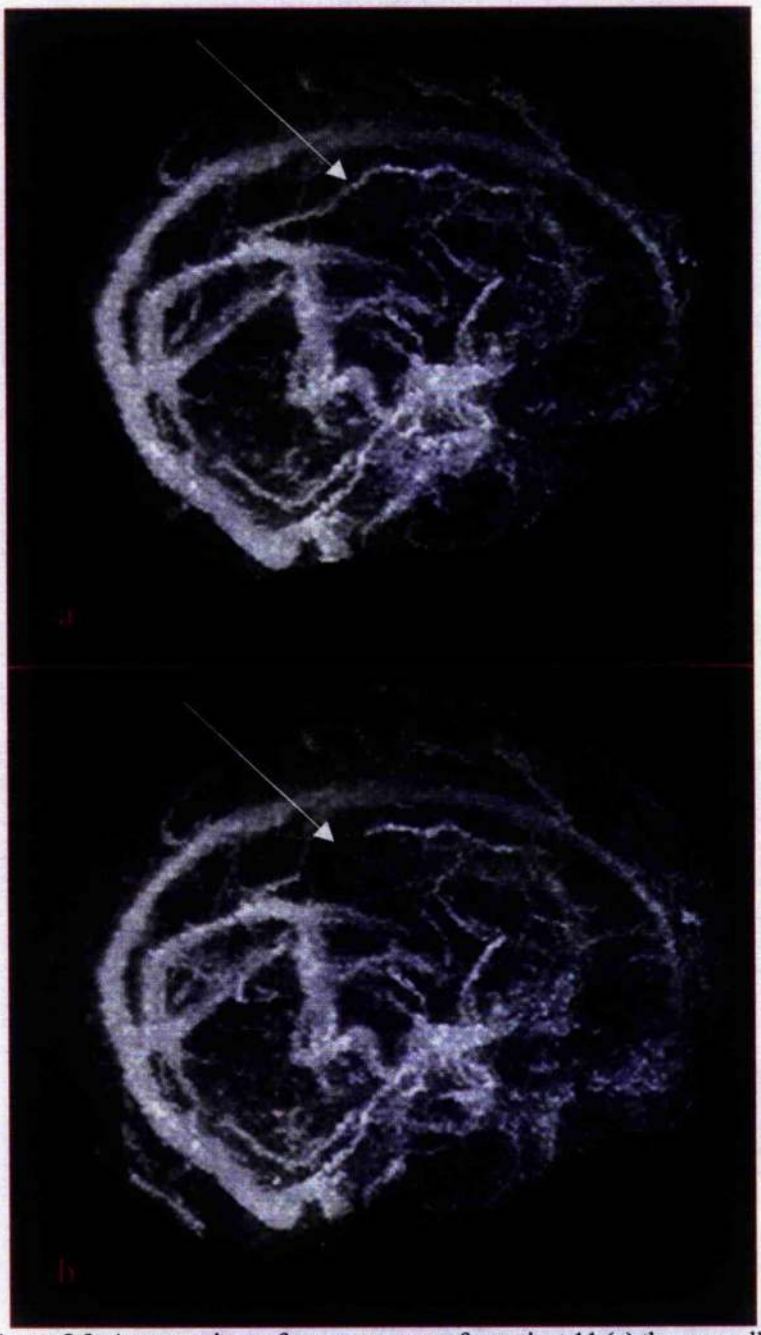

Figure 8.3: A comparison of two venograms for patient 11 (a) the manually produced venograms, (b) the automatically produced venograms. The long white arrows indicates where a vessel was correctly visualised in the manual data but was partially excluded from the automatic data. It should be noted that the signal to noise in the automatic data is lower due to unnecessary tissue being included in the visualisation mask.

Further differences were detected when there was a large enhancing lesion in the data set. The lesions were not always fully contained within the automatically segmented data. Therefore, any veins close to this lesion were excluded as in patient

10. However, in these patients it is unlikely that lesion visualisation is required using MIPs. Viewing a lesion on a MIP results in the loss of internal detail, due to overlapping structures, therefore these structures are best viewed in multislice mode.

In general veins were excluded as a direct result of the limited number of dilations used to produce the final data visualisation mask. This is confirmed by the location of the poorly visualised veins (table 8.2). All of these veins are located at brain CSF boundaries (with the exception of the tumour draining veins).

However, if the number of dilations was increased this would result in reduced signal to noise in the final visualised data. Therefore, the optimal number of dilations would depend on the data set being examined and on the acceptable signal to noise. The optimal number of dilations would also depend on the clinical area of interest. For example if visualisation of the superior petrosal sinus, the cavernous sinus, the cortical veins and veins close to large enhancing tumours were required then a larger number of dilations would probably be required. This will be further discussed in the conclusions section.

When the signal to noise was calculated for the manually produced and the automatically produced MIPs and compared and analysed statistically (paired T-test) it was found that there was a statistically lower signal to noise ($p<0.05$) in the automatically produced data. As has already been discussed this is most likely due to the extra data included in the automatically produced mask compared to the manually produced mask and is a direct result of the number of dilations used.

These results suggest that the algorithm was only partially successful in producing accurately aligned pre and post-contrast data and producing masked data for MIP visualisation. However, it should be noted that these data sets were real clinical data and were not a specifically collected normal data set. Though the initial

application of this technique has had limited success further investigation of this technique may provide improved results. This will be discussed further in the conclusion section.

8.4 Conclusions and Further Work

This chapter aimed to develop an automatic segmentation algorithm for application to pre and post-contrast data sets where realignment and MIP visualisation of the resulting subtraction data was required. The algorithm was designed taking into account the findings of the previous chapters in this study.

8.4.1 Rational for Designing the Algorithm

Chapters 2 and 3 discovered that realignment was required when the pre and post-contrast data were to be subtracted, even when the patient had not been removed from the magnet between scans. Only by accurately realigning the data sets could inter-scan motion artefacts be excluded from the final results. Misalignment between the pre and post-contrast data would be especially problematic if the resulting data sets were to be used for quantification purposes such as those described in chapter 3

Chapters 4 and 5 investigated segmentation accuracy on phantom data, relating this to realignment accuracy. The results suggested that it was most important to exclude contrast-enhanced data in the post-contrast data use for realignment purposes. The results also suggested that very accurate segmentation of

the brain parenchyma was not essential for good quality realignment of the pre and post-contrast data. It was suggested that inter-scan motion could be satisfactorily corrected when segmentation accuracy was of lower quality. However, these conclusions were based on a patient based phantom data set, therefore further investigation was required if firm conclusions in segmentation accuracy were to be applied to real patient data sets.

Chapter 6 applied the same procedures to two patient data sets. The data sets were chosen to represent a normal and abnormal data set. The first patient's data contained normal contrast-enhanced anatomy and represented an ideal data set for segmentation and realignment purposes. The second patient's data contained a large enhancing, space occupying lesion, which would test the effects of segmentation accuracy on a data set with completely different contrast-enhancing properties. More significantly the data in this chapter contained real noise differences between the pre and post-contrast data.

It was found that noise did introduce a significant effect on realignment with respect to segmentation accuracy. However, it would appear to be very difficult to model the effects that noise has on the realignment accuracy due to the random nature of the effects that the noise introduces. Therefore, this chapter reached similar conclusions to chapter 5 with respect to the requirements for segmentation accuracy. It concluded that a significant amount of over-segmentation was acceptable when realigning the type of pre and post-contrast data described in this thesis.

Based on the principles investigated in this thesis an algorithm was devised using a morphological approach.

8.4.2 Algorithm Conclusions – Brain Segmentation

It was reported in section 8.3 that the algorithm had a limited amount of success in both producing the segmentation required for realignment and for producing the mask for the final visualisation of the subtraction data using a MIP algorithm. However, despite the limited success some firm conclusions can be drawn with regards to this technique and to techniques that could be subsequently derived from it.

The brain segmentation algorithm failed in two specific parts of the protocol. Two data sets failed to reach the required segmentation accuracy due to the requirement of at least one further conditional dilate. In both cases this additional step would have produced acceptable segmentation accuracy, with respect to the manual segmentations applied in chapter 2. This situation could simply be rectified by applying one further erode to all of the data set.

The initial decision to apply two additional dilations when compared to the number of erosions was based on previously published experience (Stokking 1998) where one extra dilation was used, and the knowledge that the histogram thresholds were stringently set to exclude contrast-enhanced voxels suggesting one further dilation would be required. In testing this appeared to produce satisfactory results. It was also found that if three additional dilations were applied to all of the data sets that on some occasions non-enhancing extra-cranial tissue would be included in the segmented volume. Although the effects of this non-enhancing tissue inclusion on realignment accuracy were not explicitly tested in this thesis, it is expected that inclusion of such tissue is undesirable. Therefore, it would appear that in some cases

two dilations would be optimal and in some cases three would be required. It may be possible to include a test within the algorithm to determine the number of dilations required.

The second area the algorithm failed in was the threshold determination from the data histograms. As described in section 8.3 this was due to poor determination of the maximum threshold and was a direct result of the methods used to determine it. In both cases the threshold was set too low and therefore, a large quantity of white matter was excluded from the threshold mask.

The failure of the threshold determination for certain data sets suggests that this part of the algorithm should be changed to take account of these findings. It is likely that a totally different method of determining the thresholds is required. For example the Gaussian distributions of voxel values associated with the different tissue types could be modelled using techniques similar to Lemieux (Lemieux *et al* 2003 and Shan *et al* 2002). However, although this technique was applied to a patient data set (epilepsy patients by Lemieux) it remains uncertain if the technique would work with the diverse morphology and resulting variable histograms found in contrast-enhanced data sets. However, future work to improve the algorithm should include a detailed investigation of these techniques.

Despite the failings of the algorithm to segment the brain tissue to the required accuracy for all the patients in this study, it should be remembered that the data used here was a true representation of the wide variety in terms of pathology, imaged in a clinical scanning environment. Additionally, as was previously described, the scanner used in this study has now been superseded by scanners that have superior signal to noise characteristics. Therefore, it is likely that on newer scanners that this algorithm, or a version of it optimised for that particular scanner,

would have a significantly higher success rate in accurately segmenting the brain structures. Therefore, future work should be conducted to test this hypothesis.

It is also possible that the algorithm could be altered to provide a semi-automatic method of segmentation that would not suffer from the problems highlighted here. For example, if the operator was given control of the thresholding it is likely that this would improve the overall segmentation success rate. Control over the number of final conditional dilates could also be operator controlled ensuring that sufficient brain is available for realignment purposes. Allowing operator intervention at this stage would introduce variability in the segmentation due to observer bias and error, however, for realignment purposes small variations in histogram definition are likely to result in acceptable variations in segmentation accuracy in the hands of an experienced operator.

The requirement for experienced operator intervention is contrary to the aims of this study. The aim was to fully automate the procedure and exclude the requirement for experienced operator time. Changing the algorithm to become semi-automated is acceptable however, due to the still considerable time saving afforded by removing full manual segmentation. It is expected that thresholding would involve only minutes of the operator's time. This time requirement would still be significantly less than the hours typically required for manual segmentation.

With computing power increasing all the time it is likely that such semi-automated segmentation software could be designed to be fully interactive. For example it should be possible to instantly see the effects of varying the histogram thresholds on a visualisation of the resulting brain segmentation. Therefore, future work should also include the investigation of such a semi-automated software package for segmentation of the brain in post-contrast data.

8.4.3 Algorithm Conclusions – Visualistion Mask

The production of the visualisation mask was also of limited success. However, this is a result of the number of dilations used at this stage. Part of the aim of this study was to produce a visualisation mask that would contain the relevant data required for the MIP visualisation, whilst including a minimal amount of unwanted data. It was especially important to remove contrast-enhancing structures that were not of clinical value. To limit the inclusion of unwanted data the segmented brain mask was conditionally dilated using a mask derived from the CSF data. This was used to ensure that structures beyond the CSF were not included in the visualisation mask.

Using this mask, however, it was found that the overall signal to noise would still decrease with increasing use of dilations at this stage. Therefore, in this instance the dilations were limited to 12, although as was discussed in section 8.3 for some data sets some surface vessels were not fully included within this dilated mask. Also despite limiting the number of dilations, signal to noise was still significantly reduced.

It was possible to eliminate the poor inclusion of vessels by increasing the number of dilations. For example figure 8.4 shows the automatically produced subtraction data using a MIP where 8.4(a) is the result produced with the default 12 dilations and 8.4(b) is the equivalent result using 20 dilations (a large part of the CSF mask)

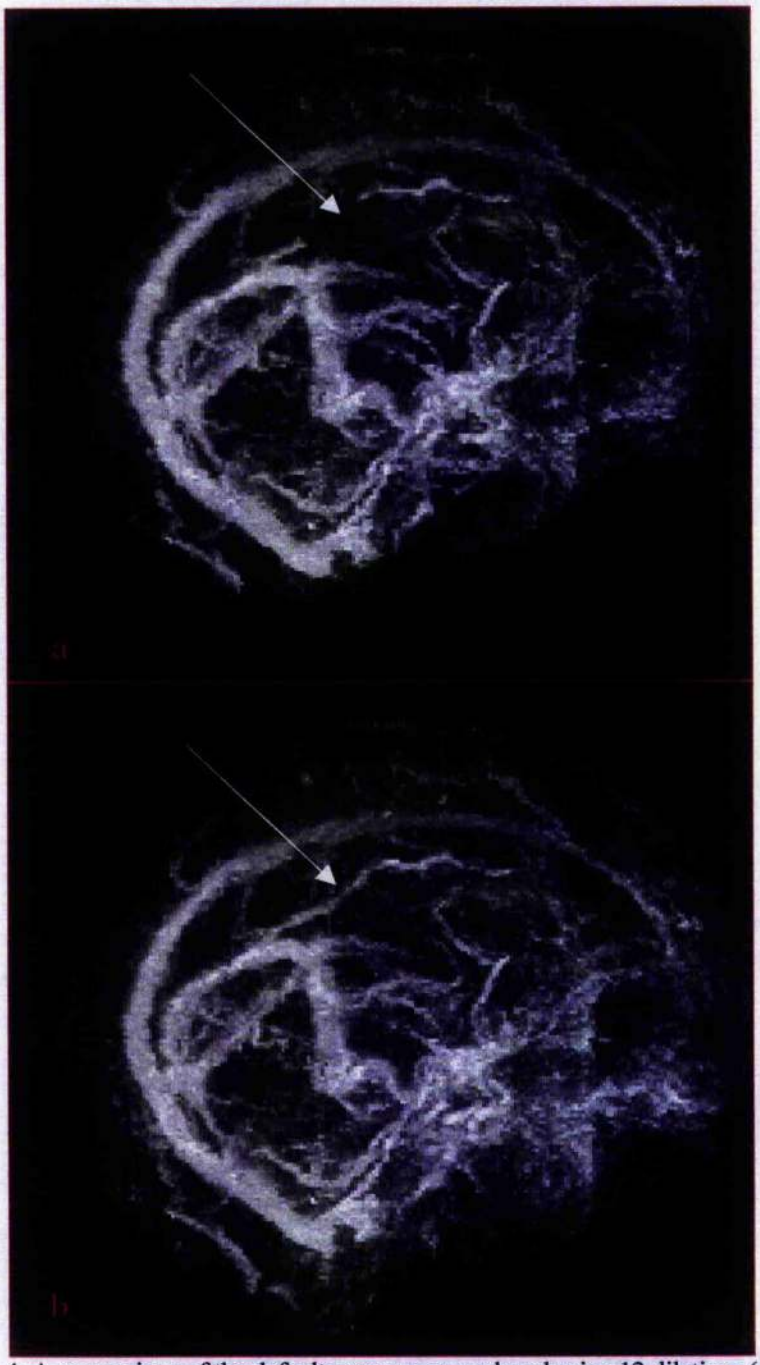

Figure 8.4: A comparison of the default venograms produced using 12 dilations (a) and the automatically produced venograms produced using 20 dilations (b) for patient 11.
The long white arrows indicate where a vessel was correctly visualised in the 20 dilations data but was partially excluded from the 12 dilation data. There is, however a further decrease in signal to noise with the use of 20 dilations.

Assuming that all of the venous vessels are contained within the CSF (which from the experience of this study was found to be the case) then with the correct number of dilations it should be possible to ensure that no cerebral venous vessels

are excluded from the final visualistion. However, by applying this to every data set might result in poorer than necessary signal to noise in a large number of cases.

By adopting a similar approach to that described in section 8.4.2 it may be possible to compromise if this section of the algorithm was modified to become semi-automatic. Here the user controlled variable would be the number of conditional dilates required to produce the visualistion mask. Therefore, where possible the number of dilations could be kept minimal resulting in improved signal to noise in the visualisation.

The main disadvantage in using a semi-automated technique is the requirement for user intervention as discussed in section 8.4.3. It is possible that an inexperienced operator would define a number of dilations that would exclude vessels of interest without the operator noticing the exclusion. This could be countered, however, by starting the intervention with all of the data from within the CSF and allowing the number of dilations into the CSF to be reduced. The loss of an important vessel would be more obvious by applying the technique in this way.

Chapter 9

Final Conclusions

The overall aim of this thesis was to investigate some of the methods used in contrast MR imaging. Its specific aim was to investigate methods used for the comparison of 3D pre and post-contrast data collected within a single imaging session which can be used for determining tumour progression or visualisation of the cerebral venous system. It was found in chapter 2 that realignment of the pre and post-contrast data was required when using the technique for venous visualisation. Chapter 3 went on to demonstrate that realignment is also a requirement when this technique is used for tumour volume measurement. Failure to correct for intra-scan patient motion would result in incorrect tumour volume measurement.

To ensure that the realignment was accurate in these data sets, brain segmentation is required. Chapters 4, 5 and 6 investigated the effects of segmentation accuracy on the realignment of pre and post-contrast data. These chapters concluded that very accurate segmentation was not an absolute requirement for accurate realignment of these data sets. However, care was required to ensure that contrast enhanced data was not included in volumes used for the purposes of realignment.

The results of chapters 4-6 were important considering the likely data that would require segmentation in clinical situations. Clinically acquired data morphology can vary to a large extent due to enhancing pathology, reducing the likelihood of designing an automatic algorithm that could accurately segment all the data sets it was provided with. Therefore, chapter 7 set out to design an algorithm that could produce adequate segmentations of the brain from these data sets allowing accurate realignment resulting in good quality subtraction data sets.

Despite using morphology which is well suited to segmenting variable data sets, chapter 8 discovered that although the algorithm worked well for some data

sets, others were poorly segmented and visualistion could be compromised by exclusion of data. However, the data examined were of the variable nature expected to be encountered in the clinical setting, therefore, as a first attempt the results were promising. Chapter 8 suggested that modifications to the technique could provide significant improvements suggesting that future follow up work is worthwhile.

For simplicity this study investigated registration and the effects of segmentation on registration using only one registration algorithm. It was chosen due to its capability of registering to sub-voxel accuracy. However, there are a number of other registration techniques available that are likely to be of comparable accuracy. It was not an aim of this thesis to compare different registration techniques. However, it is likely that the general conclusions of this thesis will apply to these registration algorithms, although, different algorithms are likely to have different sensitivities to segmentation accuracy. As yet there has been no study on the effects of segmentation accuracy on different algorithms, therefore, this could be investigated in future work.

With the trend in MR imaging for resolving smaller and smaller structures, single-session inter-scan motion correction will become an increasing requirement for any protocol that requires inter-scan comparisons or calculations. This work provides a template for assessing the efficacy of these protocols.

References

Allroggen H, Abbot R.J. Cereral venous thrombosis. Journal of Postgraduate Medicine, 2000; 76: 12-15.

Altman DG. Practical Statistics for Medical Research. Chapman & Hall/CRC 1991.

Ardekani BA, Brain M, Kanno I, Hutton BF. Automatic detection of intradural spaces in MR images. Journal of Computer Assisted Tomography 1994; 18: 963-969.

Ashburner J, Friston KJ. The role of registration and spatial normalization in detecting activations in functional imaging. Clinical MR/Developments in MR 1997; 7: 26-28.

Atkinson DJ, Burstein D, Edelman RB. First-pass cardiac perfusion: evaluation with ultrafast MR Imaging. Radiology 1990; 174: 757-762.

Axel L, Constantini J, Listerud J. Intensity correction in surface coil MR imaging. American Journal of Roentgenology 1987; 148: 418-420.

Bailes DR, Gilderdale DJ, Bydder GM, Collins AG. Respiratory ordered phase encoding (ROPE): a method for reducing respiratory motion artifacts in MR imaging. Journal of Computer Assisted Tomography 1985; 9: 835-838.

Baker M. Maths- Conversion Euler to axis-angle. Available http://www.euclideanspace.com/maths/geometry/rotations/conversions/EulerToAngle/index.htm. Published 1998. Accessed June 2004.

Barra V, Boire JY. Tissue segmentation on MR images of the brain by possibilistic clustering on a 3D wavelet representation. Journal of Magnetic Resonance Imaging 2000; 11: 267-278.

Barr-Sella P, Front D, Hardoff R, *et al.*. Ultrastructure basis for different pertechnetate uptake patterns by various human brain tumours. Journal of Neurology, Neurosurgery and Psychiatry 1979; 42: 924-930.

Berberich J, Hirsch S. Die rontgenographische Darslellung der arterien und venen am lebenden. Munchen Klin Wochenschr 1923; 49: 2226.

Bloch F, Hansen WW, Packard M. Nuclear induction. Physical Review 1946; 69: 127.

Bradley WG, Waluch V. Blood flow: magnetic resonance imaging. Radiology 1985; 154: 443-450.

Brandt ME, Bohan TP, Kramer LA, Fletcher JM. Estimation of CSF, white and gray matter volumes in hydrocephalic children using fuzzy clustering of MR images. Computerized Medical Imaging and Graphics 1994; 18: 25-34.

Brant-Zawadzki M, Gillan GD, Nitz WR. MP RAGE: A three dimensional, T1-weighted gradient-echo sequence – Initial experience in the brain. Radiology 1992; 182: 769-775.

Brennan D, Condon B, Hadley D. Determining the effects of segmentation accuracy on the registration of pre- and post-gadolinium MR images. Proceeding of the ISMRM (Glasgow) 2002: 2479.

Brennan D, Hadley D, Patterson J, Condon B. Comparison of MRI and SPECT volume measurement following minimally invasive surgery for a phase 1 trial of a genetically modified viral therapy. Proceedings of ISMRM 2001: 1397

Brennan D, Hadley D, Patterson J, Condon B. Comparison of MRI and SPECT tumour volume measurement following minimally invasive surgery. 6th British ISMRM Meeting (Liverpool) 2000.

Brennan D, Condon B, Hadley D. The application of subvoxel coregistration in subtraction venography: a comparison with non-registered data. Proceedings of ISMRM (Philadelphia) 1999: 2177.

Brinkmann BH, Manduca A, Robb RA. Optimized homomorphic unsharp masking for greyscale inhomogeneity correction. IEEE Transactions on Medical Imaging 1998; 17: 161-171.

Brinkmann BH, Manduca A, Robb RA. Quantitative analysis of statistical methods for greyscale inhomogeneity correction in MR images. SPIE Proceedings 1996; 2710: 542-552.

Brooks B. Intraarterial injection of sodium iodide. JAMA 1924; 82: 1016

Brown SM, Harland J, MacLean AR, *et al.*. Cell type and cell state determine differential in vitro growth of non-neurovirulent ICP34.5-negative herpes simplex virus types 1 and 2. The Journal of General Virology 1994; 75: 2367-2377.

Carr DH, Brown J, Bydder GM, *et al.* Intravenous chelated gadolinium as a contrast agent in NMR imaging of cerebral tumours. Lancet 1984; 1: 484-486.

Chen C-N, Hoult DI. Biomedical Magnetic Resonance Technology. New York: Adam Hilger 1989.

Clarke LP, Velthuizen RP, Camacho MA, *et al.* MRI Segmentation: Methods and Applications. Magnetic Resonance Imaging 1995; 13: 343-368.

Clarke LP, Velthuizen RP, Phuphanich S *et al.* Stability of three supervised segmentation techniques. Magnetic Resonance Imaging 1993; 11: 95-106.

Cline HE, Dumoulin CL, Hart HR Jr, *et al.* 3D reconstruction of the brain from magnetic resonance images using a connectivity algorithm. Magnetic Resonance Imaging 1987; 5: 345-352.

Cochran ST, Bomyea K, Sayre JW. Trends in adverse events after IV administration of contrast media. American Journal of Roentgenology 2001; 176: 1385-1388.

Collins DL, Zidjenbos AP, Kollokian V, *et al.* Design and construction of a realistic digital brain phantom. IEEE Transcripts in Medical Imaging 1998; 17: 463-468.

Collins VP. Gliomas. *Cancer Surveys* 1998; 32: 37-51.

Condon BR, Patterson J, Wyper D, *et al.* Image nonuniformity in magnetic resonance imaging: Its magnitude and methods for its correction. British Journal of Radiology 1987; 60: 83-87.

Cotton F, Weiner HL, Jolesz FA, Guttmann CR. MRI contrast uptake in new lesions in relapsing-remitting MS followed at weekly intervals. Neurology 2003; 60: 640-646.

Curé JK, Van Tassel P, Smith MT. Normal variant anatomy of the dural venous sinuses. Seminars in Ultrasound CT and MR 1994; 15: 499-519.

Damadian R. Tumour detection by nuclear magnetic resonance. Science 1971; 19; 1151-1153.

Dale AM, Fischl B, Sereno MI. Cortical surface based analysis. I. Segmentation and surface reconstruction. Neuroimage 1999; 9: 179-194.

DeAngelis LM. Medical Progress: Brain Tumors. The New England Journal of Medicine 2001; 344: 114-123.

Dumoulin CL, Cline HE, Souza SP *et al.* Three-dimensional time-of-flight magnetic resonance angiography using spin saturation. Magnetic Resonance in Medicine 1989(a); 11: 35-46.

Dumoulin CL, Souza SP, Darrow RD *et al.* Simultaneous acquisitions of phase-contrast angiograms and stationary-tissue images with Hadamard encoding of flow-induced phase shifts. Journal of Magnetic Resonance Imaging 1991; 1: 399-404.

Dumoulin CL, Souza SP, Walker MF, Wagel W. Three-dimensional phase contrast angiography. Magnetic Resonance in Medicine 1989(b); 9: 139-149.

Earnest F, Forbes G Sandok BA *et al* Complications of cerebral angiography: Prospective assessment of risk. American Journal of Roentgenology 1984; 142: 247-253.

Edelman RR, Ahn SS, Chien D, *et al.* Improved time-of-flight MR angiography of the brain with magnetization transfer contrast. Radiology 1992; 184: 395-399.

Edelman RR, Chien D, Atkinson DJ, Sandstrom J. Fast time-of-flight MR angiography with improved background suppression. Radiology 1991; 179: 867-870.

Edelstein WA, Hutchison JMS, Johnson G, Redpath TW. Spin warp NMR imaging and applications to the human whole body imaging. Physics in Medicine and Biology 1980; 25: 751-766.

Ehman RL, Felmlee JP. Adaptive technique for high definition MR imaging of moving structures. Radiology 1989; 173: 225-263.

Ehman RL, McNamara MT, Brasch RC *et al.* Influence of physiologic motion on the appearance of tissue in MR images. Radiology 1986; 159: 777-782.

Essig M, Reichenbach JR, Schad LR, *et al.* High-resolution MR venography of cerebral arteriovenous malformations. Magnetic Resonance Imaging 1999; 17: 1417-1425

Fischl B, Salat DH, Busa E, *et al.* Whole brain segmentation: automated labelling of neuroanatomical structures in the human brain. Neuron 2002; 33: 341-355.

Fletcher LM, Barsotti JB, Hornak JP. A multispectral analysis of brain tissues. Magnetic Resonance in Medicine 1993; 29: 623-630.

Franck O and Alwens W. Kreislanfstudien am rontgenschirm. Munchen Medizinische Wochenscrift 1910; 51: 1950-1953.

Gadian DG, Payne JA, Bryant DJ, *et al.* Gadolinium-DTPA as a contrast agent in MR imaging - theoretical projections and practical observations. Journal of Computer Assisted Tomograpy 1985; 9: 242-251.

Gao JH, Holland SK, Gore JC. Nuclear magnetic resonance signal from flowing nuclei in rapid imaging using gradient echoes. Medical Physics 1988; 15: 809-814.

Gariboldi MB, Ravizza R, Petterino C, *et al.* Study of in vitro and in vivo effects of piperdine nitroxide Tempol – a potential new therapeutic agent for gliomas. European Journal of Cancer 2003; 39: 829-837.

Gerig G, Martin J, Kikinis R, *et al.* Unsupervised tissue type segmentation of 3D

dual-echo MR head data. Image and Vision Computing 1992; 10: 349-360.

Giovannoni G, Miller DH, Losseff NA, *et al.* Serum inflammatory markers and clinical/MRI markers of disease progression in multiple sclerosis. Journal of Neurolgy 2001; 248: 487-495.

Gorter CJ, Broer LJF. Negative result of an attempt to observe nuclear magnetic resonance in solids. Physica (The Hague) 1942; 9: 591.

Graves MJ. Magnetic resonance angiography. British Journal of Radiology 1997; 70: 6-28.

Groothuis DR, Vriesendorp FJ, Kupfer B, *et al.* Quantitative measurements of capillary transport on human brain tumors by computed tomography. Annals of Neurology 1991; 30: 581-588.

Guerbert Web site. 2003 Financial Strategy Document. Available: http://www.guerbet.com/_pdf_swf/strategy_03_04.ppt. Published March 2004. Accessed: June 2004.

Haacke EM, Lenz GW. Improving MR image quality in the presence of motion by using rephasing gradients. American Journal of Roentgenology 1987; 148: 1251-1258.

Haase A, Matthaei D, Bartkowski R, *et al.* Inversion recovery snapshot FLASH MR imaging. Journal of Computer Assissted Tomography 1989; 13: 1036-1040

Haase A. Snapshot FLASH MRI. Applications to T1, T2, and chemical-shift imaging. Magnetic Resonance In Medicine 1990; 13: 77-89.

Hajnal JV, Saeed N, Oatridge A, *et al.* Detection of subtle brain changes using subvoxel registration and subtraction of serial MR images. Journal of Computer Assisted Tomography 1995; 19: 677-691.

Haney SM, Thompson PM, Cloughesy TF, *et al.* Tracking tumor growth rates in patients with malignant gliomas: a test of two algorithms. American Journal of Neuroradiology 2001: 22; 73-82.

Haschek E, Lindenthal OT. A contribution to the practical use of the photography according to Rontgen. Wein Klin Wochenschr 1896; 9: 63

Hassenbusch SJ, Nardone EM, Levin VA, *et al.* Stereotactic injection of DTI-015 into recurrent malignant gliomas: phase I/II trial. Neoplasia 2003; 5: 9-16.

Hausmann R, Lewin JS, Laub G. Phase-contrast MR angiography with reduced acquisition time: new concepts in sequence design. Journal of Magnetic Resonance Imaging 1991; 1: 514-522.

Heiserman JE, Dean BL, Hodak JA *et al.* Neurologic complications of cerebral angiography. American Journal of Neuroradiology 1994; 15: 1401-1407.

Hesselink JR, Press GA. MR contrast enhancement of intracranial lesions with Gd DTPA. Radiological Clinics of North America 1988; 26: 873-887.

Hinks RS, Xiang QS, Henkelman RM. Ghost phase cancellation with phase-encoding gradient modulation. Journal of Magnetic Resonance Imaging 1993; 3: 777-785.

Höhne KH, Hanson WA. Interactive 3D segmentation of MRI and CT volumes using morphological operations. Journal of Computer Assisted Tomography 1992; 16: 285-294.

ICRP. 1990 Recommendations of the International Commission on Radiological Protection. 1st edition. International Commission on Radiological Protection; ICRP publication 60; 1991, Oxford, New York: Pergamon Press.

Jack CR, Bentley MD, Twomey CK, Zinsmeister AR. MR imaging-based volume measurements of the hippocampal formation and anterior temporal lobe: validation studies. Radiology 1990; 176: 205-209.

Jain AK. Fundamentals of digital image processing. Englewood Cliffs: Prentice Hall 1989.

James K, Eisenhauer E, Christian M, *et al.* Measuring response in solid tumors: unidimensional versus bidimensional measurement. Journal of the National Cancer Institute 1999; 91: 523-528.

Jenkinson M, Bannister P, Brady M, Smith S. Improved optimization for the robust and accurate linear registration and motion correction of brain images. Neuroimage 2002; 17: 825-841.

Jennings MT, Frenchman M, Shehab T, *et al.* Gliomatosis cerebri presenting as intractable epilepsy during early childhood. Journal Child Neurology 1995; 10: 37-45.

Joshi M, Cui J, Doolittle K, *et al.* Brain segmentation and the generation of cortical surfaces. Neuroimage 1999; 9: 461-467.

Just M, Thelen M. Tissue characterization with T1, T2, and proton density values: Results in 160 patients with brain tumours. Radiology 1988; 169: 779-785.

Kao YH, Sorenson JA, Bahn MM, Winkler SS. Dual-echo MRI segmentation using vector decomposition and probability techniques: a two-tissue model. Magnetic Resonance in Medicine 1994; 32: 342-357.

Keller PJ, Drayer BP, Fram EK, *et al.* MR angiography with two-dimensional acquisition and three dimensional display: work in progress. Radiology 1989; 171: 801-806.

Kelly PJ, Daumas-Duport C, Scheithauer BW, *et al.* Stereotactic histologic correlations of computed tomography and magnetic resonance imaging-defined abnormalities in patients with glial neoplasms. Mayo Clinic Procedings 1987; 62: 450-459.

Kikinis R, Gleason PL, Moriarty TM, *et al.* Computer-assisted interactive three-dimensional planning for neurosurgical procedures. Neurosurgery 1996; 38: 640-649.

Kikinis R, Shenton ME, Gerig G, *et al.* Routine quantitative analysis of brain and cerebrospinal fluid spaces with MR imaging. Journal of Magnetic Resonance Imaging 1992; 2: 619-629.

Kischell ER, Kehtarnavaz N, Hillman GR, *et al.* Classification of brain compartments and head injury by neural networks applied to MRI. Diagnostic Neuroradiology 1995; 37: 535-541.

Kohn MI, Tanna NK, Herrman GT *et al.* Analysis of brain and cerebrospinal fluid volumes with MR imaging; part I. Methods, reliability and validation. Radiology 1991; 178: 115-122.

Kovanen J, Erkinjuntti T, Iivanainen M, *et al.* Cerebral MR and CT imaging in Creutzfeldt-Jakob disease. Journal of Computer Assisted Tomography 1985; 9: 125-128.

Kruger DG, Slavin GS, Muthupillai R, *et al.* An orthogonal correlation algorithm for ghost reduction in MRI. Magnetic Resonance in Medicine 1997: 38; 678-686.

Kumar A, Welti D, Ernst RR. NMR-Fourier-Zeugmatography. Journal of Magnetic Resonance 1975: 18; 69-83.

Kwon SU, Kim JC, Kim, JS. Sequential magnetic resonance imaging findings in hypereosinophilia-induced encephalopathy. Journal of Neurology 2001; 248: 279-284.

Lauterbur PC. Image formation by induced local interactions: examples employing nuclear magnetic resonance. Nature 1973; 242: 190-191.

Lee JM, Yoon U, Nam SH *et al.* Evaluation of automated and semi-automated skull stripping algorithms using similarity index and segmentation error. Computers in Biology and Medicine 2003; 33: 495-507.

Lemieux L, Hagemann G, Krakow K, Woermann FG. Fast, accurate, and reproducible automatic segmentation of the brain in T1-weighted volume MRI data. Magnetic Resonance in Medicine 1999; 42: 127-135.

Lemieux L, Hammers A, MacKinnon T, Liu RSN. Automatic segmentation of the brain and intracranial cerebrospinal fluid in T1-weighted volume MRI scans of the head, and its application to serial cerebral and intracranial volumetry. Magnetic Resonance in Medicine 2003; 49: 872-884.

Lenzlinger PM, Morganti-Kossmann KC, Laurer HL, McIntosh TK. The duality of the inflammatory response to traumatic brain injury. Molecular Neurobiology 2001; 24: 169-181.

Lerski RA, Straughan K, Schad LR, *et al.* MR image texture analysis: an approach to tissue characterization. Magnetic Resonance Imaging 1993; 11: 873-887.

Li D, Haacke EM, Mugler JP *et al.* Three dimensional time-of-flight MR angiography using selective inversion recovery RAGE with fat saturation and ECG-triggering: application to renal arteries. Magnetic Resonance in Medicine 1994; 31: 414-422.

Liauw L, van Buchem MA, Spilt A, *et al.* MR angiography of the intracranial venous system. Radiology 2000; 214: 678-682

Lin W, Mukherjee P, Hongyu A, *et al.* Improving high-resolution MR BOLD venographic imaging using a T1 reducing contrast agent. Journal of Magnetic Resonance Imaging 1999; 10: 118-123

Lin W, Tkach JA, Haacke EM, Masaryk TJ. Intracranial MR angiography: application of magnetisation transfer contrast and fat saturation to short gradient-echo velocity-compensated sequences. Radiology 1993; 186: 753-761.

Logothetis NK, Pauls J, Augath M, Trinath T, Oeltermann. Neurophysiological investigation of the basis of the fMRI signal. Nature 2001; 412: 150-157.

Long DM. Capillary ultrastucture in human metastatic brain tumors. Journal of Neurosurgery 1970; 32: 127-144.

Loubeyre P, De Jaegere T, Tran-Minh VA. Three-dimensional phase contrast MR cerebral venography with zero filling interpolation in the slice encoding direction. Magnetic Resonance Imaging 1999; 17: 1227-1233.

MacDonald D, Kabani N, Avis D, Evans AC. Automated 3-D extraction of inner and outer surfaces of cerebral cortex from MRI. Neuroimage 2000; 12: 340-365.

Magnevist German Patent. No: 3129906

Mallard J, Hutchinson JM, Edelstein W, *et al.* Imaging by nuclear magnetic resonance and its bio-medical implications. Journal of Biomedical Engineering 1979; 1: 153-160.

Mansfield P, Maudsley AA. Medical imaging by NMR. British Journal of Radiology 1977; 50: 188-194.

Mansfield P, Morris PG. NMR Imaging in Biomedicine: Supplement 2 – Advances in Magnetic Resonance. London: Academic Press 1982.

Månsson S, Bjørnerud A. Physical principles of medical imaging by nuclear medicine. In: Merbach AE, Tóth É, ed. The chemistry of contrast agents in medical magnetic resonance imaging. Chichester: John Wiley & Sons 2001: 1-43.

Markert JM, Medlock MD, Rabkin SD, *et al.* Conditionally replicating herpes simplex virus mutant G207 for the treatment of malignant glioma: results of a phase 1 trial. Gene Therapy 2000; 7: 867-874.

Martini FH. Fundamentals of anatomy & physiology 5th Edition. New Jersey: Prentice-Hall 2001.

Maruyama Y, Chin HW, Young AB, *et al.* Implantation of brain tumors with Cf-252. Use of computed tomography and magnetic resonance imaging to guide insertion and evaluate response. Radiology 1984; 152: 177-181.

Mattle H, Wentz K, Edelman R, *et al.* Cerebral venography with MR. Radiology 1991; 178: 453-458.

McParland. A study of patient radiation doses in interventional radiological procedures. British Journal of Radioloy 1998; 71: 175-185.

Meder JF, Chiras J, Roland J, *et al.* Venous territories of the brain. Journal of Neuroradiology 1994; 21: 118-133.

Merbach AE, Toth E. Preface. In: Merbach AE, Tóth É, ed. The chemistry of contrast agents in medical magnetic resonance imaging. Chichester: John Wiley & Sons 2001 xi-xii.

Miller AB, Hogestraeten B, Staquet M, Winkler A. Reporting results of cancer treatment. Cancer 1981; 47: 207-214.

Mitchell DG, Tasciyan T, Ortega HV, *et al.* Pulsation artifact in short TR MR imaging and angiography: Exacerbation with signal averaging. Journal of Magnetic Resonance Imaging 1994; 4: 709-718.

Moonis G, Liu J, Udupa JK, Hackney DB. Estimation of tumor volume with fuzzy-

connectedness segmentation of MR images. American Journal of Neuroradiology 2002; 23: 356-363.

Morris PP, Choi IS, Cerebral vascular anatomy. Neuroimaging Clinics of North America 1996; 3: 541-560.

Mugler J, Brookeman J. Three-dimensional magnetization-prepared rapid gradient-echo imaging (3D MP RAGE). Magnetic Resonance in Medicine 1990; 15: 152-157.

Mugler J, Brookeman J. Rapid three-dimensional T1-weighted MR imaging with the MP-RAGE sequence. Journal of Magnetic Resonance Imaging 1991; 1: 561-567.

Murphy KP, Szopinski KT Cohan RH, *et al*. Occurrence of adverse reactions to gadolinium-based contrast material and management of patients at increased risk: a survey of the American Society of Neuroradiology Fellowship Directors. Academic Radiology 1999; 6: 656-664.

Nelson SJ, Vigneron DB, Dillon WP. Serial evaluation of patients with brain tumours using volume MRI and 3D 1H MRSI. NMR in Biomedicine 1999; 12: 123-138.

Nir I, Kohn S, Doron Y, *et al*. Quantitative analysis of tight junctions and the uptake of 99mTc in human gliomas. Cancer Investigations 1986; 4: 519-524.

Nishimura DG, Macovski A, Pauly JM, Conolly SM. MR angiography by selective inversion recovery. Magnetic Resonance in Medicine 1987; 4: 193-202.

Nishimura DG. Time of Flight MR Angiography. Magnetic Resonance in Medicine 1990; 14: 194-201.

Ogawa S, Tank DW, Menon R, *et al.* Intrinsic signal changes accompanying sensory stimulation: Functional brain mapping with magnetic resonance imaging. Proceedings of the National Academy of Sciences of the United States of America 1992; 89: 5951-5955.

Ojeda L, Borenstein J. FLEXnav: Fuzzy logic expert rule-based position estimation for mobile robots on rugged terrain. Proceedings of IEEE International Conference on Robotics and Automation (Washington DC) 2002: 317-322.

Patel SH, Kolson DL, Glosser G, *et al.* Correlation between percentage of brain parenchymal volume and neurocognitive perfomance in HIV-infected patients. American Journal of Neuroradiology 2002; 23; 543-549.

Peck DJ, Windham JP, Soltanian-Zadeh H, Roebuck JR. A fast and accurate algorithm for volume determination in MRI. Medical Physics 1992; 19: 599-

605.

Pelc NJ, Bernstein MA, Shimakawa A, Glover GH. Encoding strategies for three-direction phase-contrast MR imaging of flow. Journal of Magnetic Resonance Imaging 1991; 1: 405-413.

Perkins TG, Wehrli FW. CSF signal enhancement in short gradient-echo images. Magnetic Resonance Imaging 1986; 4: 465-467.

Pham DL, Prince JL. Adaptive fuzzy segmentation of magnetic resonance images. IEEE Transactions on Medical Imaging 1999: 18; 737-752.

Phillips WE 2nd, Velthuizen RP, Phuphanich S, *et al.* Application of fuzzy c-means segmentation technique for tissue differentiation in MR images of a hemorrhagic glioblastoma multiforme. Magnetic Resonance Imaging 1995; 13: 277-290.

Pike GB, Hu BS, Glover GH, Enzmann DR. Magnetisation transfer time-of-flight magnetic resonance angiography. Magnetic Resonance in Medicine 1992; 25: 372-379.

Pomeranz SJ, Soila K, Tobias J, *et al.* Sensitivity of MRI in metastatic neoplasia: a case report. Magnetic Resonance Imaging 1985; 3: 291-293.

Powell HC, Lampert PW. Pathology of multiple sclerosis. Neurological Clinics 1983; 1: 631-644.

Press WH, Teukolsky SA, Vetterling WT, Flannery BP. Numerical recipes in C. 2nd edition. Cambridge University Press 1992; 683.

Purcell E, Torrey H, Pound R. Resonance absorption by nuclear magnetic moments in a solid. Physical Review 1946; 69: 37-38.

Rabi II, Zacharias JR, Millman S, Kusch P. A new method of measuring nuclear magnetic moment. Physical Review 1938; 53: 318.

Rajan B, Ross G, Lim CC, *et al.* Survival in patients with recurrent glioma as a measure of treatment efficacy: prognostic factors following nitrosourea chemotherapy. European Journal of Cancer 1994; 30A: 1809-1815.

Rampling R, Cruickshank G, Papanastassiou V, *et al.* Toxicity evaluation of replication competent herpes simplex virus (ICP 34.5 null mutant 1716) in patients with recurrent malignant glioma. Gene Therapy 2000; 7: 859-866.

Rao AB, Richert N, Howard T *et al.* Methylprednisolene effect on brain volume and enhancing lesions in MS before and during IFNbeta-1b. Neurology 2002; 59: 688-694.

Redpath TW. Signal-to-noise ratio in MRI. British Journal of Radiology 1998; 71: 704-707.

Reichenbach JR, Barth M, Haacke EM, *et al.* High-resolution MR venography at 3.0 tesla. Journal of Computer Assisted Tomography 2000; 24: 949-957.

Reichenbach JR, Essig M, Haacke EM *et al.* High-resolution venography of the brain using magnetic resonance imaging. Magnetic Resonance Materials in Physics, Biology and Medicine 1998; 6: 62-69

Reichenbach JR, Venkatesan R, Schillinger DJ *et al.* Small Vessels in the Human Brain: MR Venography with Deoxyhemoglobin as an Intrinsic Contrast Agent. Radiology 1997; 204: 272-277

Roberts TPL, Chuang N, Roberts HC. Neuroimaging: do we really need new contrast agents for MRI? European Journal of Radiology 2000; 34: 166-178.

Roux FE, Ibarrola D, Tremoulet M, *et al.* Methodological and technical issues for integrating functional magnetic resonance imaging data in a neuronavigational system. Neurosurgery 2001; 49: 1145-1157.

Ruggeri PM, Laub GA, Masaryk TJ, Modic MT. Intracranial circulation: pulse-sequence considerations in three-dimensional (volume) MR angiography. Radiology 1989; 171: 785-791.

Runge VM, Carollo BR, Wolf CR, *et al.* Gd DTPA: a review of clinical indications in the central nervous system magnetic resonance imaging. Radiographics 1989; 9: 929-958.

Runge VM, Clanton JA, Partain CL, James AK Jr. Respiratory gating in magnetic resonance imaging at 0.5T. Radiology 1984; 151; 521-523.

Runge VM, Muroff LR, Jinkins JR. Central nervous system: review of clinical use of contrast media. Topics in Magnetic Resonance Imaging 2001; 12; 231-263.

Saeed N, Hajnal JV, Oatridge A. Automated brain segmentation from single slice, multislice, or whole-volume MR scans using prior knowledge. Journal of Computer Assisted Tomography 1997; 21: 192-201.

Salcman M. The morbidity and mortality of brain tumours. A perspective on recent advances in therapy. Neurological Clinics 1985; 3: 229-257.

Schellinger PD, Meinck HM, Thron A. Diagnostic accuracy of MRI compared to CCT in patients with brain metastases. Journal of Neurooncology 1999; 44; 275-281.

Schott JM, Fox NC, Frost C, *et al.* Assessing the onset of structural change in familial Alzheimer's disease. Annals of Neurology 2003; 53: 181-188.

Scott JN, Rewcastle NB, Brasher PM *et al.* Which glioblastoma multifome patient willl become a long-term survivor? A population-based study. Annals of Neurology 1999; 46: 183-188.

Seitz RJ, Wechsler W. Immunohistochemical demonstration of serum proteins in human cerebral gliomas. Acta Neuropathologica 1987; 73: 145-152.

Setton A, Davis AJ, Bose A, Nelson PK, Berenstein A. Angiography of cerebral aneurysms. Neuroimaging Clinics of North America 1996; 6: 705-738.

Shan ZY, Yue GH, Liu JZ. Automated histogram-based brain segmentation in T1 weighted three dimensional magnetic resonance head images. Neuroimage 2002; 17: 1587-1598.

Shibata T. Ultrastucture of capillary walls in human brain tumours. Acta Neuropathologica 1989; 73: 145-152.

Simmons A, Arridge SR, Barker GJ, Williams SC. Sources of intensity nonuniformity in spin echo images at 1.5T. Magnetic Resonance in Medicine 1994; 32: 121-128.

Singer JR. Blood flow rates by nuclear magnetic resonance measurements. Science 1959; 130: 1652.

Smith SM. Fast robust automated brain extraction. Human Brain Mapping 2002; 17: 143-155.

SRI International Web Site. Magnetic resonance imaging: An MRI chronology. Available: http://www.sri.com/policy/stp/techin/mri2.html. Published Feb 1997 Accessed August 2003.

Stevenson J, Knopp EA, Litt AW. MP-RAGE Subtraction Venography: A New Technique. Journal of Magnetic Resonance Imaging 1995; 5: 239-241.

Stokking R, Vincken KL, Viergever MA. Automatic morphology-based brain segmentation (MBRASE) from MRI-T1 Data. Neuroimage 2000; 12: 726-738.

Stokking R. Integrated visualization of functional and anatomical brain images. Thesis (PhD). University of Utrecht 1998.

Studholme C, Cardenas V, Song E, *et al.* Accurate template-based correction of brain MRI intensity distortion with application to dementia and aging. IEEE Transactions on Medical Imaging 2004; 23: 99-110.

Suetens P, Bellon E, Vandermeulen D, *et al.* Image segmentation: methods and applications in diagnostic radiology and nuclear medicine. European Journal of Radiology 1993; 17: 14-21.

Surjan G. Nuclear resonance in flowing liquids. Proceedings Indian Academy of Science 1951; A33: 107.

Takeoka M, Kim F, Caviness VS, *et al.* MRI volumetric analysis in Rasmussen encephalitis: a longitudinal study. Epilepsia 2003; 44: 247-251.

Tan IL, van Schijndel RA, Pouwels PJW, *et al.* MR venography of multiple sclerosis. American Journal of Neuroradiology 2000; 21: 1039-1042

Taveras JM. Neuroradiology. Baltimore: Williams & Wilkins 1996.

Taxt T, Lundervold A, Fuglaas B, *et al.* Multispectral analysis of uterine corpus tumours in magnetic resonance imaging. Magnetic Resonance in Medicine 1992; 23: 55-76.

Thacker NA, Jackson A. Mathematical segmentation of grey matter, white matter and cerebral spinal fluid from MR image pairs. British Journal of Radiology 2001; 74: 234-242.

Therasse P, Arbuck SG, Eisenhauer EA, *et al.* New guidelines in evaluating the response to treatment in solid tumours. Journal of the National Cancer Institute 2000; 92: 205-216.

Udupa JK, Samarasekera S. Fuzzy connectedness and object definition: theory, algorithms and applications in image segmentation. Graphical Models and Image Processing 1996; 58: 246-261.

Van der Meulen P, Groen JP, Cuppen JJ. Very fast MR imaging by field echoes and small angle excitation. Magnetic Resonance Imaging 1985; 3: 297-299.

Vannier MW, Butterfield RL, Jordan D, *et al.* Multispectral analysis of magnetic resonance images. Radiology 1985; 154: 221-224.

Vannier MW, Speidel CM, Rickman DL. Magnetic resonance imaging multispectral tissue classification. News in Physiological Sciences 1998; 3: 148-154.

Wang CM, Yang SC, Chung PC, *et al.* Orthogonal subspace projection-based approaches to classification of MR image sequences. Computerized Medical Imaging and Graphics 2001; 25: 465-476.

Wang Y, Best DE, Hoffman JG *et al.* ACR-NEMA digital imaging and communications standards: minimum requirements. Radiology 1998; 166: 529-532.

Waugh JS. NMR Spectroscopy in solids: A historical perspective. Analytical Chemistry 1993; 65: 725A-729A.

Wehrli FW. Principles of Magnetic Resonance. In Magnetic Resonance Imaging. Ed: Stark DD, Bradley WG. Missouri: C.V. Mosby 1988.

WHO. WHO Classification of tumours of the nervous system.. In: Kleihues P and Cavenee WK (Eds). Pathology and Tumours of the nervous system. Lyon: International Agency for research on Cancer (IARC) Press 2000.

WHO. WHO handbook for reporting results of cancer treatment. Geneva (Switzerland). World Health Organisation Offset Publication No. 48; 1979.

Wood ML, Ehman RL. Effects of motion in MR imaging. In: Magnetic Resonance Imaging. Ed: Stark DD, Bradley WG. St Louis: Mosby- Year Book 1992: 145-164.

Wood ML, Henkelman RM. MR image artifacts from periodic motion. Medical Physics 1985; 12: 143-151.

Woods RP, Cherry SR Mazziotta JC. Rapid automated algorithm for aligning and reslicing PET images. Journal of Computer Assisted Tomography 1992; 16: 620-633.

Xu C, Pham DL, Rettmann ME, *et al*. Reconstruction of the human cerebral cortex from magnetic resonance images. IEEE Transcripts in Medical imaging 1999; 18: 467-480.

Zhou LQ, Zhu YM, Bergot C *et al*. A method of radio-frequency inhomogeneity correction for brain tissue segmentation in MRI. Computerized Medical Imaging and Graphics 2001; 25: 379-389.

Zijdenbos A, Dawant BM, Margolin RA, Palmer AC. Morphometric analysis of white matter lesions in MR images. IEEE Transcripts in Medical Imaging 1994; 13: 716-724.

Appendix 1

Binary Morphological Operators

A1.1 General Definitions

The morphological operators can be described using mathematical sets, where the following definitions apply:

A	is the image
$A \cup B$	is the union of the images A and B
$A \cap B$	is the intersection of the images A and B

A1.2 Dilation

It is possible to define dilation as

$$A \oplus B = \bigcup_{t \in A} B_t \tag{A1.1}$$

Here we take copies of B and translate them by movement vectors defined by each voxel in A. This can be interpreted as putting a copy of B at each voxel in A. Therefore, if we take the union all of the B copies with A we get $A \oplus B$. In this way, dilation works as a convolution, where the B kernel slides to each position in the image where it is applied (union). Dilation enlarges a volume and removes holes and indentations that are smaller than or equal to the applied kernel.

A1.3 Erosion

Erosion can be defined as

$$A \ominus B = \bigcap_{i \in B} B_{-i} \qquad (A1.5)$$

Here we take copies of A and translate them by movement vectors defined by each voxel in B, however, this time the translation is in the opposite direction and intersect the two copies. The intersect of B is applied at each voxel in A.

Erosion diminishes a volume and removes sub-volumes that cannot fill out the structuring element.

Appendix 2

Initial Venogram Protocol from Analyze Study

1. Load postcont data
2. Produce histogram of postcont data
3. Do analyze equivalent inhomogeneity correction on data with minimum threshold set to the minimum on the histogram data
4. Determine greyscale value of minimum on histogram of corrected data
5. Determine greyscale value of maximum on histogram of corrected data
6. Set threshold levels on corrected data to 1.5*min to max+min
7. If the number of pixels at the higher threshold is greater than the number of pixels at min then increase higher threshold until reverse is true
8. Threshold corrected data and save binary map (thres_bin) and corrected data (postcont_corr)
9. Erode binary map once and then low pass filter using kernal (3x3x3)
10. Run a connect algorithm on the data to display the two largest structures
11. (a) Test the two structures for size and relative size to each other, to check that segmentation will work. If it will not work stop here.

    (b) If largest structure is very large and the smallest very small a further erode is require.

    (c) Go back to data produced from 9 and erode 2, filter and connect.

    (d) One extra dilate must be carried out at the time of conditional dilate
12. Calculate the average inferior/posterior position for the two sets of data.
13. The more superior set of data in retained and the other is deleted
14. Conditionally dilate the data using the threshold data from 8 three times (four if extra erode was used in 11)
15. Multiply resulting binary with postcont data to produce postcont_fA

16. Threshold corrected data from 3 from voxel value 1 to twice the minimum calculated in 4.

17. This data is complimented and then filled and then multiplied with the data from 16 to produce the CSF mask.

18. Conditionally dilate the binary data from 14 using csf_mask as the condition and fill.

19. Connect this data to keep the largest object' i.e. removing noise

20. Multiply this data with postcont and precontrs! and subtract the results

21. Resultant data should be saved and can be viewed using Analyze as a maximum intensity projection (MIP).

Appendix 3

IDL Automatic Venography Program

A3.1 Main Program

```
pro auto_veno


; This section finds out the name and location of the files and does
;some data checks

print,'Please enter the name of the pre contrast file'
filename_pre=dialog_pickfile(filter='*.img',title='Please enter the
name of the pre contrast file')


; Use unix command 'readspacing' to determine image dimensions and
; voxel sizes for pre data

name_len = strlen(filename_pre)
short_len = name_len-4
filename_pre_short = strmid(filename_pre,0,short_len)
spawn_command = 'readspacing ' + filename_pre_short
spawn, spawn_command,header_info
sizematx_pre=float(header_info(0))
sizematy_pre=float(header_info(1))
slicemat_pre=float(header_info(2))
scalex_pre=float(header_info(3))
scaley_pre=float(header_info(4))
scalez_pre=float(header_info(5))

print,'Please enter the name of the post contrast file '
filename_post = dialog_pickfile(filter='*.img',title='Please enter
the name of the post contrast file')

; Use unix command 'readspacing' to determine image dimensions and
; voxel sizes for
; post data

name_len = strlen(filename_post)
short_len = name_len-4
filename_post_short = strmid(filename_post,0,short_len)
spawn_command = 'readspacing ' + filename_post_short
spawn, spawn_command,header_info
sizematx_post=float(header_info(0))
sizematy_post=float(header_info(1))
slicemat_post=float(header_info(2))
scalex_post=float(header_info(3))
scaley_post=float(header_info(4))
scalez_post=float(header_info(5))

; Compare image attributes for pre and post. Should be the same

if (sizematx_pre NE sizematx_post) OR (sizematy_pre NE
sizematy_post) OR (slicemat_pre NE slicemat_post) then begin
      print, 'The matrix sizes do not match'
      stop
endif
if (scalex_pre NE scalex_post) OR (scaley_pre NE scaley_post) OR
(scalez_pre NE scalez_post) then begin
```

```
      print, 'The voxel dimensions do match'
      stop
endif


; Select name for final data to be saved as

print,'Please enter the name of the output final file'
filename_out = dialog_pickfile(filter='*.img',title='Please enter
the name of the output final file')



;Open post contrast file and set variable postcont_data to data

openr,lun_post,filename_post,/get_lun

; Determine file attributes ie what is the file size and thus the
; bytes per pixel then initiate variable

poststatus=fstat(lun_post)
postbytes=
poststatus.size/(sizematx_post*sizematy_post*slicemat_post)
if (postbytes eq 1) then begin
      postcont_data =
bytarr(sizematx_post,sizematy_post,slicemat_post)
      filtpost=bytarr(sizematx_post,sizematy_post,slicemat_post)
endif
if (postbytes eq 2) then begin
      postcont_data =
intarr(sizematx_post,sizematy_post,slicemat_post)
      filtpost=intarr(sizematx_post,sizematy_post,slicemat_post)
endif
readu,lun_post,postcont_data
free_lun,lun_post


;;;;;;;;;;;;;;;;;;;;;;;;;;;;;;;;HISTOGRAM AND FILTER;;;;;;;;;;;;;;;;
;
;
; This section produces a histogram of the post contrast data and
; finds the minimum value below the gray and white matter peak.
;

; This section tests to find maximum value position so that range to
; find minimum can be determined


postcont_max_min,postcont_data,temp_max,post_minimum

print,post_minimum

; Now filter post contrast data using post_minimum as the minimum
; threshold for the filter. This filter is a INHOMOGENEITY FILTER
; based on the one used by analyze

; First threshold the data to only include pixels above the variable
; minhisto
```

```
; Now filter threshpost using filter of size 65

; calculate global mean!!!!!! ADD THIS SECTION!!!!!!!


global_thresh = postcont_data ge post_minimum
wh_global = where(global_thresh,cnt)
global_mean=mean(postcont_data[wh_global])

for filt_loop=0,slicemat_post-1 do begin
      print,filt_loop
      l=postcont_data[*,*,filt_loop]
      m = l ge post_minimum
      l =
l*global_mean*(smooth(float(m),65,/edge)/(smooth(l*m,65,/edge)+1.e-
30))
      filtpost[*,*,filt_loop]=l
endfor
filtzero = filtpost LE 0
whzero = where(filtzero,cnt)
filtpost[whzero]=postcont_data[whzero]



;;;;;;;;;;;;;;;;HISTOGRAM OF FILTERED DATA TO SET THRESHOLDS;;;;;;;;
;
;
; This section takes the now filtered data and using histogram
; decides on the thresholds for the segmentation section
;

postcont_max_min,filtpost,filt_max,filt_min,histo_filt

thresh_min = ceil(float(filt_min)*0.5)+ filt_min
thresh_max = filt_max+filt_min
;histo_filt_size=size(histo_filt)

; Check that no. of pixels in higher threshold is less than the
; number of pixels in the lower threshold. This improves
; segmentation.

if (histo_filt[filt_min] lt histo_filt[thresh_max]) then begin
      true = 0
      while(true EQ 0) do begin
            thresh_max= thresh_max+1
            if (histo_filt[filt_min] gt histo_filt[thresh_max]) then
break
      endwhile
endif
print, thresh_min,thresh_max



;;;;;;;;;;THRESHOLD THE FILTERED DATA WITH THE NEW THRESHOLDS;;;;;;;
;
;
; This section takes the calculated thresholds and applies them to
; the filtered data producing binary thresholded data. This data is
; then segmented using morphology. This data is also used as the
; conditional mask for the conditional dilations within the
```

```
; segmentation section
;

binary_thresh_map = (filtpost ge thresh_min) AND (filtpost le
thresh_max)



;;;;;;;;;;;;;;;;;;;;;;;;;;;;;;;;MORPHOLOGY SECTION;;;;;;;;;;;;;;;;;;;;;;
;
;
; This section contains the segmentation morphology routines. This
; includes erode, low pass filter conditional dilate and connect.
; The aim is to produce a seperated brain for use in MATCH
;


; First erode the binary map once
erode_kernal=replicate(1,3,3,3)
eroded_seg = erode(binary_thresh_map,erode_kernal)


; Now need to do low pass filter on data. First do convol and then
; threshold this. If all pixels are 1's a pixel would be given a
; value of 27. Therefore set threshold to slightly above half this
; value, i.e. 15 to low pass.


eroded_seg_temp = convol(eroded_seg,erode_kernal,/edge_truncate)
eroded_seg = eroded_seg_temp gt 15


; Now use label_region command to do connections. Need to use
; histogram to determine the two largest connected regions


connected_seg = label_region(eroded_seg)
histo_connected = histogram(connected_seg)
histo_connected[0]=0
large_blob_no = max(histo_connected,large_blob_level)
histo_connected[large_blob_level]=0
small_blob_no = max(histo_connected,small_blob_level)
large_blob= connected_seg EQ large_blob_level
large_blob_temp = where(large_blob,large_blob_pixels)
large_blob_pixels=float(large_blob_pixels)
small_blob= connected_seg EQ small_blob_level
small_blob_temp = where(small_blob,small_blob_pixels)
small_blob_pixels=float(small_blob_pixels)



;;;;;;;;;;;;;;;;;;;;;;;;;;;;;;;;;;;;;;;;;;;;;;;;;;;;;;;;;;;;;;;;;;;;;;;;;;;;
; Now check that regions are of the correct size and ration of
; sizes. This checks that the segmentation has occurred correctly.
; If one set of data has a small amount of pixels say less than
; 10000 and small_blob/large_blob is less than 15% and       ;
; large_blob is less than 500000 pixels then the data is too noisy
; and cannot be segmented. If small_blob is less than 10000 and
; small_blob/large_blob is less than 5% and large_blob is greater
; than 300000 pixels then a further erode is required.  ;
```

```
blob_ratio = small_blob_pixels/large_blob_pixels
print,blob_ratio
cond_dilate_number=3
if (blob_ratio lt 0.10) then begin
      if (large_blob_no gt 500000) then begin
            print,'Conducting extra erode on data'
            cond_dilate_number=4
            eroded_seg = erode(eroded_seg,erode_kernal)
            connected_seg = label_region(eroded_seg)
            histo_connected = histogram(connected_seg)
            histo_connected[0]=0
            large_blob_no = max(histo_connected,large_blob_level)
            histo_connected[large_blob_level]=0
            small_blob_no = max(histo_connected,small_blob_level)
            large_blob= connected_seg EQ large_blob_level
            small_blob= connected_seg EQ small_blob_level
      endif else begin
            print,'The data is too noisy for segmentation!'
            stop
      endelse
endif


; Now need to test the average inferior/superior positions of the
; two blobs. The more superior blob will be the brain, with the
; inferior blob being extracranial tissue.


large_average=0
small_average=0
for slicenum=0,slicemat_post-1 do begin
      large_wh =
fix((where(large_blob[*,*,slicenum],large_cnt))/sizematx_post)
      small_wh =
fix((where(small_blob[*,*,slicenum],small_cnt))/sizematx_post)
      if (total(large_wh) NE 0) then large_average =
(total(large_wh))/large_cnt + large_average
      if (total(small_wh) NE 0) then small_average =
(total(small_wh))/small_cnt + small_average
endfor


; The expression below is less than because data loads in upside
; down!!

if (large_average lt small_average) then begin
      brain_erode_binary = large_blob
endif else begin
      brain_erode_binary = small_blob
endelse



; The data must now be conditionally dilated 3 times if only one
; erode was done and 4 times if two were done. The conditional mask
; used here is binary_thresh_map


final_match=brain_erode_binary
```

```
for cond_dilate = 1,cond_dilate_number do begin
      final_match = dilate(final_match,erode_kernal)
      final_match = final_match*binary_thresh_map
endfor

postcont_fA=final_match * postcont_data

;;;;;;;;;;;;;;;;;;;;;;;PRODUCE VENOGRAM MASK;;;;;;;;;;;;;;;;;;;;;;;;;;
;
;
; This section now produces the venogram mask using the filtered
; postcont data 'filtpost'. It uses morphology to produce the mask
;



vein_thresh = filt_min*2
vein_thresh_data=filtpost ge vein_thresh
csf_thresh_data = filtpost lt vein_thresh



; This section fills the thresholded data so that after
; multiplication with the csf_thresh data a mask of the csf will be
; produced. This section uses the procedure AUTO_FILL



filled_data = bytarr(sizematx_post,sizematy_post,slicemat_post)
auto_fill,vein_thresh_data,filled_head,sizematx_post,sizematy_post,s
licemat_post

csf_mask = filled_head*csf_thresh_data


; Now use LABEL_REGION to remove unconnected data leaving only
; required csf_mask


csf_mask = label_region(csf_mask,/ulong)
histo_csf=histogram(csf_mask)
histo_csf[0]=0

csf_temp=max(histo_csf,csf_blob_value)

csf_mask=csf_mask EQ csf_blob_value


; Now need to conditionally dilate the segmented data 10 times using
; the csf_mask as the condition. This data is then filled and this
; is the final mask data that is used to produce the final
; subtraction data


for cond_dilate = 1,12 do begin
      final_match = dilate(final_match,erode_kernal)
      final_match = final_match*csf_mask
endfor
```

```
; Filling section

final_mask=bytarr(sizematx_post,sizomaty_post,slicemat_post)
auto_fill,final_match,filled_mask,sizematx_post,sizematy_post,slicem
at_post

;Do a final connect in sagittal 2D slices to get rid of noise around
; brain and vessels

final_mask=filled_mask
histo_final=histogram(csf_mask)
histo_final[0]=0

final_temp=max(histo_final,final_value)

final_mask=final_mask EQ final_value



mask_out=fix(final_mask)
openw,lun_out,'mask.img',/get_lun
writeu,lun_out,mask_out
free_lun,lun_out

;;;;;;;;;;;;;;;;;;;;;RUNNING MATCH SOFTWARE;;;;;;;;;;;;;;;;;;;;;;;;;
;
;
; This section now saves the segmented data, postcont_fA and runs
; the MATCH software. It works out the file names that need to be
; used. The program waits for MATCH to finish.
;


postcont_fA_name=filename_post_short +"_fA.img"
openw,lun_fA,postcont_fA_name,/get_lun
writeu,lun_fA,postcont_fA
free_lun,lun_fA

header_orig=filename_post_short +".hdr"
header_copy=filename_post_short +"_fA.hdr"
copycommand="cp " +header_orig + " " +header_copy
spawn,copycommand

matchcommand="match " +filename_post +" " +filename_pre
print
print,"RUNNING THE MATCH SOFTWARE"
print,'This may take some time!!'

print,matchcommand
spawn,matchcommand


;;;;;;;;;;;;DELETION OF UNECESSARY FILES FROM MATCH;;;;;;;;;;;;;;;;;
;
;
; This section saves on disk space by deleting unecessary files
; produced by the match program
;
```

```
file1=filename_post_short +"_21.*"
file2=filename_post_short +"t.*"
file3=filename_pre_short +"rslt.*"

spawn,"/bin/rm " + file1 + " " + file2 + " " + file3




; Now need to multiply mask with postcont and precontrsl data and do
; subtraction. First need to load the precontrsl data


filename_prersl=filename_pre_short + "rsl.img"
openr,lun_pre,filename_prersl,/get_lun



; Determine file attributes ie what is the file size and thus the
; bytes per pixel then initiate variable


prestatus=fstat(lun_pre)
prebytes= prestatus.size/(sizematx_pre*sizematy_pre*slicemat_pre)
if (prebytes eq 1) then begin
      precont_data = bytarr(sizematx_pre,sizematy_pre,slicemat_pre)
endif
if (prebytes eq 2) then begin
      precont_data = intarr(sizematx_pre,sizematy_pre,slicemat_pre)
endif
readu,lun_pre,precont_data
free_lun,lun_pre

;Now that data is loaded multiply mask with pre and post data

postcont_masked = postcont_data*final_mask
precont_masked = precont_data*final_mask

final=postcont_masked - precont_masked


; The data should now be saved to disk to allow it to be viewed
; using a MIP algorithm


openw,lun_out,filename_out,/get_lun
writeu,lun_out,final
free_lun,lun_out


end
```

A3.2 Function 1: postcont_max_min

```
pro postcont_max_min, postcont_data,max_val,post_minimum,histo_post

histo_post = histogram(postcont_data,min=0)
histo_post_max = histo_post
histo_post_min=histo_post
histo_size = size(histo_post)
first=1
test = 0
while (test NE 1) do begin
      maxim = max(histo_post_max,max_val)
      if (max_val GT 5) AND (first EQ 1) then begin
            print,' Problem with histogram data'
            stop
      endif
      if (first EQ 1) then begin
            if (max_val GT 0) then begin
                  histo_post_max[0:max_val-1]=0
                  histo_post_min[0:max_val-1]=maxim
            endif
            first =0
      endif else begin
            submax = max_val-old_max
            if (submax NE 1) AND (max_val GT 10) then begin
                  histo_post_max[old_max+1]=0
                  max_temp = max(histo_post_max,max_val)
                  min_temp =
min(histo_post_min[0:max_val],post_minimum)
                  break
            endif
      endelse

      histo_post_max[max_val]=0
      old_max=max_val
endwhile

print,post_minimum,max_val

end
```

A3.3 Function 2: auto_fill

```
pro auto_fill,data_in,filled,sizematx,sizematy,slicemat

print,'Starting Analyze equivalent fill'

filled = bytarr(sizematx,sizematy,slicemat)
print,'Stage 1'
y =bytarr(sizematx,sizematy)
for slicez = 0,slicemat-1 do begin
      y(*,*)=1

      ; The following lines are added to ensure that search2d works
      ; even when the head extends beyond the imaging volume. If
      ; this occurs unwanted areas can be filled. By setting the
      ; edges to zero this is avoided

      x = data_in(*,*,slicez)
      x(0,*)=0
      x(*,0)=0
      x(sizematx-1,*)=0
      x(*,sizematy-1)=0

      ; Search assumes that point 0,0 in each image has value of
      ; zero

      region = search2d(x,0,0,0,0)
      y(region)=0
      filled(*,*,slicez)=y

endfor

print,'Stage 2'
y = bytarr(sizematy,slicemat)
for pixelx = 0,sizematx-1 do begin
      y(*,*)=1
      x = reform(filled(pixelx,*,*),sizematy,slicemat)
      x(0,*)=0
      x(*,0)=0
      x(sizematy-1,*)=0
      x(*,slicemat-1)=0
      region=search2d(x,0,0,0,0)
      y(region)=0
      filled(pixelx,*,*)=y
endfor


print,'Stage 3'
y = bytarr(sizematx,slicemat)
for pixely = 0,sizematy-1 do begin
      y(*,*)=1
      x = reform(filled(*,pixely,*),sizematx,slicemat)
      x(0,*)=0
      x(*,0)=0
      x(sizematx-1,*)=0
      x(*,slicemat-1)=0
      region=search2d(x,0,0,0,0)
      y(region)=0
      filled(*,pixely,*)=y
endfor
```

```
Print,'Final stage'
y =bytarr(sizematx,sizematy)
for slicez = 0,slicemat-1 do begin
      y(*,*)=1
      x = filled(*,*,slicez)
      x(0,*)=0
      x(*,0)=0
      x(sizematx-1,*)=0
      x(*,sizematy-1)=0
      region = search2d(x,0,0,0,0)
      y(region)=0
      filled(*,*,slicez)=y

endfor
end
```